Aus dem Biomedizinischen Zentrum
Institut der Ludwig-Maximilians-Universität München
Lehrstuhl für Stoffwechselbiochemie
Vorstand: Prof. Dr. rer. nat. Dr. h.c. Christian Haass

Pathological Consequences of NPC1 Loss in Microglia on Brain Function

Dissertation
zum Erwerb des Doktorgrades der Naturwissenschaften
an der Medizinischen Fakultät der
Ludwig-Maximilians-Universität zu München

vorgelegt von

Lina Dinkel

aus

Nagold, Deutschland

2023

Mit Genehmigung der Medizinischen Fakultät
der Universität München

Betreuer:	Prof. Dr. rer. nat. Harald Steiner
Zweitgutachterin:	Prof. Dr. rer. nat. Antje Grosche
Dekan:	Prof. Dr. med. Thomas Gudermann
Tag der mündlichen Prüfung:	22. November 2023

In dedication to all NPC patients.

Table of Contents

Zusammenfassung

Die Niemann-Pick-Krankheit Typ C (NPC) ist eine lysosomale Speicherkrankheit, die hauptsächlich durch Mutationen im späten endosomalen/lysosomalen Transmembranprotein NPC1 verursacht wird. Charakteristisch für NPC ist die abnormale Lipidspeicherung in späten endosomalen/lysosomalen Kompartimenten, die zu einer schweren und schnell fortschreitenden Neurodegeneration führt, die von Hypomyelinisierung, Astrogliose und Mikrogliose begleitet wird. Bislang wurden die zellspezifischen Folgen des Verlustes von NPC1 in Neuronen, Oligodendrozyten und Astrozyten untersucht, während über die Folgen des Verlustes von NPC1 für die Mikroglia und ihren Beitrag zum Fortschreiten der NPC-Krankheit weniger bekannt ist. In dieser Arbeit habe ich die zellautonomen Folgen des Verlustes von NPC1 in den Mikroglia sowie deren Auswirkungen auf andere Gehirnzellen und auf das Fortschreiten der Krankheit charakterisiert. Ich konnte zeigen, dass Veränderungen der Mikroglia in NPC vor der Neurodegeneration auftreten. NPC1-defiziente Mikroglia wechselten zu einem krankheitsassoziierten Mikroglia-Phänotyp, bei dem sich Veränderungen in späten endosomalen/lysosomalen Kompartimenten als früheste Veränderung manifestierten, begleitet von einer schweren Dyshomöostase von Lipiden. Die molekularen Konsequenzen des Verlustes von NPC1 wandelten sich in funktionelle Beeinträchtigungen um, die sich in erhöhter Phagozytose und Defekten im Transport von Lipiden widerspiegelten. Phagozytiertes Myelin sammelte sich in multivesikulären Körperchen (MVK) an, die in NPC1-defizienten Mikroglia angereichert waren. Im Gegensatz dazu waren die lysosomalen Veränderungen begrenzt, und ihre proteolytische Aktivität blieb in NPC1-defizienten Mikroglia erhalten, was darauf hindeutet, dass die größte pathologische Belastung bei NPC in den MVKs und nicht in den Lysosomen auftritt. Da die auffälligen mikroglialen Veränderungen bei NPC früh auftreten, wurden ihre Auswirkungen auf andere Gehirnzellen in einem Mausmodell untersucht, bei dem NPC1 nur aus myeloischen Zellen und damit nur aus den Mikroglia im Gehirn entfernt wurde. Der Verlust von NPC1 in den Mikroglia reichte aus, um die wichtigsten Merkmale von NPC auszulösen, nämlich Mikrogliose, Astrogliose und neuronale Pathologie. Diese Ergebnisse bestätigen, dass Mikroglia zum Fortschreiten der Pathologie in NPC beitragen und dass der Verlust der Mikrogliafunktion nachteilige Folgen für die Homöostase des Gehirns hat. Molekulare und funktionelle Veränderungen der Mikroglia wurden in Makrophagen aus dem Blut von NPC-Patienten rekapituliert, was die Bedeutung der NPC1-Funktion in myeloischen Zellen weiter unterstreicht. Diese enge Beziehung ermöglicht es, NPC-Makrophagen als Stellvertreter für die Mikrogliafunktion zu verwenden, was ein leistungsstarkes Instrument zur Überwachung therapeutischer Interventionen darstellt. Zusammenfassend lässt sich sagen, dass Mikroglia aktiv zur Pathologie des Gehirns in NPC beitragen und für therapeutische Interventionen in Betracht gezogen werden sollten.

Summary

Niemann-Pick disease type C (NPC) is a lysosomal storage disorder primarily caused by mutations in the late endosomal/lysosomal transmembrane protein NPC1. NPC is characterised by abnormal lipid storage within late endosomal/lysosomal compartments driving a severe and fast progressive neurodegeneration accompanied by hypomyelination, astrogliosis and microgliosis. Up to now, cell-specific consequences of NPC1 loss in neurons, oligodendrocytes and astrocytes have been investigated, while less is known about microglial consequences upon NPC1 loss and the contribution to NPC progression. Here, I deeply characterised cell-autonomous consequences of NPC1 loss in microglia as well as their impact on other brain cells and disease progression. I could show that microglial alterations in NPC occur ahead of neurodegeneration. NPC1-deficient microglia switched to a disease-associated microglial phenotype in which late endosomal/lysosomal alterations manifested as earliest alteration accompanied by severe lipid dyshomeostasis. Molecular consequences of NPC1 loss converted into functional impairments reflected by increased phagocytosis and lipid trafficking defects. Phagocytosed myelin accumulated in multivesicular bodies (MVBs), which were enriched in NPC1-deficient microglia. In contrast, lysosomal alterations were limited and their proteolytic activity was still preserved in NPC1-deficient microglia, revisiting that the major pathological burden in NPC occurs in MVBs rather than in lysosomes. Since prominent microglial changes occurred early in NPC, their impact on other brain cells was assessed in a mouse model in which NPC1 was only depleted from myeloid cells, and thereby, only from the microglia in the brain. Loss of NPC1 in microglia was sufficient to drive major hallmarks of NPC disease, namely microgliosis, astrogliosis and neuronal pathology. These results confirm that microglia contribute to NPC progression and that loss of microglial function has detrimental consequences for brain homeostasis. Microglial molecular and functional alterations were recapitulated in blood-derived macrophages from NPC patients, further highlighting the relevance of NPC1 function in myeloid cells. This close relation allows to use NPC macrophages as a proxy for microglial function, providing a powerful tool to monitor therapeutic interventions. Concludingly, microglia actively contribute to NPC brain pathology and should be considered for therapeutic interventions.

List of Figures

List of Tables

List of Abbreviations

Abbreviation	**Definition**
ABC	ATP-binding cassette
ABI3	ABI gene family member 3
ACACA	Acetyl-CoA carboxylase 1
ACAT1/2	Acetyl-CoA acetyltransferase 1/2
ACSA-2	Astrocyte cell surface antigen-2
AD	Alzheimer’s disease
AGC	Automatic gain control
ANXA6	Annexin A6
APOB48	Apolipoprotein B48
APOE	Apolipoprotein E
APP	Amyloid-beta precursor protein
APS	Ammoniumperoxodisulfat
ATG5/7	Autophagy protein 5/7
ATP	Adenosine triphosphate
Aβ	Amyloid-β
BBB	Blood-brain barrier
BMP	Bis(monoacylglycero)phosphate
BSA	Bovine serum albumin
C1QA/B/C	Complement component 1 q subcomponent subunit A/B/C
C4B	Complement C4-B
CCL3	C-C chemokine ligand 3
CD11b	CD11 antigen-like family member B
CD31	Cluster of differentiation 31
CD68	Cluster of differentiation 68
CE	Cholesteryl ester
CLEC7A	C-type lectin domain family 7 member A
CNPase	2',3'-cyclic-nucleotide 3'-phosphodiesterase
CNS	Central nervous system
CR3	Complement receptor 3
CSF1R	Macrophage colony-stimulating factor 1 receptor
CTD	C-terminal domain
CTSB/D	Cathepsin B/D
CtxB	Cholera toxin subunit B
Cvs	Coverslips
CX3CR1	CX3C chemokine receptor 1
CYBB	Cytochrome b-245 heavy chain
CYP46A1	Cholesterol 24-hydroxylase
DAM	Disease-associated microglia
DDA	Data dependent acquisition
DG	Diacylglycerol
DHCR	7-dehydrocholesterol reductase
DIA	Data independent acquisition
DIA-PASEF	Data Independent Acquisition Parallel Accumulation Serial Fragmentation
DIV	Days *in vitro*
EDTA	Ethylenediaminetetraacetic acid
EGFR	Epidermal growth factor receptor
ER	Endoplasmic reticulum

ESCRT	Endosomal sorting complex required for transport
FACS	Fluorescence activated cell sorting
FASP	Filter aided sample preparation
FDG	Fluoro-D-glucose
FDPS	Farnesyl pyrophosphate synthase
FDR	False discovery rate
FGE	Formylglycine-generating enzyme
FPP	Farnesyl pyrophosphate
FTD	Frontotemporal dementia
GALC	Galactocerebrosidase
GalCer	Galactosylceramide
GBA	Beta-glucocerebrosidase
GFAP	Glial fibrillary acidic protein
GGPS1	Geranylgeranyl pyrophosphate synthase
GlcCer	Glucosylceramide
GO	Gene ontology
GRN	Progranulin
GSR	Glutathione reductase
GSTM1/5	Glutathione S-transferase Mu 1/5
GSTO1	Glutathione S-transferase omega-1
HBSS	Hanks' balanced salt solution
HDACi	Histone deacetylase inhibitor
HDL	High density lipoprotein
HEXA	Beta-hexosaminidase subunit alpha
HEXB	Beta-hexosaminidase subunit beta
HexCer	Hexosylceramide
HMGCR	3-hydroxy-3-methylglutaryl-CoA reductase
HP-β-CD	Hydroxypropyl-β-cyclodextrin
Iba1	Ionized calcium-binding adapter molecule 1
ICC	Immunocytochemistry
IGF1	Insulin-like growth factor I
IHC	Immunohistochemistry
IL1B	Interleukin-1β
IL-3	Interleukin-3
ILV	Intraluminal vesicle
IPA	Ingenuity pathway analysis
ITGAX	Integrin alpha-X
LacCer	Lactosylceramide
LAMP1	Lysosome-associated membrane glycoprotein 1
LC3	Microtubule-associated protein 1A/1B-light chain 3
LDL	Low-density lipoprotein
LDLR	Low-density lipoprotein receptor
LFQ	Label-free quantification
LGALS3	Galectin-3
LIPA	Lysosomal acid lipase
LPG	Lysophosphatidylglycerol
LPLA2	Lysosomal PLA2
LSD	Lysosomal storage disorder
M6PR	Mannose-6-phosphate receptor
MACS	Magnetic-activated cell sorting
MaLR	Mammalian apparent LTR

MAO-B	Monoamine oxidase type B
MBP	Myelin basic protein
MCS	Membrane contact site
MLD	Middle luminal domain
MRC1	Macrophage mannose receptor 1
MRI	Magnetic resonance imaging
MRM	Multiple reaction monitoring mode
MS	Mass spectrometry
mTORC1	Mechanistic target of rapamycin complex 1
MVB	Multivesicular body
MβCD	Methyl-β-cyclodextrin
NALL	*N*-acetyl-L-leucine
NCE	Normalised collision energy
NCL	Neuronal ceroid lipofuscinoses
NeuN	Neuronal nuclei antigen
NF200	Neurofilament heavy chain
NF-L	Neurofilament light chain
NGF	β-nerve growth factor
NOX-2	NADPH oxidase 2
NPA/B/C/D	Niemann-Pick disease type A/B/C/D
NPC1/2	Niemann-Pick C1/2 protein
NPC1L1	Niemann-Pick C1-like-1
NT3	Neurotrophin-3
NTD	N-terminal domain
OPC	Oligodendrocyte precursor cell
ORP1L	Oxysterol-binding protein-related protein 1
P2RY12	P2Y purinoceptor 12
PBMC	Peripheral-blood mononuclear cells
PBS	Phosphate buffered saline
PD	Parkinson’s disease
Pen/Strep	Penicillin/streptomycin
PET	Positron emission tomography
PFA	Paraformaldehyde
PG	Phosphatidylglycerol
PI(3)P	Phosphatidylinositol 3-phosphate
PLA2	Phospholipase A2
PLIN2/4	Perilipin 2/4
PLL	Poly-L-lysine hydrobromide
PLP1	Proteolipid protein 1
PS1	Presenilin-1
PtdIns4P	Phosphatidylinositol 4-phosphate
PUFA	Polyunsaturated fatty acid
PVDF	Polyvinylidene difluoride
RAB5/7/8A/27A/43	Ras-associated binding protein 5/7/8A/27A/43
ROS	Reactive oxygen species
RT	Room temperature
SCAP	SREBP cleavage-activating protein
scRadiotracing	Single cell radiotracing
SDS	Sodium dodecyl sulfate
SEM	Standard error of the mean
SLC38A	Sodium-coupled neutral amino acid transporter

SNARE	Soluble N-ethylmaleimide-sensitive-factor attachment receptor
SP3	Single-pot solid-phase enhanced sample preparation
SPP1	Secreted phosphoprotein 1
SRD5A3	Polyprenol reductase
SRE	Sterol regulatory element
SREBP	Sterol regulatory element-binding protein
SSD	Sterol-sensing domain
STARD3	StAR-related lipid transfer protein 3
SUV	Standardised uptake value
SVZ	Subventricular zone
SYP	Synaptophysin
TAE	Tris-acetate-EDTA
TBC1D15	TBC1 domain family member 15
TBS	Tris-buffered saline
TEMED	Tetramethylethylenediamine
TFEB	Transcription factor EB
TG	Triacylglyceride
TGFB1	Transforming growth factor beta-1 proprotein
TGFBR1	TGF-beta receptor type-1
TGN	*Trans*-Golgi network
TLR	Toll-like receptor
TMD	Transmembrane domain
TMEM109/119	Transmembrane protein 109/119
TSPO	18-kDa translocator protein
VOI	Volume-of-interest

1. Introduction

1.1 Lysosomal Storage Disorders

Lysosomal storage disorders (LSDs) are inherited monogenic diseases characterised by lysosomal dysfunction and accumulation of undegraded metabolites. Around 70 metabolic diseases are classified as LSD, each of them occurs rarely, but LSDs have in sum a prevalence of 1 in 8,000 live births. Patients carry homozygous mutations that affect diverse spectrum of lysosomal function, including defects in lysosomal acidic hydrolases (i.e. Gaucher disease; beta-glucocerebrosidase (GBA) defect), integral membrane proteins (i.e. mucolipidosis IV; mucolipin 1 defect) or modulators of lysosomal function (i.e. multiple sulfatase deficiency; formylglycine-generating enzyme (FGE) defect) [1, 2]. LSDs represent chronic and progressive diseases which manifest in multiple organs compromising visceral, hematologic, ocular, skeletal, and neurological signs. LSDs are heterogenous in their age of onset but usually manifest during childhood [1, 3]. The absence of distinct clinical symptoms of patients suffering from a certain LSD as well as their rare occurrence challenges the correct diagnosis and requires a panel of clinical and biochemical tests [3]. Phenotypes of LSD patients have been described before the affected organelle “the lysosome” was identified [4]. Therefore, studying LSDs has a tremendous impact on the knowledge about the endolysosomal system [1, 4].

1.1.1 The Endolysosomal System

Endocytosis is a process in which cargo is internalised, recycled or degraded and is largely subdivided into endocytic, phagocytic and autophagic routes [5, 6]. It is involved in numerous cellular pathways including nutrient uptake, regulation of receptor signalling, migration, host-defence or neurotransmission [7]. The endocytic and phagocytic pathway involves dynamic rearrangements of distinct vesicles which have been identified as early, recycling and late endosomes [8]. These different endosomal populations have discrete membrane domains with defined Rab GTPases and phosphoinositides, which provide a crucial docking station for recruitment of additional factors involved in endosomal trafficking [9].

Macromolecules or membrane-bound cargos (i.e. receptors with their bound substrate) enter the cell by the budding of the plasma membrane via clathrin- or caveolae-mediated endocytosis or clathrin-independent endocytosis [6, 10]. The resulting primary endocytic vesicle with ingested cargo fuses with the highly pleiomorphic early endosomes, which represent a key sorting hub [6, 8]. From here, the cargo is either routed back to the plasma membrane via recycling endosomes or to late endosomes, where the cargo proceeds further to the *trans*-Golgi network (TGN) or to lysosomes for degradation [11]. Early endosomes are mildly acidic (pH 6.0 – 6.8), which promotes ligand-receptor dissociation and fast recycling back of the receptor to the plasma membrane (e.g. low-density lipoprotein receptor (LDLR)), while cargos routed to the TGN dissociate in a more acidic pH (~5.5) found in late endosomes (e.g. mannose-6-phosphate receptor (M6PR)) [6, 12]. In addition, there are other receptors involved in signalling like the epidermal growth factor receptor (EGFR) that do not dissociate from their ligands even at low pH, and thereby, are sorted for degradation into intraluminal vesicles (ILVs) in early endosomes [6, 13]. Early endosomes further mature to late endosomes. This maturation program includes among others the acidification of the endosomal lumen, a Rab GTPase switch from ras-associated binding protein 5 (RAB5) to RAB7 and enrichment of ILVs [5, 14]. During this maturation step, the maturing endosome is in close exchange with the TGN, where lysosomal cargo (e.g. lysosomal enzymes carried by M6PR) is transported to the late endosome and cargo such as M6PR are transported back to the TGN [6, 8].

A late endosome enriched in ILVs is termed as multivesicular body (MVB), which constitutes another sorting hub along the endocytic route [15]. ILV biogenesis is dependent on the endosomal sorting complex required for transport (ESCRT) machinery, which is composed of four ESCRT units known as ESCRT-0 [16], ESCRT-I [17], ESCRT-II [18] and ESCRT-III [19], which jointly and sequentially initiate the formation of ILVs [20]. Moreover, three different lipid species seem to be important for ILV biogenesis due to high enrichment of these lipids in ILVs, which are the phosphatidylinositol 3-phosphate (PI(3)P), cholesterol and bis(monoacylglycero)phosphate (BMP) [15, 21]. MVBs sequester cargo in ILVs for either extracellular release (termed as exocytosis) or for lysosomal degradation [15].

The delivery of the cargo from late endosomes/MVBs to lysosomes is still controversial comprising different theories: (1) the maturation of late endosome/MVBs to lysosomes, (2) vesicles containing lysosomal cargo bud from the late endosome/MVB, and subsequently, fuse with the lysosome, (3) transient fusion of late endosome/MVBs with lysosomes to transfer the cargo and (4) fusion of late endosomes/MVBs with lysosomes generating a hybrid organelle [22]. Of note, also cytoplasmic cargo can be delivered to lysosomes via a process termed as autophagy (referred from the Greek and means “eating itself”). In brief, a phagophore (a lipid bilayer) sequesters intercellular cargo (e.g. protein aggregates or organelles), and thereby, forms an autophagosome which delivers its cargo to the lysosomes [23].

The final destination of the endocytic route, the lysosome, harbours an acidic pH ranging from 4.5 - 5, guaranteed by an adenosine triphosphate (ATP) driven vacuolar ATPase, pumping protons from the cytosol into lumen of the lysosome [24-26]. In order to protect the lysosomal membrane from these harsh conditions, a layer of highly glycosylated proteins, a ‘glycocalyx’-like surface, covers the internal phosphobilayer [27, 28]. The lysosomes serve an optimal pH for over 50 acidic hydrolases, which degrade different lysosomal substrates [25, 26]. Lastly, degraded macromolecules are exported out of the lysosome via several transporters (sugar and ion channels, amino acid, nucleoside and cholesterol transporters). The lysosome is not only the hub for degradative processes, but also serves as intracellular signalling centre. Lysosomes sense the nutrient status via the mechanistic target of rapamycin complex 1 (mTORC1), thereby, inducing metabolic adaptation through the transcription factor EB (TFEB), which is the master regulator of the autophagosome/lysosome biogenesis [29, 30]. Furthermore, lysosomes are equipped with pathogen sensors like the toll-like receptors (TLRs) to promote pro-inflammatory programs and support host defence [31]. Lysosomes do not only serve as receptor signalling hubs, but also appear crucial for Ca^{2+} storage. Calcium regulates endosomal fusion events (regulated by soluble N-ethylmaleimide-sensitive-factor attachment receptor (SNARE) proteins) as well as the establishment of membrane contact sites (MCSs). Indeed, it has been shown that lysosomes create MCSs with several organelles (endoplasmic reticulum (ER), Golgi, peroxisome, and mitochondria) highlighting their function as a crucial signalling hub for other organelles [30, 32].

1.1.2 Endolysosomal Dysfunction in Neurodegeneration

Alterations in the endolysosomal system has far-reaching consequences for the cell. On a cellular level, many LSDs share a similar biochemical phenotype. In general, a built up of undegraded metabolites which can inhibit other catabolic enzymes and/or autophagic flux resulting in secondary storage of further metabolites [33]. Exocytosis seems to be the last resort of the cell to dispose the accumulated substrates due to the fact that increased levels of these metabolites are detected in blood or urine of LSD patients [34]. Furthermore, it has been shown that lysosomal dysfunction in LSDs affects endosomal fusion, calcium homeostasis or homeostasis of the ER, Golgi or peroxisomes [33]. Especially the central nervous system (CNS) is affected in several LSDs (Table 1), which highlights the critical role of endolysosomal pathways in cellular homeostasis and function in the brain [35, 36].

Table 1. LSDs with CNS involvement. Selected LSDs in which the CNS is affected are shown with their disease-associated gene/protein as well as their main storage material. NCL, neuronal ceroid lipofuscinoses. Information is retrieved from Ellison *et al.*[36].

LSD	Gene	Deficient Protein	Main storage material
Gaucher Disease Type II and III	*GBA*	Beta-glucocerebrosidase	Glucosylceramide
Krabbe Disease	*GALC*	Galactocerebrosidase	Galactosylceramide and galactosylsphingosine
Metachromatic leukodystophy	*ARSA*	Arylsulfatase A	Sulfatide
Niemann-Pick Disease Type A	*SMPD1*	Sphingomyelinase	Sphingomyelin
Niemann-Pick Disease Type C	*NPC1/NPC2*	NPC intracellular cholesterol transporter 1/2	Cholesterol and sphingolipids
GM1-gangliosidosis type I, II and III	*GLB1*	Beta-galactosidase	GM1 gangliosides
GM2 gangliosidosis, Tay-Sachs disease	*HEXA*	Beta-hexosaminidase subunit alpha	GM2 gangliosides
GM2 gangliosidosis, Sandhoff disease	*HEXB*	Beta-hexosaminidase subunit beta	GM2 gangliosides
CLN1 disease (infantile NCL)	*PPT1*	Palmitoyl-protein thioesterase	Lipofuscin
CLN2 disease (late-infantile disease)	*TPP1*	Tripeptidyl peptidase 1	Lipofuscin
CLN3 disease (Batten disease)	*CLN3*	Battenin	Lipofuscin
CLN4 disease (Parry disease)	*DNAJC5*	Cysteine string protein	Lipofuscin
CLN5 disease (variant late-infantile NCL)	*CLN5*	CLN5, soluble lysosomal protein	Lipofuscin
CLN6 disease (variant late-infantile)	*CLN6*	CLN6 transmembrane protein in ER	Lipofuscin
CLN7 disease (variant late-infantile NCL)	*MFSD8*	Major facilitator superfamily domain-containing protein 8	Lipofuscin
CLN8 disease (variant late-infantile NCL)	*CLN8*	CLN8 transmembrane protein in ER	Lipofuscin
CLN10 disease	*CTSD*	Cathepsin D	Lipofuscin, Saposin A and D
CLN11 disease	*GRN*	Progranulin	Lipofuscin

Certain genes which are implicated in LSDs are also known as a risk factor for neurodegenerative diseases like Alzheimer’s disease (AD), Parkinson’s disease (PD) or frontotemporal dementia (FTD). These diseases are, among others, characterised by accumulation and deposition of aggregated β-sheet structured proteins (i.e. amyloid-β (Aβ) plaques, tau tangles and α-synuclein, respectively) suggesting limited clearance of these proteins [37-39]. Indeed, numerous genetic variants have been identified in AD, PD and FTD which are implicated in endolysosomal and autophagic pathways (Figure 1) [40, 41].

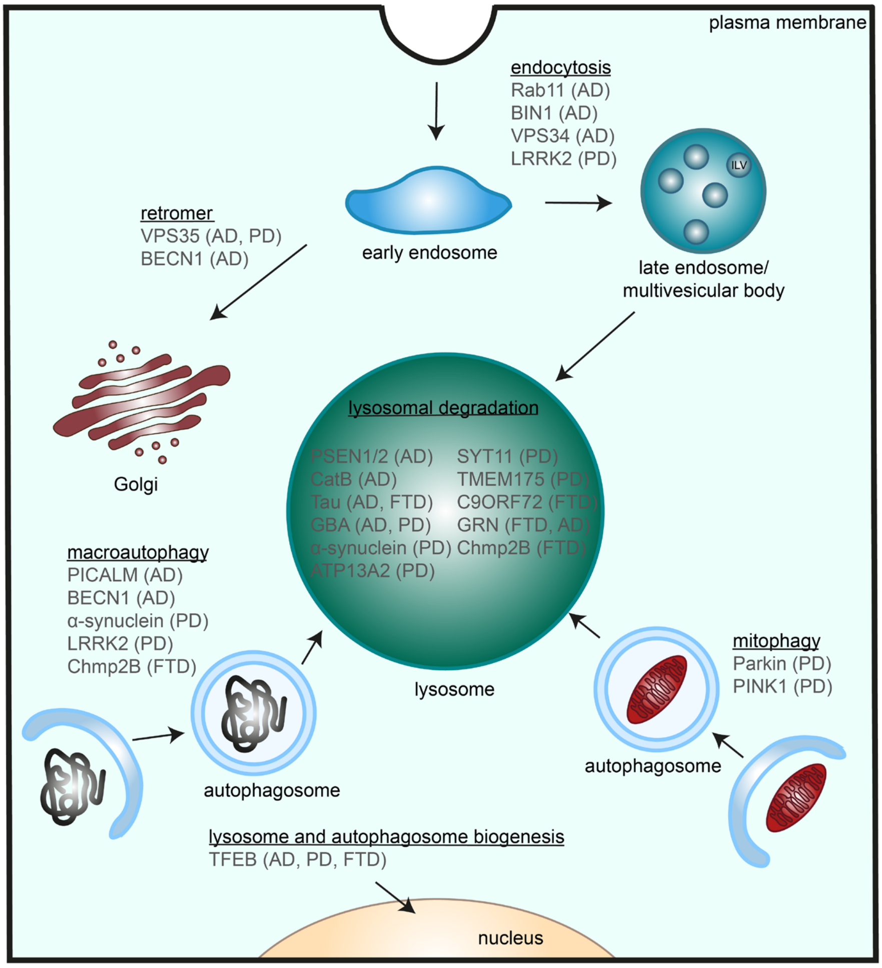

Figure 1. Overview of proteins of the endolysosomal system implicated in the pathogenesis of neurodegenerative diseases like AD, PD or FTD. Risk factors (displayed in grey) for AD, PD and FTD are involved in certain stages of the endolysosomal system: endocytosis, retromer function, lysosomal degradation, macroautophagy, mitophagy or lysosome and autophagosome biogenesis. Adapted from Wang *et al*. [41].

As an example, homozygous mutations in *GBA*, which encodes for the beta-glucocerebrosidase and catalyses the catabolism of glucosylceramide (GlcCer) and glucosylsphingosine, cause Gaucher disease, an LSD affecting infantile patients [2, 36, 37]. In contrast, heterozygous mutations are associated with PD which affects elderly patients [41].Both mentioned diseases are accompanied with neuronal loss and neuroinflammation [35, 42], implying that loss-of-function in an endolysosomal component increases the risk for neurodegenerative diseases.

Why the CNS is heavily affected by endolysosomal dysfunction is still debated. Lysosomal storage in neurons occurs mainly in the cell body, postulating an impaired transport of the lysosomes along the axons [43]. This transport defect is also reflected by the reduced numbers of synaptic vesicles at synaptic terminals as well as axonal swellings, which are commonly detected in LSDs [44]. Specifically mitochondrial function seems to be impaired in several LSDs due to the compromised mitophagy, referring to macroautophagy of mitochondria, favouring persistence of dysfunctional and reactive oxygen species (ROS) generating mitochondria [33]. Especially the brain seems to be susceptible for oxidative stress due to its enormous oxidative metabolism, its lipid composition (which is prone to peroxidation) and the large number of immune cells [45]. Along these lines, neuroinflammation is a shared hallmark between LSDs [35]. Therefore, impaired immune response might further contribute to neuropathology, making the brain vulnerable for lysosomal dysfunction.

1.2 Niemann-Pick Disease Type C

The rare autosomal recessive LSD called Niemann-Pick disease type C (NPC) is caused by mutations in one of the two key players of the cholesterol metabolism, Niemann-Pick C1 protein (*NPC1*) or Niemann-Pick C2 protein (*NPC2*). NPC is characterised by cholesterol accumulation within late endosomal/lysosomal compartments. Most of the NPC patients (~95%) carry a loss-of-function mutation in *NPC1* rather than in *NPC2* (< 5%), with a disease prevalence of 1:120,000 live births [46]. NPC is a subgroup of the umbrella term “Niemann-Pick disease” determined by Albert Niemann and Ludwig Pick, summarising LSDs with similar symptoms and visceral sphingomyelin storage [47, 48]. Later, Niemann-Pick diseases were subgrouped into A, B, C and D, according to their sphingomyelin storage. NPA has an early and severe sphingomyelin storage including cerebral involvement, followed by NPB which in contrast does not show cerebral involvement. NPC and NPD show milder sphingomyelin storage, while NPD is separated from NPC due to the homogenous Nova Scotia Acadian origin [46]. Years later, the biochemical cause of the different severity of sphingomyelin storage has been found. NPA and NPB are caused by deficiency of the sphingomyelinase, with a distinction that NPA patients show neurological involvement while NPB patients do not [49, 50]. NPC and NPD do not have a defect in sphingomyelinase, and were thus reclassified as cholesterol storage diseases [46]. Nowadays, NPD is considered as a variant of NPC [51]. The clinical presentation of NPC patients is heterogenous with visceral and neurological involvements, but the majority of NPC patients is not living longer than 10-25 years [46]. NPC patients show splenomegaly with or without hepatomegaly, followed by neurological symptoms like hypotonia, delay in speech and motor mile stones, ataxia, seizures, vertical supranuclear gaze palsy and cognitive decline [46, 52]. These broad neurological symptoms suggest detrimental CNS consequences upon NPC1 dysfunction. Indeed, neurons of NPC patients show disrupted growth of neurites and dendrites, neurofibrillary tangles, neuroaxonal dystrophies and the most prominent phenotype is the loss of the Purkinje cells in the cerebellum [46, 53]. This severe neuropathology is accompanied by neuroinflammation [54] and hypomyelination of the brain [55, 56].

The mentioned heterogeneity of NPC onset and disease progression impedes NPC diagnosis. The correlation between the genotype and phenotype is difficult to predict [57-59]. Over 400 disease-causing mutations have been identified affecting differently NPC1 trafficking and function, and thereby, leading to different severities of the lipid storage and a diversity of NPC phenotypes [59, 60]. For example, the most prevalent mutation NPC1(I1061T) encodes for a misfolded protein, which is retained and degraded at the ER [61], and causes a severe biochemical phenotype with a juvenile symptom onset [59]. In contrast, NPC1(P1007A), the second most prevalent mutation in Europe, shows a wildtype-like processing, mild biochemical phenotype and adult onset of symptoms [46, 59]. While the above-mentioned scenarios are described for these NPC1 mutations in homozygosity, the phenotypical consequences in combination with another NPC1 mutation (compound heterozygous mutations), which is most common among NPC patients, might be different [60, 62]. Considering that both mutations are located in the same functional domain, but result in different NPC severities, illustrates the complexity of dissecting NPC geno- and phenotypes.

1.2.1 The Key Players in Cholesterol Trafficking: NPC1 and NPC2

The late endosomal/lysosomal protein NPC1 constitutes of 1278 amino acids with 13 transmembrane domains (TMDs) and resides in the limiting membrane (Figure 2) [63, 64]. It harbours three luminal domains, classified as the N-terminal domain (NTD), middle luminal domain (MLD) and the C-terminal domain (CTD) [64]. It has been shown that the NTD harbours a cholesterol binding pocket [65], while MLD has been suggested to bind NPC2 under low pH conditions [66, 67]. Furthermore, NPC1 harbours five transmembrane domains which are homologous to the sterol-sensing domain (SSD) found in proteins involved in cholesterol homeostasis like the 3-hydroxy-3-methylglutaryl-CoA reductase (HMGCR) [64].

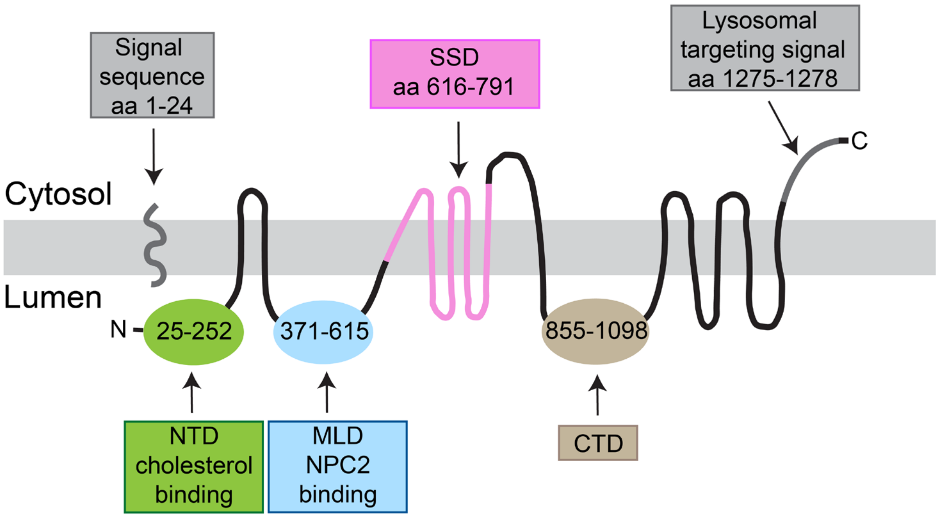

Figure 2. Proposed topology of the transmembrane protein NPC1. Functional domains are highlighted in different colours: NTD in green, MLD in blue, SSD in pink and CTD in brown. The signal sequence and the lysosomal targeting signal are coloured in grey. aa: amino acids, NTD: N-terminal domain, MLD: middle luminal domain, CTD: C-terminal domain, SSD: sterol-sensing domain. Adapted and modified from Lu *et al*. [68].

NPC2, in contrast, is a soluble 132 amino acid long protein found in the lumen of late endosomes/lysosomes [69]. It binds cholesterol at its sterol moiety [70], while NPC1 NTD binds cholesterol at its hydroxyl moiety [70, 71]. It is still debated how cholesterol is exactly transported through the lysosomal membrane [72]. A “hydrophobic hand-off” of cholesterol between NPC2 and NPC1 has been proposed (Figure 3) [71, 73]. Thereby, NPC2 sequesters cholesterol at its sterol moiety, binds to the MLD of NPC1 and transfers cholesterol to the NTD of NPC1. The NTD passes then cholesterol to the SSD by an unknown mechanism [74]. Li *et al*. suggested two possibilities: an intramolecular cholesterol transfer in which, upon cholesterol binding, the linker between TMD1 and TMD2 moves TMD1 to allow cholesterol transfer from NTD to SDD or cholesterol transfer is operated in concert of two NPC1 proteins [74, 75]. Additionally, it has been proposed that cholesterol shuttles through NPC1 through a putative tunnel [76]. Höglinger *et al*. postulated a novel mechanism where NPC1 acts as a tethering factor in endosomal-ER MCS controlling thereby cholesterol egress [77]. Altogether, NPC1 fulfils important roles in lipid homeostasis that may not be limited to its initially proposed function as cholesterol exporter.

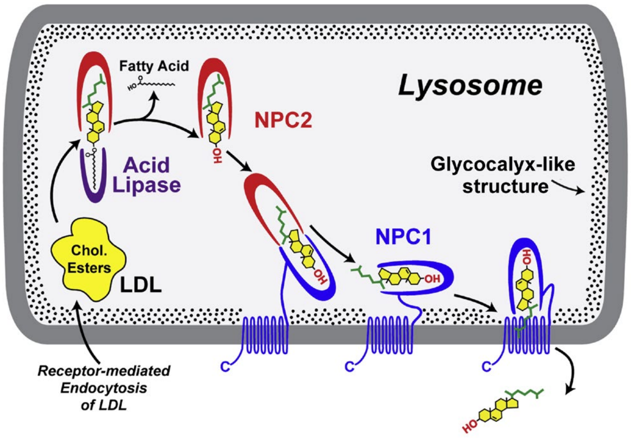

Figure 3. Postulated "hydrophobic hand-off" model of cholesterol export by NPC1 and NPC2. LDL particles containing cholesteryl esters (chol. esters) are taken up by the cell via receptor-mediated endocytosis and traffic to the lysosome. Within the lysosome the acid lipase is hydrolysing the cholesteryl ester into free cholesterol. The soluble protein NPC2 binds cholesterol at its hydrophobic moiety and transports it to the transmembrane bound NPC1, which binds cholesterol from the opposite side. NPC1 exports then cholesterol through the glycocalyx-like strucutre and lysosomal membrane, respectively, and cholesterol traffics further to other organelles and the plasma membrane. LDL, low density lipoprotein; NPC1/2, Niemann-Pick C1/2 protein; ER, endoplasmic reticulum. Adapted from Kwon *et al*. [71].

1.2.2 Cholesterol Homeostasis

Cholesterol is an essential lipid for eukaryotic cells, being important for membrane integrity and production of bile acid, steroid hormones and vitamin D [78]. Within the cell, the plasma membrane accounts for the largest cholesterol pool (60-90%), while intermediate amounts are found in the endosomal system with heterogenous cholesterol amounts (with MVBs being the cholesterol richest endocytic compartment) [78, 79]. In order to keep this cholesterol gradient within the cell, dynamic cholesterol rearrangements are necessary which are operated either by vesicular trafficking or non-vesicular transfer at MCS [78].

Cholesterol homeostasis is accomplished by *de novo* synthesis or dietary uptake. Each cell has the equipment to synthesise *de novo* cholesterol from the precursor acetyl-CoA through the mevalonate pathway, where HMGCR catalyses the first rate-limiting step. Most of the enzymes needed for this pathway are located at the ER. Nevertheless, not all cells efficiently synthesise cholesterol, with hepatocytes being the main producers of cholesterol in the periphery [80, 81]. However, the rationale for cell specific contribution to cholesterol synthesis is still not understood. Conclusively, certain cell types are dependent on exogenous cholesterol supply.

Diet-derived cholesterol is absorbed in the intestine by enterocytes which express the transmembrane protein Niemann-Pick C1-like-1 (NPC1L1) on their plasma membrane that is responsible for cholesterol import [82, 83]. Absorbed cholesterol is esterified by acetyl-CoA acetyltransferase 2 (ACAT2) and packed in chylomicrons with apolipoprotein B48 (APOB48) as associated apolipoprotein. The chylomicron is exported out of the enterocyte via exocytosis and reaches the blood circulation through the lymph vessels, from where it is transported to peripheral tissue and the liver [82, 84].

Cholesterol is also endogenously synthesised in the liver, being the main producer of cholesterol *in vivo*. Synthesised cholesterol is mainly transported via LDL particles throughout the body [85]. The recipient cell uptakes LDL particles via an LDLR-mediated endocytosis and traffics through the endocytic pathway to late endosomes/lysosomes (Figure 4). Here, the lysosomal acid lipase (LIPA) hydrolyses the LDL-packed cholesteryl esters (CEs) and releases cholesterol. Cholesterol is exported out of the lysosomal compartment via NPC1 and NPC2 (Figure 3) [80, 86]. It has been proposed that cholesterol transport to the plasma membrane is regulated by concerted action of the late endosomal/lysosomal protein NPC1, the GTPase RAB8A and tetraspanin CD63 [87]. Excess of cholesterol is transported to the ER through MCSs. Especially the ER is cholesterol poor (~0.5 - 1%) and serves as cholesterol sensor and induces transcriptomic changes upon cholesterol fluctuations, via the sterol regulatory element-binding protein (SREBP)/SREBP cleavage-activating protein (SCAP) complex. Upon cholesterol depletion, SCAP traffics together with SREBP from the ER to the Golgi via vesicular trafficking. At the Golgi, SREBP is cleaved and the N-terminal fragment translocates to the nucleus. Here, it promotes the transcription of lipogenic genes by binding to a sterol regulatory element (SRE) found in the promotors of lipogenic proteins i.e. involved in cholesterol biosynthesis and LDL import [78, 88]. If the cholesterol load at the ER exceeds 5 mol %, the SREBP/SCAP complex signalling is suppressed, and thereby, the transcription of lipogenic proteins. Excessive free cholesterol is esterified at the ER via acetyl-CoA acetyltransferase 1 (ACAT1) into CEs and stored together with triacylglycerides (TGs) in a lipid storage organelle called lipid droplet [78]. Additionally, CEs can be exported out of the cell through ATP-binding cassette (ABC) transporters and incorporated in a lipoprotein complexed with apolipoproteins[80]. Of note, it has been proposed that small portions of LDL-derived cholesterol are transferred to the mitochondria through late endosomal/lysosomal MCSs mediated by StAR-related lipid transfer protein 3 (STARD3) and NPC2, and thereby, bypassing NPC1 function [89, 90].

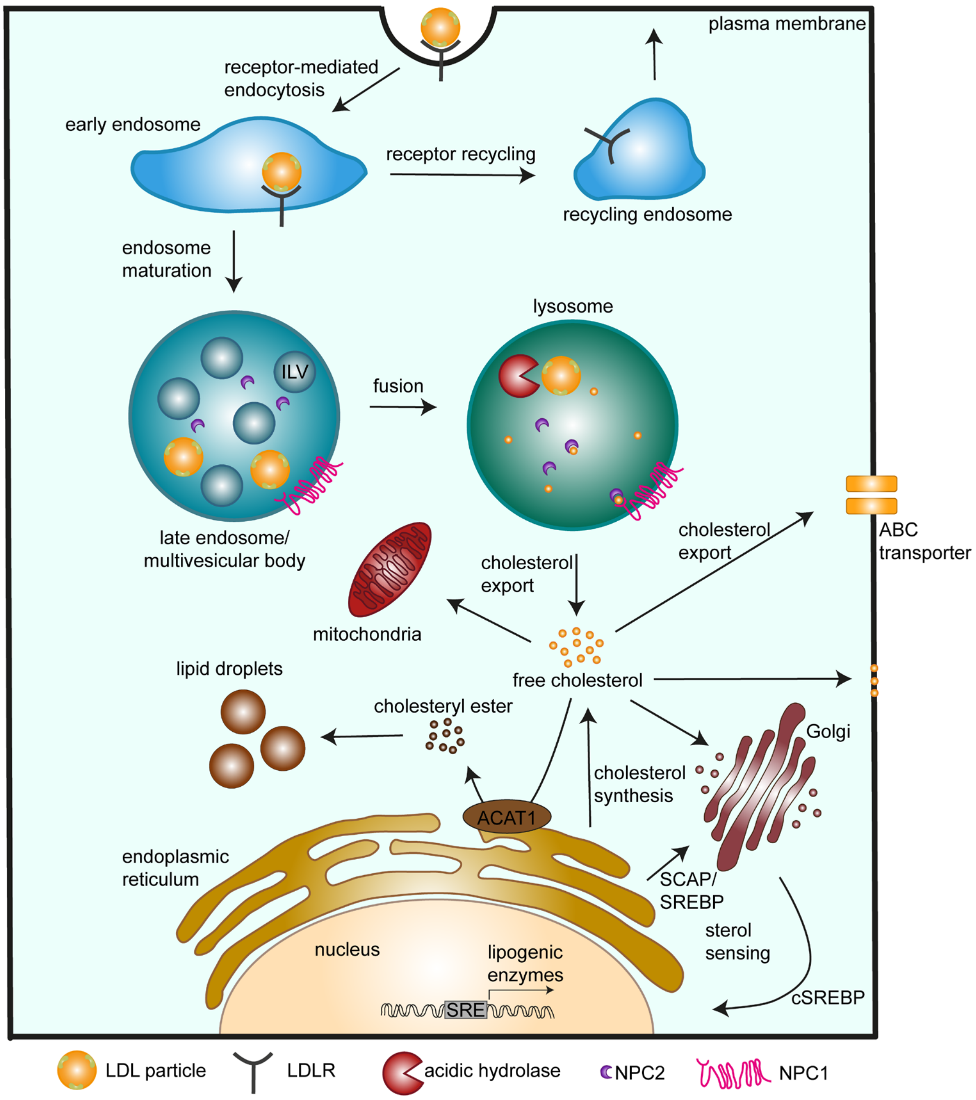

Figure 4. Schematic representation of cholesterol homeostasis in a cell. Cholesterol and cholesterol derivates containing LDL particles are endocytosed via LDLR-mediated endocytosis. The receptor bound LDL particle traffics to early endosome, where the receptor dissociates form LDL and traffics back to the plasma membrane via recycling endosomes. Subsequently, the early endosome containing LDL matures to late endosomes/multivesicular bodies (MVBs) which fuse together with the lysosomes (of note, other cargo transfer mechanisms from late endosomes/MVBs to lysosomes are possible as discussed before). The LDL particle is degraded within the lysosome, cholesterol is released and exported out of the lysosomal compartment via NPC2 and NPC1. The accessible free cholesterol pool is transported to various organelles (e.g. mitochondria, Golgi, endoplasmic reticulum (ER) or the plasma membrane) or exported out of the cell via ABC transporters. Low levels of cholesterol at the ER initiates the transport of the SCAP/SREBP complex to the Golgi where SREBP is cleaved and acts as transcription factor by binding to the sterol regulatory element (SRE) of several promotors inducing transcription of lipogenic enzymes. Excess of free cholesterol is esterified into cholesteryl esters at the ER by an enzyme called ACAT1. Cholesteryl esters are then stored in lipid droplets. Besides the LDL-derived cholesterol serving as cholesterol pool, cholesterol is also synthesised *de novo* at the ER. LDL, low density lipoprotein; LDLR, LDL receptor; NPC1/2, Niemann-Pick C1 protein 1/2; SREBP, sterol regulatory element-binding protein; SCAP, SREBP cleavage-activating protein, cSREBP, cleaved SREBP, SRE, sterol regulatory element; ABC, ATP-binding cassette.

In the brain, cholesterol is independently regulated from the periphery. The brain contains cholesterol in high amounts when compared to the whole body (~20%). Within the brain, unesterified cholesterol is primarily found in myelin sheaths (70-80%), while the minor pool of unesterified cholesterol in the brain arises from the plasma membrane/endosomes of brain cells. Cholesterol does not only constitute a structural element but also serves as a precursor for several biological active lipids in the brain (e.g. steroid hormones or oxysterols) [91]. Cholesterol is mainly synthesised *de novo* in the brain. Recently a second source has been proposed from LDL particles containing ApoA1 that might transcytose through the blood-brain barrier (BBB) [91, 92]. *De novo* synthesis rates differ between brain cells. Oligodendrocytes and astrocytes show the highest capacity to synthesis cholesterol, while neurons seem to rely mainly on LDLR-dependent uptake of cholesterol [81, 93]. This cellular diversity in cholesterol demands is also reflected by different levels of NPC1 transcripts. NPC1 is ubiquitously expressed in every tissue of the body with heterogenous transcription levels [94]. In the brain, NPC1 transcripts are mostly abundant in the white matter (including corpus collosum), and consequently, showing the highest levels in oligodendrocytes, followed by microglia, astrocytes and neurons (the human protein atlas, NPC1; accessed on 03.15.2023). Excess of cholesterol is either esterified and stored in lipid droplets or, in case of certain neurons, hydroxylated to 24-hydoxycholesterol and exported out of the cell [91]. Taken together, it is clear that different brain cells have different needs for cholesterol and cellular equipment to metabolise it.

1.2.3 Lipid Dyshomeostasis and Cellular Consequences in NPC

Given the importance of NPC1 in cholesterol trafficking, it not surprising that unesterified cholesterol is accumulating in late endosomes/lysosomes in NPC [46, 95, 96]. Cholesterol is not exclusively accumulating, but also various additional lipid classes accumulate in NPC such as sphingomyelin, glycosphingolipids and sphingosine [96-99]. Of note, there are or may be differences in lipid storage between the periphery and the CNS, but also among different brain cell types. In case of cholesterol, cellular accumulation of cholesterol was observed in the brain, while total cholesterol loads where not increased in NPC brains [99]. This was argued by a redistribution of cholesterol within neurons with accumulation of cholesterol in cell bodies and loss of cholesterol from processes and the prominent hypomyelination that collectively mask detection of increased levels of cholesterol in the brain [100-102]. Moreover, cholesterol distribution between cell organelles seems to be disbalanced (i.e. cholesterol is enriched in mitochondria, while it is depleted in the Golgi) [103-105].

There are different aspects in NPC which lead to accumulation of broad lipid classes. Accumulation of diverse lipids can be caused by impaired fusion events, especially of late endosomes with lysosomes [106]. It has been shown that a high cholesterol load in endosomes immobilises endosomal trafficking and is thereby impairing fusion [107, 108]. In addition, lysosomes in NPC have low luminal levels of calcium, a factor that is important for fusion [97]. Another hypothesis is that cholesterol storage impairs the catabolism of secondary storage lipids, due to mis-localisation of catabolic enzymes and their substrate as well as reduced enzyme activity [109, 110]. Additionally, one of the key components of endosomal identity and trafficking, the phosphoinositides, have been shown to be altered upon NPC1 dysfunction. Phosphatidylinositol 4-phosphate (PtdIns4P) enriches at the Golgi, which causes aberrant anterograde trafficking to the plasma membrane, further illustrating impaired trafficking in NPC [111]. Still, it is unclear if a certain lipid class or different lipid classes in concert is/are driving lipid storage, and subsequently, the NPC pathology [99]. Considering the role of NPC1 as mediator of MCS [77] and its major impact on endosomal trafficking, it is possible that endolysosomal trafficking defects are the primary consequence of NPC1 dysfunction, leading to storage of various lipid classes.

Along these lines, also autophagy has been shown to be altered in NPC, but which kind of impairment is still under debate. Levels of autophagic cargos like p62 or markers like microtubule-associated protein 1A/1B-light chain 3 (LC3), autophagy protein 5 (ATG5) and ATG7 are increased in NPC, which have been interpreted as defective fusion between autophagosomes and lysosomes [112-114]. It has been postulated that NPC1 mediates fusion events between late endosomes and autophagosomes resulting in amphisomes as well as their fusion with lysosomes [114]. In contrast, other studies suggest an overactive autophagy, in which substrates accumulate due to impaired lysosomal function [115, 116]. Of note, it has been shown that lysosomal pH, an important factor for lysosomal catabolic function, is not altered in NPC, in line with the hypothesis that lysosomal catabolic function may still be preserved [97, 116]. Concludingly, impaired autophagy is a key hallmark in NPC but the fundamental mechanism leading to defective autophagic flux is still not clear.

Along these lines, the key regulator of autophagy and cellular metabolism mTOR has been shown to be regulated by NPC1 [117]. It has been shown that NPC1 inhibits mTOR signalling in concert with the sodium-coupled neutral amino acid transporter (SLC38A), and thereby, acting directly on cellular metabolism [117]. Indeed, mTOR signalling is aberrant in NPC [117, 118], which might be an additional trigger for impaired autophagy, since active mTOR signalling is inhibiting the initiation of autophagy [119].

Another aspect of NPC1 dysfunction is the increase of mitochondrial damage [106]. It has been shown that oxidative stress is prominent in NPC, as measured by increased levels of ROS [103, 120-124]. Moreover, mitochondria display a reduced consumption of oxygen and impaired ATP production [103, 104, 125]. Increased mitochondrial damage accompanied with impaired autophagy might drive further cellular impairments, and potentially, cell death in NPC [106, 118]. Altogether, NPC1 deficiency impairs endolysosomal trafficking, lipid homeostasis, autophagic flux and mitochondrial function, and thereby, sharing similar cellular phenotypes described in several LSDs [33].

1.2.4 Investigating NPC: the *Npc1*$^{-/-}$ mouse model

Most of the achievements in deciphering NPC disease mechanisms were gained by using the mouse model BALB/cNctr-*Npc1*^{m1n} (also known as npc^{nih}; termed as *Npc1*$^{-/-}$ mice in this thesis). These mice have a complete loss of NPC1 caused by a spontaneous insertion of a mammalian apparent LTR (MaLR) retrotransponson-like DNA fragment in exon 9 of *Npc1* which results in multiple stop codons [126, 127]. *Npc1*$^{-/-}$ mice recapitulate disease progression and symptoms seen in NPC patients [128, 129]. This includes a pre-symptomatic stage in which no major behavioural phenotypes are detected and a symptomatic stage starting at an age of 5 weeks where symptoms become present (i.e. tremors, motor deficiencies, ataxia and seizures) until they reach the humane endpoint which is at an age between 10-14 weeks (Figure 5).

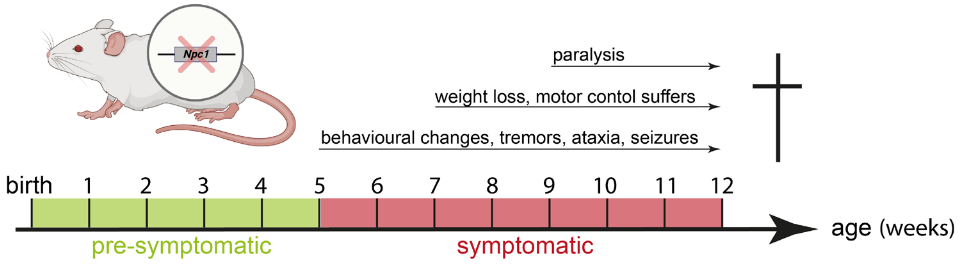

Figure 5. Disease progression of *Npc1*$^{-/-}$ mice (BALB/cNctr-*Npc1*^{m1n}). *Npc1*$^{-/-}$ mice do not show any behavioural phenotype until the age of 5 weeks (pre-symptomatic). Symptomatic mice display weight loss and neurological symptoms like tremors, ataxia, motor deficiencies and paralysis. These mice die usually at an age between 10-14 weeks. Adapted from Platt *et al.* [129].

Thereby, this mouse model serves as a powerful tool to study the severe/juvenile NPC disease phenotype which is mostly prominent among NPC patients [129]. Of note, neurofibrillary tangles, a common pathology found in NPC patients, are not recapitulated in *Npc1*$^{-/-}$ mice underscoring some limitations of NPC1 mouse models in reflecting NPC disease phenotypes [130-134].

Besides BALB/cNctr-*Npc1*^{m1n}, also a *Npc1*$^{-/-}$ mouse model in the C57BL/6 background exists and displays even a more aggressive NPC phenotype [135]. As mentioned before, NPC patients harbour mutations, which do not lead to a complete but rather partial loss of NPC1 function [59]. An NPC mouse model which harbours a D1005G NPC1 mutation (*Npc1*^{nmf164}) shows normal *Npc1* mRNA levels, but protein levels are drastically decreased (10-15% NPC1 protein are left compared to wild-type) [136].

Another mouse model which harbours the most common NPC1 mutation I1016T has been generated, which similarly has no major effect on the NPC1 mRNA levels, but causes a significant reduction in NPC1 protein levels [137]. These mouse models recapitulate the same phenotype as BALB/cNctr-*Npc1*^{m1n}, but due to the residual levels of NPC1, have a slowed disease progression and are thereby a perfect tool to study an adult onset of NPC as well as proteostatic therapies [138].

1.2.5 Brain Pathology

1.2.5.1 NPC1 Dysfunction in Neurons

Widespread neurodegeneration is prominently observed in NPC which includes brain areas like brainstem, substantia nigra, thalamus, corpus callosum, cortex and cerebellum [139-143]. Especially the Purkinje cells in the cerebellum are heavily affected in NPC and are depleted in the first eight lobes of the cerebellum [144, 145]. Loss of Purkinje cells has been assigned as a cell-autonomous consequence of NPC1 loss, suggesting that Purkinje cell survival is dependent on NPC1 function [112, 146]. Which mechanisms drive the cell death of Purkinje neurons is still not understood [138]. However, multilamellar body and autophagic vesicle accumulation were observed in Purkinje cells pointing towards defects in the autophagic flux [112, 140, 147-149]. Specific loss of NPC1 in Purkinje cells does not recapitulate premature lethality nor weight loss in *Npc1*$^{-/-}$ mice [146]. In contrast, loss of NPC1 under a more global neuronal promotor (synpasin 1) leads to premature lethality underscoring neuronal involvement in NPC1 disease [150]. Besides neurodegeneration, also other neuronal pathologies are observed in NPC. Axonal swellings and ectopic dendrites are prominent in different NPC models and human patients

[151]. In line with this phenotype, also axonal transport of cholesterol has been shown to be impaired [100]. Interestingly, it has been postulated that NPC1 is also expressed in in recycling endosomes at pre-synaptic terminals and is locally expressed during long-term potentiation in post-synapses [152, 153]. This suggests that synaptic functions are disturbed upon NPC1 loss. Indeed, *Npc1*$^{-/-}$ neurons display a deficient turnover of synaptic vesicles, which might be linked to neurological symptoms like seizures [154]. Of note, hyperphosphorylated tau, an aspect of neuropathology of NPC patients, is also detected in *Npc1*$^{-/-}$ neurons [131, 133, 155].

1.2.5.2 NPC1 Dysfunction in Oligodendrocytes

Oligodendrocytes are myelinating neuronal axons to support neuronal conduction as well as to provide metabolic support [156]. Since myelin represent the largest cholesterol pool in the brain, the process of myelination is dependent on proper cholesterol metabolism and homeostasis [157, 158]. Oligodendrocyte function is heavily impaired in NPC, as NPC patients show impaired myelination [55, 56]. Myelin is absent from the corpus callosum already at symptomatic stages in NPC mouse models [159, 160]. Mature myelinating oligodendrocytes are lacking in hypomyelinated regions, while pre-myelinating oligodendrocytes and oligodendrocyte precursor cells (OPCs) are present, suggesting impaired maturation of oligodendrocytes in NPC [161]. Indeed, Yan and colleagues have shown that loss of NPC1 results in reduced expression of a transcription factor important for oligodendrocyte maturation (myelin gene regulatory factor) in oligodendrocytes [162]. Furthermore, it has been shown that specific loss of NPC1 in oligodendrocytes is sufficient to drive hypomyelination, pinpointing that NPC1 function is important for oligodendrocyte development [163]. Interestingly, specific loss of NPC1 in neurons also triggered hypomyelination and oligodendrocyte maturation defects [163]. These results suggest that oligodendrocyte maturation and function is dependent on endogenous NPC1 function in oligodendrocytes, but also effected by the non-cell-autonomous mechanisms and the crosstalk between neurons and oligodendrocytes. Along these lines, Berghoff and colleagues have shown that upon demyelinating conditions, neuronal-derived cholesterol is of significant importance for myelin repair as it induces OPC proliferation, and thereby, accurate myelination of the brain [164], further supporting the relevance of intercellular crosstalk in myelination process.

1.2.5.3 NPC1 Dysfunction in Astrocytes

Since astrocytes are the most abundant cells in the brain, and of critical importance for cholesterol metabolism, their contribution to NPC disease has to be considered. Astrocytes fulfil various functions in the CNS homeostasis including clearance of neurotransmitter, control of ion homeostasis, support of neuronal glucose metabolism and are important during synapse development [165]. Moreover, astrocytes react to CNS injury or brain pathology leading to vast transcriptomic and morphological changes, summarised as “astrogliosis” [166]. In NPC, astrogliosis is a prominent hallmark observed at early pathological stages in *Npc1*$^{-/-}$ mice [167]. Loss of NPC1 in astrocytes leads to accumulation of cholesterol in late endosomal/lysosomal compartments and to reduced production and secretion of estradiol, a steroid hormone synthesised from a cholesterol precursor [150, 168, 169]. Reduced levels of estradiol are observed *in vivo*, where administration of estradiol was sufficient to diminish symptoms seen in NPC, pointing towards astrocytic contribution in NPC disease progression [169]. Along these lines, specific rescue of NPC1 in astrocytes in *Npc1*$^{-/-}$ mice alleviated neuronal cholesterol storage, neurodegeneration, and consequently, increased life-span [170]. In contrast, specific loss of NPC1 in astrocytes did not result in any phenotype seen in *Npc1*$^{-/-}$ mice [150]. Of note, NPC1 dysfunction does not influence cholesterol synthesis and secretion since the quality and quantity of apolipoprotein E (APOE)-containing lipoproteins are not altered in NPC conditions [168]. These studies hypothesise that although astrocytes might be involved in NPC disease progression, cell-autonomous function of NPC1 in astrocytes still remains controversial.

1.2.5.4 NPC1 Dysfunction in Microglia

1.2.5.4.1 Microglial Function in Health and Disease

Microglia are the innate immune cells of the brain and have undeniably important functions to maintain brain homeostasis (Figure 6) [171]. Microglia arise from the same common myeloid progenitor like peripheral macrophages, but are a distinct cell population arisen from progenitor cells which emerged from the yolk sac colonizing the brain during early development (before E8) [172]. As a consequence, microglia are an unique cell population in the brain that self-renews locally and are distinguishable from myeloid cells at the periphery [172]. Microglia self-renew several times during life [173]. Their self-renewal capacity is demonstrated well by Huang *et al.* [174]. They have shown that upon microglia depletion using a macrophage colony-stimulating factor 1 receptor (CSF1R)

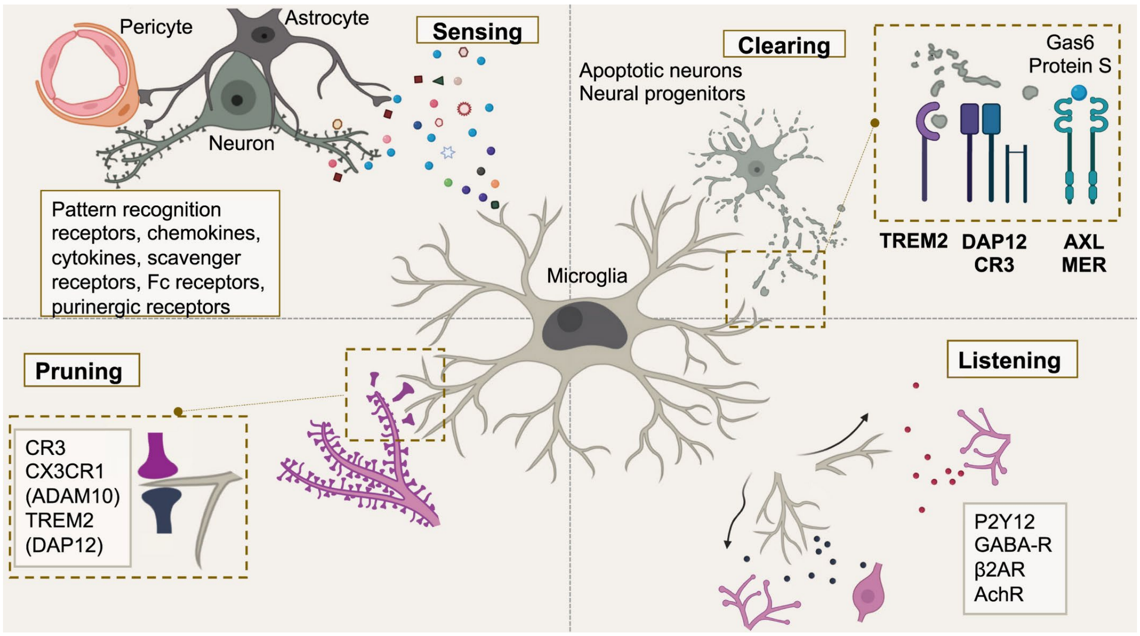

Figure 6. Homeostatic functions of microglia in the brain. Homeostatic microglia display a ramified morphology and express several receptors on their cell surface for surveillance of the brain and initiating different processes. Microglia use different receptors and factors to monitor neuronal function, to clear apoptotic neurons or neuronal progenitors as well as sculping the synaptic density of neurons. Microglia also "listen" to neuronal activity by expressing receptors for neurotransmitters. Taken from De Schepper *et al.* [175].

inhibitor, the microglia resistant to CSF1R inhibition had the capacity to repopulate the brain parenchyma [174]. Still, under certain pathological circumstances, peripheral macrophages can engraft into the brain parenchyma and represent a unique functional and transcriptional CNS cell population [176].

Microglia are a very dynamic cell population, which are able to switch their phenotype between homeostatic and pathological conditions as illustrated by their unique transcriptomic signatures [177-179]. Even in homeostatic conditions, microglial signatures are complex and heterogenous and adjust their transcriptional phenotype in a spatio-temporal manner [180, 181]. Microglia express various cell surface receptors for surveilling and sensing disturbances in brain homeostasis [182]. These receptors (i.e. complement receptor 3 (CR3) or P2Y purinoceptor 12 (P2RY12)) are particularly important for governing synaptic plasticity during development to remove improper or surplus synaptic connections [183, 184]. At aged stages, microglia also control synaptic plasticity in an ATP- and complement-dependent manner as well as neuronal activity preventing excitotoxicity [185, 186]. Microglia play also important roles during neurogenesis by phagocytosing surplus new-born cells as well as secreting neurotrophic factors (e.g. insulin-like growth factor I (IGF1), neurotrophin-3 (NT3), β-nerve growth factor (NGF)) [171]. Indeed, microglia accumulate postnatally in the subventricular zone (SVZ), a niche for neuronal stem cells, to promote neurogenesis [187]. Microglia also play essential roles in oligodendrocyte development and myelination and support remyelination [187-189]. Lastly, microglia represent the first line of host defence in the brain and express various of immune receptors (i.e. TLRs) in order to recognise, ingress and annihilate pathogens [190]. Upon phagocytosis of pathogens, microglia switch their phenotype into an activated state (roundish, amoeboid morphology) and release pro-inflammatory cytokines to support pathogen clearance, referred as neuroinflammation [191]. This physiological and beneficial function of microglia becomes detrimental as soon as the source of the stimuli is not resolved. Microglia become chronically activated and potentially neurotoxic as seen in various neurodegenerative diseases [171].

Although the pathological trigger is different across distinct neurodegenerative diseases, inflammation is their common disease hallmark [192, 193]. Various studies identified a unique transcriptomic signature of microglia arising from different neurodegenerative diseases, the so-called disease-associated microglia (DAM), or alternatively termed as “microglial neurodegenerative phenotype” or “activated response microglia” (Figure 7) [178, 179, 194].

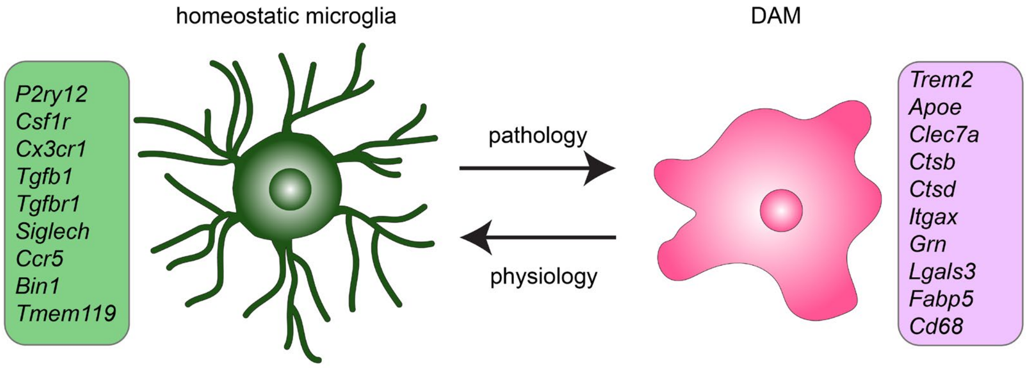

Figure 7. Homeostatic and DAM microglia describe an unique transcriptional signature. Microglia change their morphology and transcriptomic profile upon a pathological stimulus into a certain disease-associated microglia (DAM) phenotype [178, 179]. Homeostatic microglia are ramified and transcribe homeostatic genes like *P2ry12*, *Cx3cr1*, *Tgfb1* etc. (picked genes are shown in the green box on the left), while DAM microglia display an amoeboid morphology and transcribe distinct disease signatures including *Trem2*, *Apoe*, *Ctsd* (picked genes are shown in the pink box on the right).

These microglia are described with decreased transcription of homeostatic signatures (i.e. *P2ry12*, *Csf1r*, CX3C chemokine receptor 1 (*Cx3cr1*), transforming growth factor beta-1 proprotein (*Tgfb1*)) and increased expression of DAM signatures (i.e. triggering receptor expressed on myeloid cells 2 (*Trem2*), *Apoe*, progranulin (*Grn)*, *Npc2*, cathepsin D (*Ctsd*), integrin alpha-X (*Itgax*)*,* C-type lectin domain family 7 member A (*Clec7a*)*,* cluster of differentiation 68 (*Cd68*)) driven by an APOE-TREM2 axis [178, 179]. Recent work by Sebastian Monasor *et al.*, has shown that these signatures were conserved on a proteomic level in amyloidosis mouse models [195]. While more insights about microglial signatures in disease conditions were collected in the recent years, their contribution to neurodegenerative disease (beneficial or detrimental) is still not fully understood [196]. Most of the knowledge about microglia phenotypes were established in murine mouse models and less is known about human microglia. Recent studies have shown that homeostatic signatures and DAM signatures are poorly conserved across species (i.e. 28 out of 228 DAM genes were detected in human microglia) and current investigations seek for microglial molecular changes that are causative for human disease [197]. Several genome-wide association studies in human AD cases showed remarkable enrichment of several microglial genes as risk factors (i.e. *TREM2* or *APOE4*) [196]. This underscores that microglia are no longer considered as a consequence of neurodegeneration, but as active players. Their dynamic functions still have to be understood in order to decipher optimal molecular targets for therapeutic approaches.

1.2.5.4.2 NPC1 Dysfunction in Microglia

Neuroinflammation is a prominent feature in NPC [46, 54]. NPC1 is highly expressed in microglia (the human protein atlas, NPC1; accessed on 03.15.2023), which is why their functional alteration upon NPC1 loss has to be considered and elucidated. Phenotypic changes of microglia are already prominent at postnatal stages in the cerebellum before Purkinje cell loss is obvious in an NPC mouse model [144, 145, 167]. It has been shown that microglia differentiation from microglia precursor cells is impaired, and additionally, microglia display an amoeboid and highly phagocytic phenotype [198, 199]. In line with this, microglia display an active morphology in other brain regions [167] as well as increased inflammatory markers (i.e. C-C chemokine ligand 3 (CCL3) or interleukin-3 (IL-3)) in the brain of pre-symptomatic NPC mice [54], suggesting that microglial activation occurs prior to neuronal death and is not brain region specific. At a symptomatic stage, microglia display an amoeboid morphology, in line with increased transcripts of DAM signatures (e.g. interleukin-1β (*Il1b*) and secreted phosphoprotein 1 (*Spp1*)) and decreased homeostatic signatures (e.g. TGF-beta receptor type-1 (*Tgfbr1*) and transmembrane protein 119 (*Tmem119*)) [200], implying dysfunctional microglia as seen in other neurodegenerative diseases. Indeed, also myelin-related proteins like the myelin basic protein (MBP) were detected in NPC1-deficient microglia suggesting altered phagocytic function also at symptomatic stages [201]. In line with this aberrant microglial phenotype, combinatorial therapy strategies with lipid-lowering drugs and anti-inflammatory drugs showed the most beneficial effect [128, 202]. In conclusion, the *in vivo* data implies a contribution of microglia in NPC progression. In contrast, *in vitro* data showed that *Npc1*$^{-/-}$ microglia are not neurotoxic when co-cultured with neurons [203]. Furthermore, microglia depletion in an NPA mouse model worsened the NPA phenotype, suggesting beneficial effects of microglia in the NPA mouse model [201]. These contradictory results reveal the complexity and the need to further elucidate microglial contribution to NPC disease progression.

1.2.6 Therapeutic Targeting of NPC

There are currently several therapeutic strategies used in clinical trials with NPC patients [204]. Considering NPC as a cholesterol storage disorder, cholesterol lowering agents which were commonly used for hypercholesterolaemia (i.e. Lovastatin) in combination with reduced cholesterol uptake in the diet were first used to intervene with the NPC progression. Cholesterol levels were reduced in liver and plasma, while no beneficial effect was observed on the neurological symptoms [205]. In line with this study, also treatment with cholesterol lowering drugs, which were postulated to act on cholesterol efflux (nifedipine and probucol), did not reveal any beneficial effect on brain pathology [206]. It has been concluded that these drugs are not BBB penetrant [206], displaying that brain cholesterol pools are independent from the periphery and stressing the pitfalls and difficulties of treating CNS diseases.

Another drug candidate in NPC therapy, which is acting on the cholesterol efflux, is the cyclic oligosaccharide hydroxypropyl-β-cyclodextrin (HP-β-CD). Its hydrophilic surface and hydrophobic cavity makes it to a commonly used vehicle for drug delivery [207]. Griffin and colleagues were using this vehicle to deliver allopregnanolone, a neurosteroid decreased in NPC, to *Npc1*$^{-/-}$ mice. Interestingly, HP-β-CD treated mice showed beneficial effects like Purkinje cell survival, reduced glucosphingolipid storage and increased life-span, which were attributed to the vehicle cyclodextrin, since allopregnanolone treatment alone did not show any effect [208]. It has been shown that cyclodextrin is endocytosed by the cell, where it complexes free cholesterol and makes it available for other organelles by extracting it from endosomal compartments [209, 210]. Several *in vitro* studies showed beneficial effects of cyclodextrin treatment in NPC, including reduced cholesterol levels in the lysosomes, cholesterol trafficking to the ER, reduced *de novo* synthesis of cholesterol and reduced oxidative stress [124, 209-211]. All together, these results pinpoint towards a restored cholesterol trafficking and signalling upon cyclodextrin treatment. Unfortunately, the translational aspect for human therapy is limited due to its low BBB penetrance [212]. Therefore, HP-β-CD has to be intrathecally administered. Monthly administration of HP-β-CD was efficient to slow down disease progression and showed an acceptable safety profile [213, 214].

A more promising and BBB penetrant drug is the small iminosugar miglustat, which was originally FDA-approved for another LSD, namely Gaucher disease which is characterised by glucocerebroside accumulation [215-218]. It is acting on the biosynthesis of glycosphingolipids by inhibiting glucosylceramide synthetase [216]. Treatment with miglustat in a murine and feline NPC model resulted in reduced glucosphingolipid storage, slowed down neurological pathology and increased life-span [219]. These promising results were translated to the clinics. Oral administration of miglustat was either improving or stabilising neurological symptoms, with early intervention resulting in the most promising outcome [220-223]. Moreover, further combinatorial therapies of miglustat with the anti-inflammatory drug ibuprofen or cytosolic calcium elevating drug curcumin in murine NPC models revealed even better outcomes (prolonged life-span and postponed neurological symptoms), however these interventions have not been explored in clinical trials [128, 202].

Besides acting directly on lipid accumulation, other approaches are currently in clinical trials [204]. Firstly, a histone deacetylase inhibitor (HDACi), which beneficial effect on lipid accumulation in NPC was detected during a high-throughput screen [224]. The mode of action is still not understood, but it has been postulated that inhibiting HDACs affects transcription of several proteins including protein chaperones assisting NPC1 transport from the ER to the late endosomal/lysosomal compartments [225]. Treatment with HDACi in a murine NPC mouse model resulted in reduced lipid accumulation in lysosomes, but beneficial effects are only detected in the periphery, limiting its efficacy to visceral symptoms of NPC [226]. A combinatorial treatment with HDACi (complexd in polyethylene glycol) and HP-β-CD improves brain pathology, delays onset of symptoms and increases life-span [227, 228]. Similar as for allopregnanolone treatment, beneficial effects have been assigned to HP-β-CD [229]. Still, a clinical trial in phase 1/2 was already started to access the safety and tolerability of HDACi (ClinicalTrials.gov Identifier: NCT02124083).

A hydroxylamine derivative named arimoclomol has been also exploited as a potential therapeutic drug. Arimoclomol induces the transcription of heat shock proteins and thereby enhancing protective mechanisms upon cellular stress. Treatment in a murine NPC mouse model reduces cholesterol storage in lysosomes and shows beneficial effects on neurological symptoms and increased life-span [230]. Arimoclomol was tested in a phase 2/3 clinical trial and slowed down disease progression in NPC patients [231].

Thirdly, a derivate of the amino acid leucine, namely *N*-acetyl-L-leucine (NALL), became a drug of interest [232, 233]. It has been already used to treat vertigo and has a good safety profile. The mechanism of action is still not fully understood, but it has been proposed that it stabilises membrane potential, decreases excitability of neurons and acts on glucose and antioxidant metabolism [232, 234]. Treatment with NALL in a $Npc1^{-/-}$ mouse model slowed down Purkinje cell degeneration and increased life-span [232]. Moreover, NALL treatment in NPC patients resulted in slowed disease progression and stabilisation/improvements of neurological symptoms [232, 235].

In summary, treating NPC is still an ongoing challenge impeded by clinical heterogeneity and efficient drug delivery to the brain. Especially early interventions are needed to increase beneficial impact of the treatments [221, 222]. Unfortunately, there is not yet a specific biomarker for NPC, while an array of different tests has to be done to diagnose NPC, slowing down early therapeutic interventions [236].

1.3 Aim of this Work

NPC is a rare autosomal recessive LSD mainly caused by mutations in NPC1 leading to progressive neurodegeneration. Mutations in NPC1 drive cholesterol accumulation within late endosomal/lysosomal compartments. NPC is a multisystemic disease, in which multiple cell types suffer from NPC1 dysfunction, contributing to neurodegeneration. Current therapeutic strategies which target only one pathological process (i.e. acting on lipid homeostasis) resulted in limited clinical benefits, underlying the need to identify new disease modifying strategies. To this end, mechanistic insights into NPC pathology are still not understood, highlighting the need to understand the cell-autonomous contributions of various brain cells to disease pathology and their intercellular cross-talks. In contrast to other brain cells, cell-specific contribution of microglia to NPC pathology was so far underinvestigated. Prominent neurodegeneration was mainly attributed to cell-autonomous loss of NPC1 in neurons. Therefore, the aim of my thesis was to explore molecular and functional consequences of NPC1 loss in microglia and to elucidate their contribution to neurodegeneration using a mouse model with specific loss of NPC1 in myeloid cells. Further aim was to complement studies of rodent microglia with in-depth molecular and functional analysis of blood-derived macrophages from NPC1 patients. This is important as identification of translationally relevant changes upon loss of NPC1 in myeloid cells can be further explored towards disease biomarkers and new translational tools to monitor therapeutic interventions in NPC patients.

2. Materials und Methods

2.1 Materials

2.1.1 Lab Equipment

2.1.1.1 General

Table 2. General lab equipment used in this thesis.

Product	Supplier
Analytical balance (0.0001 - 200 g)	Denver Instrument
Balance (0.01 - 2000 g)	Sartorius
Cryostat (CryS1AR NX70)	Thermo Fisher Scientific
DNA electrophoresis gel system	Bio-Rad
Electrophoresis system Mini-Protean	Bio-Rad
Heating and stirring plate	IKA RH
Imager for agarose gels	INTAS Science Imaging
Luminescent image analyser (iBright)	Thermo Fisher Scientific
Luminescent image analyser (Image Quant LAS-400)	GE Healthcare
MilliQ plus filtration system	Merck Millipore
NanoQuant Infinite M200 PRO	TECAN
Netwell™ inserts for 12-well plate	Thermo Fisher Scientific
Orbital Shaker	GFL
Peristaltic pump	World Precision Instruments
pH meter	Mettler Toledoa
Pipette controller accu-jet pro	BrandTech
Pipette set	Gilson
Protein electrophoresis and transfer system	Bio-Rad
Qubit™ 3 fluorometer	Thermo Fisher Scientific
Real-time PCR (QuantStudio™ 5)	Thermo Fisher Scientific
Savant™ SpeedVac™ SPD120	Thermo Fisher Scientific
Sonifier	Branson
SW32 Ti rotor	Beckmann Coulter
Table top centrifuge (Heraeus Fresco 17 and Pico 17)	Thermo Fisher Scientific
Thermocycler	AnalytikJena
Thermomixer compact	Eppendorf
Tissue grinder (glass potter with pestle)	VWR
Ultracentrifuge Optima LE-80K	Beckmann Coulter
Ultrasonic bath (Sonorex Super)	Brandelin
Universal oven UF30	Memmert
Vortex (Vortex-2 genie)	Scientific industries

2.1.1.2 Cell Culture

Table 3. Cell Culture equipment used in this thesis.

Product	Supplier
Cell culture hood (Herasafe™)	Thermo Fisher Scientific
CO_2 Incubators	Binder
Counter	NeoLab®
Dumont #2, Laminectomy Forceps (11223-20)	Fine Science Tools
Dumont #5, straight fine forceps (11252-20)	Fine Science Tools
Hardend fine scissors straight (14090-11)	Fine Science Tools
Laboratory gas burner (Fuego SCS basic)	WLD-TEC
Laminar flow hood (Heraeus HeraGuard™)	Thermo Fisher Scientific
QuadroMACS separator	Miltenyi Biotec
Table top centrifuge (5810R)	Eppendorf
Vacuum pump	Vacuubrand Chemistry

2.1.1.3 Microscopes and Transmission Electron Microscopy

Table 4. Microscopes used in this thesis.

Product	Supplier
Confocal microscope (LSM 900)	Zeiss
Confocal microscope TC5 SP5	Leica
Dissection microscope (SZ61)	Olympus
Epifluorescence microscope (AxioImager A2)	Olympus
Light microscope (CHX53)	Olympus

2.1.1.4 Mass Spectrometry, ELISA, PET, EM and FACS

Table 5. Equipment used for mass spectrometry, ELISA, PET, EM and FACS in this thesis.

Product	Supplier
1200 nanoHPLC	Thermo Fisher Scientific
3T Mediso nanoScan PET/MR scanner	Mediso Ltd
CaptiveSpray Source	Bruker Daltonics
Column Toaster	Bruker Daltonics
Easy nLC 1000	Thermo Fisher Scientific
gentleMACS™ Octo Dissociator	Miltenyi Biotec
HD-X™ Automated Immunoassay Analyzer	Quanterix
High sensitive gamma counter	Hidex AMG Automatic Gamma
MACSQuant10™	Miltenyi Biotec
JEM 1400plus	JEOL
MoFlo Astrios EQ cell sorter	Beckman Coulter
nanoElute system	Bruker Daltonics
Nanospray Flex Ion Source	Thermo Fisher Scientific

Product	Supplier
Precellys Evolution homogeniser	Bertin Technologies
PRSO-VI column oven	Sonation
Q-Exactive HF mass spectrometer	Thermo Fisher Scientific
QTRAP 6500+	AB Sciex
timsTOF pro mass spectrometer	Bruker Daltonics
TQ 6495C	Agilent
UHPLC ExionLC	AB Sciex
UHPLC Nexera X2	Shimadzu
XF416 camera	TVIPS

2.1.2 Consumables

2.1.2.1 General

Table 6. General consumables used in this thesis.

Product	Supplier	Cat. No.
ACLAR® fluoropolymer-film	Science Services	A50426-10
Cell culture well plates (6, 12 and 24-well)	Thermo Fisher Scientific	140685 150628 142485
Cell scraper	Omnilab	CORN3008
Cell Strainer, 100 µm	Falcon	352360
Falcon™ tubes (15 and 50 mL)	VWR	734-0451 734-0448
Glass coverslip (12 and 15 mm Ø)	Marienfeld	117520 111550
Needle (G 21 x 4 3/4" 0.8 x 120 mm)	Braun	466 5643
Needle (G 25 x 5/8" 0.5 x 16 mm)	Braun	4670012S-01
Needle (G 27 x 3/4" 0.4 x 20 mm)	Braun	4657705
Nunclon™ Delta 100 x 15 mm Schale	Thermo Fisher Scientific	150350
Nunclon™ Delta 60 x 15 mm dish	Thermo Fisher Scientific	150288
Open-Top thinwall ultra-clear tube (38.5 mL)	Beckmann Coulter	344058
Parafilm® M Sealing Film	Merck	HS234526B-1EA
PCR plate (384-well, clear)	Bio-Rad	HSP3801
PCR Plate Sealing Film	Bio-Rad	MSB1001
PCR tubes, 8-stripe	NeoLab®	4-1980
Pipette tips (10, 20, 300 and 1000 µL)	Sarstedt	701.130.210 703.030.265 703.040.255 703.050.255
Porcellain racks	Thomas Scientific	8542-E40
Serological pipettes (2, 5, 10 and 25 mL)	Sarstedt	86.1252.025 86.1253.025 86.1254.025 86.1255.025
S-Monovette® K3 EDTA, 9 mL	Sarstedt	21.066.001
Stericup Vacuum Filtration system (0.22 µm)	Millipore	S2GPU02RE
Syringe (0.1 - 1 mL)	Braun	9161406V
Syringe 10 mL (12 mL)	Henke Sass Wolf	4100-000V0

Syringe 50 mL	Terumo	SS+50L1
Syringe filter (0.2 μm)	VWR	28145-505
Tubes (0.5, 1 and 2 mL)	Eppendorf	0030121023 0030120086 0030120094

2.1.2.2 Histology and Immunofluorescence Staining

Table 7. Consumables used for histology and immunofluorescence staining in this thesis.

Product	Supplier	Cat. No.
Camel hair brushes	Ted Pella inc.	11870
Cork sheet	Thermo Fisher Scientific	12396447
Coverslip, 24 x 50 mm	Marienfeld	101.222
Infusion Set (23 G x 3/4" 0.65 x 19 mm)	Terumo	SV-23BLK
Microscope slide (26 x 76 x1 mm)	Thermo Fisher Scientific	15998086
Microtome blades Feather C35 type	FisherScientific	12-634-1F
Peel-A-Way® Embedding Mold (Square - S22)	Polysciences, inc.	18646A-1
Scalpel	Braun	5518059

2.1.2.3 Cell Culture

Table 8. Consumables used for cell culture in this thesis.

Product	Supplier	Cat. No.
C-Chip, Neubauer improved disposable counting chamber	Science Services	NE63508-01
Corning® 15 mL PET centrifuge tubes	Corning	430053
Falcon® 40 μm Cell Strainer	VWR	612-1799
Glass pasteur glass pipettes (non-plugged)	VWR	612-1702
Glass pasteur glass pipettes (pre-plugged)	VWR	612-1799
Greiner LeucoSep-tube	Sigma Aldrich	Z642843-300EA
LS columns	Miltenyi Biotec	130-042-401

2.1.2.4 Western Blot Analysis

Table 9. Consumables used for western blot analysis in this thesis.

Product	Supplier	Cat. No.
Immobilon-P polyvinylidene difluoride (PVDF) membrane	Millipore	IPVH00010
Nitrocellulose membrane, precut	Bio-Rad	1620145

2.1.2.5 Mass Spectrometry

Table 10. Consumables used for mass spectrometry in this thesis.

Product	Supplier	Cat. No.
BEH C18 1.7 µm, 2.1×100 mm column	Waters	186002352
C18 column material	Empore	66883-U
Corning® Costar® Spin-X® centrifuge tube filters	Merck	32119210
Cytiva Sera-Mag SpeedBeads™ carboxyl-magnet-beads, hydrophob	Thermo Fisher Scientific	11829912
Eppendorf Protein LoBind tubes (1.5 mL)	Eppendorf	0030 108.116
HALO HILIC 2.0 µm, 3.0 × 150 mm column	Advanced Materials Technology	PN 91813-701
Precellys soft tissue lysis kit	Bertin Technolo-	P000912-LYSK0-A
ReproSil-Pur 120 C18-AQ (1.9 µm)	Dr. Maisch	r119.aq.0003
Vivacon® spin filter 10k or 30 k cut off	Sartorius	VN01H02, VN01H22

2.1.3 Reagents

2.1.3.1 Genotyping

Table 11. Reagents used for genotyping in this thesis.

Product	Supplier	Cat. No.
DNA ladder, 1 kB Plus	Invitrogen	10787018
GelRed, 10,000X	Biotium	41003-1
GoTaq G2 DNA polymerase	Promega	M784B
Green GoTaq PCR buffer, 5X	Promega	M791A
NaOH, 1 M	Fluka Analytical	71463-1L
Nuclease-free water (not DEPC-Treated)	Thermo Fisher Scientific	AM9937
PCR nucleotide mix	Roche	11814362001
SYBR™ Green PCR Master Mix	Thermo Fisher Scientific	4367659

2.1.3.2 Histology and Immunofluorescence Staining

Table 12. Reagents used for histology and immunofluorescence staining in this thesis.

Product	Supplier	Cat. No.
Donkey anti-mouse FAB fragment	Jackson laboratories	715-007-003
Donkey serum	Sigma Aldrich	S30-100ML
Epredia™ M-1 embedding matrix	Thermo Fisher Scientific	1310
Fluoromount™	Sigma Aldrich	F4680-25ml
Normal goat serum, New Zealand origin	Thermo Fisher Scientific	16210064
O.C.T.™ Compound	Sakura	4583

2.1.3.3 Cell Culture

Table 13. Reagents used for cell culture in this thesis.

Product	Supplier	Cat. No.
ACK lysing buffer	Thermo Fisher Scientific	A1049201
Bovine serum albumin (BSA) - fatty acid free	Sigma Aldrich	A7030-50G
BSA	Sigma-Aldrich	A706-100G
CD11b (Microglia) MicroBeads, human and mouse	Miltenyi Biotec	130-093-634
Cholera toxin subunit B (CtxB) Alexa Fluor™ 647	Thermo Fisher Scientific	C34778
DMEM, high glucose, GlutaMAX™ supplement, pyruvate	Gibco	31966047
DMEM-F12	Gibco	11330-057
DPBS, no calcium, no magnesium	Thermo Fisher Scientific	14190169
DQ™ Red BSA	Thermo Fisher Scientific	D12051
EGF recombinant mouse protein	R&D System	2028-EG-200
FBS	Sigma Aldrich	F7524
Ficoll® Paque Plus	Sigma Aldrich	GE17-1440-02
Hanks' balanced salt solution (HBSS)	Gibco	14025100
HEPES Buffer Solution (1M)	Gibco	15630-056
M-CSF Recombinant Human Protein	Thermo Fisher Scientific	PHC9501
MEM Non-Essential Amino Acids Solution (100X)	Gibco	11140035
Papain from papaya latex	Sigma Aldrich	P3125-250MG
Phosphate buffered saline (PBS), 1X, pH 7.4	Gibco	10010056
Penicillin/streptomycin (Pen/Strep)	Gibco	15070063
PKH67 Green Fluorescent Cell Linker Mini Kit	Sigma Aldrich	PKH67GL-1KT
Recombinant mouse GM-CSF protein	R&D Systems	415-ML-010
RosetteSep™ Human Monocyte Enrichment Cocktail	Stem Cell Technologies	15068
RPMI 1640 medium	Gibco	21875091
Sodium Pyruvate	Gibco	11360070
Trypan-blue	Sigma	T8154-20 mL
UltraPure™ 0.5M EDTA, pH 8.0	Thermo	4 15575020
Versene® (EDTA), 0.02%	Lonza	BE17-711E

2.1.3.4 Western Blot Analysis and Mass Spectrometry

Table 14. Reagents used for western blot analysis and mass spectrometry in this thesis.

Product	Supplier	Cat. No.
BC assay protein quantitation kit	VWR	UP40840A
Benzonase	Sigma-Aldrich	E1014
Bio-Rad Protein Assay Dye Reagent Concentrate	Bio-Rad	5000006
cOmplete™, EDTA-free protease inhibitor cocktail	Thermo Fisher Scientific	11873580001
ECL™ Blotting Reagent	GE Healthcare	GERPN2106
ECL™ Prime Western Blotting System	GE Healthcare	RPN2232
iRT Kit	Biognosys	Ki-3002
Laemmli SDS sample buffer, reducing 4X	Alfa Aesar	J60015
LysC	Promega	V1671

PhosSTOP phosphatase inhibitor cocktail tablets	Roche	04 906 837 001
Pierce 660 nm protein assay	Thermo Fisher Scientific	22660
Precision plus Protein™ dual color standards	Bio-Rad	1610374
Qubit protein assay	Thermo Fisher Scientific	Q33212
Restore™ Western Blot Stripping Buffer	Thermo Fisher Scientific	21059
Tris/glycine buffer, 10X	Bio-Rad	1610771
Trypsin	Promega	V5111

2.1.3.5 Single Cell Radiotracing

Table 15. Reagents used for single cell radiotracing in this thesis.

Product	Supplier	Cat. No.
ACSA-2- APC-VIO® 770	Miltenyi Biotec	130-116-247
AstroMACS separation buffer	Miltenyi Biotec	130-117-336
Adult Brain Dissociation Kit (mouse and rat)	Miltenyi Biotec	130-107-677
CD11b-VioBlue® antibody	Miltenyi Biotec	130-113-810
MS columns	Miltenyi Biotec	130-042-201

2.1.4 Positron Emission Tomography Tracers

Table 16. Positron emission tomography (PET) tracers used in this thesis.

Product	Target	Supplier
[^{18}F]GE-180	TSPO	All PET tracers were produced in-house according to an established, standardised protocol
[^{18}F]D2-Deprenyl	MAO-B	
[^{18}F]FDG	Glucose uptake	

2.1.5 Chemicals

Table 17. Chemicals used in this thesis.

Product	Supplier	Cat. No.
Acetic acid (glacial) 100%	Merck	1.00063.251
Acetonitrile	Biosolve	01204101
Acrylamide/Bis Solution (40%)	SERVA	10681.03
Agarose ultrapure	Thermo Fisher Scientific	16500500
Ammonium bicarbonate	Thermo Fisher Scientific	15645440
Ammoniumperoxodisulfat (APS)	Roth	9592.3
Citric acid monohydrate	Merck	5949-29-1
Cycloheximide	C4859	Sigma Aldrich
Dithiothreitol	Thermo Fisher Scientific	10666885
Epon	Serva	21045.02
Ethylene glycol	Merck Millipore	1096212500
Ethylenediaminetetraacetic acid (EDTA)	Merck	1.084.181.000
Fish gelatine	Sigma-Aldrich	G7765-250mL

Product	**Supplier**	**Cat. No.**
Formic acid, 0.1%	Roth	CP03
Formic acid, 8%	Thermo Fisher Scientific	34692
Glutaraldehyde	Science Services	E16216
Glycerol	Roth	3783.1
HEPES Buffer Solution, 1 M	Gibco	15630-056
HNO_3, 65%	Merck	1.004.561.000
Iodoacetamide	Sigma Aldrich	I1149
Isopropanol	Merck Millipore	1096342511
K_2HPO_4	Merck	1.048.771.000
KCl	Merck	1.049.361.000
Ketamine	belapharm	
L-Cysteine	Sigma Aldrich	C6852-25G
LX 112 Embedding Kit	LADD Research Laboratories	21210
Methyl-β-cyclodextrin (MβCD)	Sigma Aldrich	C4555-5G
Milk powder	Sigma Aldrich	70166-500G
Na_2HPO_4 x 2 H_2O	Merck	1.065.805.000
NaCl	Roth	3957.2
NH_4Cl	Merck	1.011.450.500
Osmium tetroxide	Science Services	E19130
Paraform aldehyde (PFA)	Merck	104005
Poly-L-lysine hydrobromide (PLL)	Sigma-Aldrich	P2636
Potassium hexacyanoferrate(II) trihydrate	Sigma	455989
Sodium azide 10 %	Morphisto	13553.00100
Sodium cacodylate trihydrate	Science Services	E12300
Sodium dodecyl sulfate (SDS)	Merck	8.220.501.000
Tetramethylethylenediamine (TEMED)	Roth	2367.1
Tris base	PanReac	A1086.5000
Tris/glycine buffer, 10X	Bio-Rad	1610771
Triton X-100	Merck	1086031000
Tween-20	Merck	8.22184
Uranyl acetate	Science Services	E22400-05G
Urea	Merck	1.08487
Xylanzine	Serumwerk	

2.1.6 Buffer and Solutions

2.1.6.1 Genotyping

Table 18. Buffers and solutions prepared for genotyping in this thesis.

Buffer/Solution	**Components**
Agarose gel (1 or 2%)	1 or 2 g agarose in dH_2O
Neutralisation buffer (pH 8.8)	1.5 M Tris in dH_2O
Tris-acetate-EDTA (TAE), 1X	40 mM Tris 20 mM acetic acid 10 mM EDTA in dH_2O

2.1.6.2 Histology and Immunofluorescence Staining

Table 19. Buffers and solutions prepared for histology/immunofluorescence staining in this thesis. IHC = immunohistochemistry, ICC = immunocytochemistry.

Buffer/Solution	**Components**
Blocking buffer	5 % NGS or donkey serum in PBS-T
Blocking solution (ICC)	2 % FBS 2 % BSA 0.2 % fish gelatine in 0.01 M PBS
Citrate buffer	10 mM citric acid in dH_2O (pH 6.0)
Ketamine/xylazine mixture	60% 100 mg/mL ketamine 20% 20 mg/mL xylazine 20% NaCl
NH_4Cl, 50 mM	50 mM NH_4Cl in dH_2O
PBS, 0.01 M	10% 0.1 M PBS in dH_2O
PBS, 0.1 M	1370 mM NaCl 27 mM KCl 100 mM Na2HPO4 18 mM KH2PO4 in dH2O (pH 7.4)
PBS-T	0.5 % Triton X-100 in 0.01 M PBS
PFA, 4%	4% PFA in 0.1 M PBS (pH 7.4)
PFA/sucrose, 4%	4% PFA 4% sucrose in 0.01 M PBS
primary/ secondary antibody solution (ICC)	primary/secondary antibodies in 10% blocking solution (ICC)
Primary/secondary antibody solution (IHC)	primary/secondary antibodies in blocking solution (IHC)
Storage solution	25% glycerol 25% ethylene glycol in 0.1 M PBS
Sucrose, 30%	30% sucrose in 0.1 M PBS
Triton X-100, 0.01%	0.01% Triton X-100 in 0.01 M PBS

2.1.6.3 Cell Culture

Table 20. Buffers and solutions prepared for cell culture in this thesis.

Buffer/Solution	Components
HBSS buffer	7 mM HEPES in 1X HBSS
BSA, 4%	4% BSA in dH_2O
Magnetic-activated cell sorting (MACS) buffer	0.5 % BSA 2 mM EDTA in 1X PBS
MβCD, 250 µM	250 µM MβCD in dH_2O
Sonication buffer	10 mM HEPES 5 mM EDTA 0.3 M sucrose in dH_2O

Sucrose, 0.32 M (pH 7.4)	0.32 M sucrose 10 mM HEPES 5 mM EDTA in dH$_2$O
Sucrose, 0.85 M (pH 7.4)	0.85 M sucrose 10 mM HEPES 5 mM EDTA in dH$_2$O
Wash buffer	2% FBS 1 mM EDTA in DPBS

2.1.6.4 Western Blot Analysis

Table 21. Buffers and solutions prepared for western blot analysis in this thesis.

Buffer/Solution	Components
Blocking buffer	5% milk powder in TBS-T
Lower Tris buffer (pH 8.8)	1.5 M Tris (pH 8.8) 0.4% SDS in dH$_2$O
Primary antibody solution	primary antibody 1 mL BSA 60 µL 10% Sodium azide 10 % in 11 mL TBS-T
Running buffer	1X Tris/glyicine buffer 0.1% SDS in dH$_2$O
Secondary antibody solution	secondary antibody 1 mL BSA in 11 mL TBS-T
STET lysis buffer	50 mM Tris 150 mM NaCl 2 mM EDTA 1 % Triton X-100 + protease inhibitors (1:500) + phosphatase inhibitors (1X) in dH$_2$O
TBS-T	0.05% Tween-20 in TBS
Transfer buffer	1X Tris/glyicine buffer in dH$_2$O
Tris-buffered saline (TBS)	50 mM Tris (pH 7.6) 150 mM NaCl in dH$_2$O
Upper Tris buffer (pH 6.8)	0.5 M Tris (pH 6.8) 0.4% SDS in dH$_2$O

2.1.6.5 EM Analysis

Table 22. Buffers and solutions prepared for EM analysis in this thesis.

Buffer/Solution	Components
Cacodylate buffer, 0.1 M	0.1 M sodium cacodylate trihydrate in dH$_2$O

Uranylacetate, 1%	1% uranylacetate in dH_2O
Fixative solution 1	2% PFA, 2.5% glutaraldehyde in 0.1 M cacodylate buffer (pH 7.4)
Fixative solution 2	5% glutaraldehyde in 0.2 M cacodylate buffer (pH 7.4)
Reduced osmium tetroxide	2% osmium tetroxide 2.5% potassium hexacyanoferrate in 0.1 M cacodylate buffer

2.1.7 Cell Culture Medium

Table 23. Medium prepared for cell culture in this thesis.

Medium	Components
Blocking medium	10% FBS in DMEM
Macrophage medium	1 mM Na pyruvate 1X NEAA 1% PenStrep 10% FBS in RPMI 1640 medium
Microglia medium	10 % FBS 1 % Pen/Strep + 10 ng/mL GM-CSF (for cultures from adult mice) in DMEM-F12
Papain digestion medium	300 µL papain (200 U) 0.01 g L-cysteine in 9.7 mL DMEM (adjust pH to DMEM colour with 1 M NaOH)

2.1.8 Antibodies and Dyes

Table 24. Primary antibodies used for immunofluorescence staining in this thesis.

Antibody	Species	Dilution	Supplier	Cat. No.
APP (Y-188)	Rabbit	1:200	Abcam	ab32136
Aβ (2D8)	Rat	3 µg/mL	Self-made	[237]
Aβ (3552)	Rabbit	1:500	Self-made	[238]
Aβ (6E10)	Mouse	5 µg/mL	BioLegend	SIG-39320
Calbindin	Mouse	1:500	Swant	300
CD31	Goat	1:500	R&D Systems	AF3628
CD68 (mouse)	Rat	1:500	AbD Serotec	MCA1957GA
CNPase	Mouse	1:300	Abcam	ab6319
CtxB	Biotinylated	1 µg/mL	Sigma	C9972-.5MG
GFAP	Chicken	1:2000	ThermoFisher Scientific	PA1-10004
GM2	Mouse	1:100	TCI	A2576
Iba1	Rabbit	1:300	Wako	019-19741
Iba1	Guinea pig	1:500	Synaptic Systems	234 308
NeuN	Rabbit	1:500	Millipore	ABN78
NF200	Rabbit	1:200	Sigma	N4142

Perilipin 2	Guinea pig	1:200	Progen Biotechnik	GP40
Synaptophysin	Rabbit	1:500	Abcam	ab32594
TSPO	Rabbit	1:500	Abcam	ab109497

Table 25. Secondary antibodies used for immunofluorescence staining in this thesis.

Antibody	Species	Dilution	Supplier	Cat. No.
Alexa 488, anti-guinea pig IgG (H+L)	Goat	1:500	Thermo Fisher Scientific	A-11073
Alexa 488, anti-mouse IgG (H+L)	Goat	1:500	Thermo Fisher Scientific	A-11029
Alexa 488, anti-rabbit IgG (H+L)	Goat	1:500	Thermo Fisher Scientific	A-11034
Alexa 488, anti-rabbit IgG (H+L)	Donkey	1:500	Thermo Fisher Scientific	A-21206
Alexa 488, anti-rat IgG (H+L)	Goat	1:500	Thermo Fisher Scientific	A-11006
Alexa 555, anti-chicken IgY (H+L)	Goat	1:500	Thermo Fisher Scientific	A-21437
Alexa 555, anti-goat IgG (H+L)	Donkey	1:500	Thermo Fisher Scientific	A-11055
Alexa 555, anti-guinea pig IgG (H+L)	Goat	1:500	Thermo Fisher Scientific	A-21435
Alexa 555, anti-mouse IgG (H+L)	Goat	1:500	Thermo Fisher Scientific	A-21424
Alexa 555, anti-rabbit IgG (H+L)	Goat	1:500	Thermo Fisher Scientific	A-21428
Alexa 555, anti-rat IgG (H+L)	Goat	1:500	Thermo Fisher Scientific	A-21434
Alexa 647, anti-mouse IgG (H+L)	Goat	1:500	Thermo Fisher Scientific	A-21235
Alexa 647, anti-rabbit IgG (H+L)	Goat	1:500	Thermo Fisher Scientific	A-21244
Alexa 647, anti-rat IgG (H+L)	Goat	1:500	Thermo Fisher Scientific	A21247

Table 26. Primary antibodies used for immunoblot in this thesis.

Antibody	Species	Dilution	Supplier	Cat. No.
APOE	Goat	1:1000	Millipore	AB947
Calnexin	Rabbit	1:1000	Stressgen	ADI-SPA-860
Cathepsin B	Goat	1:2000	R&D Systems	AF965
Cathepsin D	Rabbit	1:1000	Novus Biologicals	NBP1-50682
CD63 (mouse)	Rabbit	1:1000	Abcam	ab217345
CD68 (human)	Mouse	1:500	Acris	AM33123SU-N
CNPase	Mouse	1:300	Abcam	ab6319
EGFR	Rabbit	1:1000	Abcam	ab52894
GAPDH	Mouse	1:2000	Abcam	ab8245
GFAP	Rabbit	1:1000	Dako	Z-0334
GRN (8H10)	Rat	1:50	Home made	[239]
GRN (human)	Rabbit	1:1000	Thermo Fisher Scientific	40-3400
Iba1	Rabbit	1:300	Wako	019-19741
LAMP1	Rabbit	1:1000	Sigma	L1418
Mouse CD68	Rat	1:500	AbD Serotec	MCA1957GA
NeuN	Mouse	1:1000	Millipore	MAB377
NPC1	Rabbit	1:1000	Abcam	ab134113
NPC2	Rabbit	1:1000	Sigma	HPA000835
PLP1	Rabbit	1:1000	Abcam	ab83032
TGFB1	Goat	1:1000	R&D Systems	AF-246-NA
TREM2 (5F4)	Rat	1:10	Home made	[240]
Tuj1 (βIII tubulin)	Mouse	1:1000	Covance	MMS-435P

Table 27. Secondary antibodies used for western blot in this thesis.

Antibody	Species	Dilution	Supplier	Cat. No.
Anti-goat IgG (H+L), HRP conjugate	Donkey	1:4000	Dianova	705-035-003
Anti-mouse IgG (H+L), HRP conjugate	Goat	1:4000	Promega	W402B
Anti-rabbit IgG (H+L), HRP conjugate	Goat	1:4000	Promega	W401B
Anti-rat IgG antibody, HRP conjugate	Goat	1:4000	Merck	AP136P

Table 28. Dyes used in this thesis.

Dye	Dilution	Supplier	Cat. No.
Filipin from Streptomyces filipinensis	0.1 mg/mL	Sigma	F9765-25MG
Fluoromyelin red	1:300	Thermo Fisher Scientific	F34652
Hoechst 33342	1:2000	Thermo Fisher Scientific	H3570
Thiazine Red (ThR)	1:1000	Morphisto	12648

2.1.9 Animals

In this study, both, female and male mice were used for experiments. Mice were kept in specific pathogen-free conditions with a 12h/12h light-dark cycle, had access to standard mouse chow (Sniff® Ms-H, SSniff Spezialdiäten GmbH) and water *ad libitum*. Animal experiments were conducted according to the German animal welfare law and approved by the government of Upper Bavaria. Mouse lines used in this study are listed in Table 29.

Table 29. **Mouse lines used in this thesis.**

Mouse line	Mouse strain	Genetic modification	Reference
APP/PS1	C57BL/6J	Human mutated *APP* (Swedish) and *PS1* (L166P) expressed constitutively under neuronal promotor *Thy-1*	[241]
B6.Cx3cr1tm1.1 (cre)Jung/N (*Cx3cr1Cre*)	C57BL/6N	Constitutive expression of the Cre recombinase under the myeloid promotor *Cx3cr1*	[242]
BALB/cNctr-Npc1m1N/J (*Npc1*^{m1n})	BALB/cNctr	Spontaneous insertion of MaLR retroponson-like DNA resulting in premature truncation of NPC1	The Jackson laboratory (JAX stock #003092)
C57BL/6J		No genetic modifications were done	The Jackson Laboratory (JAX stock #000664)
C57BL/6-Npc1tm1.2Apl (*Npc1* cKO)	C57BL/6	Insertion of *loxP* sites flanking exon 9 of *Npc1*	[146]
Npc1 cKO x *Cx3cr1Cre*	C57BL/6	Specific loss of *Npc1* in myeloid cells	[243]

2.1.10 Primers Used for Genotyping

2.1.10.1 PCR

The following oligonucleotide primers were purchased from Sigma Aldrich, resuspended in dH_2O and diluted 1:10 in dH_2O for a working concentration of 10 µM (listed in Table 30).

Table 30. Primers used for genotyping in this thesis.

Mouse line	Primer	Sequence (5’→3’)
APP/PS1	APP-forward	GAATTCCGACATGACTCAGG
	APP-reverse	GTTCTGCTGCATCTTGGACA
	PS1-forward	CAGGTGCTATAAGGTCATCC
	PS1-reverse	ATCACAGCCAAGATGAGCCA
Npc1^{m1n}	WT-oIMR0928	CTG TAG CTC ATC TGC CAT CG
	WT-oIMR0929	TCT CAC AGC CAC AAG CTT CC
	KO-oIMR0927	TGA GCC CAA GCA TAA CTT CC
	KO-oIMR4125	GGT GCT GGA CAG CCA AGT A
Npc1 cKO	Flox-forward	TACTTGGTAGTTGTCAGGTAGGCTTATGCT
	Flox-reverse	ACACTGCAACGGGCTCCTTTG
Cx3Cr1Cre	Cx3-forward	CCTCTAAGACTCACGTGGACCTG
	Cx3-reverse wt	GACTTCCGAGTTGCGGAGCAC
	Cx3 spec	GCCGCCCACGACCGGCAAAC

2.1.10.2 qPCR

The following oligonucleotide primers were purchased from Sigma Aldrich, resuspended in dH_2O and diluted 1:40 in dH_2O for a working concentration of 2.5 µM (listed in Table 31).

Table 31. Primers used for analysing *Npc1* heterozygosity via qPCR.

Mouse line	Primer	Sequence (5’→3’)	Loci	Size
Npc1 cKO x *Cx3cr1Cre*	loxP-forward	AGAGAATAGGAACTTCGGAATAGG	first *loxP* site	69 bp
	loxP-reverse	CGAAGTTATTAGGTCCCTCGAC		
	Exon9-forward	TTGAAAGCATCACCGCATCT	exon 9 of *Npc1*	92 bp
	Exon9-reverse	GGTGCAGTTCTTGTTGTATGGA		
	Npc1-forward	GCTGGCGATTGTTGCTTTCA	5`UTR of *Npc1*	92 bp
	Npc1-reverse	TCACATGCAGCTCTACCCAC		

2.1.11 Human Material

Human blood samples from three healthy controls (CTR) and seven NPC patients (NPC) were included in this study (Table 32). Experiments were approved by the Ethics Committee of the University of Munich and performed in agreement with the 1964 Declaration of Helsinki.

Table 32. Data of human material used in this study (age, gender, severity grade, *NPC1* mutation, current therapy). The cross indicates if samples were used for functional analysis and/or mass spectrometry (MS) analysis. The table is retrieved and adapted from Colombo and Dinkel *et al*. [243]. n.a. = not available.

N°	Age	Gender	Severity grade	Mutation	Current therapy	Functional analysis	MS analysis
CTR 1	43	M	n.a.	n.a.	n.a.	X	X
CTR 2	25	F	n.a.	n.a.	n.a.	X	X
CTR 3	31	F	n.a.	n.a.	n.a.	X	X
NPC 1	18	M	Severely ill, wheel chair bound	Homozygous for c.2974G>T (p.Gly992Trp)	Miglustat	X	X
NPC 2	25	M	Severely ill, wheel chair bound	Homozygous for c.2974G>T (p.Gly992Trp)	Miglustat was discontinued in 2017	X	X
NPC 3	20	M	Severely ill (palliative care), final stage, early-infantile, epilepsy	Homozygous for c.2861C>T (p.Ser954Leu)	Miglustat	X	X
NPC 4	12	F	Severely ill (SARA Score Visit 1: 14/40)	c.2130+2T>C (NM_000271) and c.3019C>G (p.Pro1007Ala)	Miglustat	X	X
NPC 5	32	M	Moderately ill (SARA Score Visit 1: 8/40)	c.709C>T (p.Pro237Ser) and unknown	Miglustat	X	X
NPC 6	34	M	Markedly ill	c.2861C>T (p.Ser954Leu) and c.3019C>G	Miglustat		X
NPC 7	36	M	Moderately ill (SARA Score Visit 1: 9/40)	Homozygous for c.3182T>C (p.Ile1061Thr)	Miglustat	X	X

2.1.12 Software Used for Analysis

Table 33. Software used for analysis in this thesis.

Name	Source
Amica (version 2022.09.08)	[244]
DIA-NN (version 1.8)	[245]
EM-Menu software	TVIPS
Fiji	https://imagej.net/software/fiji/downloads
GraphPad Prism	https://www.graphpad.com/scientific-software/prism/
Maxquant version 1.6.3.3	maxquant.org, Max-Planck Institute Munich [246]
Multi Gauge V3.0	FUJIFILM
MultiQuant (version 3.02)	AB Sciex
Perseus	[247]
Skyline (version 19.1)	University of Washington
Spectronaut (version 12.0.20491.14.21367)	Biognosys
ZEN 3.1	ZEISS

2.2 Methods

2.2.1 Genotyping of Transgenic Mouse Lines

Genomic DNA was extracted from tail or ear biopsies via alkaline lysis. Samples were lysed in 100 µL 50 mM NaOH for 45 min at 95°C while shaking (600 rpm). Lysis was neutralised with 10 µL neutralisation buffer and centrifuged for 5 min at 17,000 × *g* at 4°C in order to precipitate tissue debris. PCR reactions for amyloid-β precursor protein (*APP*) and presenilin-1 (*PS1*) or *Npc1*$^{+/+}$ and *Npc1*$^{-/-}$ were performed separately. The supernatant was diluted 1:10 in dH$_2$0 and was used for PCR reactions, besides for APP/PS1 genotyping, where undiluted DNA was used (Table 34 and Table 35). PCR products were analysed with an agarose gel electrophoresis (agarose gels were supplemented with GelRed® 1:10,000) and the expected PCR products are shown in Table 36.

Table 34. Pipetting scheme for one PCR reaction for genotyping.

Reagent	APP/PS1	*Npc1*^{m1n}	*Npc1* cKO	*Cx3cr1Cre*
5X reaction buffer	4 µL	5 µL	5 µL	5 µL
Each primer (10 µM)	1 µL	1 µL	1 µL	1 µL
dNTPs (10 mM)	0.5 µL	0.5 µL	0.5 µL	0.5 µL
dH$_2$O	12.3 µL	16.375	14.375 µL	15.375 µL
DNA polymerase (5 U/µL)	0.2 µL	0.125 µL	0.125 µL	0.125 µL
DNA	1 µL	1 µL	3 µL	1 µL
Total volume	20 µL	25 µL	25 µL	25 µL
Loaded on agarose gel	20 µL	12.5 µL	25 µL	12.5 µL

Table 35. **PCR programs for genotyping mice.** T = temperature**.**

APP/PS1				*Npc1*^{m1n}			
Step	**T**	**Time**	**Cycles**	**Step**	**T**	**Time**	**Cycles**
1	95°C	10 min	1	1	94°C	3 min	1
2	95°C	30 s	35	2	94°C	30 s	35
3	63°C	30 s		3	63°C	45 s	
4	72°C	30 s		4	72°C	45 s	
5	72°C	5 min	1	5	72°C	2 min	1
6	10°C	∞		6	10°C	∞	
***Npc1* cKO**				***Cx3cr1Cre***			
Step	**T**	**Time**	**Cycles**	**Step**	**T**	**Time**	**Cycles**
1	95°C	3 min	1	1	95°C	3 min	1
2	95°C	30 s	35	2	95°C	30 s	35
3	63°C	30 s		3	59°C	30 s	
4	72°C	150 s		4	72°C	60 s	
5	72°C	7 min	1	5	72°C	7 min	1
6	10°C	∞		6	10°C	∞	

Table 36. Lengths of expected PCR products and agarose gel concentration used for separation of DNA fragments.

Mouse line	**Agarose gel**	**Wildtype**	**Transgene**
APP/PS1	1%	-	APP: ~250 bp; PS1: ~250 bp
Cx3cr1Cre	2%	750 bp	304 bp
Npc1 cKO	2%	1377 bp	1625 bp
Npc1^{m1n}	1%	173 bp	475 bp

2.2.2 Genotyping for *Npc1* Heterozygosity in *Npc1*cKO x *Cx3cr1Cre* Mice

In this study, a new mouse line with specific loss of *Npc1* in myeloid cells was generated. Therefore, mice which have two *loxP* sites flanking exon 9 of *Npc1* (C57BL/6-Npc1tm1.2Apl [146]), termed as *Npc1* cKO in this thesis, were crossed with mice expressing the Cre recombinase under the myeloid specific promotor *Cx3cr1* (B6.Cx3cr1tm1.1(cre)Jung/N [242]), termed as *Cx3cr1Cre* in this thesis. Excision of exon 9 by Cre recombinase leads to a frameshift resulting in a *Npc1* null allele similar as seen in *Npc1*^{m1n} [146]. It has been reported that *Cre* driver lines might have spontaneous expression of the Cre recombinase in the germline, resulting in recombination of the target gene in the parental genome. Thereby, the offspring would inherit the recombined gene causing heterozygosity of the target gene [248]. In order to control for *Npc1* heterozygosity, a qPCR approach was established (Figure 8).

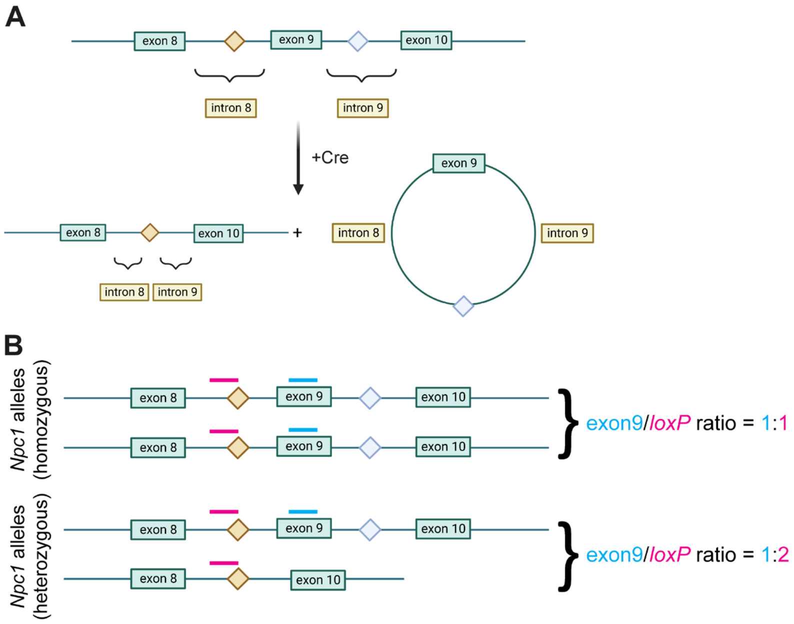

Figure 8. Scheme for genotyping *Npc1* heterozygosity in *Npc1*cKO x *Cx3cr1Cre* mice. A Exon 9 of the *Npc1* allele is flanked by two *loxP* sites located in the intron 8 and 9 (orange and light blue squares). In presence of the active Cre recombinase, exon 9 is excised and the first *loxP* site remains integrated in the genomic DNA. **B** To exclude germline activation of the Cre recombinase (which leads to *Npc1* heterozygosity), I controlled for the spontaneous excision of exon 9. Primers were designed to amplify the first *loxP* site (orange square) and exon 9 (blue line). The quantity of each amplification was determined using qPCR, and the ratio of exon 9 to the first *loxP* site was calculated. A ratio of 1 would indicate *Npc1* homozygosity, while a ratio of 0.5 indicates *Npc1* heterozygosity.

The DNA concentration of the same DNA sample, which was used for PCR (1:10 diluted), was determined using the NanoQuant. The pipetting scheme and qPCR program are shown in Table 37.

Table 37. Pipetting scheme for one qPCR reaction (10 µL) and the qPCR program used for genotyping *Npc1* heterozygosity. qPCR steps 4 - 6 represent the melt curve.

qPCR reaction		**qPCR program**			
Reagent	**Amount**	**Step**	**T**	**Time**	**Cycles**
SYBR™ Green PCR Master Mix	5 µL	1	95 °C	10 min	1
DNA	10 ng	2	95°C	15 s	40
Forward primer (2.5 µM)	0.5 µL	3	60°C	60 s	
Reverse primer (2.5 µM)	0.5 µL	4	95°C	15 s	continuous
Nuclease-free water	Add up to 10 µL	5	60°C	60 s	
		6	95°C	15 s	

A dilution series (undiluted, 1:10, 1:100, 1:1,000 and 1:10,000) of a standard (mix of 2 µL of each DNA sample) was always run in parallel. The qPCR was run in triplicates for each primer set using the QuantStudio 5. The absolute amounts (2^{-ct}) of exon 9 and the first *loxP* site were normalised to the absolute amount of the reference gene *Npc1*. The ratio of exon 9/*loxP* was calculated and a ratio of 1 indicates *Npc1* homozygosity, while an exon 9/*loxP* ratio of 0.5 indicates *Npc1* heterozygosity. In this study, only mice with an exon 9/*loxP* ratio ≥ 0.8 were used.

2.2.3 Histology

2.2.3.1 Transcardiac Perfusion and Brain Fixation

Mice were anesthetised by injecting around 200 µL of a ketamine/xylazine mixture intraperitoneally. Reflexes of the mice were checked by pinching into the mouse paws. When paw pinch reflexes were absent (around 5 min), the mouse was fixed with its limbs to a Styrofoam pad using needles. The skin at the level of the stomach was lifted up with forceps and a transversal cut through the skin and muscle layers was made. Sagittal cuts in direction of the heart were made until the sternum. The sternum was lifted up and a cut into the diaphragm was made to expose the lung and the heart. In order to have better access to the heart, additional big cuts into the left and right costal arch were made. The upper part of the thorax was fixed with a needle to the Styrofoam pad. Afterwards, a butterfly needle (which is connected to cold 0.1 M PBS) was introduced into the left ventricle (white part at the tip of the heart) and fixed to the Styrofoam pad to prevent moving of the needle. The peristaltic pump was started (with a speed of 5 mL/min) and a cut into the right atrium (dark part of the heart) was made in order to allow PBS flow through the blood circulation. After 5 min, the butterfly was connected to 4% PFA and the mouse was further perfused with 4% PFA for 15 min, the mouse brain was extracted and post-fixed for another 20 min in 4% PFA. Alternatively, when the mice were not perfused with 4% PFA, but only with 0.1 M PBS for 5 min, the brain was extracted and post-fixed in 4% PFA for 6 h on ice. For fixation of neonatal (1-week) brain, the pups were decapitated, brains were extracted and fixed for 6 h in 4% PFA on ice.

For cryoprotection, the PFA-fixed brains were transferred to 30% sucrose and incubated at 4°C until the brain sunk down in the solution (typically takes 2-3 days). Afterwards, the two hemispheres were separated, embedded in O.C.T.^{TM} using embedding molds and frozen on dry ice. Embedded brains were stored at -80°C until usage.

2.2.3.2 Brain Cryosectioning

Embedded brain hemispheres stored at -80°C were equilibrated at -20°C as well as all tools needed for cryosectioning (blade, scalpel, brushes) for 20-30 min. Afterwards, the hemisphere was taken out from the embedding mold and fixed to the cutting specimen with an Epredia™ embedding matrix. Next, sagittal brain sections (30 µm thick) were cut using the cryostat. Ten sequential brain sections were transferred to a 6-well plate filled with 5 mL of 0.01 M PBS (one hemisphere results in roughly two 6-well plates with 10 brain sections/well). At the end, the brain sections were put onto a shaker for 30 min in order to wash away excess of O.C.T.^{TM}. Afterwards, sections were either immediately used for immunohistochemistry or stored in 0.01 M PBS at 4°C (up to 2 weeks) or transferred into the storage solution (1 mL storage solution in a 2 mL Eppendorf tube) and stored at -20°C until usage.

2.2.3.3 Immunohistochemistry of Free-floating Brain Sections

All incubation and washing steps were performed on a shaker to assure even agitation. Furthermore, washing steps are performed using Netwell™ inserts (3 mL/well), while incubation steps were performed in a 24-well plate to reduce the volume of the antibody solution (500 µL/well). Brain sections were transferred using a small brush.
Brain sections stored in 0.01 M PBS or storage solution were transferred into Netwell™ inserts, filled with 3 mL PBS-T and were washed three times for 10 min with PBS-T. When antibodies were used which are raised in mouse, a treatment with a donkey anti-mouse FAB fragment was performed in order to mask unspecific mouse epitopes. Therefore, brain sections were incubated with the FAB fragment (1:1,000 in 0.01 M PBS) for 1 h at RT. After three washes for 10 min in PBS-T, brain sections were blocked in blocking buffer for 1 h, and subsequently, incubated in primary antibody solution over night at 4°C. The next day, brain sections were washed three times for 10 min with PBS-T and incubated in secondary antibody solution for 2 h at RT in the dark (from now on all steps were performed in light-reduced conditions). Hoechst (nuclear stain) and other dyes were added to the secondary antibody solution. Lastly, brain sections were washed three times for 10 min in PBS-T and transferred to a 10 cm dish filled with 0.01 M PBS for mounting brain sections on a glass slide. Mounted brain sections were dried for 30 min, before sealing in Flouromount™ with a coverslip, dried over night at RT (in the dark) and slides were transferred to 4°C for long term storage.

2.2.4 Coverslip Preparation

Coverslips (cvs) were treated with nitric acid in order etch the glass for better cell attachment. Therefore, cvs were put into porcelain racks and incubated in 65% nitric acid over night while shaking. The next day, cvs were washed five times for 20 min with dH_2O. Subsequently, cvs were autoclaved for 1 h at 100°C, followed by 6 h at 220°C. Afterwards, cvs were transferred to 6 cm dish under the hood and were used for culturing of microglia/macrophages.

For the *ex vivo* Aβ plaque phagocytic assay, nitric acid treated cvs were coated with poly-L-lysine (PLL) in order to enhance tissue attachment to the cvs. Therefore, cvs were treated with sterile filtered 1 mg/mL PLL overnight. On the next day, cvs were washed four times with dH_2O and dried in porcelain racks for 1-2 h, and subsequently, used for preparing phagocytic assay plates.

2.2.5 Microglia Isolation

CD11 antigen-like family member B (CD11b)-positive microglia were isolated either from 1-week, 2 months or 5 months old mice using the magnetic activated cell sorting (MACS) technology (Miltenyi Biotec). Mice were sacrificed (either by decapitation for neonatal mice or by CO_2 for adult mice) and brains were collected in a 6 cm dish filled with 3 mL HBSS buffer. Brainstem, cerebellum and olfactory bulb were separated and the meninges were removed from the remaining cerebrum under a dissection microscope using fine forceps. Afterwards, the cerebrum was chopped into small pieces (they have to pass through a 5 mL pipette) and transferred into a 15 mL Falcon tube. Excess of HBSS buffer was removed and the brain tissue was enzymatically digested with papain digestion medium (pre-warmed at 37°C) for 15 min at 37°C in a water bath. After a quick spin down (300 × *g* for 10 s), the supernatant was removed that 2.5 mL were left and the papain digestion was stopped by adding 7.5 mL blocking medium (pre-warmed at 37°C). Subsequently, tissue pieces were quickly spin down (300 × *g* for 10 s) and the tissue was manually dissociated in 2 mL (for neonatal mice) or 3 mL (for adult mice) of blocking medium using pipettes with descending diameter (first 2 mL plastic Pasteur pipette, glass Pasteur pipette and glass Pasteur pipette with a half of the diameter). Of note, glass pipettes were pre-coated with 4% BSA to reduce attachment of the tissue to the glass wall. A single-cell suspension was achieved by filtering the tissue homogenate through a 40 µm cell strainer (pre-equilibrated with 5 mL of HBSS buffer) and collected in a 50 mL Falcon tube. Afterwards, the cell strainer was washed with 5 mL HBSS buffer. The cell suspension was centrifuged for 10 min at 300 × *g*, the supernatant was removed and the cell pellet was washed again in 10 mL HBSS buffer. After another centrifugation step (300 × *g* for 10 min), the cell pellet was resuspended either in 90 µL (for 1-week old mice) or in 180 µL (for adult mice) of MACS buffer. Either 10 µL (for 1-week old mice) or 20 µL (for adult mice) of CD11b magnetic beads were added and incubated for 15 min at 4°C. The cell suspension was washed with 3 mL MACS buffer, followed by centrifugation for 10 min at 300 × *g*. The supernatant was removed, and the cell pellet was resuspended in 1 mL MACS buffer. Before applying the cell suspension to the LS columns, the LS columns were equilibrated with 3 mL MACS buffer. Afterwards, columns were washed three times with 1 mL MACS buffer and microglia were eluted with 2.5 mL MACS buffer into a new 15 mL Falcon tube. The elution was applied again on a pre-equilibrated LS column and washed three times with 1 mL MACS buffer and the final CD11b-positive fraction (microglia enriched) was eluted with 2.5 mL MACS buffer in a clear 15 mL Falcon tube and the number of living cells was determined (mixed 10 µL of the cell suspension with 10 µL Trypan blue). Additionally, 1 mL of the first flow through (CD11b-negative fraction; microglia depleted) was kept for further analysis. Both, microglia-enriched and microglia-depleted fraction were centrifuged for 5 min at 300 × *g* and washed twice in 1X PBS, snap frozen in liquid nitrogen and stored in -80°C for biochemical analysis or immediately prepared for EM analysis.

For culturing primary microglia, the microglia pellet was not washed with 1X PBS but immediately resuspended in 1 mL microglia medium, seeded in the desired density (with or without cvs) and cultured for at least 5 days in vitro (DIV) in microglia medium before any assay was applied. For culturing primary microglia from adult mice, GM-CSF was freshly added to the microglia medium (final concentration of 10 ng/mL).

2.2.6 Isolation of Peripheral-Blood Mononuclear Cells

Blood (18 mL) from healthy controls (CTR) and NPC patients (NPC) was collected in two 9 mL EDTA monovettes and was equilibrated at room temperature (RT) for 20-30 min (starting the isolation with warm blood would result in a lower yield). Subsequently, the blood of one patient is transferred into one 50 mL Falcon tube and supplemented with 40 µL 0.5 M EDTA and mixed by inversion (additional EDTA prevents further clogging of the blood). Peripheral-blood mononuclear cells (PBMCs) were isolated from the blood by negative selection using 980 µL of RT-equilibrated RosetteSep Monocyte Isolation antibody cocktail. The blood was gently mixed by rolling for 20 min at RT. Afterwards, 20 mL wash buffer was added and mixed by inversion. Two LeucoSep tubes were filled with 15 mL RT-equilibrated Ficoll and centrifuged at 800 × *g* for 1 min. The diluted blood was distributed between the two LeucoSep tubes, the Falcon tube was rinsed once with

10 mL wash buffer and the wash buffer was equally distributed between the two LeucoSep tubes. After centrifugation at 800 × *g* for 15 min at RT (with a deceleration of 1), the plasma (upper layer) was removed until approximately 5 mL above the PBMC layer (whitish thin layer). The remaining content of the LeucoSep tubes was gently poured into a new 50 mL Falcon tube containing 30 mL wash buffer and mixed immediately by inversion. Tubes were centrifuged at 300 × *g* for 7 min at RT. The supernatant was aspirated and the PBMC pellets were resuspended in 4 mL ACK lysing buffer and incubated for 2 min at RT in order to remove contamination of red blood cells (red blood cells are permeable to the containing ammonium chloride of the ACK lysis buffer and will undergo an osmotic shock). Excess of ACK lysis buffer was quenched with 35 mL wash buffer, and subsequently, centrifuged at 300 × *g* for 7 min at RT. The resulting PBMC pellets were resuspended in 1 mL macrophage medium supplemented with 50 ng/mL human M-CSF. Afterwards, the content of both tubes was combined (2 mL in total) and 10 mL macrophage medium supplemented with 50 ng/mL human M-CSF was added. Living cells were manually counted using a Neubauer chamber (mixed 10 µL of the cell suspension with 10 µL Trypan blue; a cell number of 6 - 12 × 10^6 is expected). All cells were plated into a 10 cm dish and placed into the incubator. After 2 DIV, 1 mL of fresh macrophage medium supplemented with 50 ng/mL human M-CSF was added (human M-CSF amounts have to be calculated for 13 mL medium).

After 5 DIV, PBMC-derived macrophages were collected for biochemistry or used for cellular assays. Therefore, the medium was removed and cells were washed carefully once with 10 mL 1X PBS. After removing the 1X PBS, 5 mL Versene/EDTA was added and incubated for 3 min, followed by another wash with 10 mL 1X PBS. The 1X PBS was removed and 5 mL macrophage medium supplemented with human M-CSF (50 ng/mL) was added. The cells were gently scraped off with a cell scraper and collected in a 15 mL Falcon tube. Cells were manually counted as described above and 250,000 cells/well were seeded for the phagocytic assay and 500,000 cells were seeded in a 6 cm dish for the myelin phagocytic assay. The remaining cells were washed two times with 1 mL 1X PBS (300 × *g* for 5 min). Lastly, the supernatant was removed, the pellet was snap frozen in liquid nitrogen and stored at -80°C until usage.

2.2.7 Immunocytochemistry of Cultured Microglia and Macrophages

All following steps were carried out at RT and a volume of 100 - 200 µL of solutions were applied to the cvs. For immunocytochemistry, microglia were cultured on cvs at a density of 1 × 10^6 in a 6 cm dish or 100,000 cells/well in a 24-well plate for 7 DIV and fixed in 4%PFA/sucrose for 15 min. After three washes with 0.01 M PBS, cvs were transferred into a wet chamber in order to prevent that cvs were drying out, which could increase autofluorescence. Fixed cells were quenched for 10 min using 50 mM NH_4Cl, and subsequently, washed three times with 0.01 M PBS. Cells were permeabilized for 3 min using 0.01% Triton X-100, washed three times with 0.01 M PBS and blocked for 1 h with blocking solution. Afterwards, blocking solution was removed and the primary antibody solution was applied and incubated for 1 h. Subsequently, cells were washed four times with 0.01 M PBS, the secondary antibody solution was applied and incubated for 1 h. The nuclear stain Hoechst or fluorescent dyes were added to the secondary antibody solution. Next, cells were washed three times with 0.01 M PBS, the cvs was dipped three to four times into dH_2O, excess of water was removed, and subsequently, mounted on a glass slide using Fluoromount™ and cured over night at RT in the darkness. On the next day, cvs were transferred to 4°C for long term storage.

2.2.8 Cellular Assays

2.2.8.1 *Ex Vivo* Aβ Plaque and Myelin Phagocytic Assay

For this assay, 6-9 months old mice from the amyloidosis mouse model APP/PS1 [241] were sacrificed via CO_2 inhalation. The brain was extracted and cut into its two hemispheres. A squared piece of cork was placed on dry ice and a small drop of 0.01 M PBS was put into the middle of the cork. Straight away, one hemisphere was placed onto the drop of PBS and fixed until the PBS started to freeze. Afterwards, freshly frozen hemispheres on cork were stored at -80°C until usage.

In order to prepare the phagocytic assay plates, brain hemispheres on cork were taken out from the -80°C and equilibrated at -20°C (as well as all needed tools) for 20-30 min. The cork was fixed to the cutting specimen using an embedding matrix. Sagittal brain sections (10 µm thick) were cut using the anti-roll glass to prevent rolling of the brain sections. The freshly cut brain section was flattened, transferred onto a PLL-coated cvs and placed into a 12-well plate which is stored on dry ice. Only consecutive brain sections were collected in order to have similar Aβ load in both brain sections. Full 12-well plates were sealed with parafilm and stored at -80°C until usage.

On the day of the assay, the phagocytic plates stored at -80°C were placed at RT and thawed for 30 min. Afterwards, brain sections were hydrated in 1 mL 1X PBS for 10 min. Subsequently, brain sections were incubated with anti-amyloid antibodies (i.e. either

6E10 for microglia (5 µg/mL) or 2D8 for macrophages (3 µg/mL) for 1 h at RT. Next, brain sections were washed once with 1X PBS for 10 min and 1 mL of either microglia or macrophage medium was added. Acutely isolated microglia or cultured macrophages were added onto one of the consecutive brain sections in a density of 300,000 cells/well (microglia) or 250,000 cells/well (macrophages). The brain section was incubated with the cells for 5 DIV (microglia) or 1 DIV (macrophages) and fixed with 4% PFA/sucrose for 15 min. Subsequently, brain sections were washed three times with 1X PBS and subjected for immunocytochemistry (carried out as described in chapter 2.2.7), using antibodies against CD68 (rat) and Aβ (3552; rabbit). Hoechst was used as nuclear stain and Thiazine red (ThR) was used to visualise fibrillar Aβ (plaque cores).

2.2.8.2 *In Vitro* Myelin Phagocytic Assay

Wildtype mice (C57BL/6J) older than 2 months were used to prepare crude myelin extracts. Therefore, three snap frozen brains were collected in a 15 mL Falcon tube and 5 mL of the sonication buffer was added. Brains were sonicated for 5 min (with a 50% amplitude) on ice using the Branson Digital Sonifier.

Myelin was isolated from the full brain homogenate via a sucrose gradient. To this end, 15 mL of 0.32 M sucrose was first added into a 38.5 mL ultracentrifuge tube. Underneath the 0.32 M sucrose, a layer of 15 mL 0.85 M sucrose was applied via a syringe with a cut needle (G 21 x 4 3/4" 0.8 x 120 mm). After slowly applying the brain homogenate on top of the sucrose gradient, the tubes were centrifuged for 38 min at 75,000 × *g* (25,000 rpm) at 4°C using a SW32 Ti rotor. Next, the crude myelin fraction was carefully extracted from the interface with a 1 mL pipette and transferred into a new 38.5 mL ultracentrifuge tube. In order to induce an osmotic shock, 30 mL of autoclaved dH_2O was added (the weight of the tubes was adjusted with dH_2O if needed). Subsequently, the tubes were centrifuged at 75,000 × *g* (25,000 rpm) for 18 min at 4°C. This osmotic shock was repeated for another two times. After the last wash, the myelin was resuspended in 500 µL 1X PBS and transferred into a new Eppendorf tube and the yield of myelin was determined by measuring the total amount of protein using the Bradford assay according to manufacturers' instruction. The myelin was fluorescently labelled using the PKH67 Green Fluorescent Cell Linker Mini Kit according to manufacturers' instruction. Briefly, 350 µg of myelin was mixed with the kit buffer in a total volume of 1 mL, 4 µL of the labelling reagent was added and incubated for 5 min at RT in the dark. After two washes with 1 mL 1X PBS (17,000 × *g* for 10 min at 4°C), the fluorescently labelled myelin was resuspended in 350 µL 1X PBS (final concentration of the fluorescently labelled myelin was 1 µg/µL) and stored at -20°C until usage.

Before using fluorescently labelled myelin for the myelin phagocytic assay, myelin was thawed and resuspended using a 27G needle (5-10 strokes) in order to prevent huge aggregates of myelin. For the *in vitro* myelin phagocytic assay, cells (either microglia or macrophages) cultured on cvs were incubated with 10 µg/mL fluorescently labelled myelin for 6 h (pulse phase). Afterwards, the medium was removed and new microglia or macrophage medium was added. For the time-course experiment, the assay was stopped by fixing the cells after 0, 24, 48 or 72 h (chase phase) with 4% PFA/sucrose for 15 min, and subsequently, washed three times with 1X PBS. All other myelin phagocytic assays mentioned in this thesis, were stopped after 48 h. In case of the rescue experiment, 250 µM methyl-ß-cyclodextrin (MβCD) or dH_2O (control) was added to the microglia medium during the chase phase.

Immunocytochemistry was performed as described in chapter 2.2.7, using CD68 (rat) and perilipin 2 (PLIN 2; guinea pig) as primary antibodies. After the secondary antibody incubation step, lipid droplets were stained using the Nile Red Kit according to manufacturer’s instructions.

2.2.8.3 DQ-BSA Assay

In order to monitor trafficking of phagocytosed myelin, primary microglia cultured on cvs from 1-week old *Npc1*^{m1n} mice were incubated with 10 µg/mL Red DQ-BSA (stains lysosomal compartments) and 0.5 µg/mL cholera toxin subunit b (CtxB) Alexa Fluor™ 647 Conjugate (stains endocytic vesicles) for 30 min at 37°C in microglia medium. Afterwards, microglia were fed with 10 µg/mL fluorescently labelled myelin for 15 min and fixed after 1 h with 4% PFA/sucrose for 15 min. Cells were washed three times with 0.01 M PBS and nuclei were stained by incubating cells with Hoechst (diluted 1:2,000 in 0.01 M PBS) for 1 h at RT in the dark. After three washes with 0.01 M PBS, cvs were mounted on glass slides using Fluoromount™ and dried over night at RT in the dark. The next day, slides were transferred to 4°C until image acquisition [243].

2.2.8.4 EGFR Degradation Assay

Microglia from 1-week *Npc1*^{m1n} old mice were cultured in microglia medium in a 12-well plate (500,000 cells/well). After 5 DIV, the microglia medium was removed and serum-free microglia medium was added to the microglia culture for serum deprivation. After

3 h (t = 0), 40 ng/mL mouse recombinant EGF and 20 ng/mL cycloheximide (inhibits protein synthesis) was added to the cells. Degradation of the EGFR, was followed over 1, 3 and 6 h post-treatment. At each timepoint, microglia were lysed in STET lysis buffer supplemented with phosphatase and protease inhibitors, and protein lysates were analysed for EGFR levels via western blot as described in chapter 2.2.10.

2.2.8.5 MβCD Rescue Assay

Primary microglia from 1-week old *Npc1*^{m1n} mice were cultured in a density of 400,000 cells/well in a 12-well plate. After 5 DIV, microglia were treated with 250 µM MβCD or with dH_2O as control for 2 DIV [243]. Afterwards, microglia were directly lysed with 100 µL of STET lysis buffer (supplemented with protease inhibitors) and further analysed by western blot as described in chapter 2.2.10

2.2.9 Image Acquisition and Analysis

2.2.9.1 Image Acquisition

For image analysis, three brain sections per mouse and three mice per genotype were analysed. All images shown or used for quantification in this thesis were acquired using confocal microscopy (Leica SP5 or Zeiss LSM900). Images were taken with a resolution of 1024 × 1024 pixels (or 524 × 524 pixels for tile scans) and using a z-stack. All images shown in this thesis are maximum projections of the z-stacks. The confocal settings were kept the same when comparing two conditions and image analysis was performed using ImageJ.

2.2.9.2 GFAP Coverage

The glial fibrillary acidic protein (GFAP) coverage in the cortex, midbrain and brainstem of *Cre*- and *Cre*+ mice were quantified. Therefore, one 10X image (16-bit) of each brain region per brain section was taken (3 images of each brain region per mouse in total). Maximum projected images were used for quantification in ImageJ. First, the background was subtracted using the radius of the “rolling ball” of 50 pixels. Afterwards, images were converted into 16-bit and the threshold was set manually between the different brain regions. The sum area of all particles (size = 0 - Infinity pixel; circularity = 0 - 1 pixel) was calculated and normalised to the size of the analysed area (408,193.21 µm^2). The used macro for ImageJ is shown below.

```
n=getDirectory("Choose a Directory to save");
```

```
imageCount = nImages
for (image = 1; image <= imageCount; image++) {
    name=getTitle();
    run("Subtract Background...", "rolling=50");
    run("16-bit");
    setAutoThreshold("Default dark");
    //the threshold was adjusted manually and can differ between brain areas
    setThreshold(7, 65535, "raw");
    setOption("BlackBackground", true);
    run("Convert to Mask");
    run("Analyze Particles...", "size=0-Infinity pixel circularity=0.00-1.00 pixel summarize");
    saveAs("Jpeg", n+name+".jpg");
    close();
    }
close()
```

2.2.9.3 Quantification of the *Ex Vivo* Aβ Plaque Phagocytic Assay

Tile scans of full brain sections were acquired using a 10X objective and a resolution of 256 × 256 pixels. The total fibrillar Aβ area (ThR positive area) of the brain section without and with added cells was analysed. First, the background of stitched and maximum projected images was subtracted using a “rolling ball” diameter of 50 pixels. Afterwards, the “Otsu” threshold was applied and particles larger than 5 pixels (circularity 0 – 1 pixel) were analysed (the threshold was set to a minimum of 5 pixels to exclude ingested ThR signal from microglia). The area of each particle was summed up in order to assess the total ThR-positive area. The total ThR area of the brain section without cells was subtracted with the total ThR-positive area of brain sections with cells to calculate the phagocytic clearance. Three technical replicates were performed for one biological replicate. The automated macro used for quantification is shown below.

```
n=getDirectory("Choose a Directory to save");
imageCount = nImages
for (image = 1; image <= imageCount; image++) {
    name=getTitle();
    run("Subtract Background...", "rolling=50");
    run("16-bit");
    setAutoThreshold("Otsu dark");
    //run("Threshold...");
    //setThreshold(41, 255);
    setOption("BlackBackground", true);
    run("Convert to Mask");
    run("Analyze Particles...", "size=5-Infinity pixel circularity=0.00-1.00 show=Outlines display");
```

```
    saveAs("Jpeg", n+name+".jpg");
    close();
    saveAs("Results",n+name+"Results"+".xls");
    close();
}
```

2.2.9.4 Quantification of the DQ-BSA Trafficking

In total, 18 *Npc1*$^{+/+}$ microglia and 25 *Npc1*$^{-/-}$ microglia were analysed (derived from three independent experiments). The area of colocalised DQ-BSA with myelin was normalised to the total area of myelin in order to calculate the portion of myelin reaching the lysosomes. The area was measured by using ImageJ.

2.2.9.5 Quantification of the Myelin Phagocytic Assay

For the quantification of the myelin phagocytic assay, microglia which have Nile red-positive structures (lipid droplets) outside of CD68-positive compartments (late endosomes/lysosomes) were defined as lipid droplet positive cells. An epifluorescent microscope was used for cell counting (300 cells/technical replicate). Three technical replicates per biological replicate were analysed (900 cells/biological replicate in total).

2.2.10 Immunoblot Analysis

2.2.10.1 Protein Lysis of Microglia/Macrophages

Cell pellets were lysed in 100 µL (microglia) or 150 µL (macrophages) of STET lysis buffer supplemented with phosphatase and protease inhibitors and incubated for 20 min on ice. Afterwards, protein lysis was collected in a new Eppendorf tube and sonicated four times for 30 s using an ultrasonic bath. Between each sonication step, samples were placed quickly on ice to prevent overheating. Subsequently, protein lysis was centrifuged for 10 min at 10.000 rpm at 4°C in a table top centrifuge. The supernatant (soluble proteins) was collected in a new Eppendorf tube and the protein concentration was determined using either the Bradford Assay or the BC assay according to manufactures' instructions.

2.2.10.2 Protein Lysis of Brain Tissue

Left brain hemispheres were lysed in 1 mL STET lysis buffer supplemented with protease inhibitors using a glass potter. After 10 - 20 strokes (big tissue chunks should not be prominent anymore), the brain lysis was transferred into a new 2 mL Eppendorf tube and incubated on ice for 1 h while shaking (samples were vortexed from time to time). Subsequently, protein lysate was centrifuged for 15 min at 17,000 × *g* at 4°C in a table top centrifuge. The supernatant (soluble proteins) were collected in a new Eppendorf tube and the protein concentration was determined using either the Bradford Assay or the BC assay according to manufactures' instructions.

2.2.10.3 SDS-PAGE and Immunoblot

A volume of 10 µg protein was mixed with 4X reducing Laemmli buffer (includes β-mercaptoethanol) and proteins were denatured for 5 min at 95°C. Meanwhile, the SDS-PAGE chamber was assembled using a self-casted bis-tris acrylamide gel (receipt is shown in Table 38) and filled with running buffer.

Table 38. Receipt for 8%, 10% and 12% separating and stacking gels.

		H_2O	Lower Tris buffer	40 % acrylamide	TEMED	10% APS
Separating gel	8 %	8.8 mL	4 mL	3.2 mL	30 µL	60 µL
	10 %	8 mL	4 mL	4 mL	30 µL	60 µL
	12 %	7.3 mL	4 mL	4.5 mL	30 µL	60 µL
Stacking gel		H_2O	Upper Tris buffer	40 % acrylamide	TEMED	10% APS
		6.8 mL	2.5 mL	1 mL	30 µL	30 µL

Prepared samples were applied onto the gel together with 7.5 µL of a protein standard. The SDS-PAGE was running at constant voltage of 80 V for 10 min, and subsequently, at 120 V for ~1.5 h (until the protein front ran out of the gel). Afterwards, proteins were transferred either on a PVDF membrane (activated in isopropanol for 2 min before usage) or on a nitrocellulose membrane (only for APOE) by wet transfer using a sandwich system filled with transfer buffer. The transfer was performed at constant current (400 mA) for 65 min. When antigen retrieval was required (only for APOE), the nitrocellulose membrane was cooked (100°C) for 5 min in 1X TBS and cooled down in 1X TBS at RT afterwards. Next, the membrane was blocked in blocking buffer for 1 h, transferred into primary antibody solution and incubated over night at 4°C while shaking. On the next day, the membrane was washed three times for 10 min with TBS-T and incubated with secondary antibody solution for 1 h. After three washes with TBS-T for 10 min, membranes were incubated with ECL reagent according to manufactures' instructions. The membrane was analysed using the Image Quant LAS-400 or iBright.

2.2.10.4 Western Blot Quantification

Protein bands of the western blot images were analysed by densitometry using either ImageJ or MultiGauge. Resulting values were normalised to the control condition (*Npc1*$^{+/+}$ or *Cre*- or CTR).

2.2.11 Mass Spectrometry of Cells

2.2.11.1 Microglia/Macrophage Sample Preparation for Mass Spectrometry

Mass spectrometry (MS) was performed as described in Colombo and Dinkel *et al.* [243]. Cell pellets of microglia (n = 3) or human PBMC-derived macrophages (CTR: n = 3 and NPC: n = 7) were lysed in STET lysis buffer for 15 min on ice. Afterwards, the protein lysates were centrifuged at 16,000 × *g* at 4°C for 5 min (in order to achieve the removal of cell debris and undissolved material) and the supernatant was collected in a new protein LoBind tube. After determination of the protein concentration (Pierce 660 nm protein assay), 15 µg of protein were prepared for mass spectrometry using the filter aided sample preparation (FASP) protocol [249]. Vivacon spin filters (30 kDa cut-off) were used for FASP. Briefly, reduction and alkylation of free cysteine residues was achieved by enriching the sample with 20 mM dithiothreitol and 50 mM iodoacetamide, respectively. Samples were washed three times with 100 µL 8 M urea (14,000 × *g* for 22 min). Subsequently, 0.3 µg LysC was added and incubated for 16 h at 37°C for the first protein digestion. Afterwards, the sample was incubated with 0.15 µg trypsin were added and the sample was incubated for 4 h at 37°C for the second digestion step. Generated peptides were eluted by centrifugation into sample collection tubes, acidified with 8% formic acid to a pH less than 3, and subsequently, desalted by stop and go extraction using self-packed C18 tips [250]. The samples were dried using a SpeedVac and resuspended in 20 µL 0.1% formic acid including indexed retention time peptides from the iRT Kit [243].

2.2.11.2 MS of Microglia/Macrophages

An Easy nLC 1000 or 1200 nanoHPLC coupled online via a Nanospray Flex Ion Source equipped with a PRSO-V1 column oven to a Q-Exactive HF mass spectrometer were used for LC-MS/MS analysis. An amount of 1.3 µg peptides per sample was separated with ReproSil-Pur 120 C18-AQ resin self-packed in C18 column (30 cm × 75 µm ID). For peptide separation, a binary gradient (120 min) of water and acetonitrile supplemented with 0.1% formic acid was applied. The flow rate was set to 300 nL/min and the column temperature to 50°C.

Microglia lysates from *Npc1*^{m1n} mice and human PBMC-derived macrophages were analysed using a data dependent acquisition (DDA). Therefore, full MS scans were acquired at a resolution of 120,000 (automatic gain control (AGC) target: 3E+6; m/z range: 300-1400), followed by 15 MS/MS scans of the most intense peptide ions (isolation width: 1.6 m/z; resolution: 15,000; AGC target: 1E+5; normalised collision energy (NCE): 26%). For peptide fragmentation, a dynamic exclusion of 120 s was applied.

Microglia lysates from *Npc1*cKO x *Cx3cr1Cre* mice were analysed using a data independent acquisition (DIA), where one scan cycle included a full MS scan (m/z range: 300-1400; AGC target: 5E+6 ions; resolution: 120,000). Moreover, 30 MS/MS scans covered a range of 300-1400 m/z with successive m/z windows of variable size (AGC target: 3E+6 ions; resolution: 30,000). For peptide fragmentation, a stepped NCE of 26% ± 2.6% was applied.

2.2.11.3 MS Data Analysis of Microglia/Macrophages

The MS data from *Npc1*^{m1n} and human PBMC-derived macrophages were analysed using Maxquant software. For the analysis, the canonical fasta database of *Mus musculus* from Uniprot (downloaded 05.11.2018, 17005 entries) or *Homo sapiens* from UniProt including isoforms (downloaded 17.12.2018, 42432 entries) were used. As a protease, trypsin was defined allowing two missed cleavages. Variable modifications contained oxidation of methionines and acetylation of protein N-termini, while fixed modifications contained carbamidomethylation of cysteines. A false discovery rate (FDR) threshold of 1% was applied for peptide and protein identifications.

Only unique peptides were considered for quantification and label-free quantification (LFQ) intensities were separately normalised for each age group. Further analysis was performed using the software Perseus, calculating the log2 of the LFQ intensities and the log2 fold change between NPC1-defient and control sample (including different mouse models, age groups, and donors). LFQ intensities had to be detected in every biological replicate and no imputation was applied to replace missing values. An unpaired two-tailed Student's t-test was performed as statistical test to assess significantly changed proteins. Furthermore, a permutation-based FDR estimation, with experimentally adjusted s0 values, was used to account for multiple hypotheses (p = 5%) [251]. Proteins with a log2 fold change ± 0.5, a p-value < 0.05 and passing FDR filtering were defined as regulated proteins.

The MS data from *Npc1*cKO x Cx3cr1*Cre* microglia were analysed using the Spectronaut software (version 12.0.20491.14.21367), which included microglia spectral library [195]. In brief, an FDR threshold of 1% was applied for peptide and protein identifications. Peptide fragment ions with at least one quantified peptide per protein were used to assess LFQ of proteins. At least two and maximum three peptides per protein group were used for protein quantification. Further statistical data analysis was performed with Perseus as described above.

Pathway analysis was performed using the ingenuity pathway analysis (IPA) tool from QIAGEN. Only proteins with a log2 fold-change ± 0.5 and a p-value < 0.05 were considered as regulated.

2.2.12 MS of Brain Tissue

2.2.12.1 Sample Preparation of Brain Tissue for MS

Snap frozen brain tissues (right cerebellum and right hemisphere without cerebellum) from 12 months old *Cre*+ (n = 6) and *Cre*- (n = 7) mice were lysed in STET lysis buffer supplemented with protease inhibitors, using the Precellys soft tissue lysis kit. The brain tissue was homogenised in the Precellys Evolution homogeniser with following settings: 6,500 rpm, cycles were set to two times 30 s and the pause to 3 s. Afterwards, samples were incubated for 15 min at 4°C, and subsequently, centrifuged at 16,000 × *g* for 15 min at 4°C. The supernatant was collected in a fresh 1.5 mL protein LoBind tube and the protein concentration was determined using the BC assay according to manufactures' instructions.

An amount of 20 µg of protein was transferred to a 1.5 mL protein LoBind tube and mixed with 50 mM ammonium bicarbonate to a total volume of 35 µL. Afterwards, 5 µL 100 mM $MgCl_2$ and 10 µL of 2.5 U/µL benzonase were added and incubated for 30 min at 37°C. An amount of 2.5 µL 200 mM dithiothreitol was added and incubated for 30 min at 37°C in order to reduce the proteins. Alkylation of cysteine residues was achieved by enriching the sample with 5 µL 400 mM iodoacetamide and incubation for 30 min at RT in the dark. The reaction was quenched by addition of 2.5 µL 200 mM dithiothreitol. A modified protocol of the single-pot solid-phase enhanced sample preparation (SP3) [252] was applied for the proteolytic digestion. Briefly, proteins were bound for 30 min at RT to 40 µg of a 1:1 mixture of hydrophilic and hydrophobic magnetic Sera-Mag Speed-Beads. The final concentration of acetonitrile was 70%. Subsequently, beads were washed four times with 200 µL 80% ethanol. Samples were proteolytically digested with 250 ng trypsin and 250 ng LysC in 20 µL 50 mM ammonium bicarbonate for 16 h at RT. Supernatants were collected in fresh 0.5 mL protein LoBind tubes and enriched with 20 µL 0.1% formic acid (for improved peptide recovery) and sonicated for 30 s in a sonication bath. The combined supernatants were filtered using 0.22 µm spin-filters and dried by vacuum centrifugation. Peptides were dissolved in 20 µL 0.1% formic acid. The peptide concentration was measured with the Qubit protein assay.

2.2.12.2 MS of Brain Lysates

A nanoElute system online coupled with a timsTOF pro mass spectrometer equipped with a Column Toaster and a CaptiveSpray Source was used for LC-MS/MS analyses. In total, 400 ng peptides per sample were used for MS analysis. Samples were separated in ReproSil-Pur 120 C18-AQ resin self-packed in a 15 cm C18 column (75 µm ID). Peptides were separated with a binary gradient of acetonitrile and water (120 min). The flow rate was set to 300 nL/min and the column temperature to 50°C [253].
A Data Independent Acquisition Parallel Accumulation Serial Fragmentation (DIA-PA-SEF) method was used for MS analysis. For peptide fragment ion spectra, 34 sequential DIA windows with 26 m/z width were performed after one full MS scan with an overlap of 1 m/z covering a scan range of 350 - 1200 m/z. In total, 2 windows were scanned per ramp (with a ramp time of 100 ms), which resulted in a total cycle time of 1.9 s [253].

2.2.12.3 MS Data Analysis of Brain Lysates

LFQ was performed with the software DIA-NN (v. 1.8). A library free search was performed for each experimental dataset, searching against a canonical reference sequence database of *mus musculus* downloaded from NCBI (download date: 2022-04-08; 21993 genes). As a protease, trypsin was defined allowing two missed cleavages. Variable modifications contained oxidation of methionines and acetylation of protein N-termini, while fixed modifications contained carbamidomethylation of cysteines. The FDR threshold was set to 1% for peptide and protein identifications.
Generated LFQ outputs of proteins, which were identified with at least one unique peptide were log2 transformed and filtered for hits, which were identified in five out of six (right hemisphere without cerebellum) or five out of six to seven (right cerebellum) samples in

both conditions using the software Perseus [247]. Remaining missing values were imputated with a downshift of 1.8 and a width of 0.3 and resulting data were used to calculate the average log2 fold change for each protein. A Student's t-test was used to assess changes in protein abundance between two experimental groups. A permutation-based FDR calculation was utilised with Perseus to take into consideration several hypotheses ($p = 5\%$; $s0 = 0.1$).

Gene ontology (GO) enrichment analysis for biological processes was performed using amica. All known genes from *mus musculus* were set as statistical domain scope and only proteins with an absolute log2 fold change of 1.5 and an adjusted p-value of 0.05 were considered for analysis (performed on 03.06.2023).

2.2.13 Serum Collection and NF-L ELISA

Serum from 12 months old *Cre*- and *Cre*+ mice (n = 4) was collected by cardiac puncture. Therefore, mice were sacrificed using CO_2 and the chest was immediately open as described in chapter 2.2.3.1. The right atrium was punctured with a 25 G needle connected to a 1 mL syringe, and blood was slowly drawn (up to 1 mL). The blood was transferred to a 1.5 mL Eppendorf tube and incubated for 30 min at RT. Afterwards, the clogged blood was centrifuged at 1,000 × *g* for 10 min at 4°C and the supernatant (blood serum) was collected in a new 1.5 mL Eppendorf tube (in 50 µL aliquots). The serum was frozen at -20°C overnight, and subsequently, placed into the -80°C freezer for long-term storage. The concentration of neurofilament light chain (NF-L) in serum was measured using the commercial NF-light Advantage Assay Kit according to manufactures' instruction.

2.2.14 Transmission Electron Microscopy

Pellets from freshly isolated 1-week old *Npc1*$^{+/+}$ and *Npc1*$^{-/-}$ microglia (n = 3) were fixed with fixative solution 1 for 30 min at RT. For the *in vitro* myelin assay, microglia from 2 months old *Cre*- and *Cre*+ (n = 3) were cultured on plasma-coated ACLAR® films at a density of 150,000 cells/well in a 24-well plate and the assay was performed as described in chapter 2.2.8.2. The assay was stopped by adding 1:1 fixative solution 2 to the microglia medium and replacing it with 2.5% glutaraldehyde in 0.1 M cacodylate buffer after 5 min. Microglia were further incubated for 25 min on ice. Both, microglia pellets and cultured microglia, were washed three times for 5 min with 0.1 M sodium cacodylate and post-fixed with reduced osmium. Subsequently, samples were contrasted using 0.5% uranylacetate for 1 h at 4°C in the dark. The samples were dehydrated by incubating in an ascending ethanol series for 5 min in each concentration on ice (30%, 40%, 50%, 60%, 70%, 80%, 90% ethanol), and afterwards, samples were incubated two times for 15 min in 100% ethanol on ice. Lastly, samples were infiltrated in epon and cured at 60°C for 48 h. Ultrathin sections of 50 nm were prepared with an ultramicrotome and positioned onto formvar-coated copper grids (Plano) with post-contrasting using 1% uranyl acetate and Ultrostain (for microglia pellets) or without post-contrasting (for cultured microglia). TEM micrographs were acquired on a JEM 1400plus (JEOL) equipped with a XF416 camera (TVIPS) and the EM-Menu software (TVIPS). Image analysis was performed using ImageJ. For the quantification of lysosomes, lysosomal number was quantified and normalised to the analysed area (μm^2) or to cell number. Three independent biological replicates were analysed.

2.2.15 Lipidomic Analysis

2.2.15.1 LC-MS Analysis of Lipids in Microglia

The lipidomic analysis was performed by Denali Therapeutics similarly as described in Maloney *et al.* and Logan *et al.* [254, 255]. MACS-sorted CD11b-positive cells (100,000 cells) were resuspended in 800 µL methanol (LC-MS grade) including 2 µL of internal standard mix. Samples were centrifuged at 21,000 × *g* for 10 min at 4 °C after being vortexed for 5 min. The supernatants were collected in a fresh glass vial. Half of the sample was divided for GlcCer/galactosylceramides (GalCer) analysis and the other half for the other lipid panel analysis. Using a continuous stream of N_2, the samples were dried down and stored at -80°C until analysis [254].

2.2.15.2 Sample Preparation for GlcCer and GalCer Measurements

Dried samples were resuspended in 200 µL 92.5/5/2.5 acetonitrile/isopropanol/water (LC-MS grade) enriched with 0.5% formic acid and 5 mM ammonium formate for analysis and separation of GlcCer and GalCer [254].

2.2.15.3 LC-MS-targeted Analysis of GlcCer and GalCer

Liquid chromatography (UHPLC Nexera X2, UHPLC ExionLC) in conjunction with electrospray mass spectrometry (TQ 6495C) was used to analyse glucosylsphingosine, GlcCer and GalCer. In total, 5 µL of sample was injected for each analysis at a flow rate of 0.48 mL/min onto a HALO HILIC 2.0 µm, 3.0 × 150 mm column at 45°C. Mobile phase A contained 0.5% formic acid and 5 mM ammonium formate and was composed of 92.5/5/2.5 acetonitrile/isopropyl alcohol/water. Mobile phase B contained 5 mM ammonium formate and 0.5% formic acid and was composed of 92.5/5/2.5 water/ isopropyl alcohol/acetonitrile. The gradient was set up to last for the following durations: 1) 0 to 2 min at 100% B, 2) 2.1 min at 95% B, 3) 4.5 min at 85% B hold to 6.0 min, 4) drop to 0% B at 6.1 min and hold to 7 min, 6) ramp back to 100% at 7.1 min and hold to 8.5 min [255]. Positive mode electrospray ionisation was carried out. Agilent TQ 6495C was run as follows: gas flow 17 L/min, gas temp at 180 °C, sheath gas flow 10 L/min, nebulizer 35 psi, nozzle voltage 500 V, sheath gas temp 350°C; capillary 3500 V. Based on the retention periods and multiple reaction monitoring mode (MRM) characteristics of commercially available reference standards, GlcCer and GalCer species were determined. The data was quantified by using Skyline [254].

2.2.15.4 LC-MS-targeted Analysis of Lipids

Liquid chromatography (UHPLC Nexera X2, UHPLC ExionLC) in conjunction with electrospray mass spectrometry (QTRAP 6500+) was used to analyse lipids. In total, 5 µL of sample was injected for each analysis at a flow rate of 0.25 mL/min onto a BEH C18 1.7 µm, 2.1 × 100 mm column at 55°C. Mobile phase A contained 0.1% formic acid and 10 mM ammonium formate and was composed of 60/40 acetonitrile/water, while mobile phase B contained 0.1% formic acid and 10 mM ammonium formate and was composed of 90/10 isopropyl alcohol/acetonitrile (positive ionsation mode). Mobile phase A contained 0.1% acetic acid and 10 mM ammonium acetate and was composed of 60/40 acetonitrile/water, while mobile phase B contained 0.1% acetic acid and 10 mM ammonium acetate and was composed of 90/10 isopropyl alcohol/acetonitrile (negative ionisation mode). The gradient was set up to last for the following durations: 1) 0 to 8 min from 45% B to 99% B, 2) 8 to 9 min at 99% B, 3) 9 to 9.1 min to 45% B and 4) 9.1 to 10 min at 45% B [255]. Negative and positive mode electrospray ionisation were carried out. The QTRAP 6500+ was run as follows: collision gas at medium, curtain gas at 40/30 psi (positive/negative mode), ion spray voltage at 5500/-4500 V (positive/negative mode), ion source Gas 1 at 55 psi and Gas 2 at 60 psi, temperature at 250/600 °C (positive/negative mode), entrance potential at 10/-10 V (positive/negative mode), and collision cell exit potential at 12.5/-15.0 V (positive/negative mode) [255]. MRM was used to acquire the data. Lipids were measured by using a variety of non-endogenous internal standards. The data was quantified by using MultiQuant 3.02 [254, 255].

2.2.16 Small Animal Positron Emission Tomography/Magnetic Resonance Imaging

Positron emission tomography (PET) imaging was performed using *Npc1*cKO x *Cx3cr1Cre* (in total n = 30 for *Cre*- and n = 27 for *Cre*+) mice at different ages (2, 7 and 11 months). Prior to PET emission, two 2 min anatomical T1 (sagittal, axial) magnetic resonance imaging (MRI) were performed (head receive coil, matrix size 96 × 96 × 22, voxel size 0.24 × 0.24 × 0.80 mm³, repetition time 677 ms, echo time 28.56 ms, flip angle 90°) [256]. PET imaging was performed using a nanoScan® PET/MR 3T scanner (Mediso) with a triple-mouse imaging chamber. Mice were anesthetized with isoflurane (3.0% delivered via a mask at 1.4 L/min in oxygen during injection and 1.5% at 1.0 L/min during PET acquisition). PET tracer [^{18}F]GE-180 was used to analyse the 18-kDa translocator protein (TSPO), [^{18}F]D2-Deprenyl to analyse monoamine oxidase type B (MAO-B) and [^{18}F]fluoro-D-glucose (FDG) to analyse glucose metabolism. The tracers were dissolved in 200 µL saline and injected at a dose of 16.2 ± 2.9 MBq ([^{18}F]GE-180), 8.9 ± 2.6 MBq ([^{18}F]D2-Deprenyl) and 17.6 ± 3.8 MBq ([^{18}F]FDG). PET was acquired for 30 min for all tracers and was started 60 min post-injection for TSPO and 30 min post-injection for FDG and D2-Deprenyl. List-mode data within a range of 400 - 600 keV were reconstructed using a 3D iterative algorithm (Tera-Tomo 3D, Mediso Ltd, Hungary) using the following parameters: matrix size 55 × 62 × 187 mm³, voxel size 0.3 × 0.3 × 0.3 mm³, eight iterations, six subsets [256]. Additionally, decay, random, and attenuation correction were applied. For the attenuation correction, a body-air material map was created with the T1 image. Normalisation of TSPO-, MAO-B- and FDG-PET was performed using standardised uptake values (SUVs). The Mirrione atlas [257] was taken in order to define volumes-of-interest (VOIs; cortex, midbrain, brainstem) and served for extraction of TSPO-, MAO-B- and FDG-PET SUVs for all mice. Analysis was performed using GraphPad Prism.

2.2.17 Single Cell Radiotracing

2.2.17.1 Mouse Brain Dissociation

In order to investigate the specificity of TSPO tracer binding, 12 months old *Cre*- (n = 3) and *Cre*+ (n = 3) were subjected for single-cell radiotracing (scRadiotracing) [258]. The TSPO-tracer ([^{18}F]GE-180) was injected as for PET imaging, and subsequently, the brain was dissociated using the Adult Brain Dissociation Kit according to manufactures' instructions. Therefore, mouse brains were extracted and briefly washed in 1X PBS. The brain was chopped and incubated with enzyme mix 1 and 2 in the gentleMACS™ Octo Dissociator. The resulting cell suspension was added onto pre-wet 70 µm cell strainer and resuspended in ice-cold 1X PBS containing debris removal solution. The mixture was centrifuged at 3,000 × *g* for 10 minutes at 4°C (acceleration and deceleration at 5) after being coated with ice-cold 1X PBS. The two top phases were removed, cell pellets were collected and incubated for 10 minutes in 1 mL of ice-cold red blood cell removal solution. Cell pellets were collected for microglia and astrocyte isolation [259].

2.2.17.2 Microglia and Astrocyte Isolation

Cell pellets, which were prepared as described in chapter 2.2.17.1, were used to isolate microglia using CD11b MicroBeads as described in Xiang *et al.* [260]. Subsequently, astrocytes were isolated from the microglia-depleted fraction using ACSA2 MicroBeads as described in Xiang *et al* [260]. Cell numbers were estimated by flow cytometry (MACSQuant® Analyser) using fluorochrome-conjugated CD11b and ACSA2 antibodies.

2.2.17.3 Gamma Emission Measurements

The radioactivity concentrations of collected microglia and astrocytes were measured in a high sensitive gamma counter and were put into the relation to the injected activity and body weight (representing SUV per single cell), including decay-correction of the time between tracer injection and final activity measurement [260].

2.2.18 Rotarod Test

Female and male mice were daily trained for three continuous days before baseline acquisition. On day one and two, every animal receives three training trials per day with a maximum duration of 100 s per trial. On day three of training, mice were trained three times on the accelerating rod (8 to 40 rpm in 300 s). Finally, experimental performance was measured using the same strategy: over 300 s, the rod accelerated from 8 to 40 rpm. Three successive trails were measured per mouse. The latency to fall off the rod was determined and compared between the experimental groups [261].

2.2.19 Statistical Analysis

Statistical analyses were performed using either Microsoft Excel or GraphPad applying the appropriate statistical test (excluding MS and lipidomic analysis). All experiments were performed with at least three biological replicates and the used samples size is denoted in the figure legend. The data is represented as mean ± standard error of the mean (SEM). The p-values of the statistical tests were defined as follows: not significant (ns) = $p > 0.05$, $*p < 0.05$, $**p < 0.01$ and $***p < 0.001$.

3. Results

3.1 *Npc1*$^{-/-}$ Microglia Acquire a DAM Phenotype

Npc1^{m1n} mice (*Npc1*$^{-/-}$) recapitulate pathological hallmarks of NPC disease, including neurodegeneration with the especially prominent loss of the Purkinje cells in the cerebellum [144, 167, 262]. I therefore selected this mouse model to study the microglial involvement in NPC disease progression. In agreement with previous studies [144, 167, 262], my immunohistochemical analysis for neuronal markers in symptomatic *Npc1*$^{-/-}$ mice (2 months) revealed a pronounced loss of Purkinje cells in the cerebellum (visualised by Calbindin staining), while no obvious neuronal loss was detected in the cortex (visualised by neuronal nuclei antigen (NeuN) staining) (Figure 9A).

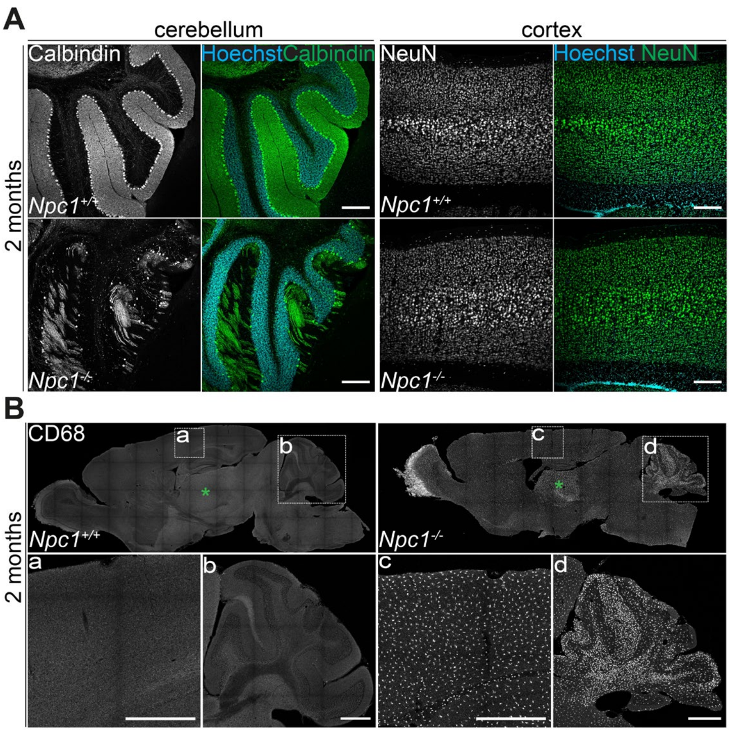

Figure 9. *Npc1*$^{-/-}$ mice display pronounced neuronal loss and microglial activation, particularly in the cerebellum. A Immunohistochemical analysis of neuronal markers in the cerebellum (Purkinje cells; Calbindin, green) and in the cortex (pan-neuronal marker NeuN, green) of 2 months old *Npc1*$^{+/+}$ and *Npc1*$^{-/-}$ mice reveals Purkinje cell loss in *Npc1*$^{-/-}$ mice, while no neuronal loss is detected in the cortex. Scale bars: 250 µm. Retrieved and modified from Colombo and Dinkel *et al.* [243]. **B** Tile scans of sagittal brain sections (upper panels) and zoom-ins (lower panels) of the cortex (a, c) and cerebellum (b, d) from 2 months old *Npc1*$^{+/+}$ and *Npc1*$^{-/-}$ mice immunostained against microglial late endosomal/lysosomal marker CD68 (white). Increased CD68 immunoreactivity is detected in *Npc1*$^{-/-}$ mice throughout the brain, with pronounced increase in specific regions like the cerebellum (d) or thalamus (green asterisks). Scale bars: 500 µm.

Microglial activity was assessed by immunostaining against CD68, a microglial late endosomal/lysosomal protein, which is upregulated in functionally active microglia [263]. At 2 months of age, a broad CD68 immunoreactivity was observed in the *Npc1*$^{-/-}$ brain (Figure 9B), including regions which were not affected by neuronal loss like the cortex (Figure 9B, zoom-in c). In brain regions which are affected by severe neurodegeneration like the cerebellum, a higher CD68 immunoreactivity was detected (Figure 9B, zoom-in d). Of note, high CD68 immunoreactivity was also detected in the thalamus (Figure 9B, green asterisk), which is as well affected by neurodegeneration in this mouse model [139]. It has been shown that microglia change their transcriptomic profile from a homeostatic to a DAM phenotype upon pathological conditions [178, 179]. In order to explore molecular changes in microglia, I selected cerebrum as a region that is less affected by neurodegeneration. To this end, the proteome of acutely isolated cerebral microglia from 2 months old *Npc1*$^{+/+}$ and *Npc1*$^{-/-}$ mice was assessed by MS analysis. Firstly, I analysed the purity of the microglia-enriched fraction (which was subjected for MS analysis) by western blot analysis, revealing depletion or reduction of specific markers for neurons (β3-tubulin), astrocytes (GFAP) and oligodendrocytes (2',3'-cyclic-nucleotide 3'-phosphodiesterase; CNPase), while the specific marker for microglia (ionized calcium-binding adapter molecule 1; Iba1) was enriched in the microglia enriched fraction (Figure 10A). MS analysis of 2 months old *Npc1*$^{+/+}$ and *Npc1*$^{-/-}$ mice revealed pronounced proteomic changes in *Npc1*$^{-/-}$ microglia (Figure 10B). Of note, the whole proteome list can be accessed in the Supplementary Data 1 of Colombo and Dinkel *et al.* [243]. Among others, an upregulation of DAM proteins, including late endosomal/lysosomal proteins (i.e. CD68, lysosome-associated membrane glycoprotein 1 (LAMP1), CTSD, cathepsin B (CTSB), GRN) and a downregulation of homeostatic proteins (i.e. CSF1R, macrophage mannose receptor 1 (MRC1), ABI gene family member 3 (ABI3), P2YR12, TMEM119, TGFB1) were detected, resembling the reported DAM phenotype [179]. Additionally, proteins involved in vesicular trafficking (e.g. RAB5B, RAB7A), lipid metabolism (e.g. farnesyl diphosphate synthase (FDPS), 7-dehydrocholesterol reductase (DHCR7), geranylgeranyl pyrophosphate synthase (GGPS1), polyprenol reductase (SRD5A3), beta-hexosaminidase subunit alpha (HEXA), GBA) and glutathione metabolism (glutathione S-transferase Mu 1 (GSTM1), glutathione S-transferase omega-1 (GSTO1)) were dysregulated. Using western blot analysis, selected DAM proteins were validated including the late endosomal protein CD63, which was only detected in the *Npc1*$^{-/-}$ microglia, and thereby, is not represented in the volcano plot (Figure 10C and D).

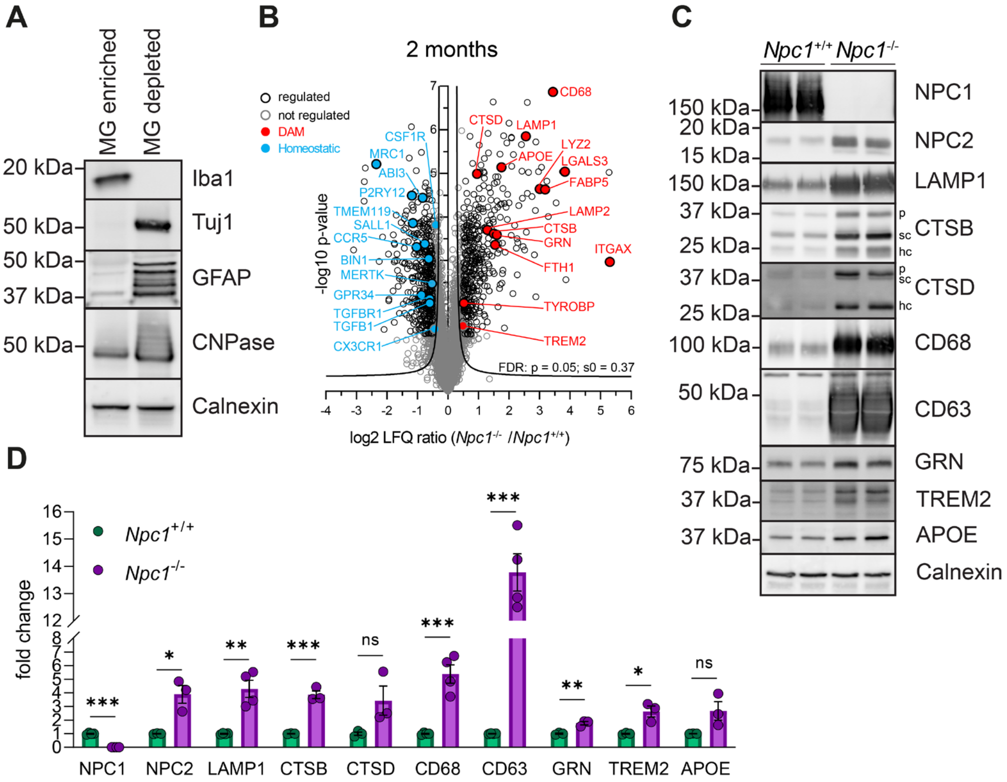

Figure 10. *Npc1*$^{-/-}$ microglia display DAM signatures at symptomatic stages. A Biochemical quality control of the microglial isolation procedure, which results in a CD11b-positive fraction (microglia enriched) and a CD11b-negative fraction (microglia depleted). Analysis of microglial (Iba1), neuronal (β3-tubulin), astrocytic (GFAP) and oligodendrocyte marker (CNPase), shows an enrichment in Iba1 and a depletion of β3-tubulin, GFAP and CNPase in the microglia enriched faction. Calnexin was used as loading control. **B** Proteomic analysis of acutely isolated *Npc1*$^{+/+}$ and *Npc1*$^{-/-}$ microglia (n = 3) from 2 months old mice. The average log2 transformed LFQ ratio between *Npc1*$^{-/-}$ and *Npc1*$^{+/+}$ microglia was plotted against the negative log10 transformed p-value. The threshold for the false discovery rate (FDR) is depicted in hyperbolic curves. Significantly changed proteins ($p < 0.05$ and FDR-positive) with a log2 fold change greater/smaller than ± 0.5 are depicted in a black circle (regulated), not regulated proteins are shown with a grey circle (not regulated). Selected disease-associated microglia (DAM) proteins and homeostatic proteins are encircled in red and blue, respectively. **C**-**D** Validation of the proteomic data using western blot analysis. Representative immunoblots (**C**) and the respective quantification (**D**) indicate depletion of NPC1 (n = 4) and an increase in the DAM proteins NPC2 (n = 3), LAMP1 (n = 4), CTSB (n = 3), CTSD (n = 3), CD68 (n = 4), CD63 (n = 4), GRN (n = 3), TREM2 (n = 3) and APOE (n = 3) of acutely isolated *Npc1*$^{-/-}$ microglia. Calnexin was used as loading control. Proteins were quantified by densitometry (ImageJ). *Npc1*$^{+/+}$-normalised values are depicted as mean ± SEM. An unpaired two-tailed Student's t-test was performed (ns = not significant, *$p < 0.05$, **$p < 0.01$, ***$p < 0.001$). For cathepsins: p = pro-form, sc = single chain form, hc = heavy chain form. Retrieved and modified from Colombo and Dinkel *et al.* [243].

Furthermore, western blot analysis of the cathepsins revealed intact maturation (Figure 10C), indicating preserved lysosomal proteolytic function. Taken together, *Npc1*$^{-/-}$ microglia acquire a DAM phenotype, which might be an event independent of neurodegeneration, pointing towards cell-autonomous microglia activation upon NPC1 loss.

3.2 *Npc1*$^{-/-}$ Microglia Show Molecular Alterations Already at a Pre-symptomatic Stage

Npc1$^{-/-}$ microglia displayed an activated phenotype in brain regions which were not affected by neurodegeneration (Figure 9), indicating that microglial activation might be independent of neuronal degeneration. In order to validate this hypothesis, I analysed the microglial phenotype at a pre-symptomatic stage of *Npc1*$^{-/-}$ mice (1-week of age), where neurodegeneration has not been reported [167, 264]. Accordingly, immunostainings of the cerebellum revealed an intact layer of Purkinje cells (visualised by Calbindin) as well as intact neuronal cell layers in the cortex (visualised by NeuN) of *Npc1*$^{-/-}$ mice (Figure 11). At the same time, increased CD68 immunoreactivity was detected in *Npc1*$^{-/-}$ mice, indicating microglial activation prior to neuronal loss.

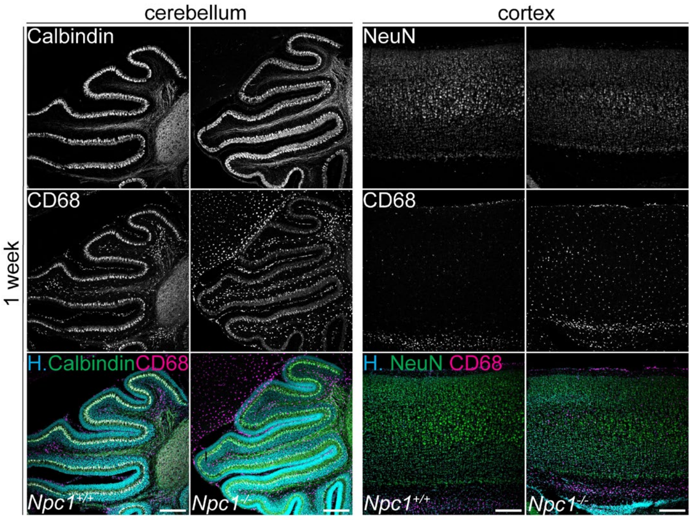

Figure 11. Microglia are activated prior to neurodegeneration. Immunohistochemical analysis of neuronal marker in the cerebellum (Purkinje cells, calbindin, green) and in the cortex (pan-neuronal marker NeuN, green) of 1-week old mice reveals no neuronal loss in *Npc1*$^{-/-}$ mice, while increased CD68 immunoreactivity is detected. Hoechst (H.) was used as nuclear stain. Scale bars: 250 µm. Retrieved and modified from Colombo and Dinkel *et al*. [243].

In order to analyse the molecular changes underlying microglia activation at early stages, acutely isolated microglia from 1-week old *Npc1*$^{+/+}$ and *Npc1*$^{-/-}$ mice were subjected for MS analysis. Proteome analysis revealed a significant upregulation of DAM proteins including mainly late endosomal/lysosomal proteins (i.e. CD68, CTSD, CTSB, GRN), pointing towards a late endosomal/lysosomal dyshomeostasis as an early and major pathological event in *Npc1*$^{-/-}$ microglia (Figure 12A). Especially CD63, a protein enriched in intraluminal vesicles [265], showed the highest upregulation suggesting endosomal

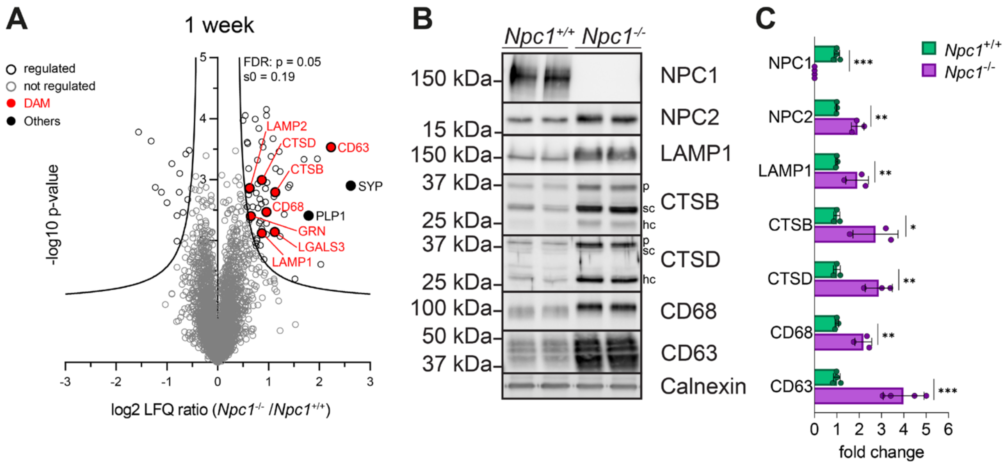

Figure 12. *Npc1*$^{-/-}$ microglia show molecular alterations prior to neuronal loss. A Proteomic analysis of acutely isolated *Npc1*$^{+/+}$ and *Npc1*$^{-/-}$ microglia of 1-week old mice (n = 3). The average log2 transformed LFQ ratio between *Npc1*$^{-/-}$ and *Npc1*$^{+/+}$ microglia is plotted against the negative log10 transformed p-value. The threshold for the false discovery rate (FDR) is depicted in hyperbolic curves. Significantly changed proteins ($p < 0.05$ and FDR-positive) with a log2 fold change greater/smaller than ± 0.5 are depicted in a black circle (regulated), not regulated proteins are shown with a grey circle (not regulated). Selected disease-associated microglia (DAM) are encircled in red and myelin protein (proteolipid protein 1; PLP1) and synaptic protein (synaptophysin; SYP) are encircled in black (others). **B-C** Validation of the proteomic data using western blot analysis. Representative immunoblots (**B**) and the respective quantification (**C**) indicate depletion of NPC1 (n = 4) and an increase in the DAM proteins NPC2 (n = 3), LAMP1 (n = 3), CTSB (n = 3), CTSD (n = 3), CD68 (n = 3), CD63 (n = 4) of acutely isolated 1-week old *Npc1*$^{-/-}$ microglia. Calnexin was used as loading control and proteins were quantified by densitometry (ImageJ). *Npc1*$^{+/+}$-normalised values are depicted as mean ± SEM. An unpaired two-tailed Student's t-test was performed ($^{*}p < 0.05$, $^{**}p < 0.01$, $^{***}p < 0.001$). For cathepsins: p = pro-form, sc = single chain form, hc = heavy chain form. Retrieved and modified from Colombo and Dinkel *et al.* [243].

sorting and trafficking defects already at early stages of NPC pathology. Of note, microglial homeostatic proteins (i.e. TGFB1, P2YR12, CX3CR1) showed a tendency of being downregulated in *Npc1*$^{-/-}$ microglia (Supplementary Data 2 of Colombo and Dinkel *et al.* [243]). Furthermore, proteins involved in vesicular trafficking (i.e. RAB7A), lipid metabolism (GGPS1, HEXA, GBA) and glutathione metabolism (GSTO1, GSTM5) were dysregulated. Using western blot analysis, selected DAM proteins were validated (Figure 12B and C). Additionally, western blot analysis revealed intact cathepsin maturation (Figure 12B), as seen at symptomatic stages of *Npc1*$^{-/-}$ microglia (Figure 10C), indicating a preserved lysosomal proteolytic function. These findings revealed that molecular alterations in microglia, especially in late endosomal/lysosomal homeostasis, are an early event in NPC disease progression and strongly suggests that NPC1 plays a role in microglia and that microglial activation is independent from neurodegeneration.

3.3 Molecular Alterations in *Npc1*$^{-/-}$ Microglia are Linked to Altered Phagocytic Function

Proteome analysis of pre-symptomatic mice displayed an enrichment in neuronal proteins like the synaptic protein synaptophysin (SYP) and the myelin associated protein proteolipid protein 1 (PLP1) in *Npc1*$^{-/-}$ microglia (Figure 12A). Especially during development, microglia are engulfing synapses to shape synaptic density and are important for accurate myelination [183, 185, 266]. Enrichment in synaptic and myelin proteins suggest an increased phagocytic activity of *Npc1*$^{-/-}$ microglia. Indeed, pathway analysis of the microglial proteome at pre-symptomatic (Figure 13A) and symptomatic (Figure 13B) stages revealed that phagosome maturation was significantly changed in *Npc1*$^{-/-}$ microglia. To further elucidate if molecular fingerprints translate into phagocytic alterations, I performed an *ex vivo* Aβ plaque phagocytic assay (Figure 13C and D). In fact, *Npc1*$^{-/-}$ microglia showed about 40% higher Aβ plaque clearance compared to *Npc1*$^{+/+}$ microglia (Figure 13E). Considering increased myelin associated proteins detected in *Npc1*$^{-/-}$ microglia (Figure 12A), the myelin uptake by *Npc1*$^{-/-}$ microglia was analysed using an *ex vivo* myelin phagocytic assay (Figure 13F). Myelin, as visualised by Fluoromyelin staining, is not detected in CD68-positive compartments of *Npc1*$^{+/+}$ microglia. In contrast, myelin accumulated in CD68-positive compartments of *Npc1*$^{-/-}$ microglia (Figure 13G). Accumulation of myelin substrates, within CD68-positive compartments in *Npc1*$^{-/-}$ microglia was also prominent *in vivo* (Figure 14). Taken together, these results indicate that *Npc1*$^{-/-}$ microglia acquired molecular and functional alterations already at pre-symptomatic stages. *Npc1*$^{-/-}$ microglia display increased phagocytic uptake towards different substrates. Additionally, *Npc1*$^{-/-}$ microglia show different clearance efficiency of the protein substrate Aβ and the lipid substrate myelin, which persist in late endosomal/lysosomal compartments of *Npc1*$^{-/-}$ microglia.

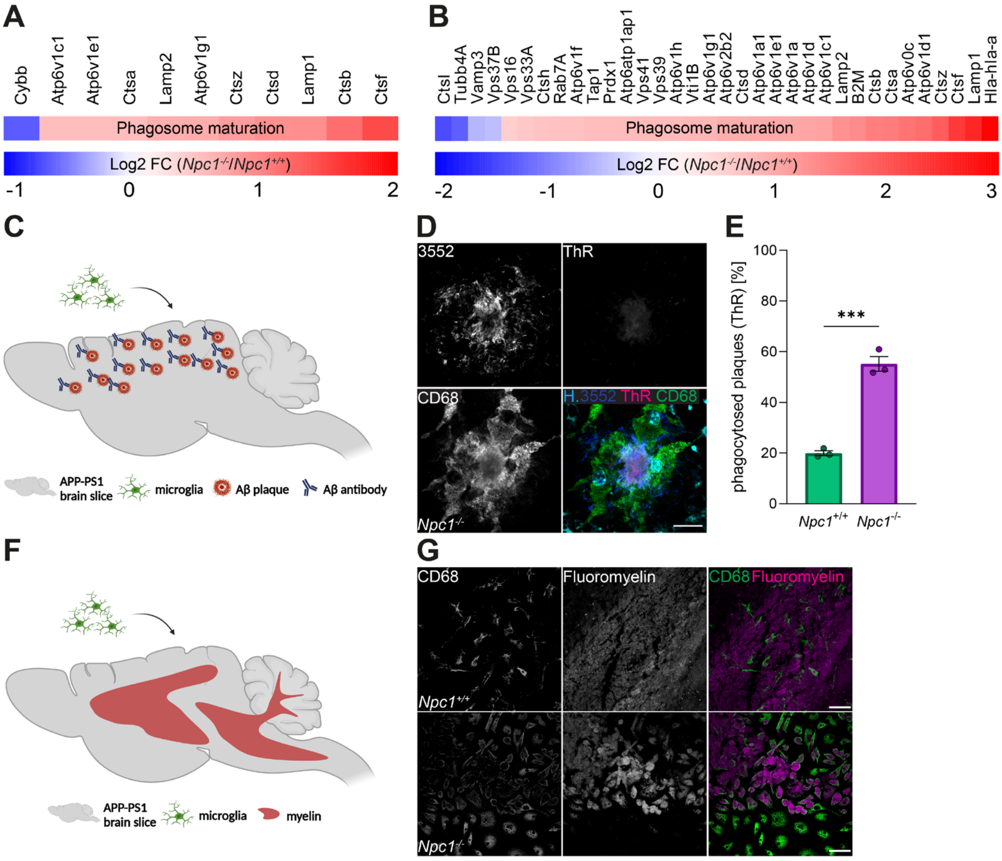

Figure 13. *Npc1*$^{-/-}$ microglia acquire an altered phagocytic function at pre-symptomatic stages. A-B Phagosome maturation is one of the most significantly altered pathways in *Npc1*$^{-/-}$ microglia in pre-symptomatic (**A**) and symptomatic stages (**B**). Heatmaps depict the log2 fold change (FC) of significantly changed proteins between *Npc1*$^{-/-}$ and *Npc1*$^{+/+}$ microglia. **C** Schematic representation of the *ex vivo* Aβ plaque phagocytic assay. A freshly frozen brain section harbouring Aβ plaques (derived from an APP/PS1 mouse) is pre-incubated with antibodies against Aβ to stimulate the migration of freshly added microglia to the plaque site and their subsequent clearance. After 5 DIV, the total load of fibrillar Aβ (plaque core) of the brain section with microglia and its consecutive brain section without added microglia is determined. **D** Representative image of *Npc1*$^{-/-}$ microglia from 1-week old mice phagocytosing an Aβ plaque in the *ex vivo* Aβ plaque phagocytic assay. Total Aβ plaque was immunostained using the anti-Aβ antibody 3552 (blue), plaque cores (fibrillar Aβ) were visualised using Thiazine red (ThR; magenta) and microglial late endosomes/lysosomes were visualised using an CD68 antibody (green). Hoechst (H.) was used as nuclear stain (cyan). Scale bar: 20 µm. **E** Quantification of the *ex vivo* Aβ plaque phagocytic assay using *Npc1*$^{+/+}$ and *Npc1*$^{-/-}$ microglia (n = 3) shows a 3-fold increase in the phagocytic clearance of fibrillar Aβ (assessed by ThR coverage) in *Npc1*$^{-/-}$ microglia. Values are depicted as mean ± SEM. A two-tailed unpaired Student's t-test was performed (***$p <$ 0.001). **F** Schematic representation of the *ex vivo* myelin phagocytic assay. The same procedure was done as described in **A**, besides that the uptake of the myelin is assessed instead of fibrillar Aβ coverage. **G** Immunohistochemical analysis of the *ex vivo* myelin phagocytic assay reveals increased uptake of myelin (stained with Fluoromyelin, magenta) in *Npc1*$^{-/-}$ microglia, which accumulates in their late endosomal/lysosomal compartments (immunostained for CD68, green). Scale bars: 50 µm. Retrieved and modified from Colombo and Dinkel *et al.* [243].

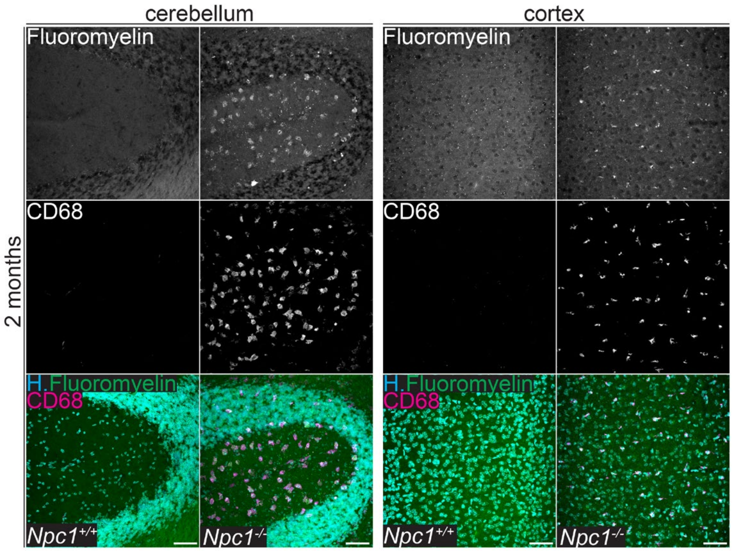

Figure 14. Myelin accumulates in late endosomes/lysosomes of microglia in *Npc1*$^{-/-}$ mice. Immunohistochemical analysis of myelin (stained with Fluoromyelin, green) reveals an accumulation within late endosomal/lysosomal compartments of microglia (immunostained for CD68, magenta) in 2 months old *Npc1*$^{-/-}$ mice. Hoechst (H.) was used as nuclear stain (cyan). Scale bars: 50 µm. Retrieved and modified from Colombo and Dinkel *et al*. [243].

3.4 Deficient Turnover of Phagocytosed Myelin in *Npc1*$^{-/-}$ Microglia

Phagocytosed myelin accumulated within late endosomal/lysosomal compartments of *Npc1*$^{-/-}$ microglia (Figure 13G and Figure 14), which is indicative for impaired myelin turnover. Therefore, I explored myelin turnover in *Npc1*$^{+/+}$ and *Npc1*$^{-/-}$ microglia using an *in vitro* myelin assay. Microglia were fed with fluorescently labelled myelin for 6 h, and the turnover of myelin was followed over 72 h (Figure 15A). Fluorescently labelled myelin was found in CD68-positive compartments of *Npc1*$^{+/+}$ and *Npc1*$^{-/-}$ microglia after 6 and 24 h, implying efficient uptake of myelin into late endosomal/lysosomal compartments in both conditions. After 48 h, fluorescently labelled myelin was detected outside of CD68-positive compartments only in *Npc1*$^{+/+}$ microglia, while fluorescently labelled myelin persisted in CD68-positive compartments in *Npc1*$^{-/-}$ microglia (Figure 15A and B). Fluorescently labelled myelin could no longer be detected after 72 h in *Npc1*$^{+/+}$ microglia, whereas it was still detectable in CD68-positive compartments of *Npc1*$^{-/-}$ microglia, suggesting deficiencies in the turnover of phagocytosed myelin. The major lipid found in myelin is cholesterol [267], which is, upon excessive intracellular accumulation, esterified at the ER and stored in a lipid storage organelle called lipid droplet [268].

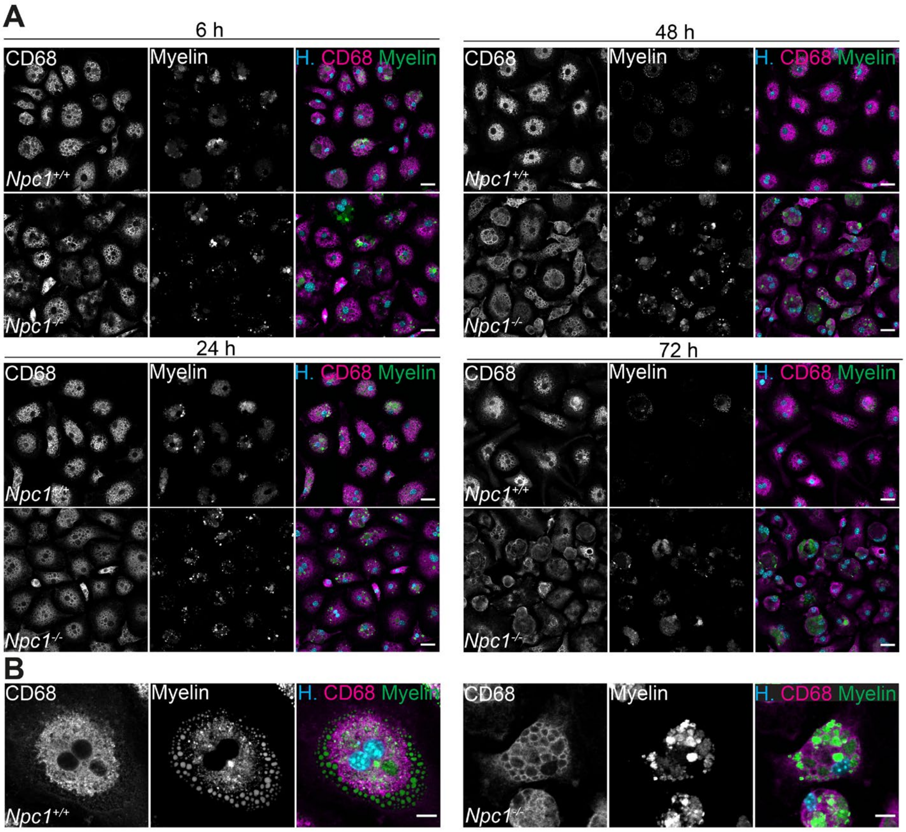

Figure 15. Phagocytosed myelin accumulates in *Npc1*$^{-/-}$ microglia. Time-course experiment of myelin processing in *Npc1*$^{+/+}$ and *Npc1*$^{-/-}$ microglia. Microglia were fed with fluorescently labelled myelin (green) and myelin processing was analysed after 6, 24, 48 and 72 h. After 6 and 24 h, myelin is prominent in CD68-positive compartments (magenta) of *Npc1*$^{+/+}$ and *Npc1*$^{-/-}$, while at 48 h, myelin starts to be detected outside of CD68-positive compartments in *Npc1*$^{+/+}$ microglia. After 72 h, myelin is mostly degraded in *Npc1*$^{+/+}$ microglia, while it persists in CD68-positive compartments of *Npc1*$^{-/-}$ microglia. Hoechst (H.) was used as nuclear stain (cyan). Scar bar: 25 µm. **B** Higher magnified image of *Npc1*$^{+/+}$ and *Npc1*$^{-/-}$ microglia fed with fluorescently labelled myelin (green) and immunostained for late endosomes/lysosomes using an CD68 antibody (magenta) illustrates that myelin is efficiently processed into structures outside of CD68-positive compartments in *Npc1*$^{+/+}$ microglia, while myelin accumulates in CD68-positive compartments of *Npc1*$^{-/-}$ microglia. Hoechst (H.) was used as nuclear stain (cyan). Scale bars: 10 µm. Retrieved and modified from Colombo and Dinkel *et al*. [243].

Accumulation of fluorescently labelled myelin in late endosomes/lysosomes of *Npc1*$^{-/-}$ microglia might indicate impaired turnover of myelin into CE-rich lipid droplets. Using two different markers for lipid droplets (PLIN2 and Nile red), confirmed that fluorescently labelled myelin outside of CD68-positive compartments was incorporated into lipid droplets in *Npc1*$^{+/+}$ microglia while these lipid droplets were absent in *Npc1*$^{-/-}$ microglia (Figure 16A and B). My findings suggest that *Npc1*$^{-/-}$ microglia have deficiencies in the processing of phagocytosed myelin into CE-rich lipid droplets.

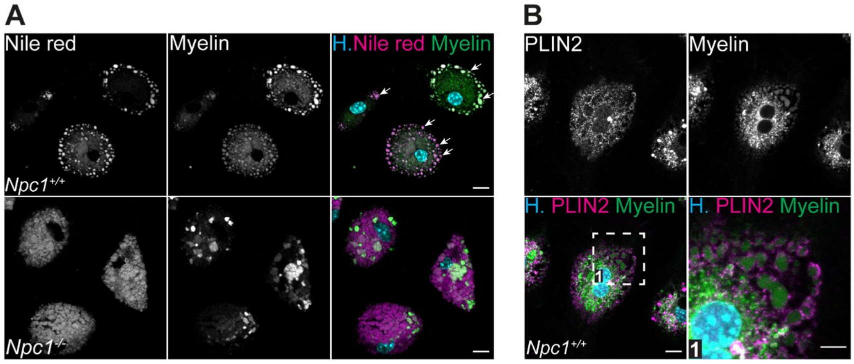

Figure 16. Phagocytosed myelin is not processed into lipid droplets in *Npc1*$^{-/-}$ microglia. A Phagocytosed fluorescently labelled myelin (green) is efficiently processed into lipid droplets (stained with lipid droplet dye Nile red, magenta, indicated with white arrows) in *Npc1*$^{+/+}$ microglia, while *Npc1*$^{-/-}$ are deficient of these structures after 48 h post-feeding. Hoechst (H.) was used as nuclear stain (cyan). Scale bars: 10 µm. **B** Immunocytochemical analysis of processed fluorescently labelled myelin (green) in *Npc1*$^{+/+}$ microglia using the lipid droplet marker perilipin 2 (PLIN2; magenta) validates that round structures in the cell periphery are lipid droplets, better visualised in the zoom-in (1). Hoechst (H.) was used as nuclear stain (cyan). Scale bars: 10 µm and 3 µm (zoom-in). Retrieved and modified from Colombo and Dinkel *et al.* [243].

3.5 *Npc1*$^{-/-}$ Microglia Bear a Specific Lipid Trafficking Defect

Phagocytosed material traffics to lysosomes in order to be degraded [269]. Deficient processing of myelin might be caused by impaired trafficking or impaired catabolism. First, the myelin trafficking in microglia was analysed. Therefore, DQ-BSA, a lysosomal tracer, and cholera toxin B (CtxB; visualises endosomal vesicles) were used to follow myelin trafficking to lysosomes within 1 h in 1-week old *Npc1*$^{+/+}$ and *Npc1*$^{-/-}$ microglia (Figure 17A). Immunocytochemical analysis revealed that *Npc1*$^{+/+}$ microglia showed a ~90 % co-localisation of DQ-BSA with fluorescently labelled myelin indicating efficient trafficking to lysosomes, while DQ-BSA poorly co-localised (~20%) with fluorescently labelled myelin in *Npc1*$^{-/-}$ microglia (Figure 17B). Furthermore, EM analysis of acutely isolated microglia from 1-week old *Npc1*$^{+/+}$ and *Npc1*$^{-/-}$ mice validated that undigested lipid material was accumulating in late endosomes/MVBs rather than in lysosomes in *Npc1*$^{-/-}$ microglia (Figure 17C). Of note, late endosomes/MVBs were highly enriched in *Npc1*$^{-/-}$ microglia in comparison to *Npc1*$^{+/+}$ microglia (Figure 17C). Furthermore, analysis of lysosomal numbers revealed no difference between *Npc1*$^{+/+}$ microglia and *Npc1*$^{-/-}$ microglia, indicating main burden of lipid accumulation at the level of the late endosomes/MVBs (Figure 17D).

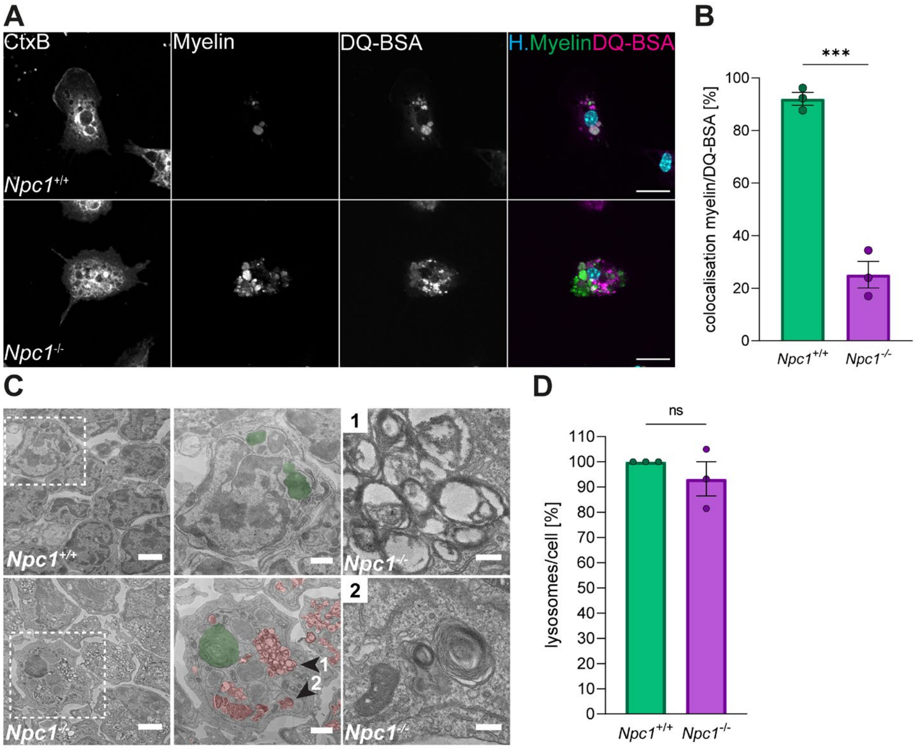

Figure 17. Phagocytosed myelin is trapped in late endosomes/MVBs in *Npc1*$^{-/-}$ microglia. A Myelin trafficking assay in *Npc1*$^{+/+}$ and *Npc1*$^{-/-}$ microglia from 1-week old mice. Representative image of microglia, which were fed with fluorescently labelled myelin (green) and the lysosomal tracer DQ-BSA (magenta) in order to analyse their localisation after 1 h post-feeding. Fluorescently labelled cholera toxin (CtxB; white) was used to label endosomal compartments and Hoechst (H.) was used as nuclear stain (cyan). Scale bars: 20 µm. **B** Quantification of the myelin trafficking assay (n = 3) reveals co-localisation of myelin with lysosomes in *Npc1*$^{+/+}$ microglia, while myelin poorly co-localises with lysosomes in *Npc1*$^{-/-}$ microglia. Data is represented as mean ± SEM and an unpaired two-tailed Student's t-test was performed (***$p < 0.001$). **C** EM analysis of acutely isolated *Npc1*$^{+/+}$ and *Npc1*$^{-/-}$ microglia shows accumulation of late endosomes/MVBs (pseudo-coloured in red) in *Npc1*$^{-/-}$ microglia. Enlargements of the late endosomes/MVBs (arrowheads 1 and 2) reveals undigested lipid material (lamellar structures) within these vesicles. Lysosomes are pseudo-coloured in green. Scale bars: 1 µm and for the enlargement 0.2 µm. **D** Quantification of lysosomal number by EM analysis indicates no difference in the number of lysosomes per cell between *Npc1*$^{+/+}$ and *Npc1*$^{-/-}$ microglia (n = 3)**.** *Npc1*$^{+/+}$ -normalised values are represented as mean ± SEM and an unpaired two-tailed Student's t-test was performed (ns = not significant). Retrieved and modified from Colombo and Dinkel *et al* [243].

Next question was whether dysfunctional trafficking to lysosomes in *Npc1*$^{-/-}$ microglia is substrate specific, since degradation of fibrillar Aβ was not impaired (Figure 13E). Therefore, a pulse-chase experiment was performed in which the degradation of a protein substrate, the EGFR, was followed upon stimulation with EGF in 1-week old *Npc1*$^{+/+}$ and *Npc1*$^{-/-}$ microglia. Western blot analysis revealed no difference in EGFR degradation between *Npc1*$^{+/+}$ and *Npc1*$^{-/-}$ microglia (Figure 18A and B), pointing towards functional trafficking of EGFR to the lysosomes and their preserved proteolytic activity.

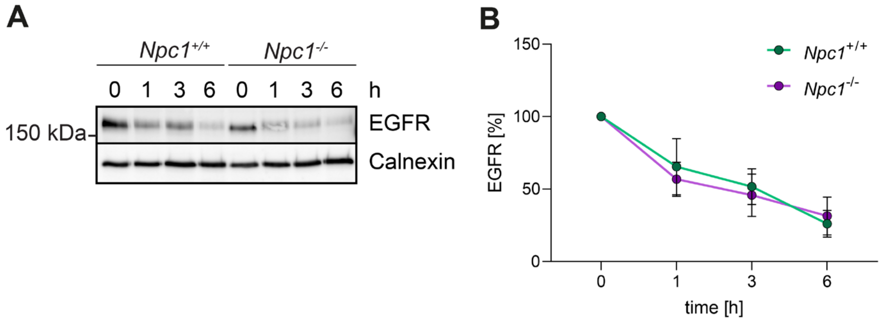

Figure 18. Lysosomal proteolytic function is preserved in *Npc1*$^{-/-}$ microglia. A-B EGFR degradation assay with *Npc1*$^{+/+}$ and *Npc1*$^{-/-}$ microglia from 1-week old mice (n = 3). Cultured microglia were fed with recombinant murine EGF under starving conditions in order to induce the degradation of its receptor EGFR. EGFR degradation was analysed after 1, 3 and 6 h via western blot analysis. Representative immunoblot (**A**) and corresponding quantification (**B**) reveals no difference in EGFR degradation between *Npc1*$^{+/+}$ and *Npc1*$^{-/-}$ microglia. Calnexin was used as loading control. Proteins were quantified by densitometry (ImageJ) and normalised to timepoint mean ± SEM. Retrieved and modified from Colombo and Dinkel *et al* [243].

Taken together, I could show that lipid trafficking to the lysosomes is disturbed in *Npc1*$^{-/-}$ microglia and that lipid material accumulates in late endosomes/MVBs rather than in lysosomes, which are proteolytically active in *Npc1*$^{-/-}$ microglia.

3.6 Lowering Cholesterol Partially Rescues Myelin Processing and Reverts Signatures of *Npc1*$^{-/-}$ Microglia

Various lipids accumulate in NPC, but their contribution to NPC development and progression is still unknown [99]. Given the importance of NPC1 in cholesterol metabolism, I tested whether lowering of cholesterol with MβCD would rescue microglial molecular and functional phenotypes. Immunocytochemical analysis revealed that treatment with MβCD lowered efficiently the cholesterol load (assessed by filipin staining) and significantly increased the numbers of lipid droplet positive *Npc1*$^{-/-}$ microglia by ~30% in the *in vitro* myelin assay (Figure 19A and B).

I hypothesised that the rescue of the lipid trafficking block might translate into reversed microglia molecular phenotypes. Therefore, protein levels of the key regulator for homeostasis TGFB1 [177] and the DAM protein CTSD were analysed after MβCD treatment (Figure 20A). Western blot analysis showed a significant increase in TGFB1 (Figure 20B) and a decrease in CTSD (Figure 20C) in *Npc1*$^{-/-}$ microglia treated with MβCD, indicating that these molecular changes may be triggered by cholesterol accumulation. Strinkingly, no difference in TGFB1 and CTSD were detected in cultured *Npc1*$^{+/+}$ and *Npc1*$^{-/-}$ microglia, which is in line with other studies reporting that microglia change their

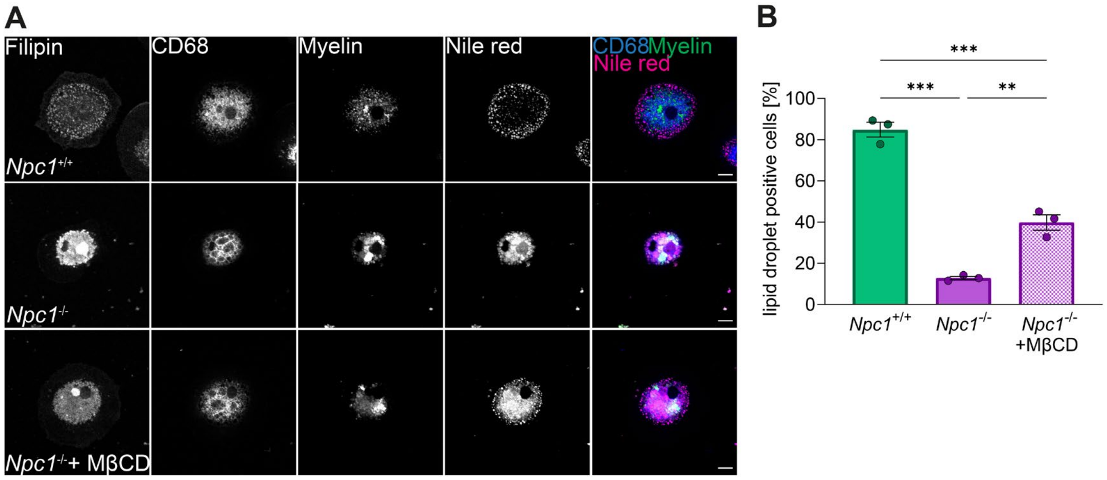

Figure 19. Dysfunctional myelin processing in *Npc1*$^{-/-}$ is rescued by cholesterol lowering agent MβCD. A Immunocytochemical analysis of the effect of methyl-β-cyclodextrin (MβCD) onto myelin processing. *Npc1*$^{+/+}$ and *Npc1*$^{-/-}$ microglia were fed with fluorescently labelled myelin (green) and the presence of lipid droplets (stained with Nile red; magenta) was analysed after 48 h in each condition. Efficacy of MβCD treatment onto cholesterol lowering was assessed by cholesterol staining dye filipin (white). Late endosomes/lysosomes were immunostained for CD68 (blue). Scale bars: 10 µm. **B** Quantification of lipid droplet positive cells in myelin fed *Npc1*$^{+/+}$ and *Npc1*$^{-/-}$ microglia reveals that treatment with 250 µM MβCD partially rescues the myelin processing into lipid droplets in *Npc1*$^{-/-}$ microglia. A one-way ANOVA with Tukey's multiple comparisons test was performed (n = 3; $^{**}p < 0.01$, $^{***}p < 0.001$). Retrieved and modified from Colombo and Dinkel *et al.*[243].

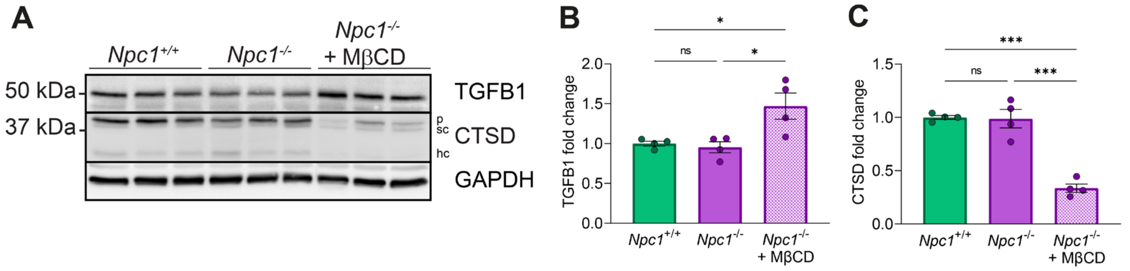

Figure 20. Microglia signatures are rescued in *Npc1*$^{-/-}$ by cholesterol lowering agent MβCD. A-C Western blot analysis of protein changes in cultured *Npc1*$^{+/+}$ and *Npc1*$^{-/-}$ microglia (n = 4) from 1-week old mice upon MβCD treatment for 2 DIV. Representative western blot (**A**) and its corresponding quantification of the homeostatic protein TGFB1 (**B**) and the DAM protein CTSD (**C**). Treatment with 250 µM MβCD increases the levels of TGFB1 and decreases levels of CTSD in *Npc1*$^{-/-}$ microglia. GAPDH was used as loading control. *Npc1*$^{+/+}$-normalised values are depicted as mean ± SEM and a one-way ANOVA with Tukey's multiple comparisons test was performed (ns = not significant, $^{*}p < 0.05$, $^{***}p < 0.001$). Retrieved and modified from Colombo and Dinkel *et al.* [243].

transcriptomic profiles upon culturing [177, 270]. This result highlights the importance to analyse transcriptomic and proteomic profiles *in vivo* (Figure 10B and Figure 12A). Altogether, these data suggest that cholesterol accumulation contributes to the impaired myelin processing and molecular alterations in *Npc1*$^{-/-}$ microglia.

3.7 PBMC-Derived Macrophages from NPC Patients Display Similar Molecular and Functional Alterations as *Npc1*$^{-/-}$ Microglia

Due to limited number of NPC patients and access to viable brain tissue [271], I explored molecular and functional alterations of the professional phagocytes of the periphery, namely macrophages [269]. In contrast to *Npc1*$^{-/-}$ microglia, NPC1 protein was still detectable in NPC patients (Figure 21A-C), since most of the *NPC1* mutations do not lead to a complete loss of NPC1 [57].

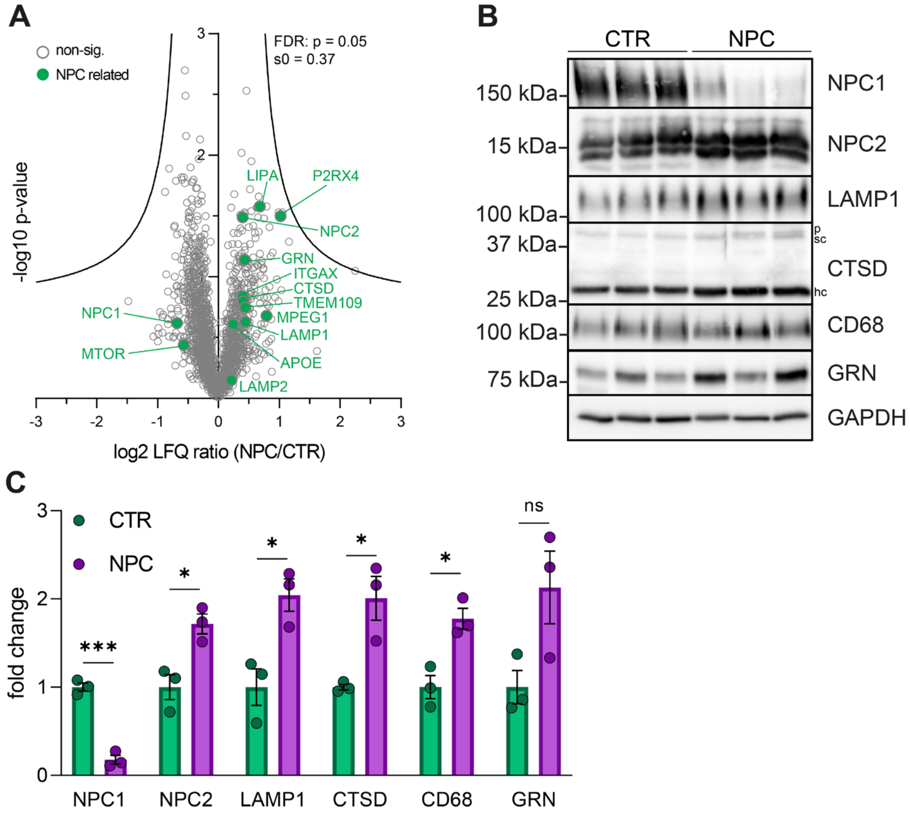

Figure 21. PBMC-derived macrophages from NPC patients display similar molecular alterations as *Npc1*$^{-/-}$ microglia. A Proteomic analysis of PBMC-derived macrophages from three healthy controls (CTR) and seven NPC patients (NPC). PBMCs were isolated from full blood and differentiated into macrophages for 5 DIV. Afterwards, cells were collected and subjected for MS analysis. The average log2 transformed LFQ ratio between NPC and CTR macrophages is plotted against the negative log10 transformed p-value. The threshold for the false discovery rate (FDR) is depicted in hyperbolic curves. Non-significant proteins are depicted with a grey circle and selected proteins altered in NPC are encircled in green. **B**-**C** Validation of the proteomic data using western blot analysis. Representative immunoblots (**B**) and the respective quantification (**C**) using macrophages from three healthy controls and three NPC patients shows residual NPC1 and increased levels of late endosomal/lysosomal proteins in NPC patients. GAPDH was used as loading control and proteins were quantified by densitometry (ImageJ). CTR-normalised values are depicted as mean ± SEM. An unpaired two-tailed Student's t-test was performed (ns = not significant, *p < 0.05, ***p < 0.001). For cathepsins: p = pro-form, sc = single chain form, hc = heavy chain form. Retrieved and modified from Colombo and Dinkel *et al.* [243].

Due to residual NPC1 function, proteome changes in human patient macrophages were less pronounced compared to *Npc1*$^{-/-}$ microglia and displayed higher variability (NPC patients had different *NPC1* mutations; Table 32). Nevertheless, MS analysis of PBMC-derived macrophages from seven NPC patients and three healthy controls revealed similar proteomic changes as detected in *Npc1*$^{-/-}$ microglia (Figure 10B and 12A), including up-regulation of late endosomal/lysosomal proteins like transmembrane protein 109 (TMEM109), NPC2, LAMP1/2, CTSD, and GRN (Figure 21A). Morover, proteins involved in vesicular trafficking (RAB27A, RAB43 and TBC1 domain family member 15 (TBC1D15)) were dysregulated. This demonstrates that murine microglia and human macrophages feature similar molecular alterations upon NPC1 loss. The whole proteome list can be accessed in the Supplementary Data 4 of Colombo and Dinkel *et al*. [243]. Upregulation of late endosomal/lysosomal proteins and downregulation of NPC1 were validated by western blot analysis (Figure 21B and C). As I detected similar molecular alterations of *Npc1*$^{-/-}$ microglia and NPC macrophages, I hypothesised their similar functional alterations. Performing the *ex vivo* Aβ plaque phagocytic assay, I could detect a tendency in increased phagocytic clearance of Aβ plaques by NPC-derived macrophages (Figure 22A).

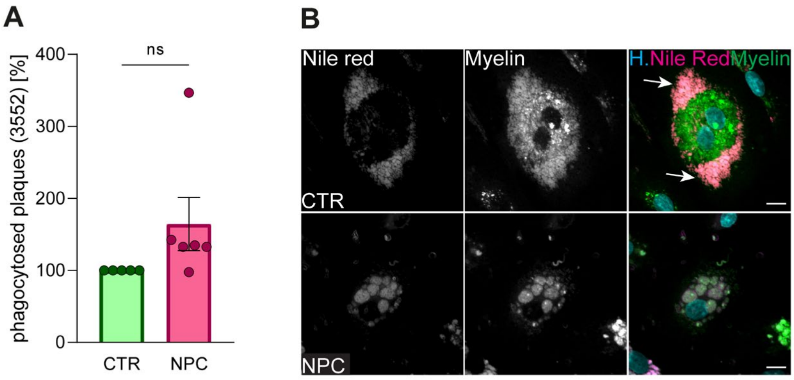

Figure 22. PBMC-derived macrophages from NPC patients feature functional alterations of *Npc1*$^{-/-}$ microglia. A Quantification of the *ex vivo* Aβ plaque phagocytic assay using PBMC-derived macrophages from CTR (n = 5) and NPC patients (n = 6) reveals and increased phagocytic clearance of Aβ (assessed by 3552 coverage) in NPC patients. Data is represented as mean ± SEM. A one sample Wilcoxon test was performed (ns = not significant). **B** PBMC-derived macrophages were fed with fluorescently labelled myelin (green) and the presence of lipid droplets (stained with Nile red; magenta, indicated with white arrows) was analysed. NPC-derived macrophages are deficient in lipid droplets, while CTR-derived macrophages efficiently process myelin into lipid droplets. Scale bars: 10 µm. Retrieved and modified from Colombo and Dinkel *et al*. [243].

Furthermore, I performed the myelin trafficking assay with PBMC-derived macrophages, which revealed that phagocytosed myelin is efficiently processed into lipid droplets (visualised by Nile red staining) in healthy control macrophages, while NPC-derived macrophages were deficient in lipid droplets (Figure 22B). My translational study revealed that PBMC-derived macrophages feature molecular and functional alterations discovered in *Npc1*$^{-/-}$ microglia, and thereby, offers a useful platform to monitor therapeutic interventions in NPC patients.

3.8 Loss of NPC1 in Microglia is Sufficient to Trigger Molecular Alterations

My results revealed that NPC1 function is critical for late endosomal/lysosomal homeostasis and function of myeloid cells (murine microglia and human macrophages). Next, I wanted to detangle if molecular and functional alterations are cell-autonomous consequences of the loss of NPC1 in myeloid cells. Therefore, I generated a new mouse model with the specific loss of NPC1 in the myeloid linage (*Npc1*cKO x *Cx3cr1Cre*) using mice which expressed the Cre recombinase under the myeloid-specific *Cx3cr1* promotor [242]. Mice were homozygous for *Npc1* which was flanked by to *loxP* sites [146]. Thereby, NPC1 was depleted only in the microglia in the brain of mice which expressed the Cre recombinase (*Cre*+). Littermates which did not express Cre recombinase (*Cre*-) were taken as wildtype controls (Figure Figure **23**A). The specificity of NPC1 loss only in microglia was assessed via western blot analysis, which revealed depletion of NPC1 only in the microglia enriched fraction of *Cre*+ mice, while no difference was detected in the microglia depleted fraction (Figure 23B). Furthermore, western blot analysis of the late endosomal/lysosomal proteins CD68, CD63 and LAMP1 showed high upregulation only in the *Cre*+ microglia enriched fraction (Figure 23C), highlighting the specificity of NPC1 loss in microglia and recapitulating late endosomal/lysosomal dyshomeostasis that I observed in *Npc1*$^{-/-}$ microglia (Figure 10B and 12A). Furthermore, MS analysis of microglia from 5 months old *Cre*- and *Cre*+ mice revealed that *Cre*+ microglia adapted the DAM phenotype [179], including increased levels of DAM proteins like CD68, LAMP1, GRN, CTSD and CTSB and decreased levels of homeostatic proteins like CSF1R, MRC1, ABI3, P2YR12, TMEM119 and TGFB1 (Figure 23D). The whole proteome list can be accessed in the Supplementary Data 3 of Colombo and Dinkel *et al*. [243]. Similarly to the proteome of *Npc1*$^{-/-}$ mice from 2 months old mice, proteins incolved in vesicular trafficking (RAB5b, RAB7a), lipid metabolism (FDPS, DHCR, GGPS1, SRD5A3, acetyl-

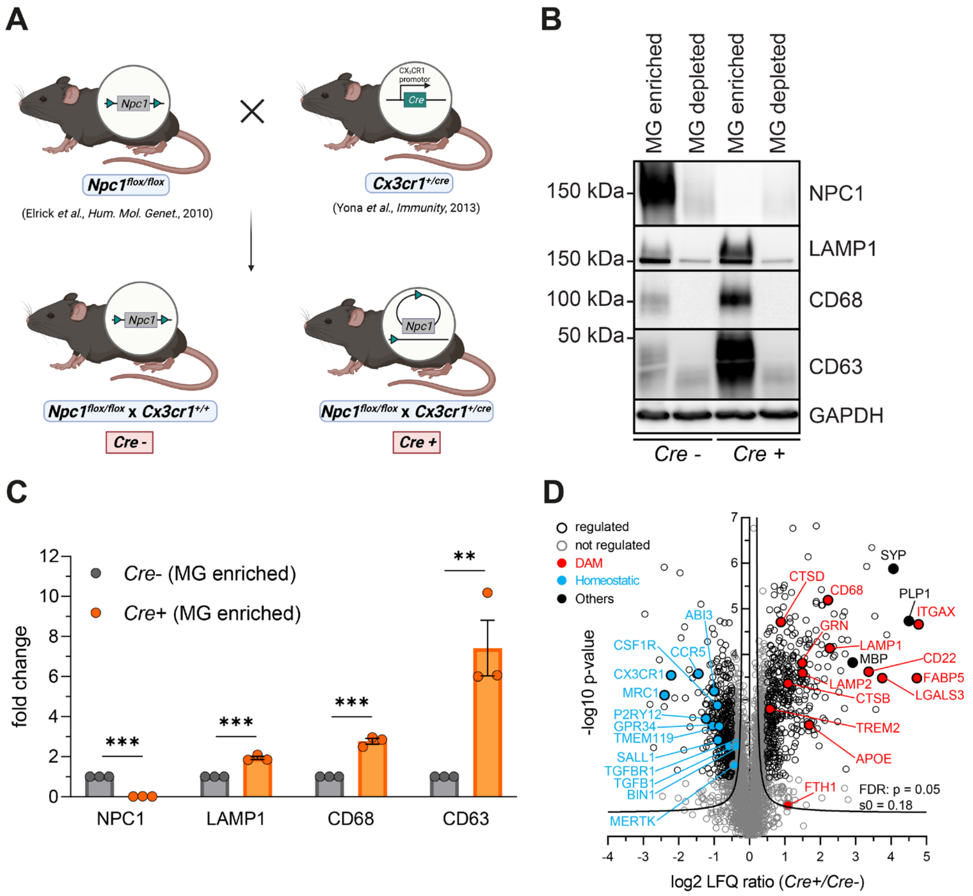

Figure 23. Specific depletion of NPC1 in microglia is sufficient to trigger DAM phenotypes. **A** Scheme of the generation of mice lacking *Npc1* in myeloid cells. Mice which have the *Npc1* gene flanked by two *loxP* sites (*Npc1*$^{\text{flox/flox}}$ [146]) are crossed with mice expressing the Cre recombinase under the myeloid specific promotor *Cx3cr1* (*Cx3Cr1*$^{+/cre}$ [242]). Offspring were intercrossed several times to generate mice homozygous for *Npc1*$^{\text{flox/flox}}$ and wildtype for *Cre* (*Cx3Cr1*$^{+/+}$), referred as *Cre*-, or heterozygous for *Cre* (*Cx3Cr1*$^{+/\text{Cre}}$), referred as *Cre*+. **B-C** Validation of the specific depletion of NPC1 in *Cre*+ microglia of 2 months old mice via western blot analysis. Representative immunoblots (**B**) and the corresponding quantification (**C**) of *Cre*- and *Cre*+ microglia (n = 3) reveal that NPC1 is only depleted in the *Cre*+ microglia (MG) enriched fraction and not in *Cre*- MG enriched fraction, nor in the MG depleted fraction of *Cre*- and *Cre*+ mice. An increase in late endosomal/lysosomal proteins (LAMP1, CD68, CD63) is only detected in the MG enriched fraction of *Cre*+ mice. GAPDH was used as loading control and proteins in the MG enriched faction were quantified by densitometry (ImageJ). Values were normalised to *Cre*- and are depicted as mean ± SEM. An unpaired two-tailed Student's t-test was performed (**$p < 0.01$, ***$p < 0.001$). **D** Proteomic analysis of acutely isolated *Cre*- and *Cre*+ microglia of 5 months old mice. The average log2 transformed LFQ ratio between *Cre*+ and *Cre*- microglia is plotted against the negative log10 transformed p-value. The threshold for the false discovery rate (FDR) is depicted in hyperbolic curves. Significantly changed proteins ($p < 0.05$ and FDR-positive) with a log2 fold change greater/smaller than ± 0.5 are depicted in a black circle (regulated), not regulated proteins are depicted with a grey circle (not regulated). Selected disease-associated microglia (DAM), homeostatic proteins and other proteins (synaptophysin, SYP; proteolipid protein 1, PLP1; myelin basic protein, MBP) are encircled in red, blue and black, respectively. Retrieved and modified from Colombo and Dinkel *et al.* [243].

CoA carboxylase 1 (ACACA), GALC, HEXA, GBA), and glutathione metabolism (GSTO1, GSTM1, glutathione reductase (GSR)) were dysregulated. Additionally, ROS producing enzyme cytochrome b-245 heavy chain (CYBB) was upregulated. These data strongly suggest that microglial molecular fingerprints are mainly driven cell-autonomously by NPC1 loss.

3.9 Processing of the Phagocytosed Myelin Relies on NPC1 Function in Microglia

Cre+ microglia displayed similar proteomic signatures as *Npc1*$^{-/-}$ microglia (Figure 10B, 12A and 23D), suggesting that *Cre*+ microglia feature *Npc1*$^{-/-}$ functional alterations. Therefore, I analysed myelin processing in *Cre*+ microglia. *Cre*- and *Cre*+ microglia from 2 months old mice were cultured and fed with fluorescently labelled myelin for 6 h and processing of myelin into lipid droplets (visualised by Nile red staining) was analysed after 48 h post-feeding (Figure 24A). Immunocytochemical analysis revealed that *Cre*+ microglia had deficiencies in processing phagocytosed myelin into lipid droplets (Figure 24B) as discovered for *Npc1*$^{-/-}$ microglia or NPC-derived macrophages (Figure 16 and 22B).

To further characterise myelin processing and lipid droplet formation, myelin fed *Cre*+ and *Cre*- microglia were analysed by EM. Consistent with the immunocytochemical analysis, undigested lipid material was present in myelin fed *Cre*+ microglia (Figure 24C; asterisks in magenta). In contrast, myelin-fed *Cre*- microglia processed the phagocytosed myelin into lipid droplets similar as seen in “foam cells” in atherosclerosis or in phagocytes in demyelination lesions [272, 273], suggesting processing of myelin into CE-rich lipid droplets (Figure 24C, blue arrows). Interestingly, small lipid droplets that may comprise another fatty acid composition than those found in *Cre*- microglia were detected in *Cre*+ microglia (Figure 24C, green arrows). Lipid storage in NPC has been discussed to affect lysosomal mass in NPC1-deficient cells [114, 116, 274]. Therefore, the lysosomal number in myelin-fed *Cre*- and *Cre*+ microglia was analysed and revealed a significant decrease in lysosomal numbers in *Cre*+ microglia (Figure 24D). Reduced lysosomal number upon myelin feeding suggests that myelin is not reaching the lysosomes to induce transcriptional changes to increase lysosomal biogenesis, which is line with my previous results (Figure 17D). Taken together these results suggest that NPC1 plays a key role in the phagocytic trafficking of myelin to the lysosomes, and subsequently, for the processing of myelin into CE-rich lipid droplets.

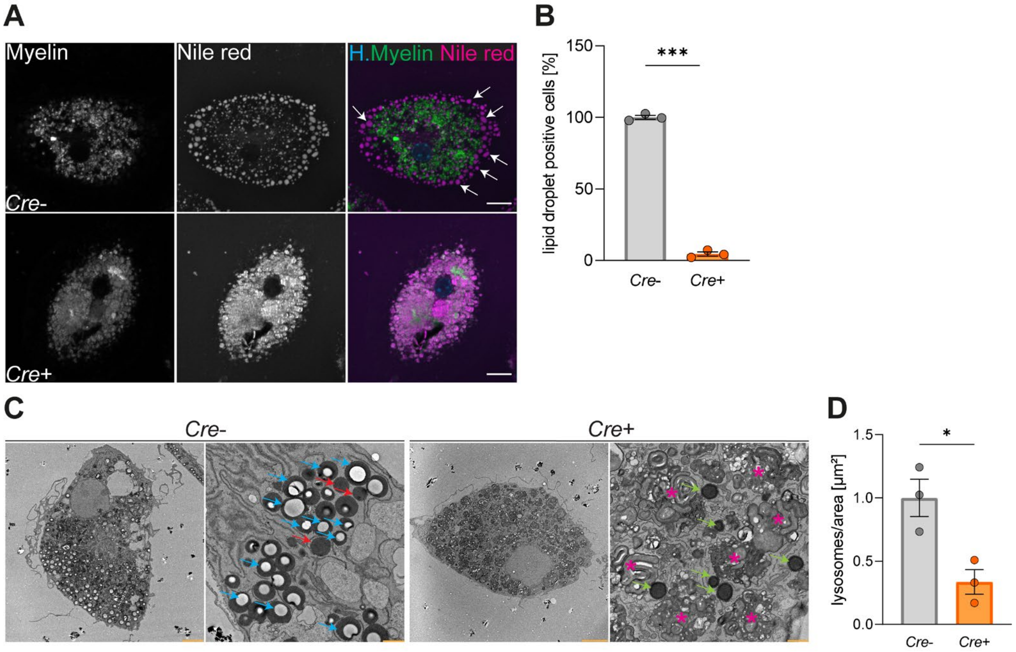

Figure 24. Myelin processing relies on cell-autonomous function of NPC1 in microglia. A Immunocytochemical analysis of myelin processing in *Cre*- and *Cre*+ microglia. *Cre*- and *Cre*+ microglia were fed with fluorescently labelled myelin (green) and the presence of lipid droplets (stained with Nile red, magenta, white arrows) was analysed after 48 h. Scale bars: 10 µm. **B** Quantification of myelin fed and lipid droplet positive cells reveals that *Cre*+ microglia are deficient in the turnover of myelin into lipid droplets. Values are normalised to *Cre*- and are represented as mean ± SEM. A two-tailed unpaired Student's t was performed (n = 3; ***p < 0.001). **C** Representative images of the EM analysis of myelin fed *Cre*- and *Cre*+ microglia (left panel). Higher magnified images (right panel) reveal less lysosomes (red arrows) in *Cre*+ microglia and accumulation of undegraded myelin (asterisks in magenta). In addition, different identities of lipid droplets are visualised in *Cre*- microglia (blue arrows) and in *Cre*+ microglia (green arrows). Scale bars: left panel (5 µm) and right panel (1 µm). **D** Quantification of lysosomal number reveals that myelin-fed *Cre*+ microglia have less lysosomes than myelin-fed *Cre*- microglia. Values are normalised to *Cre*- and are represented as mean ± SEM and a two-tailed unpaired Student's t was performed (n = 3; *p < 0.05).

3.10 Loss of NPC1 Causes Dramatic Lipid Changes in Microglia

NPC1-deficient microglia display major impairments of the late endosomal/lysosomal system and lipid trafficking suggesting disturbances in lipid homeostasis. Therefore, I explored the lipidomic profile of acutely isolated microglia from 1-week old *Npc1*$^{-/-}$ mice (pre-symptomatic stage; Figure 25A and Table 41), 2 months old *Npc1*$^{-/-}$ mice (symptomatic stage; Figure 25B and Table 42) and 2 months old *Cre*+ mice (microglial cell-autonomous lipid changes; Figure 25C and Table 43). Pronounced lipid changes were already prominent at an age of 1-week in *Npc1*$^{-/-}$ microglia, including significant increase in cholesterol and correspondingly lower levels of CEs (Figure 25A). This is fully in line with my results generated in NPC1-deficient microglia where myelin was trapped in late

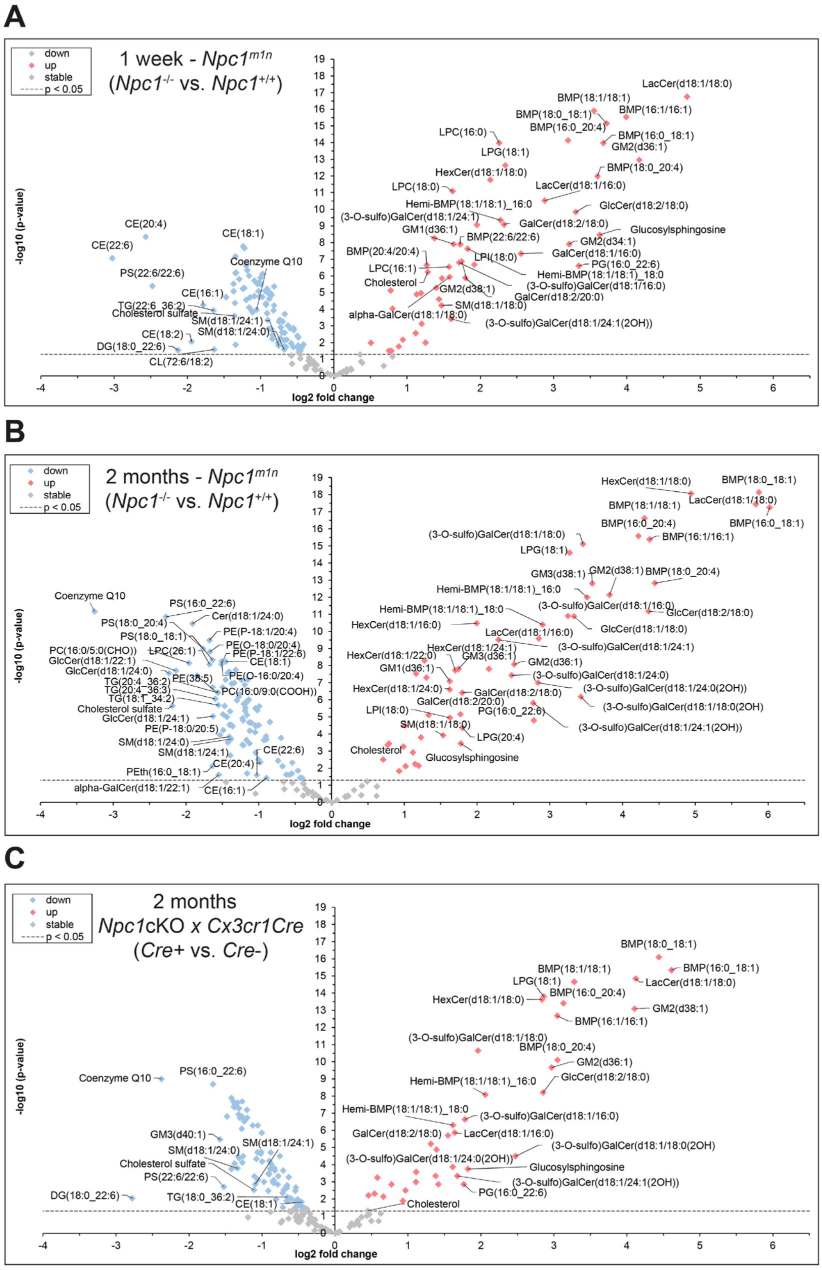

Figure 25. Loss of NPC1 impacts microglial lipid homeostasis already during developmental stages. A-C Lipidomic analysis of acutely isolated microglia from 1-week (**A**) and 2 months old (**B**) *Npc1^{m1n}* and from 2 months old *Npc1*cKO x *Cx3cr1Cre* mice (**C**). The log2 fold change between NPC1 depleted microglia (*Npc1$^{-/-}$* and *Cre*+) and control microglia (*Npc1$^{+/+}$* and *Cre*-) is plotted against the negative log10 transformed p-value. The following sample sizes were used: 1-week, n = 5 for *Npc1$^{+/+}$* and *Npc1$^{-/-}$*; 2 months, n = 5 for *Npc1$^{+/+}$*/*Cre*-/*Cre*+ and n = 4 for *Npc1$^{-/-}$*. Significantly changed lipids (adjusted $p < 0.05$) are depicted in red (upregulated) and blue (downregulated) squares, respectively. Not significantly changed lipids (adjusted $p > 0.05$) are depicted in grey squares (stable). The dotted line represents a p-value of 0.05.

endosomes/MVBs and not processed into CE-rich lipid droplets (Figure 16, 17 and 24). Moreover, this is the first study actually revealing cholesterol accumulation in a brain cell. In line with other studies [101, 151, 275, 276], a high increase in glycosphingolipids like GM2, GM3, lactosylceramide (LacCer), hexosylceramide (HexCer), GalCer and GlcCer were detected in all data sets (Figure 25A-C). Interestingly, different isoforms of a lipid highly enriched in ILVs, the BMP [277], were most abundantly enriched in all data sets (Figure 25A-C), suggesting increased amounts of ILVs in NPC1-deficient microglia. On the other side, coenzyme Q10, an important component of the electron transport chain in mitochondria [278], was drastically reduced in NPC1-deficient microglia (mostly pronounced at 2 months), suggesting mitochondrial impairments. Furthermore, the reduction of various phospholipids, which build up membrane lipid bilayers, was striking through all datasets implying vast membrane rearrangements upon loss of NPC1 in microglia (Figure 25A-C and Table 41-42). Lastly, different derivates of the neutral lipids diacylglycerol (DG) and TG were reduced in all datasets suggesting impaired metabolism of these lipids. Furthermore, lipidomic alterations of the different NPC1-deficient microglia datasets were compared in a heatmap, which revealed similar lipid changes in NPC1-deficient microglia (Figure 26A). Accordingly, $Npc1^{-/-}$ and *Cre*+ microglia from 2 months old mice shared 63.74 % of the same lipid alterations, implying that certain lipids are changed upon cell-autonomous loss of NPC1 in microglia (Figure 26B).

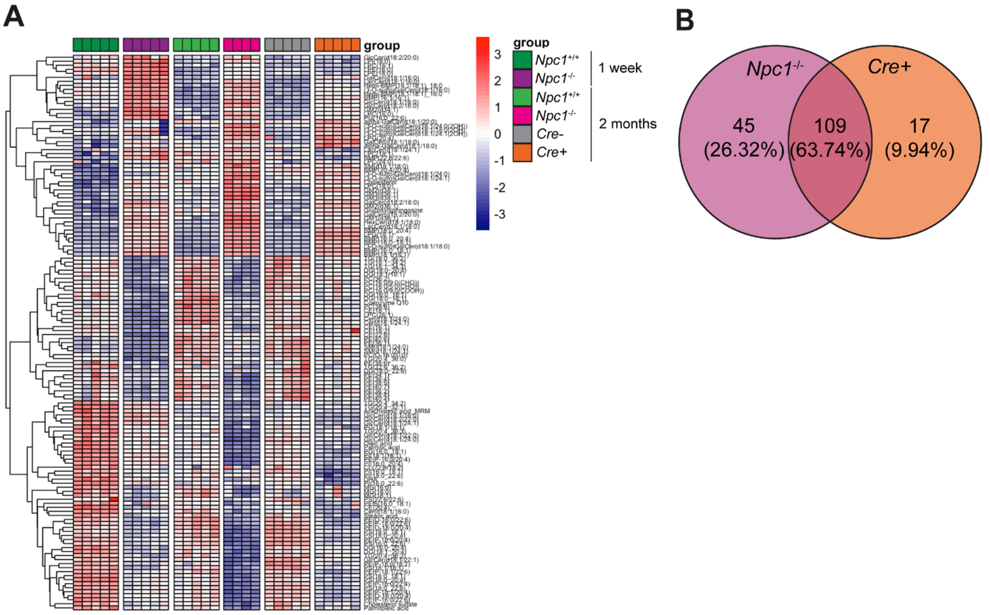

Figure 26. Lipid changes are mainly driven by cell-autonomous loss of NPC1 in microglia. **A** Heatmap of the lipidomic analysis of acutely isolated microglia from 1-week and 2 months old $Npc1^{m1n}$ and from 2 months old *Npc1*cKO x *Cx3cr1Cre* mice reveals similar, but slightly less pronounced lipid changes in *Cre*+ microglia. Lipids which were detected in all data sets are depicted. The following sample sizes were used: 1-week, n = 5 for $Npc1^{+/+}$ and $Npc1^{-/-}$; 2 months, n = 5 for $Npc1^{+/+}$/*Cre*-/*Cre*+ and n = 4 for $Npc1^{-/-}$. **B** Venn-diagram of significantly changed lipids in $Npc1^{-/-}$ and *Cre*+ microglia reveals high overlap of their lipidomic profiles (63.74%).

Next, I validated some of the lipid alterations (GM1, GM2 and cholesterol) by immunocytochemistry (Figure 27). GM1 (immunostained with CtxB) broadly co-localised with late endosomal/lysosomal membranes (immunostained with a CD68 antibody), while GM2 (immunostained with an GM2 antibody) together with cholesterol (visualised using filipin) accumulated within late endosomal/lysosomal compartment in *Cre*+ microglia (Figure 27).

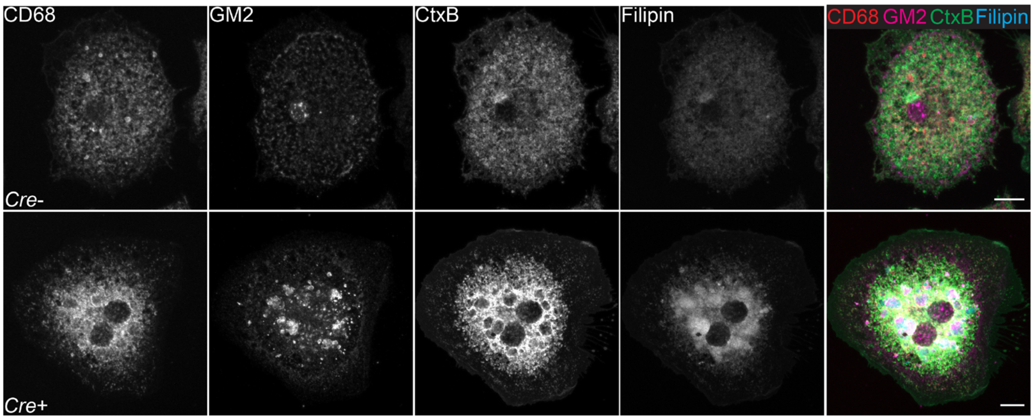

Figure 27. Lipid accumulation in *Cre*+ microglia. Validation of lipidomic analysis in cultured *Cre*- and *Cre*+ microglia from 2 months old mice. Microglia were isolated and cultured for 7 DIV and immunostained against CD68 (late endosomes/lysosomes; red), GM2 (magenta) and GM1 (using biotinylated CtxB; green). Cholesterol was stained using filipin (cyan). Scale bars: 10 µm.

Furthermore, my dataset reflected differences in lipid composition of microglia at developmental (1-week old) *versus* adult stages (2 months old) in both *Npc1*$^{+/+}$ (Figure 28A and Table 44) and *Npc1*$^{-/-}$ mice (Figure 28B and Table 45). As an example, upon aging, *Npc1*$^{+/+}$ microglia showed an increase in coenzyme Q10 and cholesterol, and decreased levels of BMPs suggesting a distinct lipid profile during developmental stages (Figure 28A). In contrast, certain lipid species were differently altered in *Npc1*$^{-/-}$ microglia upon aging, including increased levels of BMPs, implying a progressive lipid accumulation upon NPC1 loss in microglia (Figure 28B). These results highlight how relevant a strict control of lipid homeostasis is for microglial development und function. Here presented lipidomic analysis revealed that lipid changes are largely driven by a cell-autonomous function of NPC1 in microglia.

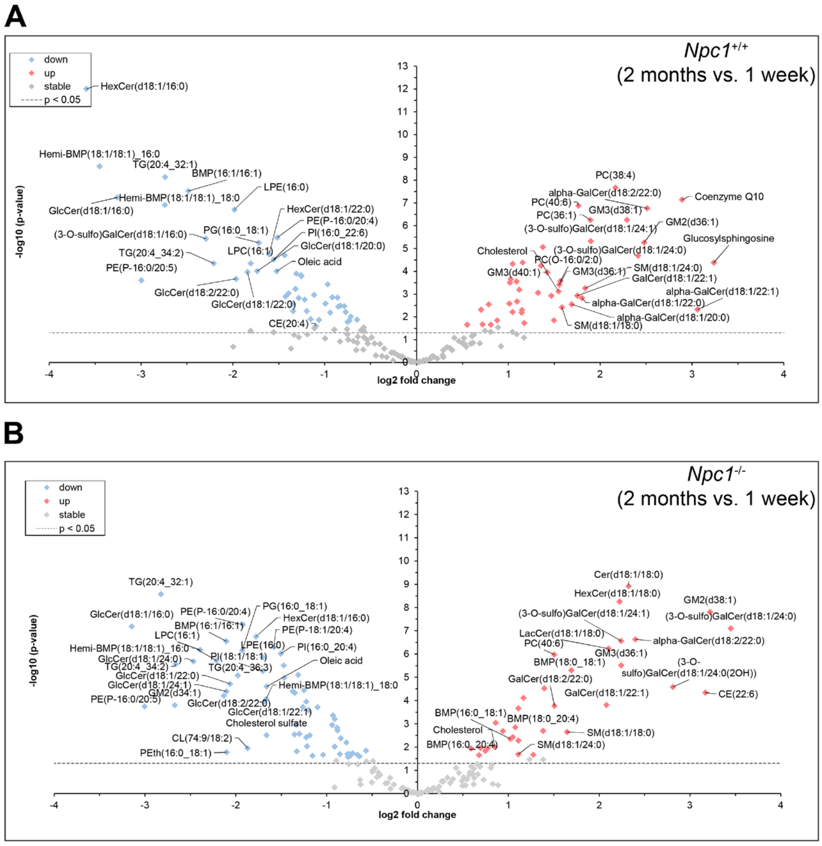

Figure 28. Postnatal and adult microglia show different lipid profiles. Lipidomic analysis of acutely isolated microglia from 1-week and 2 months old *Npc1*$^{+/+}$ (**A**) and *Npc1*$^{-/-}$ mice (**B**). The log2 fold change between microglia from 2 months old *Npc1*$^{+/+}$/*Npc1*$^{-/-}$ mice and 1-week old *Npc1*$^{+/+}$/*Npc1*$^{-/-}$ mice are plotted against the negative log10 transformed p-value. Significantly changed lipids (adjusted $p < 0.05$) are depicted in red (upregulated) and blue (downregulated) squares, respectively. Not significantly changedlipids (adjusted $p > 0.05$) are depicted in grey squares (stable). The following sample sizes were used: 1-week, n = 5 for *Npc1*$^{+/+}$ and *Npc1*$^{-/-}$; 2 months, n = 5 for *Npc1*$^{+/+}$ and n = 4 for *Npc1*$^{-/-}$. The dotted line represents a p-value of 0.05.

3.11 Loss of NPC1 is Sufficient to Trigger Microglia Activation

Proteomic analysis of *Cre*+ microglia suggests an activated microglial phenotype (Figure 23D). Immunostainings for CD68 in 2 months old *Cre*- and *Cre*+ mice revealed pronounced microglial activation throughout the brain in *Cre*+ mice (Figure 29A). At late stages, namely at 12 months, CD68 immunoreactivity is further increased in *Cre*+ mice (Figure 29B), with distinct brain regions like the midbrain (Figure 29B, zoom-in c) showing higher immunoreactivity when compared to the cerebellum (Figure 29B, zoom-in d). I used TSPO-PET imaging as a non-invasive technique to follow the progression of microglial activation in 2, 7 and 11 months old *Cre*- and *Cre*+ mice (Figure 30A). TSPO is a ubiquitously expressed mitochondrial protein, which becomes enriched in activated microglia under pathological conditions [279] and was increased in the proteomic analysis

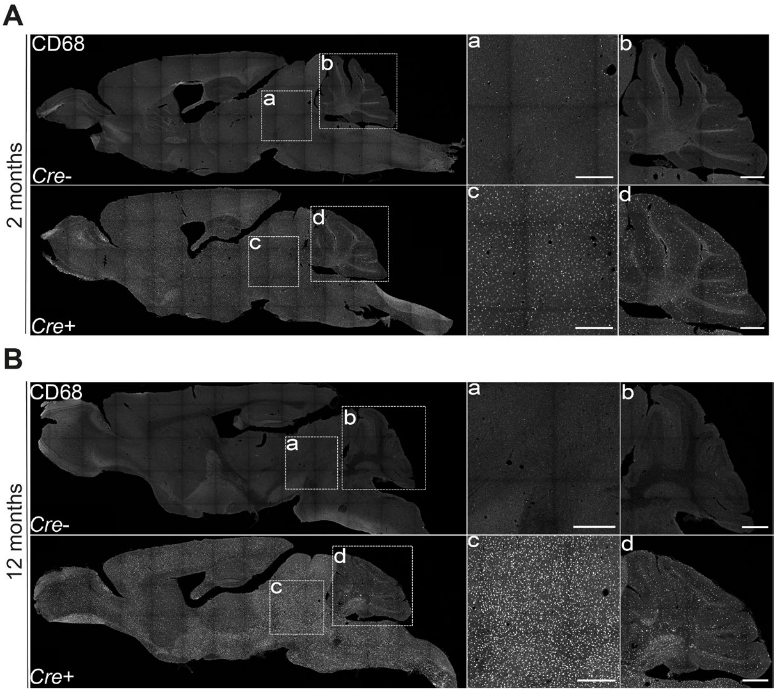

Figure 29. *Cre*+ mice display pronounced CD68 immunoreactivity throughout the brain. Sagittal brain sections of *Cre*- and *Cre*+ mice at 2 months (**A**) and 12 months of age (**B**). Tile scans (left panels) and zoom-ins (right panels) of the midbrain (a, c) and cerebellum (b, d) immunostained against microglial late endosomal/lysosomal marker CD68 (white). High CD68 reactivity throughout the brain is already prominent at 2 months of age in *Cre*+ mice, which becomes more pronounced in the midbrain at 12 months of age. Scale bars: 500 µm.

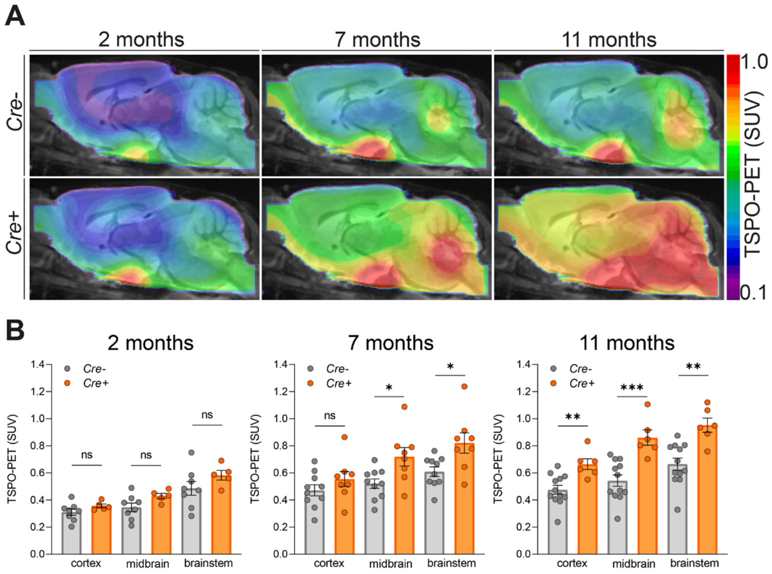

Figure 30. Loss of NPC1 in microglia leads to a strong TSPO-PET SUV increase. A Sagittal brain sections represent group average images of TSPO-PET standardised uptake value (SUV) projected upon a standard MRI T1w atlas. **B** Quantification of microglial activity measured by *in vivo* TSPO-PET in *Cre*- and *Cre*+ mice at 2, 7 and 11 months of age. Individual TSPO-PET SUVs deriving from cortex, midbrain and brainstem VOIs. An unpaired Student's t-test was performed for statistical analysis with following sample sizes: *Cre*- n = 8 and *Cre*+ n = 5 for 2 months, *Cre*- n = 10 and *Cre*+ n = 8 for 7 months and *Cre*- n = 12 and *Cre*+ n = 6 for 11 months (ns = not significant, *p < 0.05, **p < 0.01, ***p < 0.001).

of NPC1-deficient microglia (Supplementary Data 1-3 of Colombo and Dinkel *et al.* [243]). PET imaging revealed a progressive increase in TSPO-PET signal upon aging in *Cre*- and *Cre*+ mice, but a significant difference in TSPO-PET signal started to be detectable at 7 months of age in *Cre*+ mice (Figure 30B). Indeed, immunohistochemical analysis of TSPO revealed only a slight increase in *Cre*+ microglia at 2 months of age (Figure 31A), which is in contrary to the CD68 immunostainings, where prominent differences were already present at 2 months of age (Figure 29A), supporting the hypothesis that lysosomal alterations are among first pathological changes detected upon loss of NPC1. Of note, I could also detect TSPO in cells which were Iba1- and GFAP-negative, but positive for the endothelial cell marker cluster of differentiation 31 (CD31), implying strong expression of TSPO also in endothelial cells at 2 months (Figure 31B).

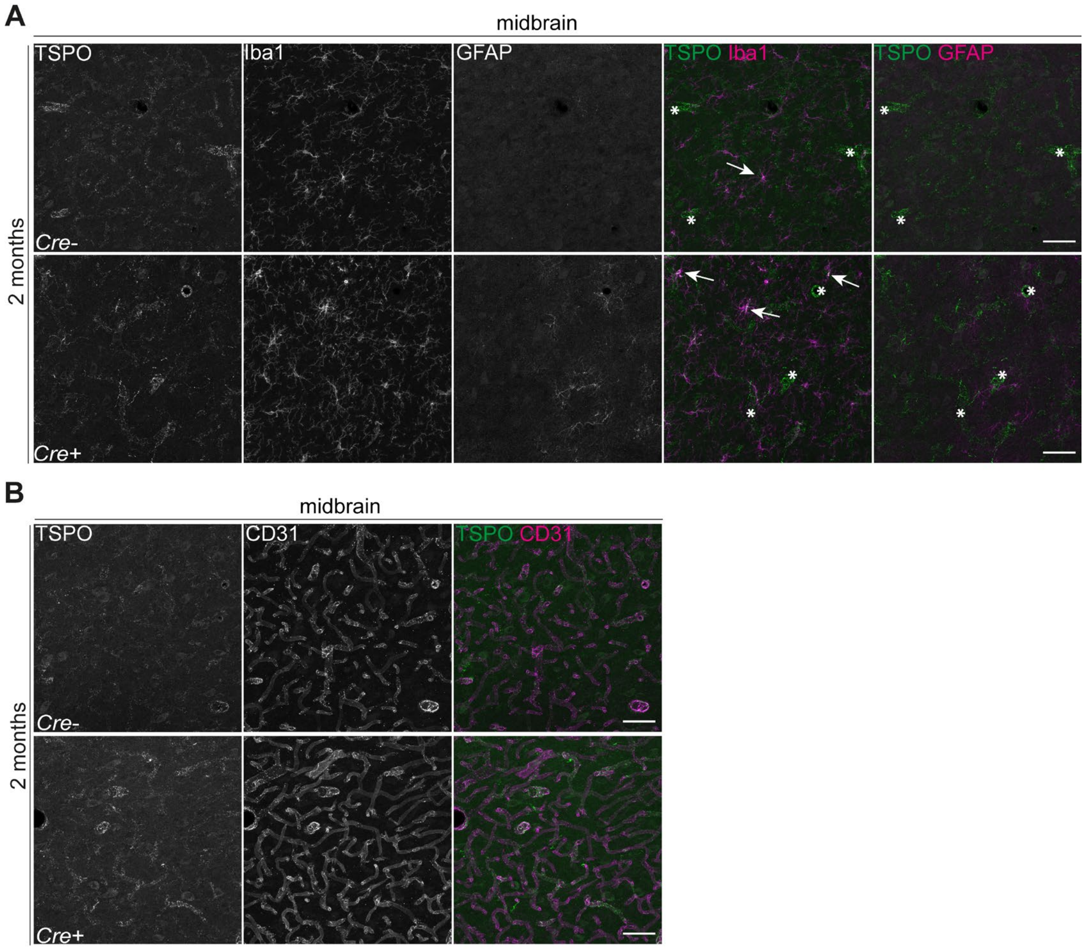

Figure 31. TSPO is mainly expressed in endothelial cells and in microglia in *Cre*- and *Cre*+ mice at 2 months of age. A-B Immunohistochemical analysis of the midbrain of *Cre*- and *Cre*+ mice at 2 months reveals that TSPO (green) mainly localises within Iba1-positive microglia (magenta, white arrows) and not within GFAP-positive astrocytes (magenta) in *Cre*- and *Cre*+ mice. TSPO is additionally detected in Iba1- and GFAP-negative cells (asterisks). Scale bars: 50 µm. **B** Immunostaining using antibodies against TSPO (green) and the endothelial cell marker CD31 (magenta) reveals localisation of TSPO within endothelial cells in *Cre*- and *Cre*+ mice at 2 months of age. Scale bars: 50 µm.

Comparing the TSPO uptake of *Cre*- and *Cre*+ mice at 11 months revealed highest difference of TSPO uptake in the midbrain and brainstem region and less pronounced changes in the cerebellum in *Cre*+ mice (Figure 32A). This result is in line with CD68 immunostainings of *Cre*+ mice at 12 months of age (Figure 29B), supporting a region-specific vulnerability of microglia upon loss of NPC1. In order to validate that TSPO-PET signal is specific for microglia, a scRadiotracing was performed [258]. After injecting the TSPO tracer, microglial (CD11b-positive cells) and astrocytic (ACSA-2-positive cells) cell populations were isolated and the radioactivity within the sample was measured and normalised to the cell number. *Cre*+ microglia showed the highest increase in TSPO

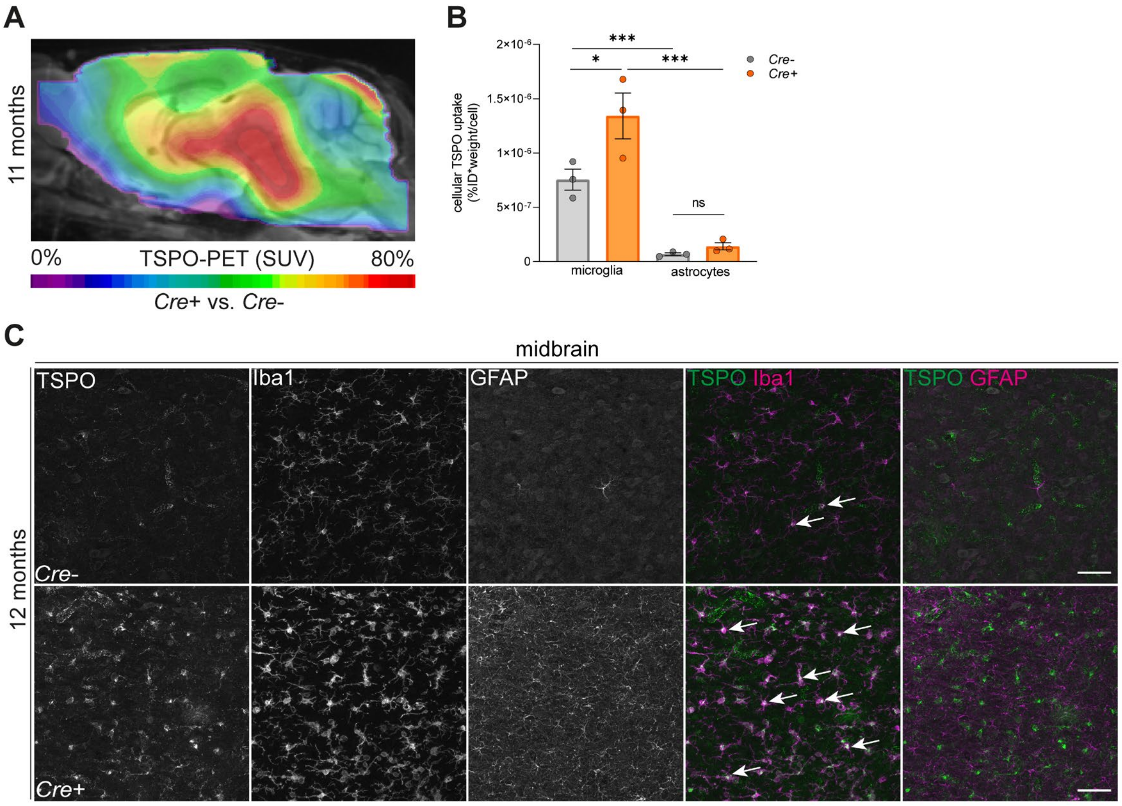

Figure 32. TSPO-PET SUV increase is mainly driven by microglial tracer uptake. A Percentage difference of TSPO-PET (SUV) between *Cre*+ and *Cre*- mice at 11 months of age, reveals high TSPO uptake in brain regions like the midbrain. **B** Analysis of cellular TSPO tracer uptake in 11 months old mice. Upon *in vivo* injection of the TSPO-PET tracer and magnetic cell separation, the radioactivity of each samples was measured. Cell count was determined using flow cytometry. After calculation of radioactivity per single cell (normalised to injected dose (ID) and body weight (BW)) in each sample, *Cre*+ microglia show significantly higher TSPO tracer uptake when compared to *Cre*- microglia. In general, microglia show far higher single cell TSPO tracer uptake when compared to astrocytes. A one-way ANOVA with Turkey's multiple comparison test was performed with n = 3 for *Cre*- and *Cre*+ (ns = not significant, $^{**}p < 0.01$, $^{***}p < 0.001$). **C** Immunohistochemical analysis of the midbrain of *Cre*- and *Cre*+ mice at 12 months of age reveals that TSPO (green) is highly enriched in Iba1-positive microglia (magenta, white arrows) and not in GFAP-positive astrocytes (magenta) of *Cre*+ mice. Scale bars: 50 µm.

tracer uptake per cell, when compared to *Cre*- microglia and astrocytes (from each, *Cre*- and *Cre*+ mice; Figure 32B). This is in line with immunohistochemical analysis of TSPO which revealed high enrichment of TSPO in Iba1-postive cells (Figure 32C). Of note, also under non-pathological conditions, the TSPO tracer was specifically enriched in microglia (Figure 32B), demonstrating the specificity of the TSPO tracer for microglia.
In summary, these results show that loss of NPC1 is sufficient to trigger a massive microglial activation.

3.12 Loss of NPC1 in Microglia Drives Brain Dyshomeostasis

Previous results showed that microglial activity is prominent throughout the brain with certain brain regions being more affected (i.e. the midbrain in contrast to the cerebellum (Figure 29B and 32A). Interestingly, *Npc1*$^{-/-}$ mice showed the highest microglial reactivity in the cerebellum (Figure 9B) that is likely potentiated due to Purkinje cell loss [146]. Given that the cerebellum is not a hotspot region of microglial reactivity in *Cre*+ mice suggests that Purkinje cells are not affected by the loss of NPC1 in microglia, but rather, as shown earlier, vulnerable due to its cell-autonomous loss of NPC1 [150]. Indeed, immunostainings did not reveal any loss of Purkinje cells (Calbindin) in *Cre*+ mice at 7 or 12 months of age (Figure 33A and B).

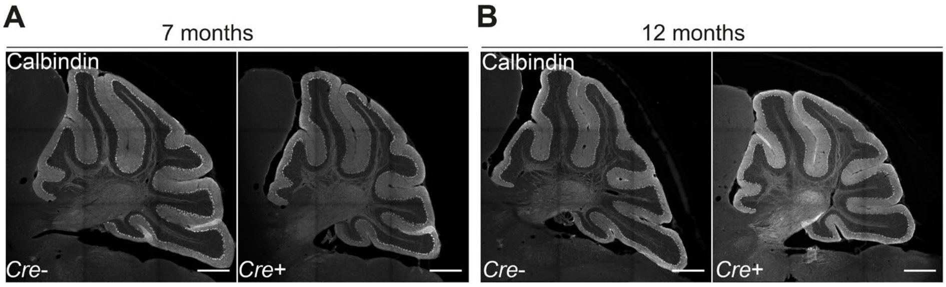

Figure 33. Specific loss of NPC1 in microglia does not affect Purkinje cell survival. A-B Immunohistochemical analysis of Purkinje cells (immunostained with Calbindin, white) in 7 months (**A**) and 12 months old (**B**) *Cre*- and *Cre*+ mice reveals intact Purkinje cell layer in *Cre*+ mice. Scale bars: 500 µm.

In order to further explore the heterogenous region-specific microglial activation upon loss of NPC1, the proteome of the cerebellum and the rest of the brain (brain w/o cerebellum) from 12 months old *Cre*- and *Cre*+ mice were analysed via MS analysis. In agreement with previous results, MS analysis revealed less significant changes in the cerebellum (Figure 34A) in line with less significant altered GO enrichment clusters (Figure 34B).

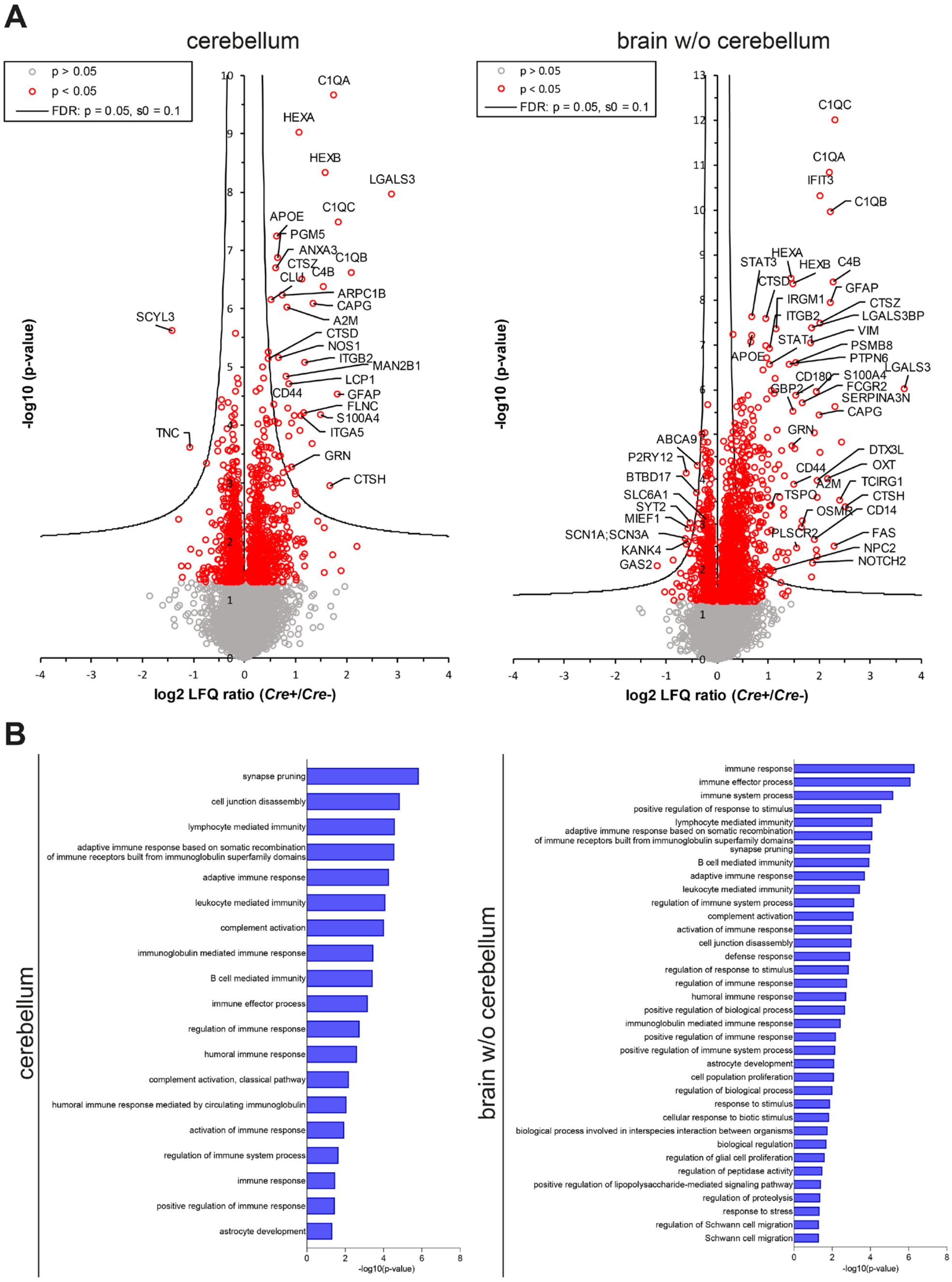

Figure 34. Brain proteomics displays broad changes in *Cre*+ mice which are region-specific. **A** Left hemisphere without the cerebellum (brain w/o cerebellum) and the left cerebellum of 12 months old *Cre*- mice (n = 7 for cerebellum; n = 6 for brain w/o cerebellum) and *Cre*+ (n = 6 for cerebellum and brain w/o cerebellum) were subjected to MS analysis. The average log2 transformed LFQ ratio between *Cre*+ and *Cre*- brain tissue is plotted against the negative log10 transformed p-value. The threshold for the false discovery rate (FDR) is depicted in hyperbolic curves. Significantly changed proteins ($p < 0.05$) are depicted with red circles, while proteins which are not changed significantly are depicted with grey circles. **B** GO enrichment analysis of the brain proteome. Significantly altered GO enrichment clusters of the cerebellum and of the brain w/o cerebellum of 12 months old *Cre*- and *Cre*+ mice are plotted against the negative log10 transformed p-value. Significantly changed proteins (adjusted p-value < 0.05) with a log2 fold change ± 1.5 were analysed.

Of note, most significant changes were linked to microglial endo-lysosomal function and DAM proteins (NPC2, GRN, CTSD, APOE, and galectin-3; LGALS3) and complement factors (complement component 1 q subcomponent subunit A – C (C1QA, C1QB, C1QC), complement C4-B; C4B). In line with increased levels of complement factors in *Cre*+ mice, the GO enrichment cluster "synaptic pruning" was significantly altered (Figure 34B). Interestingly, I could detect increased TSPO in the MS analysis of the brain w/o cerebellum (Figure 34A), while TSPO was not significantly changed in the cerebellum (log2 fold change of 0.315 with p = 0.446), further supporting that the cerebellum is a less vulnerable region upon specific loss of NPC1 in microglia. This result is also in line with the TSPO-PET analysis, where no pronounced differences between *Cre*+ and *Cre*- mice were detected in the cerebellum (Figure 32A). Furthermore, NPC1 was not changed in both datasets (cerebellum: log2 fold change of 0.078 with p = 0.503, brain w/o cerebellum log2 fold change of 0.128 with p = 0.192) strongly supporting that its loss is specific to microglia which are only a minor cellular fraction in the bulk proteomic analysis. Complementary to the increased levels of microglia related proteins in the *Cre*+ brain, GO enrichment clusters addressing immune function were abundantly altered (Figure 34B). Besides microglial proteins, also an increase in the astrocytic marker GFAP as well as significant alteration in the GO enrichment cluster "astrocyte development" were detected in both data sets indicating strong astrogliosis in *Cre*+ mice (Figure 34A and B). Lastly, GO enrichment clusters like "Schwann cell migration" and "regulation of Schwann cell proliferation" were exclusively altered in the data set of the brain w/o cerebellum of *Cre*+ mice, suggesting region-specific oligodendrocyte involvement in brain pathology (Figure 34B). Taken together, my data show that the loss of NPC1 in microglia provokes a striking region-specific immune response that has consequences for other brain cells.

3.13 NPC1 Loss in Microglia Results in Astrogliosis

It has been proposed that activated microglia can induce phenotypic changes in astrocytes [280] which is in line with the brain proteomic analysis which revealed possible astrocytic alterations in *Cre*+ mice (Figure 34). Therefore, astrocytes were examined over time in *Cre*- and *Cre*+ mice using immunohistochemical and PET imaging techniques. At 2 months of age, increased GFAP immunoreactivity was detected in the cortex of *Cre*+ mice, while the midbrain and brainstem region did not show a significant difference in GFAP immunoreactivity (Figure 35A and B). Immunohistochemical analysis of GFAP at 7 and 12 months of age revealed increased GFAP immunoreactivity throughout all analysed brain regions (cortex, midbrain and brainstem) in *Cre*+ mice (Figure 35C-F).

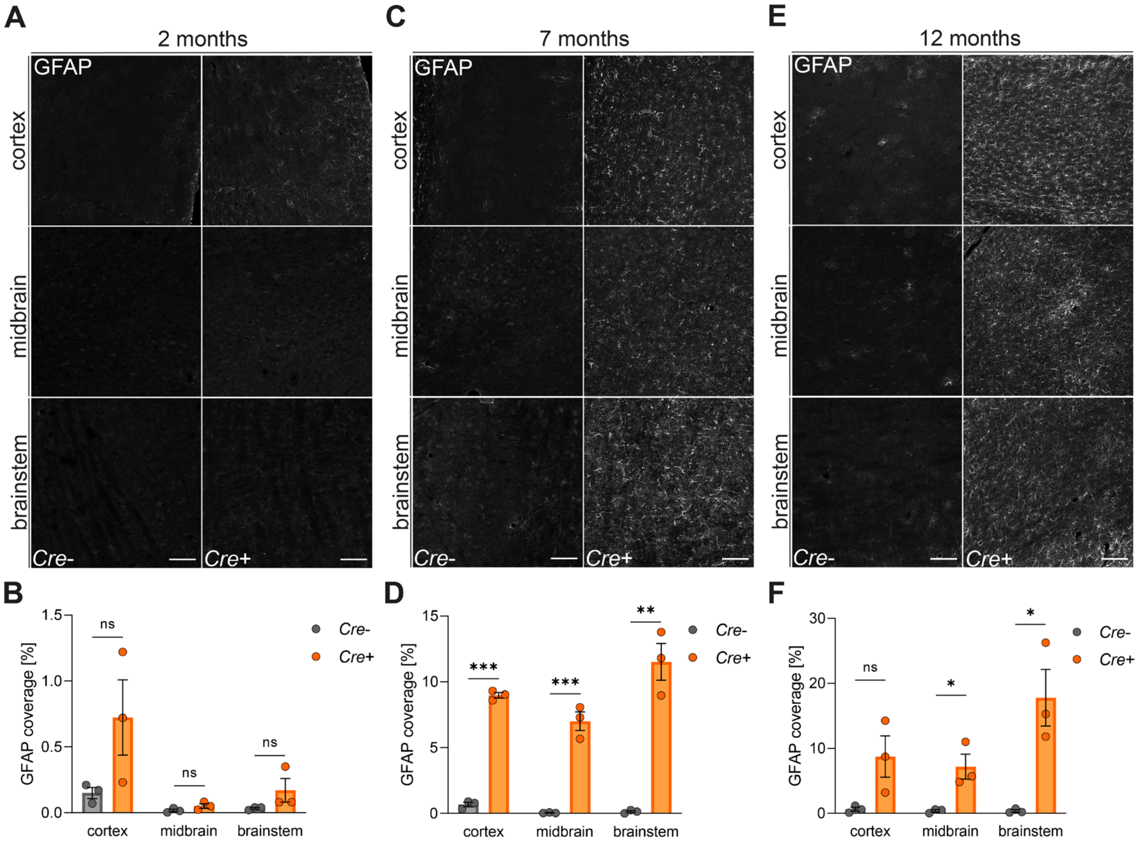

Figure 35. Broad astrogliosis is prominent in *Cre*+ mice at an age of 7 months. A-F Representative images and quantification of immunostainings in 2 months (**A, B**), 7 months (**C, D**) and 12 months old (**E, F**) *Cre*- and *Cre*+ mice using an antibody against astrocyte marker GFAP (white). Scale bars: 100 µm. Increased GFAP reactivity is mostly detected in the cortex at 2 months, while broad GFAP reactivity becomes prominent at 7 months of age. Immunohistochemical analysis was performed using ImageJ. Data is represented as mean ± SEM and an unpaired two-tailed Student's t-test was performed with n = 3 for each condition and timepoint (ns = not significant; *$p < 0.05$; **$p < 0.01$; ***$p < 0.001$).

Astrocytic changes were followed via PET imaging using the PET tracer D2-Deprenyl, which binds to astrocytic MAO-B and has been shown to be upregulated upon different disease pathologies [281]. Using this tracer, a significant increase in D2-Deprenyl-PET signal was detected in the midbrain and brainstem of *Cre*+ mice at an age of 7 months (Figure 36A and B). Comparing the D2-Deprenyl-PET signal of *Cre*+ and *Cre*- mice at 11 months of age revealed highest difference in the midbrain region, similar as it was detected for the microglial TSPO-PET imaging (Figure 32A). In summary, loss of NPC1 in microglia translated to a pronounced astrogliosis, which starts at later stages compared to microglial activation.

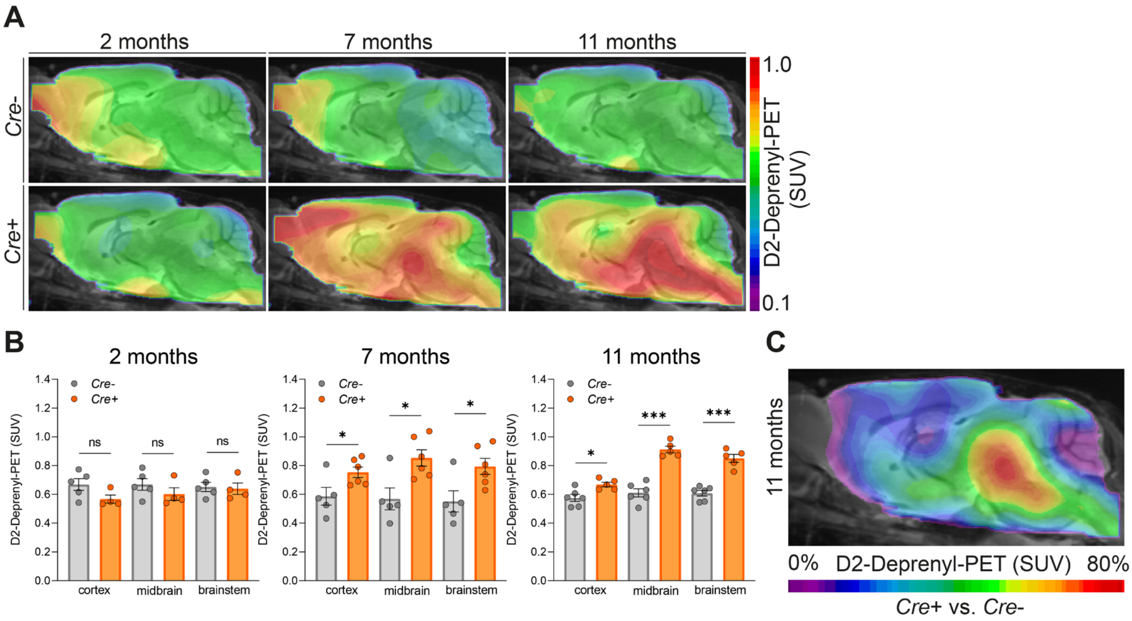

Figure 36. *Cre*+ mice show reactive astrogliosis with pronounced increase of the D2-Deprenyl PET signal in the midbrain and brainstem region. A Sagittal brain sections represent group average images of D2-Deprenyl-PET standardised uptake value (SUV) projected upon a standard MRI T1w atlas. **B** Quantification of astrocytic activity measured by *in vivo* D2-Deprenyl-PET in *Cre*- and *Cre*+ mice at 2, 7 and 11 months of age. Individual D2-Deprenyl-PET SUVs deriving from cortex, midbrain and brainstem VOIs. An unpaired Student's t-test was performed between brain areas for statistical analysis with following sample sizes: *Cre*- n = 5 and *Cre*+ n = 4 for 2 months; *Cre*- n = 6 and *Cre*+ n = 6 for 7 months and *Cre*- n = 5 and *Cre*+ n = 5 for 11 months (ns = not significant, *$p < 0.05$, ***$p < 0.001$) **C** Percentage difference of D2-Deprenyl-PET (SUV) between *Cre*+ and *Cre*- mice at 11 months of age, revealed high D2-Deprenyl tracer uptake in brain regions like the midbrain in *Cre*+ mice.

3.14 Loss of NPC1 in Microglia Does not Cause Broad Hypomyelination

Hypomyelination of the brain is one of the NPC hallmarks [56, 161, 282], which is mainly attributed to NPC1 loss in oligodendrocytes [163]. In agreement with other studies [161, 163, 282], immunostaining using an antibody against CNPase, which is expressed by myelinating oligodendrocytes, revealed a broad hypomyelination in *Npc1*$^{-/-}$ mice at 2 months of age (Figure 37).

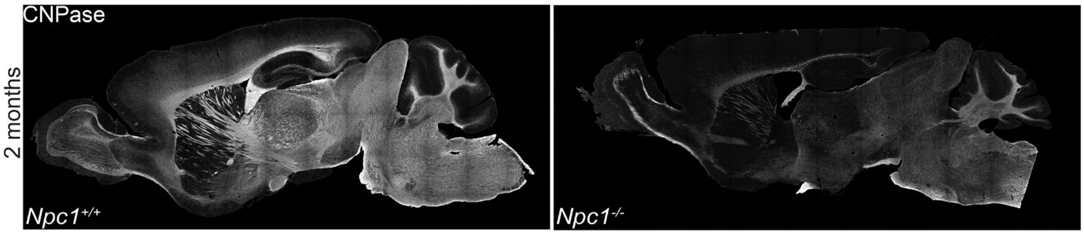

Figure 37. *Npc1*$^{-/-}$ mice display hypomyelination of the brain. A Tile scans of 2 months old *Npc1*$^{+/+}$ and *Npc1*$^{-/-}$ mice. Sagittal brain sections were immunostained against the myelin-associated protein CNPase (white) revealing hypomyelination in *Npc1*$^{-/-}$ mice.

To study possible contribution of NPC1 loss in microglia onto myelin pathology in NPC, I analysed CNPase immunoreactivity in *Cre-* and *Cre+* mice at 2 months and 12 months of age (Figure 38A).

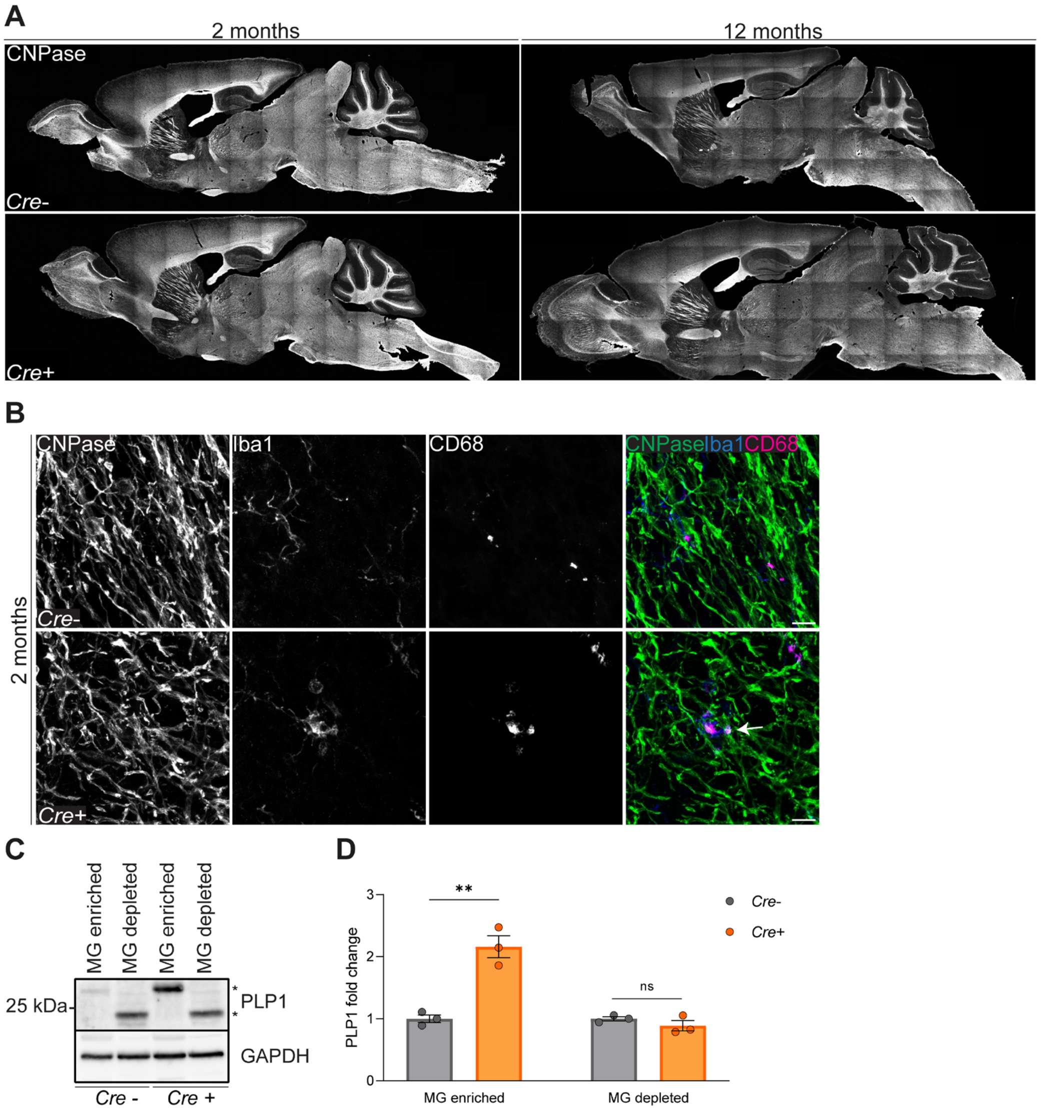

Figure 38. *Cre+* mice do not show a major hypomyelination. A Tile scans of 2 months and 12 months old *Cre-* and *Cre+* mice. Sagittal brain sections were immunostained against CNPase (white) showing no difference in myelination between *Cre-* and *Cre+* mice. **B** Immunostaining of 2 months old *Cre-* and *Cre+* mice using antibodies against CNPase (green), microglia marker Iba1 (blue) and microglial late endosomal/lysosomal marker CD68 (magenta) shows localisation of CNPase within CD68-positive compartments of Iba1-positive microglia in *Cre+* mice (white arrow). Images were acquired in the cortex due to better visualisation of myelinating axons. Scale bars: 10 µm. **C** Representative immunoblot of myelin-associated protein PLP1 in microglia enriched fraction (MG enriched) and microglia depleted fraction (MG depleted) of 2 months old *Cre-* and *Cre+* mice reveal different molecular weights of PLP1 in microglia and other brain cells (*). **D** Quantification of PLP1 in MG enriched fraction and MG depleted fraction shows increased levels of PLP1 in *Cre+* microglia, while PLP1 levels do not change in the MG depleted fraction. GAPDH was used as loading control and protein levels were quantified by densitometry (ImageJ). Values were normalised to *Cre-* and are represented as mean ± SEM. An unpaired two-tailed Student's t-test was performed (ns = not significant; **$p < 0.01$).

Immunohistochemical analysis revealed no differences in CNPase immunoreactivity between *Cre*- and *Cre*+ at 2 and 12 months of age, suggesting no major disturbances in oligodendrocytes maturation and overall myelination of the brain.

Nevertheless, NPC1 loss in microglia might affect fine-tuning of myelination considering the altered phagocytic function of NPC1-deficient microglia (Figure 13) as well as their accumulation of myelin in late endosomes/lysosomes (Figure 14 and 15). Indeed, immunohistochemical analysis revealed CNPase-positive structures within CD68 compartments (white overlay in the merge image) of Iba1-positive microglia in *Cre*+ microglia (Figure 38B). Furthermore, western blot analysis of another myelin associated protein PLP1 revealed increased PLP1 levels in *Cre*+ microglia, while no major change was detected in the microglia depleted fraction (Figure 38C and D). Additionally, the MS analysis of *Cre*+ microglia further validated increased myelin accumulation due to increased levels of MBP (Figure 23D). Taken together, NPC1-deficient microglia do not largely impair the myelination process, but more subtle myelination defects can not be excluded.

3.15 Loss of NPC1 in Microglia Leads to Neuronal Pathology

Microglia have pivotal roles in neuronal homeostasis, being involved in neurogenesis, synaptic pruning, synaptic plasticity and preventing excitotoxicity [182]. Impaired microglial function might cause neuronal dysfunction as it was already suggested by Badimon *et al.* [186]. Neuronal pathology is a prominent hallmark in NPC including axonal swellings and neuronal loss [283, 284]. Therefore, I analysed neuronal phenotypes in a spatiotemporal manner. First, I analysed axonal pathology by immunohistochemistry using an antibody against APP, which accumulates within axonal swellings [285]. Immunohistochemical analysis displayed accumulation of APP in 12 months old *Cre*+ mice (Figure 39), revealing the presence of axonal swellings.

Using another immunohistochemical marker for axonal integrity, the neurofilament heavy chain (NF200) [286], I confirmed the presence of axonal swellings in midbrain, brainstem and cortex (Figure 40A). Of note, axonal swellings were most pronounced in the midbrain region (Figure 40A). Furthermore, axonal pathology translated into significant increase of NF-L, a biomarker for neurodegeneration [287], in serum of 12 months old *Cre*+ mice as assessed by ELISA (Figure 40B), suggesting severe neuronal injury in *Cre*+ mice.

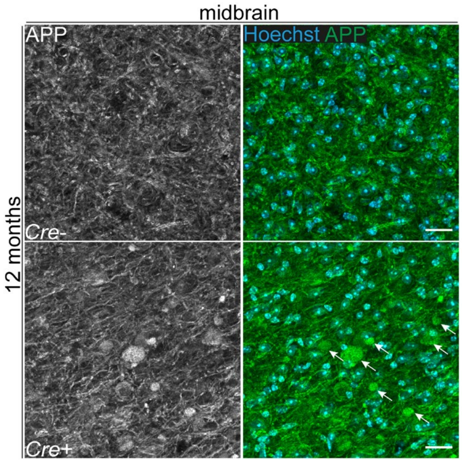

Figure 39. NPC1 deficiency in microglia provokes neuronal pathology. Immunostainings of the midbrain using an antibody against APP (green) reveals accumulation of APP in *Cre*+ mice at 12 months of age (white arrows). Nuclei were stained with Hoechst (cyan)**.** Scale bars: 20 µm.

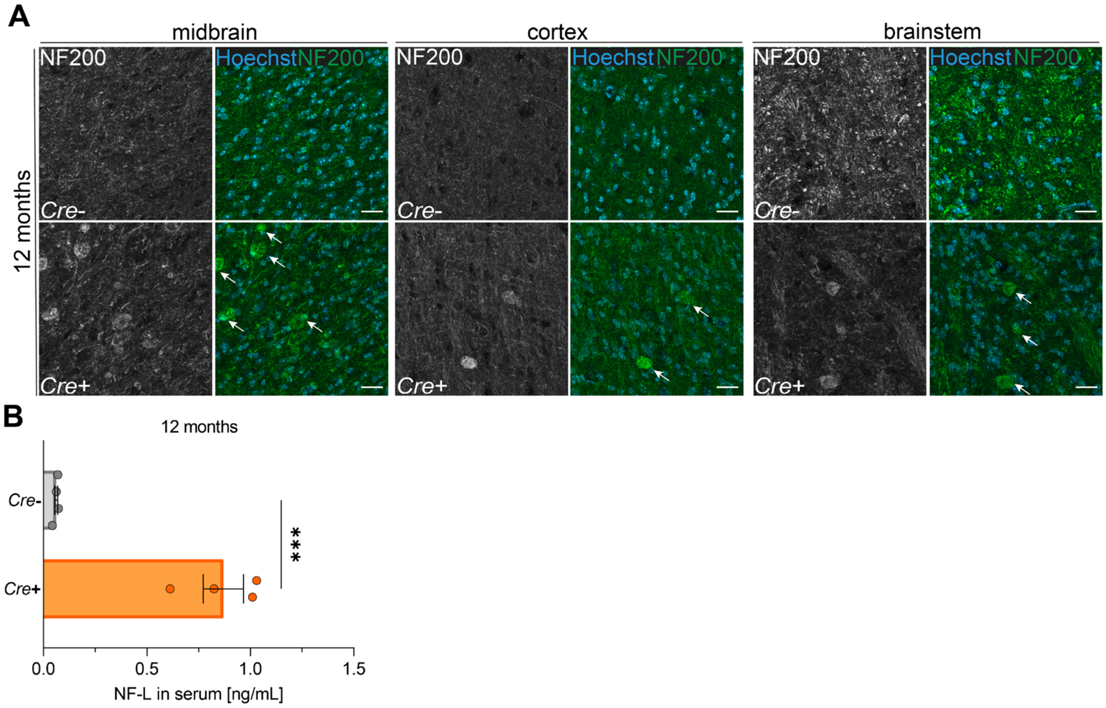

Figure 40. Axonal pathology correlates with NF-L increase in blood serum of 12 months old *Cre*+ mice. A Immunostaining of the midbrain, cortex and brainstem using an antibody against neurofilament heavy chain (NF200) reveals accumulation of NF200 in *Cre*+ mice (white arrows) mostly pronounced in the midbrain. Nuclei were stained with Hoechst. Scale bars: 20 µm. **B** Neurofilament-light chain (NF-L) ELISA of serum from 12 months old *Cre*- (n = 4) and *Cre*+ (n = 4) mice shows an increase in NF-L in *Cre*+ mice. Data is represented as mean ± SEM and an unpaired two-tailed Student's t was performed (***$p < 0.001$)**.**

The severe axonal pathology might reflect neurodegeneration. Therefore, I performed immunostainings for the pan-neuronal marker NeuN, which revealed slight differences in neuronal integrity in the cortex between 12 months old *Cre*- and *Cre*+ mice (Figure 41A).

Western blot analysis of pan-neuronal marker NeuN and β3-tubulin of full brain hemispheres revealed only a slight tendency of neuronal reduction (Figure 41B-E). This indicates that there might be a region-specific neuronal susceptibility. Notably, Purkinje cells were not affected in this mouse model (Figure 33), supporting that other neuronal populations may be more vulnerable to the loss of microglial function triggered by depletion of NPC1. In summary, axonal injury and limited neuronal loss are provoked in *Cre*+ mice.

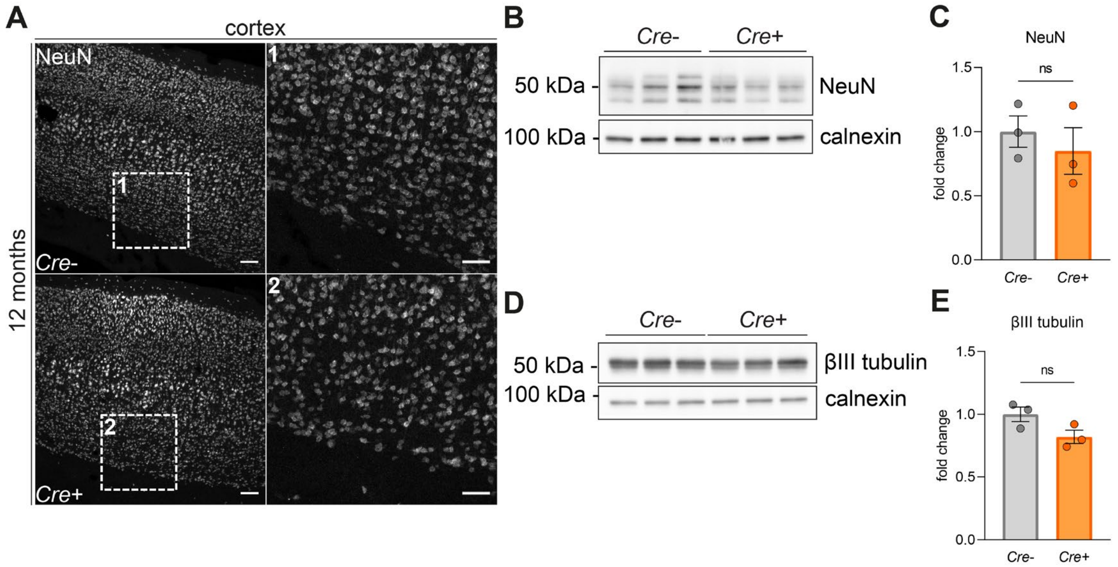

Figure 41. *Cre*+ mice show a low degree of neurodegeneration at 12 months of age. A Immunostaining of the cortex using an antibody against the pan-neuronal marker NeuN (white) reveals loss of neuronal integrity mostly pronounced in the cortical layer VI in *Cre*+ mice. Number 1 and 2 represent zoom-ins from cortical layer VI. Scale bars: left panel (100 µm) and right panel (50 µm). **B-E** Western blot analysis of the pan-neuronal marker NeuN and β3-tubulin of full brain hemispheres from 12 months old *Cre*- (n = 3) and *Cre*+ (n = 3) mice. Representative immunoblots (**B, D**) and the corresponding quantification (**C, E**) reveal no significant loss of pan-neuronal markers in *Cre*+ mice. Calnexin was used as loading control and proteins were quantified by densitometry (MultiGauge). Values were normalised to *Cre*- and are depicted as mean ± SEM. An unpaired two-tailed Student's t-test was performed (ns = not significant).

The presence of axonal swellings implies neuronal dysfunction. In order to analyse neuronal function in *Cre*+ mice, FDG-PET imaging was performed. Glucose hypometabolism has been linked to dysfunctional neurons and neurodegeneration [288]. Decreased FDG-PET was detected at the age of 7 months in *Cre*+ mice (Figure 42A and B). This result indicates neuronal dysfunction already at this pathological stage.

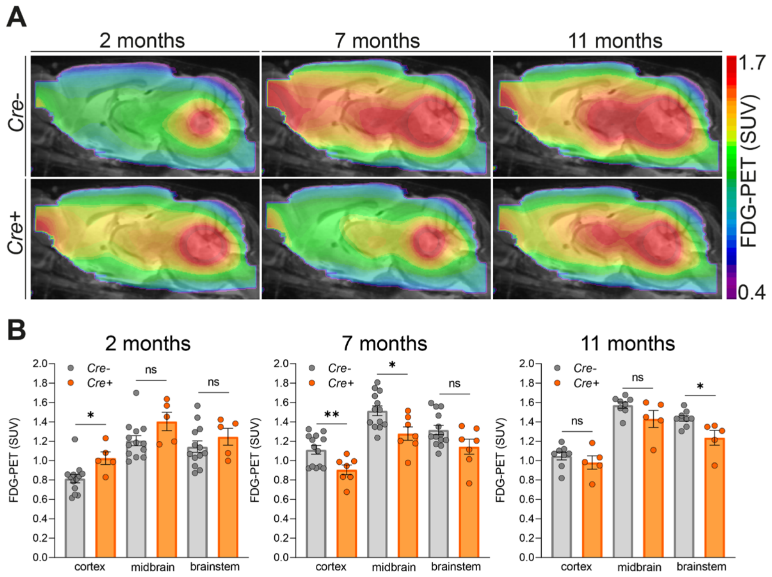

Figure 42. *Cre*+ mice show reduced FDG-PET metabolism at 7 months of age. A Sagittal brain sections display group average images of FDG-PET standardised uptake value (SUV) projected upon a standard MRI T1w atlas. **B** Quantification of glucose metabolism measured by *in vivo* FDG-PET in *Cre*- and *Cre*+ mice at 2, 7 and 11 months of age. Individual FDG-PET (SUV) values deriving from cortex, midbrain and brainstem VOIs. An unpaired Student's t-test was performed between brain areas for statistical analysis with following sample sizes: *Cre*- n = 14, *Cre*+ n = 5 for 2 months, *Cre*- n = 13, *Cre*+ n = 7 for 7 months and *Cre*- n = 8, *Cre*+ n = 5 for 11 months (ns = not significant, *p < 0.05, **p < 0.01).

In agreement with the FDG-PET, immunostainings of NF200 validated that axonal swellings were already present at 7 months in cortex, midbrain and brainstem of *Cre*+ mice (Figure 43A).

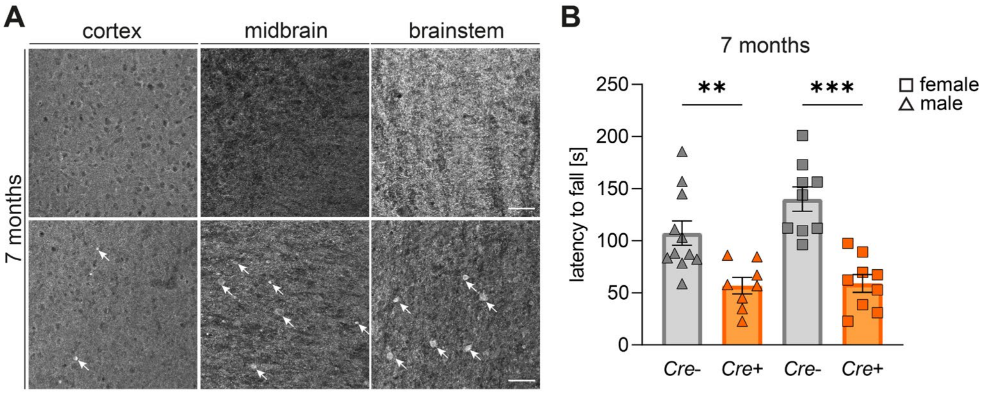

Figure 43. Axonal swellings and behavioural phenotypes are prominent in *Cre*+ mice at 7 months of age. A Immunostaining of the cortex, midbrain and brainstem using an antibody against neurofilament heavy chain (NF200) reveals accumulation of NF200 (white arrows) in *Cre*+ mice already at 7 months of age. Scale bars: 50 µm. **B** Motor function and coordination of 7 months old *Cre*- (n = 20) and *Cre*+ (n = 17) female and male mice was tested using the rotarod test. *Cre*+ mice show worse performance in this test. Data is represented as mean ± SEM and a one-way ANOVA with Tukey's multiple comparisons test was performed (**p < 0.01, ***p < 0.001).

Concomitantly with the neuronal pathology, *Cre*+ mice started to develop behavioural phenotypes such as slower movements or reduced escape reflex. To examine motor function, a rotarod behavioural test was performed. This test revealed worse performance of 7 months old *Cre*+ mice on the rotarod, indicating motor deficiencies (Figure 43B). In summary, the depletion of NPC1 in microglia triggered neuronal susceptibility and motor deficits, supporting the key function of microglia in maintaining neuronal homeostasis.

4. Discussion

Neuroinflammation is a prominent hallmark of NPC, with microglia phenotypic changes being among the earliest pathological alterations [167, 198]. Nevertheless, NPC1 function in microglia and their contribution in NPC progression have not been elucidated. Therefore, this thesis investigated the function of microglia in NPC. My results revealed that the loss of NPC1 in microglia is sufficient to drive microgliosis followed by astrogliosis and neuronal pathology highlighting the importance of NPC1 function in microglia for brain homeostasis. Microglial function and homeostatic phenotype are heavily compromised by the loss of NPC1 in a cell-autonomous manner. NPC1-deficient microglia display proteomic alterations in late endosomal/lysosomal homeostasis accompanied by functional impairments. I characterised a specific lipid trafficking dysfunction in NPC1-deficient microglia, where lipids predominantly accumulate in MVBs while lysosomes are proteolytically active. The lipid trafficking dysfunction results in deficient turnover of endocytosed myelin into CEs and further processing into lipid droplets. Furthermore, I demonstrated that mouse microglial phenotypes are partially recapitulated by PBMC-derived macrophages from NPC patients, suggesting severe alterations in the myeloid linage upon NPC1 dysfunction. Concludingly, microglia have to be considered for therapeutic targeting to modify the NPC progression.

4.1 Cellular Consequences of NPC1 Loss in Microglia

4.1.1 NPC1 Deficiency Drives Lipid Accumulation in MVBs

Unesterified LDL-derived cholesterol accumulates in late endosomes/lysosomes upon dysfunction of NPC1 [46]. Late endosomes and lysosomes are difficult to distinguish via immunofluorescence techniques, since lysosomal markers like LAMP1 are not exclusively expressed by degradative lysosomes but also visualise late endosomes, amphisomes, and MVBs [289, 290]. These technical difficulties are reflected by the discrepancies between different studies defining cholesterol accumulation in NPC within late endosomes [291-294] or within lysosomes [96, 111, 118, 274, 295]. In this study, I distinguished late endosomes from lysosomes using EM analysis as well as a lysosomal trafficking assay. Notably, I found a decrease in lysosomal number in NPC1-deficient microglia and pronounced accumulation of late endosomes/MVBs saturated with undegraded lipid substrates. Supported by a lysosomal trafficking assay, I showed that myelin does not reach the lysosome, but accumulates within MVBs.

Along these lines, the proteome and lipidome of all NPC1-deficient microglia datasets favour alterations in MVBs. The proteomic analysis of NPC1-deficient microglia revealed decreased levels of RAB5, a marker for early endosomes, and increased levels of RAB7, a marker for late endosomes, indicating an expansion of late endosomal compartments [14]. Furthermore, CD63, a membrane protein enriched in ILVs [15], was one of the most abundantly changed protein in all NPC1-deficient microglia proteomes. In parallel, BMP, which is predominantly found in ILVs [15], showed the highest abundance in the lipidomic analysis of NPC1-deficient microglia, further supporting an enrichment of ILVs. Alterations of MVBs in NPC agrees with several studies reporting increased numbers of MVBs upon treatment with the NPC1 inhibitor U18666A or upon NPC1 deficiency [147, 291, 296, 297]. Therefore, NPC1 seems to execute important functions in cholesterol homeostasis at the level of late endosome/MVBs. In fact, it has been postulated that NPC1 is mainly expressed in late endosomes [298, 299]. In parallel, cholesterol is predominantly enriched in MVBs, suggesting an important role of NPC1 in cholesterol homeostasis in MVBs rather than in lysosomes [15, 294, 298-301]. Indeed, it has been shown that NPC1 is involved in the cholesterol transport from late endosomes to the plasma membrane via CD63 [87, 302]. Moreover, MVB-ER MCSs are mediated by NPC1 [77], favouring cholesterol egress independent from lysosomes.

MVBs are a key endosomal compartment in cholesterol homeostasis underscored by the strong interplay between cholesterol and BMP at the level of MVBs [15]. Indeed, depleting cholesterol using MβCD results in reduced levels of BMPs [209]. Additionally, it has been reported that increasing levels of BMP seems to be beneficial and reduces cholesterol burden in NPC1-deficient cells [303-305] and could thus be a compensatory mechanism. Along these lines, Ilnytska *et al.* postulated that enrichment of BMPs induces cholesterol egress through exocytosis [303], and accordingly, increased levels of di-22:6-BMP are found in urine of NPC patients [306]. Not much is known about the biosynthetic pathway of BMP, but it has been postulated that phosphatidylglycerol (PG) is converted into lysophosphatidylglycerol (LPG) via phospholipase A2 (PLA2), and subsequently, converted into BMP by a yet unknown enzyme [303, 307]. Accordingly, reduced levels of PG (i.e. PG(16:0_18:1)) and increased levels of BMPs were detected in my lipidomic analysis of NPC1-deficient microglia which might reflect increased biosynthesis of BMP to correct for cholesterol dyshomeostasis.

MVBs constitute an important sorting hub [15]. Therefore, loss of NPC1 could provoke disturbances in cargo trafficking conducted by MVBs. Along these lines, I have shown that the trafficking of the lipid substrate myelin to lysosomes is impaired and myelin accumulates in MVBs. In contrast, trafficking of protein substrates like fibrillar Aβ, EGFR or DQ-BSA to the lysosome was not compromised. These data suggest that there might be a distinct trafficking machinery for protein and lipid cargos at the level of MVBs in microglia. Indeed, it has been shown that MCS between EGFR-negative MVBs and the ER are reduced upon NPC1 loss, while MCSs between EGFR-positive MVBs and the ER are not altered, highlighting different classes of MVBs [77]. The sorting of cholesterol/lipid-laden endosomes or ILVs might be dependent on NPC1 function. There are several tethering factors which facilitate MCSs between late endosomes/lysosomes and other organelles like annexin A6 (ANXA6), STARD3, oxysterol-binding protein-related protein 1 (ORP1L) and among them NPC1, which might play an important role in the tethering of cholesterol-laden endosomes with the ER [292, 308].

4.1.2 Lipid Trafficking Dysfunction Affects Massively Lipid Metabolism and Cellular Function in NPC

The lipid trafficking dysfunction further translates into impaired formation of CE-rich lipid droplets. This is in line with other studies reporting decreased levels of CEs in NPC patients, especially in patients with a severe infantile disease progression [309, 310] and CE has been postulated as a biomarker for NPC [311].

The depletion of CEs indicates that endocytosed cholesterol does not reach the ER where ACAT1 converts excessive cholesterol into CE [78]. Cholesterol load of the ER constitutes another important signalling mechanism in lipid homeostasis. Cholesterol depletion at the ER initiates the transcription of lipogenic genes (i.e. enzymes involved in the mevalonate pathway for cholesterol biosynthesis or cholesterol uptake (i.e. LDLR)) through the transcription factor SREBP [88]. My data suggests that cholesterol is not reaching the ER in NPC1-deficient microglia, and thereby, initiates a constitutive SREBP signalling as suggested by others [312]. Conclusively, cholesterol biosynthesis might be increased in order to compensate for cholesterol depletion from other organelles like the ER, Golgi or the plasma membrane [103-105].

The mevalonate pathway serves as a pool of lipid precursors (i.e. farnesyl pyrophosphate ; FPP) for different lipids such as cholesterol or coenzyme Q10 [313]. In fact, proteomic analysis of NPC1-deficient microglia revealed increased levels of FDPS, a key enzyme in FPP synthesis, and DHCR [314], a key enzyme involved in cholesterol synthesis, supporting the hypothesis that cholesterol synthesis is increased despite its overload in late endosomes/MVBs. This condition might further affect the metabolism of other lipids. Indeed, I detected significantly decreased amounts of coenzyme Q10 in line with decreased expression of an enzyme involved in coenzyme Q10 biosynthesis (GGPS1 [315]). Moreover, SRD5A3, an enzyme involved in the biosynthesis of dolichol from FPP was significantly increased, in line with reported dolichol increase in NPC [316]. Dolichol has an important role in protein glycosylation at the ER [317], since alterations in dolichol levels affect protein glycosylation [318]. Increased levels of dolichol may contribute to the reported difference in glycosylation pattern upon NPC1 dysfunction [319, 320].

Furthermore, I reported a decrease in TGs, in agreement with other studies [321], as well as DG and phospholipids. In contrast, proteomic analysis of NPC1-deficient microglia revealed a significant increase or no change of ACACA, which catalyses the first rate-limiting step in the *de novo* fatty acid biosynthesis important for the pool of DG, TGs and phospholipids. Along these lines, reduced levels of acetyl-CoA, the precursor for *de novo* fatty acid synthesis, have been reported in *Npc1*$^{-/-}$ cerebellum [322], suggesting that *de novo* synthesis is blocked due to substrate depletion. In fact, acetyl-CoA might be fuelled into the mevalonate pathway for cholesterol synthesis, since blockage of this pathway restored TG levels in NPC [321]. Taken together, the proteomic and lipidomic study of NPC1-deficient microglia revealed that lipid metabolism is heavily compromised due to cholesterol accumulation in MVBs.

The defective turnover of excessive cholesterol into CEs might cause cellular burden in terms of ER or mitochondrial stress [323]. It has been shown that glial cells accumulate lipid droplets under stress conditions [324, 325]. Indeed, I detected distinct lipid droplets in *Cre*- microglia (heterogenous white/black appearance) different of those found in *Cre*+ microglia (homogenous black appearance) under myelin-fed conditions. During the EM staining procedure, osmium tetroxide was used, which forms a black reduction compound in presence of double carbon-carbon bonds, and thereby, stains unsaturated lipids [326]. Conclusively, lipid droplets in *Cre*+ microglia are enriched in unsaturated fatty acids and depleted in CEs, compared to *Cre*- microglia that efficiently process excessive cholesterol into CEs. It is known that cholesterol dyshomeostasis and lipid storage can impact mitochondrial function and increase oxidative stress [327]. Under oxidative stress, polyunsaturated fatty acids (PUFAs) are shielded from ROS by sequestering these PUFAs into lipid droplets, and thereby, preventing peroxidation of lipids or sequestering already peroxidised lipids [328-331]. Along these lines, it has been shown that NPC1-deficient cells acquire increased ROS concentrations and enhanced lipid peroxidation [123, 332]. The proteomic analysis of NPC1-deficient microglia revealed strong increase in proteins involved in the antioxidant process mediated by glutathione (i.e. glutathione-S-transferases or glutathione reductase) [333], reflecting increased oxidative stress. In parallel, the lipidomic analysis of NPC1-deficient microglia revealed significant decrease of the antioxidant coenzyme Q10 [278] suggesting less buffering of oxidative stress which, in turn, might lead to increased lipid droplet formation of PUFAs. Noteworthy, decreased levels of coenzyme Q10 were detected in NPC patient serum, highlighting its significance in NPC [334]. Along these lines, increased numbers of microglia harbouring TG-rich lipid droplets have been found in a *Grn*$^{-/-}$ mice, a mouse model of the LSD neuronal ceroid lipofuscinoses (NCL) [324]. In this study, pathway analysis revealed that 'ROS production' is associated with these lipid droplet-enriched microglia. This certain microglia phenotype might be reflected by several LSDs, since mitochondrial dysfunction is a common phenotype in LSDs [335]. In summary, the block in cholesterol trafficking that I detected in NPC is a likely trigger of oxidative stress, visualised by the presence of lipid droplets enriched in unsaturated fatty acids in *Cre*+ microglia.

4.1.3 Lysosomes are Proteolytically Active in NPC1-deficient Microglia

NPC disease is classified as a lysosomal storage disorder, suggesting main catabolic burden at the level of the lysosomes. Endocytosed substrates which are dedicated for degradation, traffic through the endolysosomal system [6]. My data suggest that trafficking of protein substrates, like fibrillar Aβ, EGFR and DQ-BSA, as well as their catabolism are not impaired. The lysosome is equipped with lysosomal acidic hydrolases, which degrade different types of cargo including protein and lipid substrates [22]. Here, I reported intact degradation of several protein substrates like EGFR or fibrillar Aβ implying preserved function of lysosomal proteases. Along these lines, normal maturation of cathepsins, which is dependent on lysosomal pH and catalytic function, was detected in NPC1-deficient microglia. Accordingly, catalytic function of lysosomal enzymes relies on acidification of lysosomes which is not impaired in NPC [116, 336, 337]. In contrast, Elrick *et al.* reported reduced enzyme activity of CTSB implying impaired proteolysis [116], while my data show intact CTSB maturation and no difference in the degradation rate of EGFR. It remains to be investigated whether this discrepancy can be explained by the different cell types analysed (microglia vs. fibroblasts) or different experimental paradigms. NPC1-deficient cells might display slower endocytic trafficking, as suggested by Ko *et al.* [108]. Substrates dedicated for lysosomal degradation would lag behind which indeed may result in impaired degradation rates when analysing short term paradigms as done by Elrick *et al.*[116]. On the other hand, I reported increased levels of several lysosomal hydrolases like CTSB or CTSD which may contribute to preserved degradation as I observed for EGFR or fibrillar Aβ substrates. Along these lines, the dampened autophagic flux in NPC has been ascribed to lysosomal catalytic dysfunction [114, 116, 303]. My data suggests that the reported build-up of autophagic cargo like p62 is not driven by impaired lysosomal function [116, 303], but rather by impaired fusion events upon NPC1 dysfunction as suggested by others [114, 337].

Besides proteins, also lipids are degraded in the lysosome [30]. I have shown that phagocytosed myelin accumulates in MVBs and is not reaching the lysosome in NPC1-deficient microglia. Therefore, the degradative capacity of lysosomes for lipids was not evaluated, but it seems that lysosomal function is difficult to predict based on the abundance of the catabolic enzymes. As an example, a recent study postulated that NPC1-deficient lysosomes show an impaired lipid degradation as assessed by reduced activity of GALC, a lysosomal enzyme catalysing the degradation of glycolipids [118]. Indeed, increased abundance of galactosylceramides (i.e. GalCer (d18:2/18:0)) were detected in NPC1-deficient microglia, while proteomic analysis revealed no significant change of GALC in pre- and symptomatic *Npc1*$^{-/-}$ microglia, whereas- GALC was significantly decreased in *Cre*+ microglia. This heterogeneous relation of the catabolic enzyme and its corresponding lipid substrate is reflected by further enzymes. HEXA, which catalyses the degradation of glycosphingolipids like GM2, was abundantly increased in NPC1-deficient microglia as well as its substrate GM2. On the contrary to the mentioned catabolic enzymes, GBA, which is involved in the catabolism of glucosylceramides, was reduced in NPC1-deficient microglia. Accordingly, I detected increased levels of glucosylceramides (i.e. GlcCer (d18:2/18:0)). Conclusively, it remains unclear whether increased abundance of certain lipids is driven by impaired turnover or due to increased biosynthesis, or both.

4.1.4 Cholesterol Homeostasis Regulates Microglia Phenotypes and Function

In comparison to neurons, microglia do not only endocytose lipids in terms of LDL-derived cholesterol but phagocytose bulk lipids derived from myelin debris or apoptotic neurons [182]. Thereby, microglia are continuously exposed to high amounts of lipids, underlining the importance of an intact lipid trafficking and catabolism. This point is strengthened by the fact that microglia from different LSDs switch to a similar DAM phenotype, reflecting a tight link between lipid accumulation and DAM signatures [338, 339]. Along these lines, *Npc1*$^{-/-}$ microglia show increased proliferation [199] and phenotypic changes towards activated microglia. The lipidomic analysis revealed a broad lipid dyshomeostasis already at 1-week of age in *Npc1*$^{-/-}$ microglia. In parallel, increased levels of DAM proteins like CD68, CTSD, CTSB, NPC2 and decreased levels of homeostatic proteins like TGFB1 or CX3CR1 were also detected in 1-week old *Npc1*$^{-/-}$ microglia. Releasing the cholesterol block using MβCD reversed microglial phenotypes and lipid trafficking, which suggests a close relation between cholesterol homeostasis and molecular fingerprints of microglia. Interestingly, my lipidomic and proteomic analysis of NPC1-deficient microglia suggest that cholesterol is synthesised by microglia under NPC conditions in order to adjust for depletion of the LDL-derived cholesterol pool, while under physiological conditions, cholesterol synthesis has been largely ascribed to astrocytes [81]. It might be that microglia in general alter their cholesterol metabolism under pathological conditions, which is further supported by the fact that DAM signatures are regulated by the TREM2-APOE axis, both involved in cellular cholesterol metabolism [178, 340]. Furthermore, microglia phenotypes are mainly driven cell-autonomously by the loss of NPC1 in microglia as validated by similar proteomic and lipidomic alterations of *Npc1*$^{-/-}$ and *Cre*+ microglia.

Interestingly, I detected pronounced lipidomic differences between 1-week and 2 months old *Npc1*$^{+/+}$ microglia implying a tight regulation of lipid homeostasis during the vulnerable developmental phase. These lipidomic changes differ from age related changes observed in *Npc1*$^{-/-}$ microglia. During developmental stages, microglia are highly phagocytic since they are actively sculpting the brain parenchyma [182]. This process is dependent on sufficient amounts of energy in terms of ATP, which is faster generated by utilising glycolysis instead of mitochondrial oxidative phosphorylation [341, 342]. Therefore, active microglia might utilise ATP produced by glycolysis and switch to ATP production by oxidative phosphorylation under steady-state conditions, reflected by the increase of coenzyme Q10, a key factor in the mitochondrial oxidative phosphorylation [343]. NPC1-deficient microglia showed reduced abundance of coenzyme Q10, and thereby, might not switch to utilise oxidative phosphorylation (possibly due to mitochondrial dysfunction) and persist in a glycolytic metabolism as shown by Cougnoux *et al.* [200].

Although the DAM phenotype describes underlying molecular changes in microglia which are associated in different neurodegenerative conditions [178, 179], they may differ in their functional outcomes. I have shown that *Npc1*$^{-/-}$ microglia display a DAM phenotype and show an increased phagocytic uptake towards Aβ or myelin. Similar results have been shown upon loss of the lysosomal enzyme GRN in a mouse model recapitulating NCL [338]. In agreement with my results, Reva *et al.* described increased numbers of phagocytic microglia in the postnatal brain of NPC mice [344]. In contrast, microglia from AD mouse models display DAM signatures and exhibit decreased phagocytic clearance of Aβ and thereby contribute to the build-up of extracellular Aβ plaques [195, 345, 346]. These molecular-functional discrepancies highlight the complexity behind microglial phenotypes and the unmet need to expand beyond molecular characterisation of microglial states towards investigation of microglial functional consequences across various neurodegenerative conditions.

Moreover, the brain environment might also influence microglial phagocytic function. Phagocytosis is mediated by expression of so-called “eat-me” signals (i.e. complement factors) by the target cell which are sensed by microglia with their surface receptors (i.e. complement receptors) [347]. During development, phagocytic microglia are prominent due to developmentally occurring cell death [347, 348], supporting the idea that the brain environment also sculps microglial phagocytic activity. This hypothesis is supported by the fact that the phagocytic function of *Npc1*$^{-/-}$ microglia assessed by using inert latex beads does not show any difference compared to *Npc1*$^{+/+}$ microglia [203]. In contrast, my *ex vivo* Aβ phagocytic assay, in which microglia get in contact with brain tissue, revealed increased phagocytic clearance by *Npc1*$^{-/-}$ microglia. As a conclusion, microglia displaying DAM signatures acquire prerequisites for enhanced phagocytosis (increased phagocytic receptors/lysosomal function), but also the brain environment contributes to their net phagocytic activity.

In case of *Npc1*$^{-/-}$ microglia, an increased phagocytic function is counterintuitive since they do not efficiently process phagocytosed lipid substrates like myelin, suggesting that phagocytic mechanisms are uncoupled from lipid homeostasis upon loss of NPC1. SREBP1a is an important transcription factor which regulates lipid metabolism. It’s translocation to the nucleus is inhibited as soon as cholesterol at the ER exceeds 5 mol % [78, 349]. It has been postulated that SREBP1a has an important role in macrophage phagocytosis, since inhibition of SREBP1a results in impaired phagocytosis [350, 351]. In case of NPC1-deficient conditions, SREBP1 amounts are increased [312], indicating a diminished negative feedback control by cholesterol at the ER. Therefore, trafficking dysfunction of cholesterol and its accumulation in MVBs can influence the lipidomic landscape and might affect microglial phagocytic activity. That lipid profiles influence microglial phagocytosis is also illustrated during aging, where accumulation of TG-rich lipid droplets in WT or *Grn*$^{-/-}$ microglia has been associated with reduced phagocytosis [324]. Although *Grn*$^{-/-}$ microglia generally show an increased phagocytic function as demonstrated at the age of 2 months [338], during aging (9 months), they accumulate lipid droplets, and lipid droplet positive *Grn*$^{-/-}$ microglia harbour an impaired phagocytic activity [324]. Taken together, these results suggest that the lipidomic landscape of NPC1-deficient microglia might impact their phagocytic activity.

4.2 Consequences of NPC1 Loss in Microglia on Brain Function

4.2.1 Microglia Intervene Early in NPC

Microglia are highly dynamic and fulfil important functions by monitoring brain homeostasis during the whole life time [182]. As discussed before, microglial phenotype and function is highly dependent on cholesterol homeostasis and NPC1 function. Therefore, it seems not surprising that microglial alterations are among the first phenotypic changes detected in NPC disease [167, 198]. Additionally, pro-inflammatory cytokines were altered in the brain of pre-symptomatic *Npc1*$^{-/-}$ mice [54]. In line with these studies, I reported early and broad microglial activation in a pre-symptomatic stage of *Npc1*$^{-/-}$ mice before neuronal injury was prominent. Accordingly, microglial activation was the first phenotypic alteration detected in *Cre*+ mice, supporting the hypothesis that glial involvement occurs early in NPC. Of note, utilising constitutive Cre expression driven by the *Cx3cr1* promoter, which is already active during embryonic stages [352], assures that NPC1 loss and microglial phenotypic changes occurred already during embryonic and postnatal development in *Cre*+ mice, offering an advantage to study early disease-associated alterations. At this point it is also important to discuss recent insights about the consequences of Cre expression under the *Cx3cr1* promotor. It has been shown that Cre expression alone, when induced during postnatal development using a tamoxifen-inducible Cre line, is sufficient to drive microglial activity and phagocytic alterations [353]. Although I used a different (constitutive) Cre expression line, possible consequences of Cre expression on microglia alterations during development can not be fully excluded.

Notably, the uniform molecular and functional alterations of *Npc1*$^{-/-}$ and *Cre*+ microglia are strongly supporting that microglial phenotypes are driven by the loss of NPC1 rather than by Cre expression. In conclusion, my work shows that microglial activation is an early and undeniable event in NPC pathology.

NPC patients suffer from a progressive neurodegeneration [46]. Especially in brain regions which were affected by neurodegeneration like the cerebellum of symptomatic *Npc1*$^{-/-}$ mice, microglial activation was highly pronounced implying an additive effect of intrinsic microglial activation as well as extrinsic stimuli such as neuronal pathology as suggested by others [178, 195, 354, 355]. This hypothesis is supported by my findings in *Cre*+ mice. Compared to the increased microglial reactivity in the midbrain (where neuronal pathology is more prominent), the cerebellum displayed less pronounced microglial reactivity that correlated with no defects in Purkinje neurons. These results are beautifully aligned with the hypothesis that early microglial activation triggered by the loss of NPC1 initiates a pathological cascade which further drives microglial phenotypes in a feedback loop.

4.2.2 Loss of NPC1 in Microglia Does not Cause Broad Hypomyelination

Hypomyelination is a prominent pathology in NPC [55, 56, 159, 160]. Microglia play an important role in oligodendrocyte development and myelination by phagocytosing OPCs as well as secreting trophic factors to support oligodendrocyte differentiation and myelination [356]. Especially during development, when myelination is occurring, microglia control myelination by phagocytosing myelin sheaths as well as aberrant myelin debris [357-359]. Thereby, microglia are opposed to high amounts of cholesterol. I reported increased phagocytic uptake of myelin but deficiencies in myelin processing into CE-rich lipid droplets in NPC1-deficient microglia. In line with the timing of ongoing myelination [360], I detected reduced amounts of CEs in microglia mostly pronounced in 1-week old *Npc1*$^{-/-}$ mice. Along these lines, it has been shown that myelin processing into lipid droplets is essential for accurate remyelination upon demyelinating conditions [272, 361]. Therefore, microglia might contribute to the hypomyelination in NPC, even though cell-autonomous loss of NPC1 in oligodendrocytes is considered as a major trigger for myelin loss in NPC [162]. Along these lines, cell-autonomous loss of NPC1 in oligodendrocytes already causes demyelination, but the phenotype is faster and more pronounced in *Npc1*$^{-/-}$ mice [163], suggesting that other brain cells may contribute to myelin pathology as well. In *Cre*+ mice, I did not detect obvious hypomyelination, suggestive of oligodendrocyte differentiation into mature myelinating oligodendrocytes. Nevertheless, increased levels of LGALS3, a ligand for TREM2-dependent phagocytosis [362], were detected in *Cre*+ microglia and full brain proteome. Microglia upregulate LGALS3 expression upon demyelinating conditions, which is an important factor for accurate remyelination [363-365]. Therefore, more subtle microglia-mediated myelin disturbances can not be excluded in *Cre*+ mice. Similar results have been shown in a mouse model lacking microglia, in which myelination was occurring independent of microglia function [366]. Of note, distinct demyelination of axons was detected via EM analysis at around 6 months of age in this mouse model. This implies that loss of NPC1 microglia does not cause severe hypomyelination but might be important for fine-tuning of the myelination of neuronal axons.

4.2.3 Microglial Loss of NPC1 Drives Astrogliosis

Besides microgliosis, astrogliosis is a prominent feature in NPC [167, 367], whereas cell-autonomous roles of NPC1 in astrocytes and its contribution to NPC progression are uncertain. There are contradictory studies reporting on the one hand, no detrimental effects upon specific loss of NPC1 in astrocytes [150], while others report beneficial effects on NPC pathology when NPC1 function was rescued in astrocytes [170, 368]. Why the astrocytic phenotype and function are not majorly dependent on NPC1 might be explained by their role in brain cholesterol homeostasis. The circulating cholesterol, packed in high density lipoprotein (HDL)-particles, is mainly derived from astrocytes, which are the main site of cholesterol synthesis under physiological conditions [369, 370]. Loss of NPC1 in astrocytes seems not to affect their cholesterol synthesis neither cholesterol export [371]. Astrocytes might be less dependent on HDL-derived cholesterol uptake as shown in an NPC mouse model *in vivo*, where cholesterol accumulation was less severe in astrocytes compared to neurons [372]. Interestingly, NPC1 has been predominantly found in distal process of astrocytes near synapses [373] and cholesterol accumulation seems to appear rather in processes than in the soma of astrocytes *in vivo* upon NPC1 loss [150, 372]. Combining all of these results drives the hypothesis that NPC1 in astrocytes may be less critical for astrocyte homeostasis, but might fulfil crucial supportive functions for other brain cells. This hypothesis is supported by the fact that specific rescue of NPC1 in astrocytes in an NPC mouse model resulted in beneficial outcomes onto neuronal viability (i.e. less axonal swellings, decreased cholesterol storage, less degenerating neurons) [170].

Considering that microglial activation is one of the earliest phenotypes in NPC, ahead of neuronal death and that specific loss of NPC1 in astrocytes does not translate into astrocytic reactivity [150], implicates that early astrogliosis may be driven by loss of NPC1 in other brain cells such as microglia. My study revealed that NPC1 loss in microglia was sufficient to drive astrocytic reactivity, fully in agreement with a previous publication [367]. Moreover, I detected regional differences in the abundance of GFAP-positive and MAO-B-positive astrocytes (detected by D2-Deprenyl-PET) in *Cre*+ mice. GFAP immunoreactivity was equally increased throughout the brain at late stages in *Cre*+ mice. In contrast, D2-Deprenyl-PET showed the highest increase in the midbrain/brainstem, while less pronounced differences were detected in the cortex at late stages. Putting my data together, NPC1-deficient microglia drive broad astrogliosis as reflected by the increased GFAP expression throughout the brain. However, other pathological mechanisms acquired during aging might additionally contribute to the enrichment of MAO-B-positive astrocytes in specific brain regions like the midbrain of *Cre*+ mice. This result furthermore supports different astrocyte states, similarly as demonstrated for microglia [374, 375]. That activated microglia drive and modulate astrocytic phenotypes is supported by Liddelow *et al.*, where they have shown that activated neuroinflammatory microglia are capable of inducing neurotoxic astrocytes [280]. Further work has to be done to elucidate the mechanistic crosstalk between microglia and astrocytes and which astrocytic populations are reacting to NPC1 loss in microglia.

4.2.4 NPC1-Deficient Microglia Initiate a Pathological Cascade Resulting in Neuronal Pathology

Neurodegeneration is fast progressing in NPC as demonstrated by the massive Purkinje cell loss in *Npc1*$^{-/-}$ mice by the age of 2 months. Cell-specific depletion of NPC1 in Purkinje cells causes Purkinje cell death, while cell-specific depletion in astrocytes does not cause any phenotype. This data pushed the hypothesis that neuroinflammation is a bystander of neurodegeneration and not the cause [146, 150]. However, neuron-specific rescue of NPC1 does not abolish neuroinflammation nor prevents premature death [376, 377], suggesting that crucial cell-autonomous roles of NPC1 in other brain cells contribute to NPC progression. In this thesis, I have shown that loss of NPC1 in microglia occurs ahead of neuronal loss and that NPC1-deficient microglia are sufficient to initiate neuronal pathology in terms of axonal swellings and limited neuronal loss. However, as the neuronal pathology was detected at later pathological stages and occurred in a region-specific manner, I conclude that NPC1-deficient microglia are per se not neurotoxic [203]. Which microglia-stimulated mechanisms drive neuronal pathology and whether this pathological cascade relies on astrocytic changes still remains to be investigated.

Axonal swellings are a prominent phenotype in NPC disease which were mainly attributed to the loss of NPC1 in neurons causing impaired axonal transport [149]. Interestingly, it has been postulated that microglial changes precede axonal pathology in a disease called leukoencephalopathy, which is caused by mutations in the microglial homeostatic marker and key factor in microglial survival CSF1R [378, 379]. These findings support the hypothesis that dysfunctional microglia can drive axonal pathology and thereby contribute to neuronal phenotypes in NPC. Distinct neurons might have different susceptibilities to neuroinflammation as reflected by the fact that Purkinje cells do not show any defect while neurons in the midbrain display axonal injury. On the other hand, NPC1 loss in microglia might have region-specific outcomes due to their heterogeneity in the brain [181]. Indeed, Abellanas *et al.* have postulated that midbrain microglia are in an immune alert state under physiological conditions and secret distinct cytokines upon LPS stimulation [380]. Therefore, NPC1-deficient microglia might display different inflammatory phenotypes in different brain regions, contributing to regional manifestation of the neuronal pathology. This hypothesis would explain that microglia in NPC are anticipated as neither pro-inflammatory nor anti-inflammatory [200]. Transcriptomic studies were performed with microglia isolated from the whole brain tissue, and thereby, includes a mixture of different microglial signatures [200]. Performing transcriptomic analysis on a single-cell resolution would shed light on the microglial heterogeneity in NPC.

Another factor implicated in the development of axonal swellings are increased concentrations of ROS in the brain parenchyma. ROS-induced axonal pathology has been postulated in mice with experimental autoimmune encephalomyelitis mimicking multiple sclerosis conditions as well as in *in vitro* experiments in which ROS triggered axoplasmic calcium disbalances resulting in axonal swellings [381, 382]. It has been already shown that NPC1 dysfunction causes mitochondrial defects and increases ROS production [103, 120-125], which is supported by my lipidomic and proteomic analysis of NPC1-deficient microglia. Coenzyme Q10, a key component in the mitochondrial oxidative phosphorylation and anti-oxidant [383], is significantly downregulated, whereas NADPH oxidase 2 (NOX-2; also termed as CYBB), a ROS producing enzyme, is significantly upregulated in NPC1-deficient microglia. Thereby, NPC1-deficient microglia produce increased levels of ROS, but fail to buffer its excess. Along these lines, microglia-released ROS produced by NOX-2 has been postulated to activate astrocytes, which subsequently release proinflammatory and neurotrophic factors in the context of PD [384]. An increase in MAO-B positive astrocytes was detected by D2-Deprenyl-PET imaging especially in regions affected by axonal pathology like the midbrain. Interestingly, astrocytic MAO-B synthesises ROS, and thereby, might potentiate ROS production in the brain parenchyma and contribute to axonal pathology. In line with this, MAO-B inhibitors have been used to suppress MAO-B-related ROS and revealed a beneficial effect onto neuronal viability in AD and PD mouse models [385-387].

Besides an inflammatory burst or increased release of ROS, microglia might mediate neuronal pathology via extracellular vesicles. The build-up of lipid substrates in NPC1-deficient cells might initiate exocytosis as reflected by increased levels of undigested metabolites in extracellular space like plasma or cerebrospinal fluid similar seen in LSD patients [34]. It has been shown that extracellular vesicles derived from *Npc1*$^{-/-}$ choroid plexus explants induce brain pathology [388]. A similar scenario could be initiated by NPC1-deficient microglia releasing cholesterol via exocytosis [389]. It is well accepted that microglia-derived extracellular vesicles mediate brain pathology as for example shown in a tau mouse model, in which tau is propagated via extracellular vesicles derived from microglia [390]. One interesting finding supports the hypothesis of increased cholesterol secretion. PLIN4, a perilipin which preferentially resides on CE-rich lipid droplets [391], was strongly increased in the proteomic analysis of *Cre*+ brains. Due to the fact that NPC1-deficient microglia are deficient in generating CE-rich lipid droplets, other cells in the brain parenchyma might be overloaded with the released cholesterol, and consequently, store cholesterol in lipid droplets. Therefore, microglia can act on cholesterol homeostasis of other brain cells which can lead to cellular dyshomeostasis, and subsequently, brain pathology.

Neuronal synaptic function is strongly associated with glucose metabolism, and thereby, hypometabolism of FDG indicates neuronal dysfunction [392]. Significant reduction in FDG-PET signal started at an age of 7 months in *Cre*+ mice, in line with axonal and behavioural phenotypes. Similar results have been shown in a mouse model of NCL which showed increased microglial activation along with a decreased FDG-PET signal [259, 393]. Of note, an increased FDG-PET signal was detected in an AD mouse model, where it has been shown that microglial activation contributed to increased brain glucose metabolism in an AD mouse model [260]. In conclusion, better understanding of the

FDG-PET sources across different neurodegenerative conditions will help to reveal metabolic changes and functional brain alterations, which are detected in several neurodegenerative diseases [394].

Another important aspect of appropriate brain function is an accurate synaptic connectivity between neurons [395]. Microglia actively sculpt synaptic connections by phagocytosing synapses in an activity- and complement-dependent manner [183, 185]. This process, termed as synaptic pruning, peaks at postnatal developmental stages and has been shown to be enhanced in NPC mouse models [184, 198]. I revealed that NPC1-deficient microglia show an increased phagocytic activity as well as accumulate increased levels of synaptic proteins like SYP. Furthermore, brain proteomics of *Cre*+ mice revealed high expression of complement factors (i.e. C1q) which are involved in synaptic pruning. Increased synaptic pruning by microglia as well as elevated levels of complement factors C3 and C1q have been reported in NCL [396]. However, it has been postulated that C1q has only minor contribution to neurodegeneration in NPC [397], supporting more subtle mechanisms of neuronal dysfunction. Uncontrolled and excessive phagocytosis of synapses by microglia has been postulated as a pathological mechanism in neurodevelopmental diseases like schizophrenia [398, 399]. Along these lines, schizophrenia-like presentations are reported in NPC with an early-adult onset [400], suggesting that microglial aberrations over longer time periods such as in *Cre*+ mice may have consequences on neuronal function that may not manifest by massive neuronal loss. Accordingly, no striking differences in synaptic proteins (i.e. SYP) were detected in the brain proteomics of *Cre*+ mice at 12 months, suggesting that NPC1-deficient microglia are not massively removing synapses and/or that neurons (which do not suffer from NPC1 loss) can buffer synaptic changes triggered by microglia.

Another aspect, which was not mentioned so far, is the involvement of peripheral immune cells mediated by NPC1 loss in microglia which might act on neuronal fitness. It has been shown that the BBB is not leaky in the *Npc1*$^{-/-}$ mouse model implying no major contribution of infiltrating peripheral immune cells in NPC neurodegeneration [200]. However, a modest increase in B-cells has been detected upon loss of NPC1 [200]. Proteomic analysis of 12 months old *Cre*+ mice revealed a substantial increase in immune response-related pathways that may be in line with increased B-cell mediated responses and leakiness of the BBB. Aging as well as ROS favours destabilisation of the BBB [401], and thereby, infiltrating peripheral immune cells could also contribute to degenerative processes in *Cre*+ mice at late stages. A similar scenario has been described in Sandhoff disease, an

LSD caused by mutations in beta-hexosaminidase subunit beta (HEXB), in which autoantibodies might potentiate disease progression [402, 403].

In conclusion, loss of NPC1 in microglia triggered pathological events in neurons, and thereby, should not be considered only as a consequence of neurodegeneration but also as an active contributor to neuronal dysfunction in NPC.

4.3 Translational Aspects of This Study

4.3.1 PET Imaging of Neuroinflammation – What is it Detecting?

A repercussion of the deep characterisation of the neuroinflammatory phenotype in *Cre*+ mice is the better understanding of the used PET tracers TSPO and D2-Deprenyl. Non-invasive techniques like PET imaging are of importance for the characterisation and diagnosis of different neurological diseases [404]. TSPO-PET imaging is used to assess neuroinflammation, which has been discussed to reflect microglial reactivity rather than astrocytic reactivity [405]. Here, I provided in-depth characterisation of TSPO tracer uptake in an age- and single cell-dependent manner. I have shown that TSPO is mainly expressed in CD31-positve endothelial cells and Iba1-positive microglia, and that upon progressive microglial activity, TSPO enriches in Iba1-positive microglia. Using scRadiotracing, I confirmed that the TSPO tracer is mainly metabolised by microglia even under non-pathological conditions confirming the cell specificity of this TSPO tracer. Another important aspect is the sensitivity of PET tracers. I have shown that significant differences were only prominent at late pathological stages (11-12 months) in *Cre*+ mice, whereas increased CD68 immunoreactivity was already detected at 2 months. In comparison, TSPO-PET was perfectly matching with immunohistochemical analysis of CD68 at pathological stages, showing the highest microglial activity in the midbrain. Concludingly, differences in microglial reactivity detected by TSPO were obvious only in the presence of a full-blown pathology in *Cre*+ mice. Comparing the TSPO and CD68 immunoreactivity, it becomes obvious that markers directly detecting lysosomal alterations would be ideal as early markers of NPC pathology.

In contrast to TSPO-PET, PET tracers targeting specifically reactive astrocytes are still in development [406]. The D2-Deprenyl-PET tracer was used in this study, which specifically binds to MAO-B [406]. Significant increase in D2-Deprenyl tracer uptake was detected at 7 months which was in line with the immunohistochemical analysis in which increased GFAP reactivity started to be prominent at this age. Strikingly, I detected regional differences of MAO-B and GFAP reactivity. GFAP and MAO-B are both reported to be equally expressed throughout the brain (the human protein atlas, GFAP; MAO-B; accessed on 17.04.2023). D2-Deprenyl-PET imaging seems to detect a certain subset of astrocytes that may not fully match broad astrogliosis detected by GFAP. Taken together, neuroinflammation analysed by PET imaging techniques is an emerging topic under investigation as considering differences in microglial and astrocytic states, it becomes more obvious that different tracers need to be developed and better tailored to the need of neurodegenerative diseases.

4.3.2 PBMC-derived Macrophages from NPC Patients Recapitulate Molecular and Functional Phenotypes of NPC1-deficient Microglia

Throughout this whole study the severe impact of NPC1 loss onto microglial phenotype/function and its systemic consequences were discussed. Microglia undoubtedly contribute to NPC progression, as shown by the fact that loss of NPC1 only in microglia triggered neuronal pathology and premature death. As a result of limited access to human brain material, since NPC is a rare disease, I studied the phenotype and function of PBMC-derived macrophages, which share the same myeloid linage as microglia [172]. Analysis of PBMC-derived macrophages from NPC patients by MS revealed similar molecular changes (but to a lesser extent) as detected in NPC1-deficient microglia, albeit the small sample size of seven patients and residual NPC1 function in NPC patients. Especially late endosomal/lysosomal proteins (i.e. LIPA, LAMP1, NPC2, CTSD, TMEM109) as well as enzymes involved vesicular trafficking (i.e. RAB27A, RAB43, TBC1D15 [407-409]) were altered in NPC macrophages, indicating disturbances at the level of endosomal trafficking events. Along these lines, PBMC-derived macrophages from NPC patient showed also similar functional alterations as NPC1-deficient microglia in terms of the lipid trafficking defect and increased phagocytic clearance of Aβ plaques. These similarities between murine microglia and human macrophages strengthens the point that function of NPC1 in myeloid cells is critical for cell function. Accordingly, NPC1 dysfunction in myeloid cells might have far reaching detrimental effects, since myeloid populations are present in several tissues (i.e. brain, dermis, liver, gut) [410], and thereby, potentiate disease progression not only in the brain but also in the periphery [46].

This translational aspect of my study suggests that PBMC-derived macrophages can be used as a proxy in order to study microglial functions in NPC. There is a broad variety of

NPC1 mutations and disease phenotypes among NPC patients [59, 60]. Thus, this opens a translational perspective to use i.e. the myelin trafficking assay as a screening tool to identify new drugs even on an individual level. With one blood sampling, various bioavailable drugs can be tested in order to find the optimal treatment for the NPC patient. Moreover, analysis of PBMC-derived macrophages in clinical studies can be supportive to elucidate the effect of the treatment onto myeloid cells including microglia.

4.4 Conclusions

In this thesis, I elucidated the role of NPC1 in microglia and their role in NPC progression. I have shown that NPC1-deficient microglia bear a lipid trafficking defect with the main burden at the level of MVBs rather than in lysosomes, which are proteolytically active. This lipid trafficking block goes in line with severe lipid dyshomeostasis and molecular alterations driving NPC1-deficient microglia into a DAM state. Releasing this trafficking block by the cholesterol lowering agent MβCD, reverses molecular fingerprints implying a close relationship between microglial lipidomic and proteomic profiles. Additionally, *Npc1*$^{-/-}$ microglia display an increased phagocytic activity and increased uptake of synaptic proteins, which might attribute to neuropsychiatric symptoms in NPC. Moreover, I have shown that PBMC-derived macrophages from NPC patients recapitulate molecular and functional alterations of *Npc1*$^{-/-}$ microglia, providing a powerful model to study NPC function in myeloid cells as well as a tool for monitoring clinical studies.

In order to elucidate how NPC1-deficient microglia affect brain homeostasis, I generated a new mouse model, where NPC1 was depleted only in myeloid cells and thereby in the microglia in the brain (*Cre*+ mice). Using this mouse model, I could show that microglial phenotypes are driven cell-autonomously upon loss of NPC1. Microglial activation is among the earliest phenotype detected in *Cre*+ mice. This microglial activation drives further astrocytic activity as well as neuronal pathology, which subsequently, translated into motor deficiencies and premature death. This thesis underscores the undeniable contribution of microglia in NPC and highlights that neuroinflammation has to be considered for treatment strategies in NPC patients.

Appendix

Table 39. MS analysis of *Npc1*cKO x *Cx3cr1Cre* mice at 12 months (cerebellum). Detected proteins which are false discovery rate (FDR)-positive are listed.

Protein name	Gene name	log2 (*Cre+/Cre-*)	-log10 p-value	p-value (*Cre+/Cre-*)	FDR (p = 0.05; s0 = 0.1)
Galectin-3	Lgals3	2.886691593	7.959305406	1.09823E-08	+
Complement C1q subcomponent subunit B	C1qb	2.090619269	6.618860363	2.40514E-07	+
Complement C1q subcomponent subunit C	C1qc	1.840134939	7.482464541	3.29257E-08	+
Glial fibrillary acidic protein	Gfap	1.813806715	4.533923864	2.92467E-05	+
Complement C1q subcomponent subunit A	C1qa	1.75135122	9.652749754	2.22459E-10	+
Pro-cathepsin H	Ctsh	1.682139011	2.954355965	0.001110821	+
Beta-hexosaminidase subunit beta	Hexb	1.588866824	8.327169622	4.70793E-09	+
Complement C4-B	C4b	1.538460459	6.36814905	4.28401E-07	+
Protein S100-A4	S100a4	1.498226847	4.17487579	6.68535E-05	+
Macrophage-capping protein	Capg	1.337178094	6.078362855	8.34905E-07	+
Low affinity immunoglobulin gamma Fc region receptor II	Fcgr2	1.320395742	3.682517927	0.000207722	+
Integrin beta-2	Itgb2	1.186259678	5.069009608	8.53081E-06	+
Filamin-C	Flnc	1.163052037	4.206940812	6.20954E-05	+
Cathepsin Z	Ctsz	1.133701393	6.508422	3.10154E-07	+
Integrin alpha-5	Itga5	1.104142938	4.16522567	6.83556E-05	+
Integrin alpha-M	Itgam	1.082142989	3.909160692	0.000123265	+
Beta-hexosaminidase subunit alpha	Hexa	1.071631091	9.022961162	9.48503E-10	+
Rho GDP-dissociation inhibitor 2	Arhgdib	0.983386607	4.159300464	6.92946E-05	+
Progranulin	Grn	0.933297384	3.273129663	0.000533176	+
Plastin-2	Lcp1	0.87559532	4.706891279	1.96385E-05	+
Angiotensinogen	Agt	0.872229372	3.811032367	0.000154514	+
Ribosome biogenesis protein BRX1 homolog	Brix1	0.851275944	3.243694718	0.000570565	+
CD44 antigen	Cd44	0.843292373	4.293173187	5.09128E-05	+
Alpha-2-macroglobulin-P	A2m	0.834209874	6.016403896	9.62933E-07	+
Lysosomal alpha-mannosidase	Man2b1	0.815380187	4.840028567	1.44534E-05	+
Actin-related protein 2/3 complex subunit 1B	Arpc1b	0.733668191	6.22371598	5.97426E-07	+
Nitric oxide synthase. brain	Nos1	0.673358554	5.15313709	7.0285E-06	+
Annexin A2	Anxa2	0.672430175	4.030434925	9.3232E-05	+
Phosphoglucomutase-like protein 5	Pgm5	0.652923629	6.875490407	1.33202E-07	+
Apolipoprotein E	Apoe	0.633642787	7.233420987	5.84223E-08	+
Annexin A3	Anxa3	0.613993145	6.691209188	2.03606E-07	+
Regulation of nuclear pre-mRNA domain-containing protein 1A	Rprd1a	0.600174745	4.067184059	8.56675E-05	+
Alpha-N-acetylgalactosaminidase	Naga	0.570660092	4.3557642	4.40794E-05	+
Clusterin	Clu	0.514877819	6.141534092	7.21881E-07	+
Tenascin	Tnc	-1.074460506	3.619079224	0.000240392	+
Protein-associating with the carboxyl-terminal domain of ezrin	Scyl3	-1.421517032	5.611800508	2.44455E-06	+

Table 40. MS analysis of *Npc1*cKO x *Cx3cr1Cre* mice at 12 months (brain without cerebellum). Detected proteins which are false discovery rate (FDR)-positive are listed.

Protein name	Gene name	log2 (*Cre+/Cre-*)	-log10 p-value	p (*Cre+/Cre-*)	FDR (p = 0.05; s0 = 0.1)
Galectin-3	Lgals3	3.669855277	6.024072206	9.4608E-07	+
Pro-cathepsin H	Ctsh	2.512518883	3.397555567	0.000400354	+
Oxytocin-neurophysin 1	Avp;Oxt	2.432225545	4.837866563	1.45256E-05	+
V-type proton ATPase subunit a	Tcirg1	2.412789504	3.551044749	0.000281161	+
Serine protease inhibitor A3N	Serpina3n	2.319122632	5.638865807	2.29686E-06	+
Complement C1q subcomponent subunit C	C1qc	2.316673915	12.0037994	9.9129E-13	+
Tumor necrosis factor receptor superfamily member 6	Fas	2.294596354	2.521536401	0.003009287	+
Complement C4-B	C4b	2.283713341	8.399833829	3.9826E-09	+
Glial fibrillary acidic protein	Gfap	2.229853312	7.942362017	1.14193E-08	+
Complement C1q subcomponent subunit B	C1qb	2.213804881	9.978397602	1.051E-10	+
Complement C1q subcomponent subunit A	C1qa	2.207023938	10.84608754	1.42532E-11	+
Oxytocin-neurophysin 1	Oxt	2.161646843	4.037557949	9.17154E-05	+
Interferon-induced protein with tetratricopeptide repeats 3	Ifit3	2.025242011	10.32755977	4.70371E-11	+
5'-3' exonuclease PLD4	Pld4	2.018707275	4.621805722	2.38888E-05	+
Cathepsin Z	Ctsz	2.016524792	7.496175733	3.19025E-08	+
Macrophage-capping protein	Capg	1.996839841	5.438494822	3.64339E-06	+
Ig heavy chain V region 6.96		1.970372677	2.293572953	0.005086594	+
E3 ubiquitin-protein ligase DTX3L	Dtx3l	1.958745639	3.984056756	0.000103739	+
Alpha-2-macroglobulin-P	A2m	1.958361467	3.611853498	0.000244425	+
Protein S100-A4	S100a4	1.947112719	5.977772865	1.05251E-06	+
Glial fibrillary acidic protein	Gfap;Krt5;Krt76;Krt79;Vim	1.946234703	2.439043452	0.003638786	+
Monocyte differentiation antigen CD14	Cd14	1.918437799	2.668147201	0.002147103	+
H-2 class I histocompatibility antigen. L-D alpha chain	H2-L	1.911325296	5.045576358	9.00375E-06	+
Neurogenic locus notch homolog protein 2	Notch2	1.873736064	2.147945663	0.007113025	+
Galectin-3-binding protein	Lgals3bp	1.855782986	7.379170293	4.17667E-08	+
Immunoglobulin heavy variable 6-3 (Fragment)	Ighv6-3	1.849872589	1.852368557	0.014048548	+
Vimentin	Vim	1.828501383	7.05106446	8.89069E-08	+
Peripherin	Prph;Vim	1.674366951	3.098026906	0.000797945	+
Low affinity immunoglobulin gamma Fc region receptor II	Fcgr2	1.66917483	5.722202861	1.89582E-06	+

Protein name	**Gene name**	**log2 (*Cre+/Cre-*)**	**-log10 p-value**	**p (*Cre+/Cre-*)**	**FDR (p = 0.05; s0 = 0.1)**
Oncostatin-M-specific receptor subunit beta	Osmr	1.651174625	2.952435255	0.001115744	+
Phospholipid scramblase 2	Plscr2	1.561369101	2.488210573	0.003249297	+
CD180 antigen	Cd180	1.542270501	5.887392615	1.29601E-06	+
Proteasome subunit beta type-8	Psmb8	1.539515336	6.608346948	2.46407E-07	+
Filamin-C	Flnc	1.516883373	4.706105934	1.96741E-05	+
CD44 antigen	Cd44	1.513112386	3.911863514	0.0001225	+
Guanylate-binding protein 2	Gbp2	1.492002646	5.536381517	2.90816E-06	+
Beta-hexosaminidase subunit beta	Hexb	1.478891691	8.357980038	4.38551E-09	+
Progranulin	Grn	1.466488679	4.770257768	1.69724E-05	+
Beta-hexosaminidase subunit alpha	Hexa	1.442084312	8.480653456	3.30633E-09	+
Tyrosine-protein phosphatase non-receptor type 6	Ptpn6	1.41504399	6.574829186	2.66177E-07	+
Tapasin	Tapbp	1.403989315	2.382318654	0.004146497	+
Interferon-induced protein with tetratricopeptide repeats 1	Ifit1	1.366767883	2.224009516	0.005970222	+
Protein S100-A6	S100a6	1.323470434	4.08443921	8.23305E-05	+
Thromboxane-A synthase	Tbxas1	1.307018121	3.371437254	0.00042517	+
Interferon-induced transmembrane protein 3	Ifitm3	1.297264099	3.208085106	0.00061932	+
Protein mono-ADP-ribosyltransferase PARP3	Parp3	1.284204165	2.380802725	0.004160996	+
H-2 class I histocompatibility antigen. K-B alpha chain	H2-K1	1.264462312	4.661545918	2.17999E-05	+
Neutral amino acid transporter B(0)	Slc1a5	1.247835159	1.71467104	0.019289855	+
GTP-binding protein	Ifi47	1.223279953	3.609541765	0.00024573	+
Receptor-type tyrosine-protein phosphatase C	Ptprc	1.217684905	4.335042415	4.62336E-05	+
Interferon-induced protein with tetratricopeptide repeats 2	Ifit2	1.211692492	2.403066705	0.003953059	+
Pleckstrin	Plek	1.175351302	5.119759435	7.58998E-06	+
Immunity-related GTPase family M protein 1	Irgm1	1.155386448	7.360679191	4.35834E-08	+
Immunoglobulin heavy constant gamma 2C (Fragment)	Ighg2c	1.149160703	2.278844129	0.005262061	+
Antiviral innate immune response receptor RIG-I	Ddx58	1.143383821	6.267631984	5.39968E-07	+
Phytanoyl-CoA dioxygenase domain-containing protein 1	Phyhd1	1.136807919	4.230788112	5.87776E-05	+
Dedicator of cytokinesis protein 2	Dock2	1.11356322	5.926417029	1.18463E-06	+
NPC intracellular cholesterol transporter 2	Npc2	1.10995086	1.990435358	0.010222677	+
Dipeptidyl peptidase 1	Ctsc	1.072296302	4.023014465	9.48387E-05	+
Annexin A4	Anxa4	1.068036238	5.994807408	1.01203E-06	+
Translocator protein	Tspo	1.064077536	3.453970048	0.000351585	+
Tumor necrosis factor alpha-induced protein 8-like protein 2	Tnfaip8l2	1.059502443	2.875520653	0.001331924	+
Histone H1.0	H1-0	1.053881486	3.416729186	0.000383064	+
Hexokinase-3	Hk3	1.045707703	1.992745621	0.010168441	+
Proto-oncogene vav	Vav1	1.035371939	1.909690506	0.012311458	+
Signal transducer and activator of transcription 1	Stat1	1.02239275	6.572667924	2.67505E-07	+
Integrin beta-2	Itgb2	1.021565119	6.932353172	1.16855E-07	+
Proteasome subunit beta type-9	Psmb9	1.021411419	2.037203191	0.00917903	+
UDP-glucuronosyltransferase	Ugt2b1	1.021301587	3.426771969	0.000374307	+
Neutrophil cytosol factor 1	Ncf1	1.003598531	4.564099156	2.72835E-05	+
Glycosylated lysosomal membrane protein	Glmp	0.999610583	4.345771237	4.51054E-05	+
UDP-glucose 6-dehydrogenase	Ugdh	0.997285048	4.957046923	1.10396E-05	+
Alpha-N-acetylglucosaminidase	Naglu	0.996882598	3.789344875	0.000162426	+
Guanylate-binding protein 4	Gbp4	0.996785959	2.846281713	0.001424683	+
Beta-2-microglobulin	B2m	0.990430514	3.615399502	0.000242438	+
Death-associated protein 1	Dap	0.986246109	2.07823819	0.008351449	+
Beta-glucuronidase	Gusb	0.978745778	5.804307222	1.56925E-06	+
Nicotinate phosphoribosyltransferase	Naprt	0.974207242	6.717877819	1.91479E-07	+
ADP-ribosylation factor-like protein 6-interacting protein 4	Arl6ip4	0.970858177	2.005017012	0.009885144	+
Serine/threonine-protein kinase Nek6	Nek6	0.95760266	3.221622401	0.000600313	+
Plastin-2	Lcp1	0.952517351	6.999742379	1.00059E-07	+
Cathepsin D	Ctsd	0.951095263	7.593237607	2.55131E-08	+
UDP-glucuronic acid decarboxylase 1	Uxs1	0.938494523	2.00331342	0.009923996	+
Proton-coupled amino acid transporter 1	Slc36a1	0.929982344	2.449703699	0.003550555	+
Allograft inflammatory factor 1	Aif1	0.92100064	2.551433729	0.002809094	+
Actin-related protein 2/3 complex subunit 1B	Arpc1b	0.908894698	6.443455931	3.602E-07	+
PDZ and LIM domain protein 4	Pdlim4	0.898403327	4.649545214	2.24107E-05	+
Podoplanin	Pdpn	0.897319635	3.052798115	0.000885527	+
Guanylate-binding protein 4	Gbp4;Gbp7	0.892211437	3.906156053	0.000124121	+
E3 ubiquitin/ISG15 ligase TRIM25	Trim25	0.887495518	4.669536887	2.14024E-05	+
Mitochondrial 10-formyltetrahydrofolate dehydrogenase	Aldh1l2	0.884203752	4.202385171	6.27502E-05	+
Metallothionein-2	Mt2	0.88409694	4.481240873	3.30186E-05	+
Heterochromatin protein 1-binding protein 3	Hp1bp3	0.883924643	3.623352407	0.000238039	+
Filamin-B	Flnb;Flnc	0.883416812	3.980543751	0.000104582	+
Unconventional myosin-IXb	Myo9b	0.872836749	2.537065958	0.002903582	+
Phospholemman	Fxyd1	0.864175797	3.060231794	0.000870499	+
Chloride intracellular channel protein 1	Clic1	0.852068424	3.666172187	0.000215689	+
60S ribosomal protein L27a	Rpl27a	0.850302696	3.07323889	0.000844814	+
Transmembrane protein 100	Tmem100	0.846790473	2.416172819	0.003835546	+
Lysosome-associated membrane glycoprotein 1	Lamp1	0.845024109	4.708509424	1.95655E-05	+
Kallikrein-related-peptidase 6	Klk6	0.841466268	1.964493894	0.010851908	+
Guanylate-binding protein 6	Gbp6	0.840777715	3.391106119	0.000406344	+
Heat shock protein beta-1	Hspb1	0.8361365	2.590424946	0.002567882	+
Maspardin	Spg21	0.827568372	2.951384967	0.001118446	+
Retinoid-inducible serine carboxypeptidase	Scpep1	0.826910019	2.99195973	0.001018686	+
Thrombospondin-4	Thbs4	0.825516542	3.339749426	0.000457352	+
Perilipin-4	Plin4	0.820882003	3.586851016	0.00025891	+
Urea transporter 1	Slc14a1	0.810055097	2.449502661	0.003552199	+
N-acylglucosamine 2-epimerase	Renbp	0.803841591	4.65942914	2.19064E-05	+
Ubiquitin-like protein ISG15	Isg15	0.801182588	3.585276687	0.00025985	+
Moesin	Msn	0.800867399	5.611045143	2.44881E-06	+
Protein S100-A11	S100a11	0.782293161	3.653232899	0.000222212	+
Protein-tyrosine sulfotransferase 1	Tpst1	0.771158536	2.156039908	0.006981682	+
Hematopoietic lineage cell-specific protein	Hcls1	0.768755595	3.333682234	0.000463786	+

Protein name	**Gene name**	**log2 (*Cre+/Cre-*)**	**-log10 p-value**	**p (*Cre+/Cre-*)**	**FDR (p = 0.05; s0 = 0.1)**
Lysosomal alpha-mannosidase	Man2b1	0.758055051	4.050521018	8.90182E-05	+
Adaptin ear-binding coat-associated protein 2	Necap2	0.756900469	2.258072329	0.005519855	+
CD109 antigen	Cd109	0.756544272	2.830371601	0.001477843	+
1-phosphatidylinositol 4.5-bisphosphate phosphodiesterase gamma-2	Plcg2	0.756196499	4.632437325	2.33111E-05	+
Calponin-3	Cnn3	0.745330811	3.382506336	0.000414471	+
Dehydrogenase/reductase SDR family member 1	Dhrs1	0.743507067	4.287123379	5.1627E-05	+
Molybdenum cofactor biosynthesis protein 1	Mocs1	0.737961451	2.576707162	0.002650287	+
Fermitin family homolog 3	Fermt3	0.737695217	4.743110136	1.80672E-05	+
Galectin-9	Lgals9	0.728643576	2.144810604	0.007164558	+
Complement factor D	Cfd	0.727558136	2.098184132	0.007976564	+
Integrin alpha-M	Itgam	0.717017015	5.331452517	4.66173E-06	+
Proteolipid protein 2	Plp2	0.713083585	3.331831109	0.000465767	+
Carbonic anhydrase 5B. mitochondrial	Ca5b	0.708158334	2.64594303	0.002259732	+
Endothelin receptor type B	Ednrb	0.707791964	3.096311019	0.000801104	+
Filamin-B	Flna;Flnb;Flnc	0.705010414	5.139831246	7.24718E-06	+
Acyl-CoA dehydrogenase family member 10	Acad10	0.70267264	2.79034488	0.001620523	+
Aspartyl/asparaginyl beta-hydroxylase	Asph	0.700224876	3.765028767	0.000171779	+
N-acetylglucosamine-6-sulfatase	Gns	0.694805622	4.993312389	1.01552E-05	+
Clusterin	Clu	0.693230629	5.432108004	3.69736E-06	+
Apolipoprotein E	Apoe	0.686207453	7.223836527	5.9726E-08	+
2-iminobutanoate/2-iminopropanoate deaminase	Rida	0.684256554	4.001481381	9.96595E-05	+
Signal transducer and activator of transcription 3	Stat3	0.677875996	7.633090234	2.32761E-08	+
Angiotensinogen	Agt	0.665303866	3.439704583	0.000363325	+
Stomatin	Stom	0.665108363	3.44843183	0.000356097	+
Annexin A3	Anxa3	0.65541331	7.071521868	8.48161E-08	+
MARCKS-related protein	Marcksl1	0.654086749	5.578701744	2.63814E-06	+
Steryl-sulfatase	Sts	0.652855396	3.921667056	0.000119766	+
Lysosomal protective protein	Ctsa	0.652610461	4.948692486	1.1254E-05	+
Endoplasmic reticulum aminopeptidase 1	Erap1	0.651636124	3.625617863	0.0002368	+
Uncharacterized protein C2orf72 homolog		0.649365584	3.656996667	0.000220294	+
N-acetylneuraminate lyase	Npl	0.64755853	4.06256345	8.65838E-05	+
Mitochondrial calcium uniporter regulator 1	Mcur1	0.644236247	3.539969669	0.000288423	+
Aquaporin-4	Aqp4	0.641357104	3.161117525	0.000690053	+
Serum paraoxonase/lactonase 3	Pon3	0.638182004	4.548293096	2.82948E-05	+
Quinone oxidoreductase-like protein 2	Cryzl2	0.633607388	3.512979187	0.000306917	+
Sphingosine-1-phosphate lyase 1	Sgpl1	0.621225198	4.563763439	2.73046E-05	+
Protein S100-A16	S100a16	0.609026432	3.023201294	0.000947979	+
Lysosome-associated membrane glycoprotein 2	Lamp2	0.608222644	2.667638456	0.002149619	+
Cystine/glutamate transporter	Slc7a11	0.60801967	3.585601175	0.000259656	+
Ectonucleoside triphosphate diphosphohydrolase 1	Entpd1	0.602262338	5.890009165	1.28822E-06	+
Maestro heat-like repeat family member 1	Mroh1	0.59969298	4.758174039	1.74512E-05	+
Calponin-2	Cnn2	0.596972148	2.80060535	0.001582686	+
Hexokinase-2	Hk2	0.594583511	3.682137445	0.000207904	+
Rho GDP-dissociation inhibitor 2	Arhgdib	0.591128508	4.800306589	1.58377E-05	+
Peroxiredoxin-6	Prdx6	0.589519183	4.056011381	8.78999E-05	+
EGF-like repeat and discoidin I-like domain-containing protein 3	Edil3	0.587365786	3.575824125	0.000265568	+
Phospholipid-transporting ATPase ABCA3	Abca3	0.586813927	3.980105367	0.000104687	+
Cathepsin B	Ctsb	0.586711248	4.836923942	1.45571E-05	+
SH3 and PX domain-containing protein 2B	Sh3pxd2b	0.58525753	3.143096057	0.00071929	+
Torsin-1A-interacting protein 2	Tor1aip2	0.582793395	4.294891462	5.07117E-05	+
Latexin	Lxn	0.577310562	4.308613045	4.91345E-05	+
Torsin-1A-interacting protein 1	Tor1aip1	0.576255957	2.656142558	0.00220728	+
Protein fem-1 homolog B	Fem1b	0.573833625	3.311538271	0.000488047	+
Aldehyde dehydrogenase family 3 member B1	Aldh3b1	0.573606014	2.918742288	0.001205751	+
Transgelin-2	Tagln2	0.571148237	3.088479311	0.000815682	+
Major vault protein	Mvp	0.570596218	3.41945452	0.000380667	+
Protein-glutamine gamma-glutamyltransferase 2	Tgm2	0.570470174	4.125543736	7.48956E-05	+
Ceruloplasmin	Cp	0.566895962	2.619505599	0.002401565	+
Alpha-actinin-2	Actn2	0.566519101	2.54060018	0.002880049	+
40S ribosomal protein S15a	Rps15a	0.562381744	3.918765186	0.000120569	+
Glutathione hydrolase 5 proenzyme	Ggt5	0.56132253	2.481051802	0.003303301	+
60S ribosomal protein L21	Rpl21	0.560617765	3.88266633	0.000131019	+
Serine/arginine-rich splicing factor 5	Srsf5	0.560474078	2.627798312	0.002356143	+
Polypyrimidine tract-binding protein 1	Ptbp1	0.554039478	3.088820386	0.000815041	+
Filamin-A	Flna	0.552381992	4.485149312	3.27228E-05	+
Lysophosphatidylcholine acyltransferase 2	Lpcat2	0.551813285	3.634905997	0.00023179	+
Proteasome activator complex subunit 2	Psme2	0.549643199	5.28299597	5.212E-06	+
Annexin A1	Anxa1	0.548765024	2.972211419	0.001066077	+
Myoferlin	Myof	0.545451959	2.553482167	0.002795876	+
60S ribosomal protein L6	Rpl6	0.544776917	4.047761637	8.95856E-05	+
EH domain-containing protein 2	Ehd2;Ehd4	0.536502361	3.023316155	0.000947728	+
40S ribosomal protein S23	Rps23	0.536263466	3.993183427	0.000101582	+
Alpha-N-acetylgalactosaminidase	Naga	0.534906387	3.684976073	0.000206549	+
60S ribosomal protein L4	Rpl4	0.527785619	4.731806076	1.85436E-05	+
1-phosphatidylinositol 4.5-bisphosphate phosphodiesterase beta-3	Plcb3	0.527507464	5.214867022	6.09724E-06	+
Phospholipid-transporting ATPase ABCA1	Abca1	0.525383949	4.149025875	7.09535E-05	+
Integrin alpha-7	Itga7	0.52391084	3.907457621	0.000123749	+
40S ribosomal protein S3	Rps3	0.523867925	3.349306209	0.000447398	+
Alpha-1-syntrophin	Snta1;Sntb1;Sntb2	0.520814419	2.658546062	0.002195098	+
Protein S100-A13	S100a13	0.520119031	5.621765712	2.3891E-06	+
AHNAK nucleoprotein (desmoyokin)	Ahnak	0.520096461	4.224654843	5.96136E-05	+
Apoptosis-associated speck-like protein containing a CARD	Pycard	0.520080725	4.194208114	6.39428E-05	+
Ubiquitin-40S ribosomal protein S27a	Rps27a	0.519783815	2.628687342	0.002351325	+
Ras GTPase-activating-like protein IQGAP1	Iqgap1	0.516727765	4.400724827	3.97443E-05	+
60S ribosomal protein L13a	Rpl13a	0.516483943	3.215867052	0.000608321	+

Protein name	Gene name	log2 (*Cre+/Cre-*)	-log10 p-value	p (*Cre+/Cre-*)	FDR (p = 0.05; s0 = 0.1)
Protein S100-A1	S100a1	0.514752706	3.580142536	0.00026294	+
Catenin alpha-1	Ctnna1	0.513211409	4.934662567	1.16235E-05	+
60S ribosomal protein L7a	Rpl7a	0.510881106	4.256336375	5.54196E-05	+
60S ribosomal protein L13	Rpl13	0.510869662	3.446258589	0.000357883	+
60S ribosomal protein L35	Rpl35	0.510632833	3.887820044	0.000129473	+
40S ribosomal protein S13	Rps13	0.510106881	2.933807173	0.001164643	+
Epididymis-specific alpha-mannosidase	Man2b2	0.508831024	2.679570621	0.002091363	+
60S ribosomal protein L14	Rpl14	0.508501053	3.082070244	0.000827808	+
60S acidic ribosomal protein P2	Rplp2	0.507997036	3.874708927	0.000133442	+
Unconventional myosin-VI	Myo6	0.505473455	3.766829361	0.000171069	+
von Willebrand factor A domain-containing protein 5A	Vwa5a	0.504022598	4.618337851	2.40803E-05	+
Patatin-like phospholipase domain-containing protein 7	Pnpla7	0.501090686	4.740372065	1.81814E-05	+
Galectin-1	Lgals1	0.500874201	3.936355893	0.000115783	+
H(+)/Cl(-) exchange transporter 7	Clcn7	0.498079936	2.728870613	0.001866936	+
60S ribosomal protein L28	Rpl28	0.495521545	3.258628821	0.000551279	+
60S acidic ribosomal protein P0	Rplp0	0.491417567	3.783211168	0.000164736	+
40S ribosomal protein S14	Rps14	0.489281972	4.330504782	4.67192E-05	+
Mitogen-activated protein kinase 14	Mapk14	0.488937537	5.782027141	1.65186E-06	+
60S ribosomal protein L7	Rpl7	0.484406789	4.221438284	6.00567E-05	+
60S ribosomal protein L10a	Rpl10a	0.483141581	3.24432789	0.000569734	+
Membrane protein MLC1	Mlc1	0.479510307	2.986437938	0.001031721	+
40S ribosomal protein S19	Rps19	0.478704453	4.564404491	2.72644E-05	+
Lysosomal acid lipase/cholesteryl ester hydrolase	Lipa	0.478476683	3.024133873	0.000945946	+
60S ribosomal protein L10	Rpl10	0.477083206	5.041976363	9.0787E-06	+
60S ribosomal protein L18	Rpl18	0.477076848	3.041360214	0.000909159	+
60S ribosomal protein L12	Rpl12	0.475877126	3.438028532	0.00036473	+
[F-actin]-monooxygenase MICAL1	Mical1	0.47451814	3.078128388	0.000835356	+
Proteasome activator complex subunit 1	Psme1	0.473629793	5.479968767	3.31155E-06	+
40S ribosomal protein S3a	Rps3a	0.472912153	2.96790048	0.001076712	+
40S ribosomal protein S8	Rps8	0.47258536	2.929188047	0.001177096	+
Ribosome-binding protein 1	Rrbp1	0.464910189	4.434289321	3.67884E-05	+
60S ribosomal protein L37a	Rpl37a	0.464798133	3.051457768	0.000888264	+
40S ribosomal protein S20	Rps20	0.464684486	2.936605624	0.001157163	+
Erbin	Erbin	0.463151614	3.073820384	0.000843684	+
Ezrin	Ezr;Msn;Rdx	0.454670906	4.228458407	5.90938E-05	+
Palmitoyl-protein thioesterase 1	Ppt1	0.453821818	5.751383164	1.77262E-06	+
Cytochrome P450	Cyp2d22	0.44913578	3.941152015	0.000114511	+
Copine-3	Cpne3	0.447008451	4.404566048	3.93944E-05	+
Tripeptidyl-peptidase 1	Tpp1	0.446484089	5.103654329	7.87672E-06	+
40S ribosomal protein S4. X isoform	Rps4x	0.443332354	3.528287048	0.000296287	+
60S ribosomal protein L17	Rpl17	0.443058014	3.191024077	0.000644134	+
Interferon-inducible double-stranded RNA-dependent protein kinase activator A	Prkra	0.43969361	3.158285384	0.000694568	+
Cdc42 effector protein 4	Cdc42ep4	0.439297676	3.348746336	0.000447975	+
Retinal dehydrogenase 2	Aldh1a2	0.435140928	3.477318185	0.000333182	+
Glycogen phosphorylase. liver form	Pygl	0.434703827	3.603301499	0.000249286	+
40S ribosomal protein S10	Rps10	0.430795987	3.425572714	0.000375342	+
Talin-1	Tln1	0.429062525	4.659471278	2.19043E-05	+
Neutral amino acid transporter A	Slc1a4	0.423752308	5.211029441	6.15135E-06	+
60S ribosomal protein L8	Rpl8	0.422291756	3.424033813	0.000376674	+
Alpha-actinin-4	Actn4	0.417535623	3.443398099	0.000360248	+
60S ribosomal protein L5	Rpl5	0.415157	3.959255244	0.000109836	+
Phospholipase D2	Pld2	0.411143621	3.670958792	0.000213325	+
60S ribosomal protein L27	Rpl27	0.407979012	3.413773272	0.00038568	+
Ornithine aminotransferase. mitochondrial	Oat	0.385748227	5.627489768	2.35782E-06	+
Integrin-linked protein kinase	Ilk	0.382591565	5.040170178	9.11654E-06	+
5-oxoprolinase	Oplah	0.381000042	4.873940738	1.33678E-05	+
UDP-N-acetylhexosamine pyrophosphorylase-like protein 1	Uap1l1	0.380888144	4.274290411	5.31753E-05	+
PDZ and LIM domain protein 5	Pdlim5	0.371046225	3.989261676	0.000102503	+
Filamin-B	Flnb	0.368582408	3.961408462	0.000109293	+
FERM. ARHGEF and pleckstrin domain-containing protein 1	Farp1	0.363476912	5.169248673	6.77254E-06	+
Solute carrier family 23 member 2	Slc23a2	0.35685126	5.264167923	5.44292E-06	+
Proline dehydrogenase 1. mitochondrial	Prodh	0.343589465	4.38795957	4.09299E-05	+
UMP-CMP kinase 2. mitochondrial	Cmpk2	0.307457288	7.232895108	5.84931E-08	+
ATP-binding cassette sub-family A member 9	Abca9	-0.384308338	4.322955605	4.75384E-05	+
BTB/POZ domain-containing protein 17	Btbd17	-0.409521421	3.710260281	0.000194868	+
Potassium voltage-gated channel subfamily C member 3	Kcnc3	-0.474610964	2.930046541	0.001174772	+
Synaptotagmin-2	Syt2	-0.528710365	3.047662664	0.000896061	+
KN motif and ankyrin repeat domain-containing protein 4	Kank4	-0.563750108	2.636609548	0.002308822	+
Mitochondrial dynamics protein MID51	Miefl	-0.571455956	2.923087859	0.001193747	+
Beta-crystallin B1	Crybb1	-0.594371478	2.565706032	0.002718279	+
P2Y purinoceptor 12	P2ry12	-0.605059942	4.148226759	7.10842E-05	+
Sodium channel protein type 1 subunit alpha	Scn1a;Scn3a	-0.629203955	2.705801698	0.001968785	+
Sodium- and chloride-dependent glycine transporter 2	Slc6a5	-0.852210204	2.211197673	0.006148969	+
Growth arrest-specific protein 2	Gas2	-1.170302232	2.094267055	0.008048834	+

Table 41. Lipidomic analysis of acutely isolated microglia from 1-week old *Npc1*$^{+/+}$ and *Npc1*$^{-/-}$ mice. Detected lipids are listed. The log2 fold change (FC) between *Npc1*$^{-/-}$ and *Npc1*$^{+/+}$ microglia is shown. Significant changed lipids (adjusted p-value) are marked in blue (downregulated) or red (upregulated). Not significant changed lipids are marked in gray (stable).

lipid	log2 FC	p-value	adjusted p-value
CE(20:4)	-2.6	4.5E-09	4.2E-08
CE(18:1)	-1.2	1.7E-08	1.3E-07
Cer(d18:1/24:0)	-1.2	2.1E-08	1.5E-07
LPC(26:1)	-1.3	6.7E-08	4.3E-07
CE(22:6)	-3.0	8.8E-08	5.3E-07
PS(16:0_22:6)	-1.2	2.4E-07	1.3E-06
PS(16:0_20:4)	-1.2	4.6E-07	2.2E-06
MG(16:0)	-1.3	6.4E-07	2.9E-06
PC(16:0/5:0(CHO))	-1.3	6.6E-07	2.9E-06
PS(18:0_22:6)	-1.0	7.5E-07	3.2E-06
PS(18:1/18:1)	-1.2	9.8E-07	4.1E-06
PE(P-16:0/20:4)	-1.0	1.3E-06	5.1E-06
TG(18:0_36:2)	-1.3	1.6E-06	5.8E-06
Palmitic acid	-1.1	1.9E-06	7.0E-06
DG(16:0_20:4)	-1.0	2.7E-06	9.7E-06
TG(18:1_34:2)	-1.4	3.0E-06	1.1E-05
Cer(d18:1/24:1)	-1.0	3.0E-06	1.1E-05
PS(18:0_20:4)	-1.0	3.1E-06	1.1E-05
PS(22:6/22:6)	-2.5	4.0E-06	1.3E-05
Cer(d18:1/16:0)	-0.8	4.3E-06	1.4E-05
PC(16:0/9:0(COOH))	-1.2	5.4E-06	1.7E-05
DG(18:1/18:1)	-1.2	5.8E-06	1.8E-05
PE(P-16:0/22:6)	-0.9	6.0E-06	1.8E-05
PE(P-18:0/22:6)	-0.9	7.8E-06	2.3E-05
MG(18:0)	-1.4	8.3E-06	2.3E-05
PS(16:0_18:1)	-1.0	8.2E-06	2.3E-05
PE(P-18:1/22:6)	-0.9	8.3E-06	2.3E-05
PE(O-16:0/20:4)	-0.9	1.1E-05	3.0E-05
PE(P-18:0/20:4)	-0.9	1.2E-05	3.2E-05
PE(P-16:0/22:4)	-0.9	1.4E-05	3.7E-05
Oleic acid	-1.1	1.6E-05	4.1E-05
TG(20:4_32:1)	-1.0	1.8E-05	4.5E-05
PG(16:0_18:1)	-1.0	1.8E-05	4.5E-05
TG(18:1_34:3)	-1.5	1.9E-05	4.6E-05
DG(18:1_20:4)	-1.1	1.9E-05	4.7E-05
PE(O-16:0/22:6)	-0.9	2.3E-05	5.5E-05
GlcCer(d18:1/22:1)	-1.2	2.8E-05	6.5E-05
Palmitoleic acid	-1.4	4.2E-05	9.7E-05
PC(O-16:0/0:0)	-0.9	4.5E-05	1.0E-04
DG(16:0_18:1)	-0.9	5.4E-05	1.2E-04
CE(16:1)	-1.8	5.6E-05	1.2E-04
PS(18:0_18:1)	-0.8	5.8E-05	1.3E-04
GlcCer(d18:1/22:0)	-1.2	7.8E-05	1.7E-04
Coenzyme Q10	-1.1	1.1E-04	2.2E-04
MG(18:1)	-1.1	1.1E-04	2.3E-04
TG(22:6_36:2)	-1.6	1.2E-04	2.4E-04
PE(36:4)	-0.8	1.2E-04	2.4E-04
GlcCer(d18:1/24:0)	-1.1	1.5E-04	3.0E-04
PE(38:5)	-0.9	1.7E-04	3.4E-04
PE(P-18:1/20:4)	-0.7	1.9E-04	3.8E-04
Cholesterol sulfate	-1.4	2.5E-04	4.8E-04
PE(36:2)	-0.7	4.2E-04	8.0E-04
TG(20:4_36:3)	-0.9	4.5E-04	8.3E-04
DG(18:0_20:4)	-0.7	5.5E-04	1.0E-03
PI(18:0_22:6)	-0.7	5.5E-04	1.0E-03
PE(O-18:0/20:4)	-0.6	9.5E-04	1.7E-03
PE(34:1)	-0.7	1.2E-03	2.1E-03
PE(40:6)	-0.6	1.4E-03	2.4E-03
PE(40:7)	-0.6	1.4E-03	2.4E-03
PE(P-18:0/18:2)	-0.9	1.5E-03	2.5E-03
PC(16:0/9:0(CHO))	-0.9	1.5E-03	2.6E-03
PI(16:0_20:4)	-0.5	1.8E-03	3.0E-03
TG(20:4_36:2)	-0.7	2.5E-03	4.1E-03
PE(36:1)	-0.7	2.6E-03	4.2E-03
Stearic acid	-0.8	3.6E-03	5.8E-03
Arachidonic acid_MRM	-0.5	4.0E-03	6.4E-03
PC(36:2)	-0.5	4.9E-03	7.8E-03
DG(18:0_18:1)	-0.7	5.3E-03	8.4E-03
GlcCer(d18:2/22:0)	-0.8	5.9E-03	9.3E-03
PE(38:4)	-0.6	6.7E-03	1.0E-02
PG(18:1/18:1)	-0.7	7.4E-03	1.1E-02
CE(18:2)	-1.9	8.7E-03	1.3E-02
TG(20:4_34:2)	-0.8	1.0E-02	1.5E-02
TG(20:4_36:0)	-0.6	1.1E-02	1.6E-02
PC(38:6)	-0.4	1.3E-02	1.9E-02
PEth(16:0_18:1)	-1.3	1.4E-02	1.9E-02
PE(38:6)	-0.5	1.5E-02	2.1E-02
SM(d18:1/24:1)	-0.8	1.5E-02	2.1E-02
GlcCer(d18:1/16:0)	-0.7	1.8E-02	2.5E-02
GlcCer(d18:1/24:1)	-0.7	1.8E-02	2.5E-02
DHA	-0.6	1.8E-02	2.5E-02
PI(16:0_22:6)	-0.5	1.9E-02	2.6E-02
PI(16:0_18:1)	-0.4	2.0E-02	2.7E-02
CL(72:6/18:2)	-1.6	2.6E-02	3.5E-02
SM(d18:1/24:0)	-0.7	2.6E-02	3.5E-02
DG(18:0_22:6)	-2.1	2.8E-02	3.7E-02
PI(18:1/18:1)	-0.5	3.1E-02	4.1E-02
PE(40:4)	-0.5	3.7E-02	4.8E-02
LacCer(d18:1/18:0)	4.8	1.8E-17	3.1E-15
BMP(18:1/18:1)	3.6	1.2E-16	1.1E-14
BMP(16:1/16:1)	4.0	2.9E-16	1.7E-14
BMP(18:0_18:1)	3.7	7.0E-16	3.1E-14
BMP(16:0_20:4)	3.2	7.3E-15	2.6E-13
BMP(16:0_18:1)	3.7	1.1E-14	2.7E-13
LPC(16:0)	2.3	1.0E-14	2.7E-13
GM2(d36:1)	4.2	1.1E-13	2.4E-12
LPG(18:1)	2.3	2.3E-13	4.5E-12
BMP(18:0_20:4)	3.6	1.0E-12	1.8E-11
HexCer(d18:1/18:0)	2.1	1.7E-12	2.8E-11
LPC(18:0)	1.6	8.2E-12	1.2E-10
LacCer(d18:1/16:0)	2.9	3.0E-11	4.1E-10
GlcCer(d18:2/18:0)	3.3	1.5E-10	1.8E-09
Hemi-BMP(18:1/18:1)_16:0	2.3	4.5E-10	5.3E-09
GalCer(d18:2/18:0)	2.3	8.3E-10	9.0E-09
(3-O-sulfo)GalCer(d18:1/24:1)	2.0	8.6E-10	9.0E-09
Glucosylsphingosine	3.6	3.4E-09	3.4E-08
(3-O-sulfo)GalCer(d18:1/18:0)	1.4	5.5E-09	4.8E-08
GM2(d34:1)	3.2	1.2E-08	9.7E-08
BMP(22:6/22:6)	1.7	1.3E-08	9.7E-08
GM1(d36:1)	1.6	1.2E-08	9.7E-08
Hemi-BMP(18:1/18:1)_18:0	1.8	2.3E-08	1.6E-07
GalCer(d18:1/16:0)	2.6	4.6E-08	3.0E-07
GM2(d38:1)	1.7	1.4E-07	8.0E-07
(3-O-sulfo)GalCer(d18:1/16:0)	1.7	1.6E-07	9.0E-07
LPI(18:0)	1.9	2.1E-07	1.1E-06
BMP(20:4/20:4)	1.3	2.2E-07	1.2E-06
PG(16:0_22:6)	3.3	2.5E-07	1.3E-06
LPC(16:1)	1.6	2.8E-07	1.4E-06
Cholesterol	1.3	5.7E-07	2.7E-06
alpha-GalCer(d18:1/18:0)	1.6	1.2E-06	4.8E-06
GalCer(d18:2/20:0)	1.8	1.3E-06	5.1E-06
GM3(d36:1)	1.5	1.4E-06	5.3E-06
GlcCer(d18:1/18:0)	1.4	5.2E-06	1.7E-05
LPC(18:1)	0.8	7.4E-06	2.2E-05
GalCer(d18:1/18:0)	1.2	1.1E-05	2.9E-05
GM3(d38:1)	1.1	1.3E-05	3.3E-05
(3-O-sulfo)GalCer(d18:1/24:0)	1.4	2.5E-05	5.9E-05
SM(d18:1/18:0)	1.5	5.8E-05	1.3E-04
LPE(18:0)	0.8	9.1E-05	1.9E-04
(3-O-sulfo)GalCer(d18:1/24:1(2OH))	1.6	3.8E-04	7.2E-04
alpha-GalCer(d18:1/20:0)	1.2	7.3E-04	1.3E-03
(3-O-sulfo)GalCer(d18:1/24:0(2OH))	1.1	2.7E-03	4.4E-03
LacCer(d18:1/24:1)	0.9	6.7E-03	1.0E-02
(3-O-sulfo)GalCer(d18:1/18:0(2OH)	1.3	1.0E-02	1.5E-02
LPE(16:0)	0.5	1.0E-02	1.5E-02
LPC(24:0)	0.9	1.7E-02	2.4E-02
LPG(20:4)	0.8	3.1E-02	4.0E-02
GlcCer(d18:2/20:0)	0.8	3.1E-02	4.1E-02
alpha-GalCer(d18:2/22:0)	-0.5	5.0E-02	6.3E-02
Cer(d18:1/18:0)	0.4	5.2E-02	6.6E-02
GalCer(d18:1/22:1)	-0.6	6.1E-02	7.7E-02
PC(O-18:0/2:0)	0.8	6.8E-02	8.5E-02
PC(36:4)	-0.3	8.0E-02	9.9E-02
GM3(d40:1)	-0.5	8.9E-02	1.1E-01
PG(18:0_18:1)	-0.3	1.2E-01	1.5E-01
PI(20:4/20:4)	-0.3	1.2E-01	1.5E-01
PC(40:6)	-0.3	1.3E-01	1.6E-01
PC(O-16:0/2:0)	0.4	1.4E-01	1.7E-01
PE(O-18:0/22:6)	-0.3	1.6E-01	1.9E-01
PC(38:4)	-0.3	1.6E-01	1.9E-01
GM3(d34:1)	0.4	1.7E-01	1.9E-01
CL(74:9/18:2)	-0.6	1.9E-01	2.2E-01
GlcCer(d18:1/20:0)	-0.3	2.0E-01	2.3E-01
PC(34:1)	-0.2	2.2E-01	2.5E-01
alpha-GalCer(d18:1/22:1)	0.7	2.5E-01	2.8E-01
PI(18:0_18:1)	-0.3	2.6E-01	3.0E-01
EPA	-0.4	3.0E-01	3.3E-01
GalCer(d18:1/20:0)	0.2	3.7E-01	4.1E-01
PE(P-16:0/20:5)	-0.4	3.7E-01	4.1E-01
HexCer(d18:1/16:0)	0.2	4.0E-01	4.4E-01
PE(P-18:0/20:5)	-0.3	4.0E-01	4.4E-01
LacCer(d18:1/24:0)	0.2	4.2E-01	4.6E-01
SM(d18:1/16:0)	0.2	4.4E-01	4.7E-01
alpha-GalCer(d18:1/22:0)	-0.2	4.5E-01	4.8E-01
HexCer(d18:1/24:0)	-0.2	4.5E-01	4.8E-01
PG(16:0_20:4)	0.2	5.4E-01	5.8E-01
PI(18:0_20:4)	0.1	5.6E-01	5.9E-01
Palmitoylethanolamine	0.2	6.0E-01	6.3E-01
PC(36:1)	0.1	6.1E-01	6.3E-01
HexCer(d18:1/22:0)	0.1	6.8E-01	7.1E-01
HexCer(d18:1/24:1)	0.1	6.8E-01	7.1E-01
PE(P-18:0/18:1)	-0.1	7.0E-01	7.3E-01
LPC(22:6)	0.1	7.2E-01	7.4E-01
PG(18:0_20:4)	0.1	7.6E-01	7.7E-01
LPC(20:4)	0.1	7.7E-01	7.8E-01
GalCer(d18:2/22:0)	0.0	8.6E-01	8.7E-01
PC(40:5)	0.0	9.4E-01	9.4E-01

Table 42. **Lipidomic analysis of acutely isolated microglia from 2 months old** ***Npc1***$^{+/+}$ **and** ***Npc1***$^{-/-}$ **mice.** Detected lipids are listed. The log2 fold change (FC) between *Npc1*$^{-/-}$ and *Npc1*$^{+/+}$ microglia is shown. Significant changed lipids (adjusted p-value) are marked in blue (downregulated) or red (upregulated). Not significant changed lipids are marked in gray (stable).

lipid	log2 FC	p-value	adjusted p-value
Coenzyme Q10	-3.3	6.8E-12	8.0E-11
PS(16:0_22:6)	-2.3	1.4E-11	1.4E-10
Cer(d18:1/24:0)	-1.9	3.6E-11	3.1E-10
PE(P-18:1/20:4)	-1.7	3.3E-10	2.4E-09
PS(18:0_20:4)	-1.8	1.0E-09	7.4E-09
PE(O-18:0/20:4)	-1.7	1.5E-09	1.0E-08
PS(18:0_18:1)	-1.6	4.7E-09	3.1E-08
PE(O-16:0/20:4)	-1.5	5.6E-09	3.4E-08
CE(18:1)	-1.5	5.8E-09	3.4E-08
PC(16:0/5:0(CHO))	-2.0	7.1E-09	4.0E-08
LPC(26:1)	-1.7	8.6E-09	4.5E-08
PE(P-18:1/22:6)	-1.5	8.4E-09	4.5E-08
PC(36:2)	-1.3	1.8E-08	8.5E-08
GlcCer(d18:1/22:1)	-2.1	2.0E-08	9.0E-08
PE(P-16:0/20:4)	-1.4	2.2E-08	9.9E-08
PE(P-18:0/20:4)	-1.4	2.8E-08	1.2E-07
GlcCer(d18:1/24:0)	-2.2	2.9E-08	1.2E-07
PE(P-16:0/22:6)	-1.4	3.1E-08	1.2E-07
PC(16:0/9:0(COOH))	-1.9	3.9E-08	1.5E-07
Cer(d18:1/24:1)	-1.5	6.7E-08	2.4E-07
Cer(d18:1/16:0)	-1.2	6.7E-08	2.4E-07
PS(18:0_22:6)	-1.2	6.8E-08	2.4E-07
PC(38:4)	-1.3	1.0E-07	3.4E-07
PE(O-16:0/22:6)	-1.4	1.2E-07	3.8E-07
PI(16:0_20:4)	-1.2	1.3E-07	4.3E-07
PE(38:5)	-1.6	1.8E-07	5.8E-07
DG(16:0_18:1)	-1.5	1.9E-07	5.8E-07
TG(20:4_36:2)	-1.6	3.8E-07	1.1E-06
DG(16:0_20:4)	-1.3	4.7E-07	1.4E-06
PS(16:0_20:4)	-1.3	6.7E-07	1.9E-06
TG(20:4_36:3)	-1.6	9.0E-07	2.5E-06
PC(36:4)	-1.1	9.8E-07	2.7E-06
PS(16:0_18:1)	-1.3	1.1E-06	2.9E-06
PE(P-18:0/22:6)	-1.2	1.2E-06	3.3E-06
PE(O-18:0/22:6)	-1.2	1.5E-06	3.8E-06
Palmitic acid	-1.2	1.8E-06	4.4E-06
TG(18:1_34:2)	-1.6	2.1E-06	5.1E-06
Cholesterol sulfate	-2.2	2.2E-06	5.5E-06
DG(18:1_20:4)	-1.5	2.3E-06	5.6E-06
PC(34:1)	-1.0	2.4E-06	5.8E-06
PE(36:4)	-1.2	2.9E-06	6.9E-06
PE(40:7)	-1.0	3.2E-06	7.4E-06
PE(P-16:0/22:4)	-1.0	4.1E-06	9.5E-06
PG(16:0_18:1)	-1.2	4.4E-06	1.0E-05
DG(18:1/18:1)	-1.4	4.8E-06	1.1E-05
PC(16:0/9:0(CHO))	-1.5	7.1E-06	1.5E-05
PC(O-16:0/0:0)	-1.2	7.8E-06	1.7E-05
GlcCer(d18:1/24:1)	-1.6	9.2E-06	1.9E-05
DG(18:0_18:1)	-1.4	1.0E-05	2.1E-05
Oleic acid	-1.2	1.2E-05	2.5E-05
TG(18:0_36:2)	-1.2	1.6E-05	3.2E-05
PE(40:6)	-0.8	2.0E-05	3.9E-05
PE(36:1)	-1.1	2.1E-05	4.1E-05
TG(20:4_32:1)	-1.1	2.2E-05	4.2E-05
GM3(d40:1)	-1.4	2.9E-05	5.5E-05
GlcCer(d18:1/22:0)	-1.4	3.0E-05	5.6E-05
PE(36:2)	-1.0	3.0E-05	5.6E-05
PI(18:1/18:1)	-1.0	3.3E-05	5.9E-05
MG(18:0)	-1.4	3.5E-05	6.3E-05
LPC(20:4)	-1.0	3.5E-05	6.3E-05
TG(18:1_34:3)	-1.5	6.0E-05	1.1E-04
PE(38:4)	-1.1	6.5E-05	1.1E-04
MG(16:0)	-1.0	8.0E-05	1.4E-04
PE(P-18:0/20:5)	-1.5	1.1E-04	1.9E-04
PS(18:1/18:1)	-0.9	1.4E-04	2.3E-04
SM(d18:1/24:0)	-1.4	1.4E-04	2.4E-04
PC(38:6)	-0.7	1.7E-04	2.7E-04
SM(d18:1/24:1)	-1.4	2.0E-04	3.2E-04
DG(18:0_20:4)	-0.9	2.1E-04	3.3E-04
MG(18:1)	-1.2	2.3E-04	3.6E-04
PE(34:1)	-0.9	2.3E-04	3.6E-04
alpha-GalCer(d18:1/22:0)	-1.4	3.1E-04	4.9E-04
PE(P-18:0/18:2)	-1.1	3.6E-04	5.5E-04
Palmitoleic acid	-1.2	4.2E-04	6.4E-04
TG(20:4_34:2)	-1.2	4.6E-04	6.8E-04
Stearic acid	-1.0	1.2E-03	1.8E-03
TG(22:6_36:2)	-1.4	1.8E-03	2.5E-03
GlcCer(d18:2/22:0)	-1.0	3.0E-03	4.3E-03
TG(20:4_36:0)	-0.7	3.7E-03	5.2E-03
CE(20:4)	-1.0	4.5E-03	6.2E-03
PC(40:6)	-0.5	4.8E-03	6.6E-03
PEth(16:0_18:1)	-1.6	7.5E-03	1.0E-02
PE(40:4)	-0.7	7.7E-03	1.0E-02
Arachidonic acid_MRM	-0.5	1.4E-02	1.8E-02
CL(74:9/18:2)	-1.2	2.0E-02	2.6E-02
PI(18:0_18:1)	-0.5	2.1E-02	2.7E-02
PC(O-16:0/2:0)	-0.6	2.4E-02	3.0E-02
PG(18:1/18:1)	-0.6	2.4E-02	3.1E-02
alpha-GalCer(d18:2/22:0)	-0.6	2.4E-02	3.1E-02
alpha-GalCer(d18:1/22:1)	-1.5	2.5E-02	3.1E-02
CE(22:6)	-1.0	2.6E-02	3.2E-02
CE(16:1)	-0.9	3.7E-02	4.5E-02
PI(16:0_18:1)	-0.4	3.7E-02	4.5E-02
PI(18:0_20:4)	-0.4	3.7E-02	4.5E-02
BMP(18:0_18:1)	5.9	7.3E-19	7.7E-17
HexCer(d18:1/18:0)	4.9	8.7E-19	7.7E-17
LacCer(d18:1/18:0)	5.8	3.6E-18	2.1E-16
BMP(16:0_18:1)	6.0	5.6E-18	2.5E-16
BMP(18:1/18:1)	4.3	2.3E-17	8.3E-16
BMP(16:0_20:4)	4.2	2.6E-16	7.7E-15
BMP(16:1/16:1)	4.4	4.2E-16	1.0E-14
(3-O-sulfo)GalCer(d18:1/18:0)	3.5	7.7E-16	1.7E-14
LPG(18:1)	3.3	2.5E-15	4.9E-14
BMP(18:0_20:4)	4.4	1.5E-13	2.5E-12
GM3(d38:1)	3.6	1.5E-13	2.5E-12
GM2(d38:1)	3.8	7.3E-13	1.1E-11
Hemi-BMP(18:1/18:1)_16:0	3.5	1.0E-12	1.4E-11
GlcCer(d18:2/18:0)	4.4	6.7E-12	8.0E-11
GlcCer(d18:1/18:0)	3.3	1.3E-11	1.4E-10
(3-O-sulfo)GalCer(d18:1/16:0)	3.2	1.3E-11	1.4E-10
HexCer(d18:1/16:0)	2.0	3.3E-11	3.1E-10
Hemi-BMP(18:1/18:1)_18:0	2.9	4.0E-11	3.4E-10
LacCer(d18:1/16:0)	2.8	2.6E-10	2.1E-09
(3-O-sulfo)GalCer(d18:1/24:1)	2.3	3.1E-10	2.4E-09
LPC(16:0)	1.3	5.0E-09	3.2E-08
GM2(d36:1)	2.5	8.5E-09	4.5E-08
GM3(d36:1)	2.2	1.5E-08	7.7E-08
HexCer(d18:1/24:1)	1.7	1.6E-08	7.7E-08
HexCer(d18:1/22:0)	1.7	1.9E-08	8.8E-08
LPC(18:0)	1.2	3.0E-08	1.2E-07
(3-O-sulfo)GalCer(d18:1/24:0)	2.5	3.7E-08	1.4E-07
Cer(d18:1/18:0)	1.3	5.0E-08	1.9E-07
GM1(d36:1)	1.6	8.1E-08	2.8E-07
(3-O-sulfo)GalCer(d18:1/24:0(2OH))	2.8	1.0E-07	3.4E-07
HexCer(d18:1/24:0)	1.6	2.5E-07	7.7E-07
GalCer(d18:2/18:0)	1.8	3.8E-07	1.1E-06
(3-O-sulfo)GalCer(d18:1/18:0(2OH)	3.4	6.6E-07	1.9E-06
(3-O-sulfo)GalCer(d18:1/24:1(2OH))	2.8	1.5E-06	3.9E-06
GalCer(d18:2/20:0)	1.8	7.0E-06	1.5E-05
PG(18:0_20:4)	1.3	7.8E-06	1.7E-05
LPI(18:0)	1.6	1.1E-05	2.3E-05
PG(16:0_22:6)	2.8	1.6E-05	3.2E-05
BMP(20:4/20:4)	1.0	3.2E-05	5.9E-05
LPG(20:4)	1.8	4.3E-05	7.6E-05
SM(d18:1/18:0)	1.5	1.2E-04	2.0E-04
PG(16:0_20:4)	1.2	1.6E-04	2.6E-04
Glucosylsphingosine	1.8	3.6E-04	5.5E-04
LPE(16:0)	0.8	3.6E-04	5.5E-04
LPE(18:0)	0.8	4.4E-04	6.5E-04
LPC(16:1)	1.0	5.5E-04	8.0E-04
LacCer(d18:1/24:0)	1.1	1.2E-03	1.7E-03
Cholesterol	0.7	3.1E-03	4.4E-03
GlcCer(d18:2/20:0)	1.1	5.7E-03	7.7E-03
GM2(d34:1)	1.2	7.2E-03	9.8E-03
LacCer(d18:1/24:1)	1.0	7.7E-03	1.0E-02
GalCer(d18:1/16:0)	0.9	1.5E-02	1.9E-02
GalCer(d18:1/18:0)	0.5	6.1E-02	7.3E-02
Palmitoylethanolamine	-0.7	6.4E-02	7.6E-02
CE(18:2)	-1.4	6.5E-02	7.8E-02
GlcCer(d18:1/16:0)	-0.5	7.1E-02	8.4E-02
PE(38:6)	-0.4	7.5E-02	8.8E-02
PC(36:1)	-0.4	8.1E-02	9.4E-02
GalCer(d18:2/22:0)	0.4	1.1E-01	1.3E-01
LPC(24:0)	0.6	1.2E-01	1.3E-01
DHA	-0.4	1.6E-01	1.8E-01
PS(22:6/22:6)	-0.6	1.7E-01	1.9E-01
alpha-GalCer(d18:1/20:0)	-0.5	1.8E-01	2.1E-01
PI(16:0_22:6)	0.3	1.9E-01	2.1E-01
PC(40:5)	-0.3	2.3E-01	2.5E-01
LPC(22:6)	-0.3	2.5E-01	2.8E-01
GM3(d34:1)	-0.3	2.9E-01	3.2E-01
DG(18:0_22:6)	-1.0	3.1E-01	3.4E-01
PG(18:0_18:1)	-0.2	3.6E-01	3.9E-01
PC(O-18:0/2:0)	0.4	3.9E-01	4.2E-01
PE(P-16:0/20:5)	-0.4	4.1E-01	4.4E-01
GlcCer(d18:1/20:0)	0.2	4.2E-01	4.5E-01
CL(72:6/18:2)	0.6	4.2E-01	4.5E-01
alpha-GalCer(d18:1/18:0)	0.2	4.3E-01	4.5E-01
GalCer(d18:1/22:1)	-0.3	4.5E-01	4.8E-01
BMP(22:6/22:6)	0.2	4.6E-01	4.8E-01
PI(20:4/20:4)	-0.2	4.8E-01	5.0E-01
GalCer(d18:1/20:0)	0.2	4.8E-01	5.0E-01
LPC(18:1)	-0.1	7.3E-01	7.4E-01
EPA	-0.1	7.3E-01	7.4E-01
PE(P-18:0/18:1)	0.1	7.5E-01	7.6E-01
SM(d18:1/16:0)	-0.1	8.1E-01	8.1E-01
PI(18:0_22:6)	0.0	9.8E-01	9.8E-01

Table 43. Lipidomic analysis of acutely isolated microglia from 2 months old *Cre-* and *Cre+* mice. Detected lipids are listed. The log2 fold change (FC) between *Cre+* and *Cre-* microglia is shown. Significant changed lipids (adjusted p-value) are marked in blue (downregulated) or red (upregulated). Not significant changed lipids are marked in gray (stable).

lipid	log2 FC	p-value	adjusted p-value
Coenzyme Q10	-2.4	1.0E-09	1.4E-08
PS(16:0_22:6)	-1.7	2.0E-09	2.6E-08
PE(P-18:1/22:6)	-1.4	1.3E-08	1.4E-07
PS(18:0_22:6)	-1.3	2.1E-08	2.0E-07
PE(P-18:0/20:4)	-1.4	2.2E-08	2.1E-07
PE(O-16:0/20:4)	-1.3	2.4E-08	2.2E-07
PI(16:0_18:1)	-1.4	3.1E-08	2.6E-07
PS(18:0_18:1)	-1.4	4.2E-08	3.4E-07
PS(18:0_20:4)	-1.4	4.4E-08	3.4E-07
PE(O-18:0/20:4)	-1.3	5.2E-08	3.9E-07
PE(P-18:1/20:4)	-1.2	6.4E-08	4.5E-07
PE(O-16:0/22:6)	-1.3	1.2E-07	7.9E-07
PI(18:0_18:1)	-1.5	1.6E-07	1.0E-06
PE(P-18:0/22:6)	-1.3	1.6E-07	1.0E-06
PI(18:0_22:6)	-1.3	1.9E-07	1.1E-06
PE(P-16:0/22:6)	-1.2	1.9E-07	1.1E-06
PE(O-18:0/22:6)	-1.2	3.0E-07	1.7E-06
PE(P-16:0/20:4)	-1.1	5.2E-07	2.6E-06
PI(16:0_20:4)	-1.1	5.2E-07	2.6E-06
PG(16:0_18:1)	-1.3	8.1E-07	4.0E-06
PI(18:0_20:4)	-1.0	1.4E-06	6.4E-06
GM3(d40:1)	-1.6	3.4E-06	1.5E-05
PS(18:1/18:1)	-1.0	1.8E-05	7.4E-05
PI(16:0_22:6)	-1.1	1.9E-05	7.6E-05
PE(P-16:0/22:4)	-0.9	2.0E-05	7.7E-05
PS(16:0_18:1)	-1.0	2.3E-05	8.8E-05
GlcCer(d18:1/22:1)	-1.3	3.2E-05	1.2E-04
Cer(d18:1/16:0)	-0.8	3.2E-05	1.2E-04
PE(P-18:0/18:2)	-1.3	3.4E-05	1.2E-04
GlcCer(d18:1/24:0)	-1.3	4.2E-05	1.5E-04
BMP(22:6/22:6)	-1.1	4.6E-05	1.6E-04
PE(P-18:0/18:1)	-0.9	6.0E-05	2.0E-04
PE(36:1)	-1.0	6.6E-05	2.2E-04
GlcCer(d18:1/16:0)	-1.3	7.6E-05	2.4E-04
GlcCer(d18:2/22:0)	-1.4	8.6E-05	2.7E-04
Palmitic acid	-0.9	9.4E-05	2.9E-04
SM(d18:1/24:0)	-1.3	1.6E-04	4.8E-04
PS(16:0_20:4)	-0.8	1.6E-04	4.8E-04
PI(18:1/18:1)	-0.9	1.7E-04	4.9E-04
PE(P-18:0/20:5)	-1.4	1.8E-04	4.9E-04
PC(O-16:0/0:0)	-0.9	1.8E-04	4.9E-04
LPC(22:6)	-0.8	2.2E-04	5.9E-04
Cer(d18:1/24:0)	-0.7	2.2E-04	5.9E-04
Oleic acid	-0.9	3.2E-04	8.4E-04
PE(38:5)	-0.9	3.7E-04	9.5E-04
Stearic acid	-1.1	4.8E-04	1.2E-03
PG(18:0_18:1)	-0.8	4.7E-04	1.2E-03
PE(40:6)	-0.6	5.4E-04	1.3E-03
GM3(d34:1)	-1.1	7.7E-04	1.8E-03
PE(40:4)	-0.8	8.0E-04	1.8E-03
PE(38:4)	-0.9	9.5E-04	2.1E-03
DHA	-0.8	9.7E-04	2.2E-03
GlcCer(d18:1/22:0)	-1.0	1.0E-03	2.2E-03
PC(40:5)	-0.8	1.2E-03	2.6E-03
SM(d18:1/24:1)	-1.1	1.4E-03	2.9E-03
PC(16:0/5:0(CHO))	-0.8	1.4E-03	2.9E-03
DG(16:0_20:4)	-0.7	1.6E-03	3.3E-03
PS(22:6/22:6)	-1.5	2.0E-03	3.9E-03
PE(36:4)	-0.7	2.1E-03	4.1E-03
PC(38:6)	-0.5	2.1E-03	4.2E-03
PE(36:2)	-0.7	2.3E-03	4.4E-03
LPC(20:4)	-0.7	2.5E-03	4.8E-03
PI(20:4/20:4)	-0.7	3.0E-03	5.6E-03
Cholesterol sulfate	-1.1	3.0E-03	5.6E-03
GlcCer(d18:1/24:1)	-0.9	3.4E-03	6.1E-03
PC(40:6)	-0.5	3.3E-03	6.1E-03
PC(16:0/9:0(COOH))	-0.7	4.5E-03	8.1E-03
TG(18:0_36:2)	-0.7	7.7E-03	1.3E-02
DG(18:0_22:6)	-2.8	9.1E-03	1.5E-02
PE(34:1)	-0.6	9.3E-03	1.6E-02
Palmitoleic acid	-0.8	1.0E-02	1.7E-02
PC(38:4)	-0.5	1.0E-02	1.7E-02
DG(18:1/18:1)	-0.6	1.2E-02	1.9E-02
GlcCer(d18:1/20:0)	-0.7	1.3E-02	2.1E-02
DG(18:0_20:4)	-0.5	1.4E-02	2.2E-02
CE(18:1)	-0.5	1.5E-02	2.4E-02
Cer(d18:1/24:1)	-0.5	1.7E-02	2.7E-02
LPC(26:1)	-0.5	2.6E-02	4.0E-02
alpha-GalCer(d18:2/22:0)	-0.5	3.0E-02	4.6E-02
GalCer(d18:1/22:1)	-0.7	3.1E-02	4.7E-02
LPE(18:0)	-0.4	3.1E-02	4.7E-02
PE(40:7)	-0.4	3.3E-02	4.9E-02
BMP(18:0_18:1)	4.4	8.1E-17	1.4E-14
BMP(16:0_18:1)	4.6	4.6E-16	4.1E-14
LacCer(d18:1/18:0)	4.1	1.5E-15	8.6E-14
BMP(18:1/18:1)	3.3	2.2E-15	9.7E-14
LPG(18:1)	2.9	1.6E-14	5.5E-13
HexCer(d18:1/18:0)	2.8	2.3E-14	6.8E-13
BMP(16:0_20:4)	3.1	4.0E-14	1.0E-12
GM2(d38:1)	4.1	8.3E-14	1.8E-12
BMP(16:1/16:1)	3.0	2.1E-13	4.2E-12
(3-O-sulfo)GalCer(d18:1/18:0)	2.0	2.3E-11	4.0E-10
BMP(18:0_20:4)	3.0	7.9E-11	1.3E-09
GM2(d36:1)	3.0	2.2E-10	3.2E-09
GlcCer(d18:2/18:0)	2.9	6.2E-09	7.3E-08
Hemi-BMP(18:1/18:1)_16:0	2.1	8.3E-09	9.2E-08
(3-O-sulfo)GalCer(d18:1/16:0)	1.8	2.3E-07	1.3E-06
Hemi-BMP(18:1/18:1)_18:0	1.6	4.9E-07	2.6E-06
LacCer(d18:1/16:0)	1.6	1.4E-06	6.4E-06
GalCer(d18:2/18:0)	1.5	2.0E-06	9.1E-06
GalCer(d18:1/18:0)	1.3	6.2E-06	2.7E-05
GlcCer(d18:1/18:0)	1.4	1.3E-05	5.5E-05
(3-O-sulfo)GalCer(d18:1/18:0(2OH)	2.5	3.2E-05	1.2E-04
(3-O-sulfo)GalCer(d18:1/24:0(2OH))	1.6	1.4E-04	4.1E-04
Glucosylsphingosine	1.8	1.8E-04	4.9E-04
alpha-GalCer(d18:1/18:0)	1.1	2.7E-04	7.0E-04
(3-O-sulfo)GalCer(d18:1/24:1(2OH))	1.7	4.6E-04	1.1E-03
GalCer(d18:1/16:0)	1.4	4.5E-04	1.1E-03
LPC(16:0)	0.6	5.7E-04	1.4E-03
GalCer(d18:2/20:0)	1.1	1.0E-03	2.2E-03
PG(16:0_22:6)	1.8	1.4E-03	2.9E-03
GM2(d34:1)	1.4	1.4E-03	2.9E-03
(3-O-sulfo)GalCer(d18:1/24:1)	0.8	1.4E-03	2.9E-03
(3-O-sulfo)GalCer(d18:1/24:0)	1.0	3.2E-03	5.9E-03
HexCer(d18:1/16:0)	0.5	4.9E-03	8.7E-03
LPC(18:0)	0.5	6.3E-03	1.1E-02
GM3(d38:1)	0.7	7.2E-03	1.3E-02
LPG(20:4)	0.9	1.3E-02	2.1E-02
PC(36:2)	-0.4	3.9E-02	5.7E-02
PC(16:0/9:0(CHO))	-0.6	3.9E-02	5.8E-02
PG(18:1/18:1)	-0.5	4.7E-02	6.9E-02
Cholesterol	0.5	4.8E-02	7.0E-02
DG(16:0_18:1)	-0.4	4.9E-02	7.0E-02
CE(20:4)	-0.6	5.2E-02	7.4E-02
PE(38:6)	-0.4	5.6E-02	7.9E-02
TG(18:1_34:3)	-0.6	5.7E-02	8.0E-02
PE(P-16:0/20:5)	-0.9	5.7E-02	8.0E-02
TG(20:4_36:2)	-0.4	6.9E-02	9.6E-02
alpha-GalCer(d18:1/20:0)	0.6	7.2E-02	9.8E-02
PC(34:1)	-0.3	7.2E-02	9.9E-02
GM3(d36:1)	0.5	7.9E-02	1.1E-01
TG(20:4_34:2)	-0.5	8.6E-02	1.2E-01
LPC(16:1)	0.4	9.4E-02	1.2E-01
TG(18:1_34:2)	-0.4	9.4E-02	1.2E-01
LPI(18:0)	-0.5	1.1E-01	1.4E-01
LPE(16:0)	-0.3	1.1E-01	1.5E-01
TG(20:4_32:1)	0.4	1.1E-01	1.5E-01
CL(72:6/18:2)	-1.2	1.2E-01	1.5E-01
alpha-GalCer(d18:1/22:0)	-0.5	1.2E-01	1.5E-01
PC(36:1)	-0.3	1.3E-01	1.6E-01
CE(22:6)	-0.6	1.4E-01	1.8E-01
MG(16:0)	-0.3	1.5E-01	1.8E-01
Arachidonic acid_MRM	-0.3	1.6E-01	2.0E-01
LacCer(d18:1/24:1)	-0.5	1.8E-01	2.2E-01
GM1(d36:1)	0.3	1.9E-01	2.3E-01
PEth(16:0_18:1)	-0.7	1.9E-01	2.3E-01
LPC(24:0)	0.5	1.9E-01	2.3E-01
PC(O-18:0/2:0)	0.6	1.9E-01	2.3E-01
CE(16:1)	-0.5	1.9E-01	2.3E-01
DG(18:1_20:4)	-0.3	1.9E-01	2.3E-01
PC(O-16:0/2:0)	-0.3	2.0E-01	2.3E-01
EPA	-0.5	2.0E-01	2.3E-01
TG(20:4_36:0)	-0.3	2.1E-01	2.4E-01
TG(22:6_36:2)	-0.5	2.2E-01	2.5E-01
alpha-GalCer(d18:1/22:1)	-0.7	2.4E-01	2.8E-01
Cer(d18:1/18:0)	0.2	2.7E-01	3.0E-01
PG(16:0_20:4)	0.3	2.7E-01	3.1E-01
Palmitoylethanolamine	-0.4	2.8E-01	3.1E-01
HexCer(d18:1/24:1)	0.2	3.1E-01	3.4E-01
GalCer(d18:1/20:0)	0.3	3.2E-01	3.5E-01
SM(d18:1/18:0)	0.3	3.3E-01	3.6E-01
DG(18:0_18:1)	-0.3	3.4E-01	3.7E-01
TG(20:4_36:3)	-0.2	3.5E-01	3.8E-01
BMP(20:4/20:4)	-0.2	4.2E-01	4.5E-01
PG(18:0_20:4)	0.2	4.3E-01	4.6E-01
PC(36:4)	-0.1	5.4E-01	5.8E-01
SM(d18:1/16:0)	-0.1	6.1E-01	6.5E-01
CL(74:9/18:2)	-0.2	6.7E-01	7.1E-01
CE(18:2)	-0.3	7.0E-01	7.3E-01
MG(18:1)	-0.1	7.0E-01	7.3E-01
HexCer(d18:1/24:0)	-0.1	7.2E-01	7.4E-01
GalCer(d18:2/22:0)	-0.1	7.6E-01	7.8E-01
LPC(18:1)	-0.1	7.8E-01	8.0E-01
HexCer(d18:1/22:0)	0.1	7.9E-01	8.0E-01
MG(18:0)	0.0	8.9E-01	9.0E-01
GlcCer(d18:2/20:0)	0.0	9.0E-01	9.0E-01
LacCer(d18:1/24:0)	0.0	9.8E-01	9.8E-01

Table 44. Lipidomic analysis of acutely isolated microglia from 2 months old *Npc1*$^{+/+}$ and 1-week old *Npc1*$^{+/+}$ mice. Detected lipids are listed. The log2 fold change (FC) between 2 months and P7 is shown. Significant changed lipids (adjusted p-value) are marked in blue (downregulated) or red (upregulated). Not significant changed lipids are marked in gray (stable).

lipid	log2 FC	p-value	adjusted p-value
HexCer(d18:1/16:0)	-3.6	9.9E-13	1.8E-10
Hemi-BMP(18:1/18:1)_16:0	-3.5	2.5E-09	2.2E-07
TG(20:4_32:1)	-2.7	7.3E-09	4.3E-07
BMP(16:1/16:1)	-2.5	3.0E-08	1.1E-06
GlcCer(d18:1/16:0)	-3.3	5.8E-08	1.7E-06
Hemi-BMP(18:1/18:1)_18:0	-2.7	1.2E-07	2.6E-06
LPE(16:0)	-2.0	2.0E-07	3.2E-06
PE(P-16:0/20:4)	-1.5	3.3E-06	4.2E-05
(3-O-sulfo)GalCer(d18:1/16:0)	-2.3	3.7E-06	4.4E-05
PG(16:0_18:1)	-1.7	5.6E-06	5.5E-05
HexCer(d18:1/22:0)	-1.6	1.8E-05	1.6E-04
LPE(18:0)	-1.4	2.0E-05	1.6E-04
PI(16:0_22:6)	-1.6	3.0E-05	2.3E-04
TG(20:4_34:2)	-2.2	4.5E-05	3.0E-04
LPC(16:1)	-1.8	4.5E-05	3.0E-04
GlcCer(d18:1/20:0)	-1.7	9.7E-05	5.7E-04
Oleic acid	-1.5	9.9E-05	5.7E-04
GlcCer(d18:1/22:0)	-1.8	1.1E-04	5.9E-04
PG(18:0_18:1)	-1.3	1.3E-04	6.6E-04
PS(16:0_20:4)	-1.3	1.5E-04	7.5E-04
Palmitic acid	-1.3	1.6E-04	7.9E-04
GlcCer(d18:2/22:0)	-2.0	2.1E-04	1.0E-03
PE(P-16:0/20:5)	-3.0	2.5E-04	1.1E-03
Arachidonic acid_MRM	-1.0	3.7E-04	1.5E-03
BMP(16:0_18:1)	-1.3	5.9E-04	2.3E-03
PG(18:1/18:1)	-1.4	9.2E-04	3.3E-03
PI(18:1/18:1)	-1.1	1.1E-03	3.8E-03
GlcCer(d18:1/18:0)	-1.4	1.3E-03	4.1E-03
(3-O-sulfo)GalCer(d18:1/18:0)	-0.9	1.4E-03	4.4E-03
TG(20:4_36:3)	-1.3	1.5E-03	4.5E-03
PI(16:0_20:4)	-0.9	1.4E-03	4.5E-03
PG(18:0_20:4)	-1.2	1.7E-03	5.2E-03
PS(16:0_18:1)	-1.0	2.6E-03	7.5E-03
GlcCer(d18:1/24:0)	-1.3	2.7E-03	7.6E-03
PE(O-16:0/20:4)	-0.8	3.2E-03	8.7E-03
PI(18:0_20:4)	-0.8	3.4E-03	9.0E-03
BMP(18:1/18:1)	-0.9	3.5E-03	9.2E-03
Palmitoleic acid	-1.3	5.6E-03	1.3E-02
LacCer(d18:1/16:0)	-1.2	5.6E-03	1.3E-02
PE(P-16:0/22:6)	-0.8	6.1E-03	1.4E-02
PI(20:4/20:4)	-0.9	6.5E-03	1.5E-02
PE(P-16:0/22:4)	-0.7	9.7E-03	2.2E-02
GlcCer(d18:1/24:1)	-1.2	1.3E-02	2.8E-02
PS(18:0_22:6)	-0.6	1.3E-02	2.9E-02
PE(P-18:0/18:2)	-1.1	1.4E-02	2.9E-02
PI(18:0_22:6)	-0.7	1.5E-02	3.1E-02
PS(18:1/18:1)	-0.8	1.6E-02	3.4E-02
CE(20:4)	-1.1	2.5E-02	4.9E-02
PC(38:4)	2.2	2.1E-08	9.5E-07
Coenzyme Q10	2.9	7.2E-08	1.8E-06
PC(40:6)	1.8	1.3E-07	2.6E-06
alpha-GalCer(d18:2/22:0)	2.5	1.7E-07	3.0E-06
GM3(d38:1)	2.3	5.5E-07	7.6E-06
PC(36:1)	1.9	5.6E-07	7.6E-06
(3-O-sulfo)GalCer(d18:1/24:1)	1.9	4.7E-06	5.2E-05
GM2(d36:1)	2.5	5.5E-06	5.5E-05
Cer(d18:1/18:0)	1.4	8.6E-06	8.1E-05
(3-O-sulfo)GalCer(d18:1/24:0)	2.4	2.0E-05	1.6E-04
Glucosylsphingosine	3.2	4.1E-05	2.9E-04
PE(40:6)	1.2	4.1E-05	2.9E-04
LPC(18:0)	1.0	4.7E-05	3.0E-04
Cer(d18:1/24:1)	1.4	5.6E-05	3.4E-04
Cholesterol	1.4	1.1E-04	5.9E-04
PC(34:1)	1.0	2.2E-04	1.0E-03
PC(O-16:0/2:0)	1.6	2.7E-04	1.2E-03
PC(36:4)	1.1	2.8E-04	1.2E-03
Cer(d18:1/24:0)	1.0	3.1E-04	1.3E-03
GM3(d36:1)	1.6	3.9E-04	1.6E-03
SM(d18:1/24:0)	1.8	5.6E-04	2.2E-03
LPC(22:6)	1.1	6.4E-04	2.4E-03
GM3(d40:1)	1.5	7.6E-04	2.8E-03
GalCer(d18:1/18:0)	1.3	8.7E-04	3.2E-03
GalCer(d18:1/22:1)	1.8	1.2E-03	3.9E-03
alpha-GalCer(d18:1/18:0)	1.5	1.2E-03	3.9E-03
alpha-GalCer(d18:1/22:0)	1.8	1.5E-03	4.5E-03
LacCer(d18:1/18:0)	1.1	2.1E-03	6.2E-03
LPC(20:4)	1.0	2.6E-03	7.5E-03
alpha-GalCer(d18:1/20:0)	1.7	2.8E-03	7.7E-03
PC(36:2)	0.8	2.8E-03	7.7E-03
SM(d18:1/18:0)	1.6	3.8E-03	9.7E-03
alpha-GalCer(d18:1/22:1)	3.1	4.7E-03	1.2E-02
PC(38:6)	0.7	4.9E-03	1.2E-02
GalCer(d18:1/20:0)	1.1	5.0E-03	1.2E-02
GalCer(d18:2/22:0)	1.0	6.1E-03	1.4E-02
GM2(d38:1)	1.1	6.5E-03	1.5E-02
LPC(24:0)	1.5	1.4E-02	3.0E-02
BMP(22:6/22:6)	0.9	1.4E-02	3.0E-02
SM(d18:1/24:1)	1.2	1.8E-02	3.7E-02
BMP(20:4/20:4)	0.7	2.1E-02	4.2E-02
TG(20:4_36:0)	0.8	2.2E-02	4.3E-02
LPC(18:1)	0.6	2.2E-02	4.3E-02
PE(P-18:1/20:4)	-0.6	2.9E-02	5.5E-02
GalCer(d18:2/18:0)	0.9	2.9E-02	5.5E-02
GlcCer(d18:2/18:0)	-1.1	3.1E-02	5.9E-02
HexCer(d18:1/24:0)	-0.8	3.4E-02	6.4E-02
HexCer(d18:1/18:0)	-0.6	3.6E-02	6.6E-02
PG(16:0_20:4)	-0.9	3.6E-02	6.6E-02
DG(16:0_20:4)	-0.6	3.9E-02	7.0E-02
PC(16:0/9:0(COOH))	0.7	4.0E-02	7.2E-02
PEth(16:0_18:1)	-1.8	4.1E-02	7.3E-02
PI(16:0_18:1)	-0.6	4.3E-02	7.5E-02
DG(18:0_18:1)	0.8	4.5E-02	7.8E-02
Palmitoylethanolamine	1.0	4.5E-02	7.8E-02
(3-O-sulfo)GalCer(d18:1/18:0(2OH))	-1.6	4.7E-02	8.0E-02
(3-O-sulfo)GalCer(d18:1/24:0(2OH))	1.1	5.7E-02	9.6E-02
CE(16:1)	-1.2	5.8E-02	9.7E-02
GlcCer(d18:1/22:1)	-0.8	5.9E-02	9.7E-02
PS(22:6/22:6)	-1.3	6.1E-02	1.0E-01
PE(36:1)	0.6	6.2E-02	1.0E-01
GM1(d36:1)	0.6	7.0E-02	1.1E-01
DHA	-0.6	7.4E-02	1.2E-01
CL(74:9/18:2)	-1.3	7.7E-02	1.2E-01
HexCer(d18:1/24:1)	-0.6	7.8E-02	1.2E-01
PE(P-18:1/22:6)	-0.5	7.9E-02	1.2E-01
CE(22:6)	1.2	8.0E-02	1.2E-01
LPC(16:0)	0.4	8.2E-02	1.2E-01
PE(P-18:0/18:1)	0.5	8.6E-02	1.3E-01
GlcCer(d18:2/20:0)	-1.0	8.7E-02	1.3E-01
LPI(18:0)	-0.7	9.8E-02	1.5E-01
PE(34:1)	-0.5	1.0E-01	1.5E-01
Stearic acid	-0.7	1.1E-01	1.7E-01
PE(O-18:0/22:6)	0.5	1.1E-01	1.7E-01
Cholesterol sulfate	-0.8	1.2E-01	1.7E-01
MG(18:1)	0.6	1.4E-01	1.9E-01
GM3(d34:1)	-0.6	1.4E-01	1.9E-01
GalCer(d18:2/20:0)	0.7	1.4E-01	2.0E-01
PC(16:0/5:0(CHO))	0.5	1.4E-01	2.0E-01
BMP(18:0_18:1)	-0.5	1.5E-01	2.0E-01
DG(18:1_20:4)	-0.5	1.5E-01	2.0E-01
MG(18:0)	0.6	1.5E-01	2.0E-01
PC(40:5)	0.5	1.5E-01	2.0E-01
PE(P-18:0/20:4)	-0.4	1.5E-01	2.1E-01
PC(O-18:0/2:0)	0.9	1.9E-01	2.6E-01
BMP(18:0_20:4)	0.5	2.0E-01	2.6E-01
DG(18:0_22:6)	-2.0	2.0E-01	2.7E-01
CE(18:1)	0.3	2.1E-01	2.8E-01
LPC(26:1)	0.4	2.3E-01	3.0E-01
PE(36:4)	-0.4	2.5E-01	3.1E-01
CL(72:6/18:2)	-1.4	2.5E-01	3.1E-01
LacCer(d18:1/24:1)	-0.6	2.7E-01	3.4E-01
DG(18:1/18:1)	0.4	2.8E-01	3.6E-01
GM2(d34:1)	-0.7	2.9E-01	3.6E-01
PE(40:7)	0.3	2.9E-01	3.6E-01
SM(d18:1/16:0)	-0.2	3.7E-01	4.5E-01
BMP(16:0_20:4)	-0.3	3.7E-01	4.5E-01
LPG(18:1)	-0.2	3.9E-01	4.7E-01
PC(16:0/9:0(CHO))	0.3	4.7E-01	5.7E-01
PE(P-18:0/22:6)	-0.2	4.8E-01	5.8E-01
(3-O-sulfo)GalCer(d18:1/24:1(2OH))	-0.4	4.9E-01	5.8E-01
TG(22:6_36:2)	-0.4	5.2E-01	6.2E-01
Cer(d18:1/16:0)	-0.2	5.4E-01	6.3E-01
PS(18:0_18:1)	0.2	5.4E-01	6.3E-01
DG(18:0_20:4)	0.2	5.5E-01	6.3E-01
PE(O-16:0/22:6)	-0.2	5.5E-01	6.3E-01
PE(O-18:0/20:4)	0.2	5.6E-01	6.4E-01
EPA	-0.3	5.8E-01	6.6E-01
GalCer(d18:1/16:0)	0.3	5.8E-01	6.6E-01
PI(18:0_18:1)	0.2	6.0E-01	6.8E-01
PE(36:2)	-0.1	6.2E-01	6.9E-01
PS(16:0_22:6)	-0.1	6.2E-01	6.9E-01
PE(38:4)	0.2	6.7E-01	7.4E-01
LPG(20:4)	0.2	6.7E-01	7.4E-01
MG(16:0)	0.1	7.6E-01	8.2E-01
PE(38:6)	-0.1	7.6E-01	8.2E-01
TG(18:1_34:2)	0.1	7.8E-01	8.4E-01
DG(16:0_18:1)	0.1	8.1E-01	8.7E-01
CE(18:2)	-0.3	8.2E-01	8.7E-01
PE(P-18:0/20:5)	0.1	8.2E-01	8.7E-01
TG(20:4_36:2)	-0.1	8.7E-01	9.1E-01
LacCer(d18:1/24:0)	-0.1	8.7E-01	9.1E-01
TG(18:1_34:3)	0.1	8.9E-01	9.2E-01
PE(38:5)	0.0	8.9E-01	9.2E-01
TG(18:0_36:2)	0.0	9.2E-01	9.4E-01
PG(16:0_22:6)	-0.1	9.3E-01	9.5E-01
PC(O-16:0/0:0)	0.0	9.4E-01	9.5E-01
PS(18:0_20:4)	0.0	9.5E-01	9.6E-01
PE(40:4)	0.0	9.6E-01	9.6E-01

Table 45. **Lipidomic analysis of acutely isolated microglia from 2 months old *Npc1*$^{-/-}$ and 1-week old *Npc1*$^{-/-}$ mice.** Detected lipids are listed. The log2 fold change (FC) between 2 months and P7 is shown. Significant changed lipids (adjusted p-value) are marked in blue (downregulated) or red (upregulated). Not significant changed lipids are marked in gray (stable).

lipid	log2 FC	p-value	adjusted p-value
TG(20:4_32:1)	-2.8	2.7E-09	1.6E-07
PE(P-16:0/20:4)	-1.9	5.4E-08	1.6E-06
GlcCer(d18:1/16:0)	-3.1	6.5E-08	1.7E-06
HexCer(d18:1/16:0)	-1.8	1.8E-07	3.5E-06
BMP(16:1/16:1)	-2.1	2.8E-07	4.1E-06
PE(P-18:1/20:4)	-1.6	5.0E-07	6.8E-06
LPC(16:1)	-2.4	6.6E-07	7.6E-06
PG(16:0_18:1)	-1.9	6.9E-07	7.6E-06
PI(16:0_20:4)	-1.5	9.5E-07	9.9E-06
LPE(16:0)	-1.7	1.4E-06	1.3E-05
Hemi-BMP(18:1/18:1)_16:0	-2.2	1.9E-06	1.7E-05
GlcCer(d18:1/24:0)	-2.5	2.1E-06	1.8E-05
TG(20:4_34:2)	-2.7	2.7E-06	2.2E-05
PE(O-16:0/20:4)	-1.5	3.1E-06	2.3E-05
PI(18:1/18:1)	-1.7	5.4E-06	3.7E-05
PI(18:0_20:4)	-1.3	7.9E-06	5.2E-05
TG(20:4_36:3)	-2.0	8.3E-06	5.2E-05
LPE(18:0)	-1.5	1.0E-05	6.4E-05
GlcCer(d18:1/22:0)	-2.1	1.9E-05	1.1E-04
Oleic acid	-1.7	2.5E-05	1.4E-04
PE(P-16:0/22:6)	-1.2	3.6E-05	1.9E-04
GlcCer(d18:1/24:1)	-2.1	4.0E-05	2.0E-04
Palmitic acid	-1.4	4.0E-05	2.0E-04
PS(16:0_20:4)	-1.4	4.6E-05	2.2E-04
GlcCer(d18:2/22:0)	-2.1	6.2E-05	2.8E-04
Hemi-BMP(18:1/18:1)_18:0	-1.7	8.6E-05	3.7E-04
PS(16:0_22:6)	-1.2	1.1E-04	4.7E-04
GlcCer(d18:1/22:1)	-1.7	1.2E-04	4.8E-04
GM2(d34:1)	-2.7	1.6E-04	6.3E-04
PE(P-16:0/20:5)	-3.0	1.8E-04	6.8E-04
PS(16:0_18:1)	-1.3	1.9E-04	7.0E-04
PE(P-18:1/22:6)	-1.1	1.9E-04	7.0E-04
PG(18:0_18:1)	-1.2	2.6E-04	8.9E-04
Arachidonic acid_MRM	-0.9	4.3E-04	1.5E-03
PS(18:0_22:6)	-0.9	6.2E-04	2.1E-03
PG(18:1/18:1)	-1.3	1.1E-03	3.5E-03
PE(P-18:0/20:4)	-0.9	1.1E-03	3.5E-03
PE(P-16:0/22:4)	-0.9	1.5E-03	4.5E-03
PE(O-18:0/20:4)	-0.9	1.9E-03	5.8E-03
PE(P-18:0/18:2)	-1.3	2.7E-03	7.6E-03
GM3(d34:1)	-1.4	2.9E-03	7.9E-03
Cholesterol sulfate	-1.7	3.1E-03	8.4E-03
GlcCer(d18:1/20:0)	-1.2	3.1E-03	8.4E-03
LacCer(d18:1/16:0)	-1.2	3.8E-03	9.8E-03
DG(16:0_20:4)	-0.8	4.1E-03	1.1E-02
PS(18:0_20:4)	-0.8	6.4E-03	1.6E-02
Palmitoleic acid	-1.2	9.2E-03	2.2E-02
TG(20:4_36:2)	-0.9	9.6E-03	2.3E-02
CL(74:9/18:2)	-1.9	1.1E-02	2.5E-02
LPC(16:0)	-0.6	1.4E-02	3.1E-02
GalCer(d18:1/16:0)	-1.3	1.5E-02	3.3E-02
PEth(16:0_18:1)	-2.1	1.7E-02	3.6E-02
PE(36:4)	-0.7	1.9E-02	3.9E-02
DG(18:1_20:4)	-0.9	2.0E-02	4.1E-02
PI(20:4/20:4)	-0.8	2.0E-02	4.1E-02
PI(16:0_22:6)	-0.7	2.0E-02	4.1E-02
LPI(18:0)	-1.0	2.1E-02	4.1E-02
PE(O-16:0/22:6)	-0.7	2.1E-02	4.1E-02
PE(P-18:0/20:5)	-1.2	2.4E-02	4.5E-02
PE(34:1)	-0.7	2.4E-02	4.5E-02
PS(18:0_18:1)	-0.6	2.5E-02	4.6E-02
PE(38:5)	-0.8	2.7E-02	4.9E-02
GM3(d38:1)	4.7	1.1E-12	2.0E-10
Cer(d18:1/18:0)	2.3	1.2E-09	1.1E-07
HexCer(d18:1/18:0)	2.2	5.5E-09	2.5E-07
GM2(d38:1)	3.2	1.6E-08	5.5E-07
(3-O-sulfo)GalCer(d18:1/24:0)	3.4	7.9E-08	1.8E-06
alpha-GalCer(d18:2/22:0)	2.4	2.3E-07	4.1E-06
(3-O-sulfo)GalCer(d18:1/24:1)	2.2	2.7E-07	4.1E-06
LacCer(d18:1/18:0)	2.1	5.9E-07	7.4E-06
PC(40:6)	1.5	1.1E-06	1.0E-05
GM3(d36:1)	2.2	3.1E-06	2.3E-05
BMP(18:0_18:1)	1.7	5.0E-06	3.5E-05
(3-O-sulfo)GalCer(d18:1/24:0(2OH))	2.8	2.6E-05	1.4E-04
PC(36:1)	1.4	3.0E-05	1.6E-04
CE(22:6)	3.2	4.5E-05	2.2E-04
(3-O-sulfo)GalCer(d18:1/18:0)	1.2	7.6E-05	3.4E-04
GalCer(d18:1/22:1)	2.1	1.6E-04	6.3E-04
GalCer(d18:2/22:0)	1.5	1.7E-04	6.5E-04
PC(38:4)	1.1	2.2E-04	7.6E-04
PE(40:6)	0.9	9.0E-04	2.9E-03
HexCer(d18:1/24:1)	1.1	1.4E-03	4.4E-03
BMP(18:0_20:4)	1.4	2.0E-03	5.9E-03
Cer(d18:1/24:1)	0.9	2.0E-03	5.9E-03
SM(d18:1/18:0)	1.6	2.2E-03	6.4E-03
HexCer(d18:1/24:0)	1.0	3.8E-03	9.8E-03
BMP(16:0_18:1)	1.0	4.4E-03	1.1E-02
GalCer(d18:1/20:0)	1.1	5.2E-03	1.3E-02
Cholesterol	0.9	9.7E-03	2.3E-02
LPC(22:6)	0.8	1.1E-02	2.5E-02
LPG(18:1)	0.7	1.1E-02	2.5E-02
LPC(18:0)	0.6	1.1E-02	2.5E-02
BMP(16:0_20:4)	0.7	1.5E-02	3.2E-02
SM(d18:1/24:0)	1.1	2.0E-02	4.1E-02
LPG(20:4)	1.3	2.1E-02	4.1E-02
PE(P-18:0/18:1)	0.7	2.2E-02	4.3E-02
LPC(24:0)	1.2	3.4E-02	6.2E-02
Glucosylsphingosine	1.4	3.4E-02	6.2E-02
Stearic acid	-0.9	3.8E-02	6.9E-02
Cer(d18:1/16:0)	-0.5	4.0E-02	7.0E-02
PI(16:0_18:1)	-0.6	4.2E-02	7.3E-02
TG(20:4_36:0)	0.7	5.3E-02	9.2E-02
(3-O-sulfo)GalCer(d18:1/16:0)	-0.8	5.3E-02	9.2E-02
BMP(22:6/22:6)	-0.7	5.5E-02	9.3E-02
GM2(d36:1)	0.8	5.7E-02	9.6E-02
GM1(d36:1)	0.6	6.8E-02	1.1E-01
Coenzyme Q10	0.7	6.9E-02	1.1E-01
LacCer(d18:1/24:0)	0.8	7.7E-02	1.3E-01
PC(38:6)	0.4	7.8E-02	1.3E-01
SM(d18:1/16:0)	-0.5	8.1E-02	1.3E-01
GalCer(d18:1/18:0)	0.6	8.2E-02	1.3E-01
PS(18:1/18:1)	-0.5	1.0E-01	1.6E-01
DG(16:0_18:1)	-0.5	1.2E-01	1.8E-01
PC(O-16:0/2:0)	0.6	1.2E-01	1.9E-01
PE(P-18:0/22:6)	-0.4	1.2E-01	1.9E-01
BMP(20:4/20:4)	0.5	1.3E-01	2.0E-01
MG(18:0)	0.6	1.3E-01	2.0E-01
PE(O-18:0/22:6)	-0.4	1.4E-01	2.0E-01
GM3(d40:1)	0.6	1.4E-01	2.0E-01
GalCer(d18:2/20:0)	0.7	1.5E-01	2.2E-01
MG(18:1)	0.6	1.6E-01	2.3E-01
PE(36:2)	-0.4	1.6E-01	2.4E-01
DHA	-0.4	2.0E-01	2.8E-01
GlcCer(d18:1/18:0)	0.5	2.0E-01	2.8E-01
Cer(d18:1/24:0)	0.3	2.1E-01	2.9E-01
LPC(18:1)	-0.3	2.1E-01	2.9E-01
alpha-GalCer(d18:1/22:0)	0.6	2.1E-01	3.0E-01
MG(16:0)	0.4	2.4E-01	3.3E-01
SM(d18:1/24:1)	0.5	2.4E-01	3.3E-01
(3-O-sulfo)GalCer(d18:1/24:1(2OH))	0.7	2.5E-01	3.4E-01
GlcCer(d18:2/20:0)	-0.6	2.6E-01	3.5E-01
CE(20:4)	0.5	2.9E-01	3.8E-01
PC(36:4)	0.3	2.9E-01	3.9E-01
PC(34:1)	0.3	3.0E-01	3.9E-01
LacCer(d18:1/24:1)	-0.5	3.3E-01	4.3E-01
PE(38:4)	-0.3	3.4E-01	4.5E-01
GalCer(d18:2/18:0)	0.4	3.5E-01	4.5E-01
PC(16:0/9:0(CHO))	-0.4	3.6E-01	4.6E-01
alpha-GalCer(d18:1/22:1)	0.8	3.9E-01	4.9E-01
(3-O-sulfo)GalCer(d18:1/18:0(2OH)	0.6	4.0E-01	5.0E-01
PG(16:0_22:6)	-0.6	4.0E-01	5.0E-01
PC(O-16:0/0:0)	-0.3	4.0E-01	5.0E-01
CL(72:6/18:2)	0.9	4.3E-01	5.4E-01
PC(O-18:0/2:0)	0.5	4.4E-01	5.4E-01
PS(22:6/22:6)	0.5	4.6E-01	5.6E-01
DG(18:1/18:1)	0.2	5.0E-01	6.1E-01
DG(18:0_22:6)	-0.9	5.4E-01	6.5E-01
PE(40:7)	-0.2	5.6E-01	6.7E-01
PC(40:5)	0.2	5.9E-01	7.0E-01
PE(40:4)	-0.2	6.0E-01	7.1E-01
PE(36:1)	0.2	6.1E-01	7.1E-01
CE(16:1)	-0.3	6.1E-01	7.2E-01
Palmitoylethanolamine	0.2	6.6E-01	7.6E-01
CE(18:1)	0.1	6.6E-01	7.6E-01
PG(16:0_20:4)	0.2	6.8E-01	7.8E-01
PI(18:0_18:1)	-0.1	6.9E-01	7.9E-01
BMP(18:1/18:1)	-0.1	7.1E-01	8.0E-01
TG(18:0_36:2)	0.1	7.4E-01	8.2E-01
PC(16:0/9:0(COOH))	0.1	7.4E-01	8.2E-01
PC(16:0/5:0(CHO))	-0.1	7.4E-01	8.2E-01
LPC(20:4)	-0.1	7.5E-01	8.2E-01
alpha-GalCer(d18:1/18:0)	0.1	7.6E-01	8.3E-01
DG(18:0_18:1)	0.1	8.0E-01	8.6E-01
TG(18:1_34:2)	-0.1	8.2E-01	8.8E-01
TG(22:6_36:2)	-0.1	8.3E-01	8.8E-01
CE(18:2)	0.2	8.3E-01	8.8E-01
PC(36:2)	0.0	8.6E-01	9.2E-01
EPA	-0.1	8.9E-01	9.3E-01
DG(18:0_20:4)	0.0	8.9E-01	9.3E-01
GlcCer(d18:2/18:0)	-0.1	9.0E-01	9.4E-01
PG(18:0_20:4)	0.0	9.1E-01	9.4E-01
TG(18:1_34:3)	0.0	9.1E-01	9.4E-01
LPC(26:1)	0.0	9.2E-01	9.4E-01
PI(18:0_22:6)	0.0	9.2E-01	9.4E-01
alpha-GalCer(d18:1/20:0)	0.0	9.8E-01	9.9E-01
PE(38:6)	0.0	9.8E-01	9.9E-01
HexCer(d18:1/22:0)	0.0	9.9E-01	9.9E-01

References

1. Parenti G, Andria G, Ballabio A. Lysosomal storage diseases: from pathophysiology to therapy. Annual review of medicine. 2015;66:471-86.
2. Platt FM, d'Azzo A, Davidson BL, Neufeld EF, Tifft CJ. Lysosomal storage diseases. Nature Reviews Disease Primers. 2018;4(1):27.
3. Puentes-Tellez MA, Lerma-Barbosa PA, Garzón-Jaramillo RG, Suarez DA, Espejo-Mojica AJ, Guevara JM, et al. A perspective on research, diagnosis, and management of lysosomal storage disorders in Colombia. Heliyon. 2020;6(3):e03635.
4. Parenti G, Medina DL, Ballabio A. The rapidly evolving view of lysosomal storage diseases. EMBO molecular medicine. 2021;13(2):e12836.
5. Hu YB, Dammer EB, Ren RJ, Wang G. The endosomal-lysosomal system: from acidification and cargo sorting to neurodegeneration. Translational neurodegeneration. 2015;4:18.
6. Elkin SR, Lakoduk AM, Schmid SL. Endocytic pathways and endosomal trafficking: a primer. Wiener medizinische Wochenschrift (1946). 2016;166(7-8):196-204.
7. Miaczynska M, Stenmark H. Mechanisms and functions of endocytosis. The Journal of cell biology. 2008;180(1):7-11.
8. Huotari J, Helenius A. Endosome maturation. EMBO J. 2011;30(17):3481-500.
9. Jean S, Kiger AA. Coordination between RAB GTPase and phosphoinositide regulation and functions. Nature reviews Molecular cell biology. 2012;13(7):463-70.
10. Mayor S, Parton RG, Donaldson JG. Clathrin-independent pathways of endocytosis. Cold Spring Harbor perspectives in biology. 2014;6(6).
11. Grant BD, Donaldson JG. Pathways and mechanisms of endocytic recycling. Nature reviews Molecular cell biology. 2009;10(9):597-608.
12. O'Sullivan MJ, Lindsay AJ. The Endosomal Recycling Pathway-At the Crossroads of the Cell. International journal of molecular sciences. 2020;21(17).
13. Baldys A, Raymond JR. Critical role of ESCRT machinery in EGFR recycling. Biochemistry. 2009;48(40):9321-3.
14. Poteryaev D, Datta S, Ackema K, Zerial M, Spang A. Identification of the switch in early-to-late endosome transition. Cell. 2010;141(3):497-508.
15. Piper RC, Katzmann DJ. Biogenesis and function of multivesicular bodies. Annual review of cell and developmental biology. 2007;23:519-47.
16. Katzmann DJ, Stefan CJ, Babst M, Emr SD. Vps27 recruits ESCRT machinery to endosomes during MVB sorting. The Journal of cell biology. 2003;162(3):413-23.
17. Katzmann DJ, Babst M, Emr SD. Ubiquitin-dependent sorting into the multivesicular body pathway requires the function of a conserved endosomal protein sorting complex, ESCRT-I. Cell. 2001;106(2):145-55.
18. Babst M, Katzmann DJ, Snyder WB, Wendland B, Emr SD. Endosome-associated complex, ESCRT-II, recruits transport machinery for protein sorting at the multivesicular body. Developmental cell. 2002;3(2):283-9.
19. Babst M, Katzmann DJ, Estepa-Sabal EJ, Meerloo T, Emr SD. Escrt-III: an endosome-associated heterooligomeric protein complex required for mvb sorting. Developmental cell. 2002;3(2):271-82.
20. Henne WM, Buchkovich NJ, Emr SD. The ESCRT pathway. Developmental cell. 2011;21(1):77-91.
21. Katzmann DJ. No ESCRT to the melanosome: MVB sorting without ubiquitin. Developmental cell. 2006;10(3):278-80.
22. Luzio JP, Pryor PR, Bright NA. Lysosomes: fusion and function. Nature reviews Molecular cell biology. 2007;8(8):622-32.
23. Glick D, Barth S, Macleod KF. Autophagy: cellular and molecular mechanisms. The Journal of pathology. 2010;221(1):3-12.
24. Bouhamdani N, Comeau D, Turcotte S. A Compendium of Information on the Lysosome. Frontiers in cell and developmental biology. 2021;9:798262.

25. Bright NA, Davis LJ, Luzio JP. Endolysosomes Are the Principal Intracellular Sites of Acid Hydrolase Activity. Current biology : CB. 2016;26(17):2233-45.
26. Saftig P, Klumperman J. Lysosome biogenesis and lysosomal membrane proteins: trafficking meets function. Nature reviews Molecular cell biology. 2009;10(9):623-35.
27. Saftig P, Schröder B, Blanz J. Lysosomal membrane proteins: life between acid and neutral conditions. Biochemical Society transactions. 2010;38(6):1420-3.
28. Rudnik S, Damme M. The lysosomal membrane-export of metabolites and beyond. Febs j. 2021;288(14):4168-82.
29. Sancak Y, Bar-Peled L, Zoncu R, Markhard AL, Nada S, Sabatini DM. Ragulator-Rag complex targets mTORC1 to the lysosomal surface and is necessary for its activation by amino acids. Cell. 2010;141(2):290-303.
30. Ballabio A, Bonifacino JS. Lysosomes as dynamic regulators of cell and organismal homeostasis. Nature reviews Molecular cell biology. 2020;21(2):101-18.
31. Miyake K, Saitoh SI, Sato R, Shibata T, Fukui R, Murakami Y. Endolysosomal compartments as platforms for orchestrating innate immune and metabolic sensors. Journal of leukocyte biology. 2019;106(4):853-62.
32. Lloyd-Evans E, Waller-Evans H. Lysosomal Ca(2+) Homeostasis and Signaling in Health and Disease. Cold Spring Harbor perspectives in biology. 2020;12(6).
33. Platt FM, Boland B, van der Spoel AC. The cell biology of disease: lysosomal storage disorders: the cellular impact of lysosomal dysfunction. The Journal of cell biology. 2012;199(5):723-34.
34. Meikle PJ, Fietz MJ, Hopwood JJ. Diagnosis of lysosomal storage disorders: current techniques and future directions. Expert review of molecular diagnostics. 2004;4(5):677-91.
35. Bosch ME, Kielian T. Neuroinflammatory paradigms in lysosomal storage diseases. Frontiers in neuroscience. 2015;9:417.
36. Ellison S, Parker H, Bigger B. Advances in therapies for neurological lysosomal storage disorders. Journal of inherited metabolic disease. 2023;46(5):874-905.
37. Do J, McKinney C, Sharma P, Sidransky E. Glucocerebrosidase and its relevance to Parkinson disease. Molecular neurodegeneration. 2019;14(1):36.
38. Udayar V, Chen Y, Sidransky E, Jagasia R. Lysosomal dysfunction in neurodegeneration: emerging concepts and methods. Trends in Neurosciences. 2022;45(3):184-99.
39. Malik BR, Maddison DC, Smith GA, Peters OM. Autophagic and endo-lysosomal dysfunction in neurodegenerative disease. Molecular brain. 2019;12(1):100.
40. Giovedì S, Ravanelli MM, Parisi B, Bettegazzi B, Guarnieri FC. Dysfunctional Autophagy and Endolysosomal System in Neurodegenerative Diseases: Relevance and Therapeutic Options. Frontiers in cellular neuroscience. 2020;14:602116.
41. Wang C, Telpoukhovskaia MA, Bahr BA, Chen X, Gan L. Endo-lysosomal dysfunction: a converging mechanism in neurodegenerative diseases. Curr Opin Neurobiol. 2018;48:52-8.
42. Wilson DM, 3rd, Cookson MR, Van Den Bosch L, Zetterberg H, Holtzman DM, Dewachter I. Hallmarks of neurodegenerative diseases. Cell. 2023;186(4):693-714.
43. Jeyakumar M, Dwek RA, Butters TD, Platt FM. Storage solutions: treating lysosomal disorders of the brain. Nature Reviews Neuroscience. 2005;6(9):713-25.
44. Para C, Bose P, Pshezhetsky AV. Neuropathophysiology of Lysosomal Storage Diseases: Synaptic Dysfunction as a Starting Point for Disease Progression. Journal of clinical medicine. 2020;9(3).
45. Lushchak VI, Duszenko M, Gospodaryov DV, Garaschuk O. Oxidative Stress and Energy Metabolism in the Brain: Midlife as a Turning Point. Antioxidants (Basel, Switzerland). 2021;10(11).
46. Vanier MT. Niemann-Pick disease type C. Orphanet journal of rare diseases. 2010;5:16.
47. Crocker AC. The cerebral defect in Tay-Sachs disease and Niemann-Pick disease. Journal of neurochemistry. 1961;7:69-80.
48. Crocker AC, Farber S. Niemann-Pick disease: a review of eighteen patients. Medicine (Baltimore). 1958;37(1):1-95.

49. Brady RO, Kanfer JN, Mock MB, Fredrickson DS. The metabolism of sphingomyelin. II. Evidence of an enzymatic deficiency in Niemann-Pick diseae. Proceedings of the National Academy of Sciences of the United States of America. 1966;55(2):366-9.

50. Vanier MT, Revol A, Fichet M. Sphingomyelinase activities of various human tissues in control subjects and in Niemann-Pick disease - development and evaluation of a microprocedure. Clinica chimica acta; international journal of clinical chemistry. 1980;106(3):257-67.

51. Greer WL, Riddell DC, Gillan TL, Girouard GS, Sparrow SM, Byers DM, et al. The Nova Scotia (type D) form of Niemann-Pick disease is caused by a G3097-->T transversion in NPC1. American journal of human genetics. 1998;63(1):52-4.

52. Mengel E, Klunemann HH, Lourenco CM, Hendriksz CJ, Sedel F, Walterfang M, et al. Niemann-Pick disease type C symptomatology: an expert-based clinical description. Orphanet journal of rare diseases. 2013;8:166.

53. Walkley SU, Suzuki K. Consequences of NPC1 and NPC2 loss of function in mammalian neurons. Biochimica et biophysica acta. 2004;1685(1-3):48-62.

54. Cologna SM, Cluzeau CV, Yanjanin NM, Blank PS, Dail MK, Siebel S, et al. Human and mouse neuroinflammation markers in Niemann-Pick disease, type C1. Journal of inherited metabolic disease. 2014;37(1):83-92.

55. Walterfang M, Fahey M, Desmond P, Wood A, Seal ML, Steward C, et al. White and gray matter alterations in adults with Niemann-Pick disease type C: a cross-sectional study. Neurology. 2010;75(1):49-56.

56. Kodachi T, Matsumoto S, Mizuguchi M, Osaka H, Kanai N, Nanba E, et al. Severe demyelination in a patient with a late infantile form of Niemann-Pick disease type C. Neuropathology : official journal of the Japanese Society of Neuropathology. 2017;37(5):426-30.

57. Millat G, Marçais C, Tomasetto C, Chikh K, Fensom AH, Harzer K, et al. Niemann-Pick C1 disease: correlations between NPC1 mutations, levels of NPC1 protein, and phenotypes emphasize the functional significance of the putative sterol-sensing domain and of the cysteine-rich luminal loop. American journal of human genetics. 2001;68(6):1373-85.

58. Yamamoto T, Ninomiya H, Matsumoto M, Ohta Y, Nanba E, Tsutsumi Y, et al. Genotype-phenotype relationship of Niemann-Pick disease type C: a possible correlation between clinical onset and levels of NPC1 protein in isolated skin fibroblasts. Journal of medical genetics. 2000;37(9):707-12.

59. Shammas H, Kuech EM, Rizk S, Das AM, Naim HY. Different Niemann-Pick C1 Genotypes Generate Protein Phenotypes that Vary in their Intracellular Processing, Trafficking and Localization. Scientific reports. 2019;9(1):5292.

60. Garver WS, Jelinek D, Meaney FJ, Flynn J, Pettit KM, Shepherd G, et al. The National Niemann-Pick Type C1 Disease Database: correlation of lipid profiles, mutations, and biochemical phenotypes. Journal of lipid research. 2010;51(2):406-15.

61. Gelsthorpe ME, Baumann N, Millard E, Gale SE, Langmade SJ, Schaffer JE, et al. Niemann-Pick type C1 I1061T mutant encodes a functional protein that is selected for endoplasmic reticulum-associated degradation due to protein misfolding. The Journal of biological chemistry. 2008;283(13):8229-36.

62. Geberhiwot T, Moro A, Dardis A, Ramaswami U, Sirrs S, Marfa MP, et al. Consensus clinical management guidelines for Niemann-Pick disease type C. Orphanet journal of rare diseases. 2018;13(1):50.

63. Carstea ED, Morris JA, Coleman KG, Loftus SK, Zhang D, Cummings C, et al. Niemann-Pick C1 disease gene: homology to mediators of cholesterol homeostasis. Science (New York, NY). 1997;277(5323):228-31.

64. Davies JP, Ioannou YA. Topological analysis of Niemann-Pick C1 protein reveals that the membrane orientation of the putative sterol-sensing domain is identical to those of 3-hydroxy-3-methylglutaryl-CoA reductase and sterol regulatory element binding protein cleavage-activating protein. The Journal of biological chemistry. 2000;275(32):24367-74.

65. Infante RE, Abi-Mosleh L, Radhakrishnan A, Dale JD, Brown MS, Goldstein JL. Purified NPC1 protein. I. Binding of cholesterol and oxysterols to a 1278-amino acid membrane protein. J Biol Chem. 2008;283(2):1052-63.
66. Deffieu MS, Pfeffer SR. Niemann-Pick type C 1 function requires lumenal domain residues that mediate cholesterol-dependent NPC2 binding. Proceedings of the National Academy of Sciences of the United States of America. 2011;108(47):18932-6.
67. Qian H, Wu X, Du X, Yao X, Zhao X, Lee J, et al. Structural Basis of Low-pH-Dependent Lysosomal Cholesterol Egress by NPC1 and NPC2. Cell. 2020;182(1):98-111.e18.
68. Lu F, Liang Q, Abi-Mosleh L, Das A, De Brabander JK, Goldstein JL, et al. Identification of NPC1 as the target of U18666A, an inhibitor of lysosomal cholesterol export and Ebola infection. eLife. 2015;4.
69. Naureckiene S, Sleat DE, Lackland H, Fensom A, Vanier MT, Wattiaux R, et al. Identification of HE1 as the second gene of Niemann-Pick C disease. Science (New York, NY). 2000;290(5500):2298-301.
70. Xu S, Benoff B, Liou HL, Lobel P, Stock AM. Structural basis of sterol binding by NPC2, a lysosomal protein deficient in Niemann-Pick type C2 disease. The Journal of biological chemistry. 2007;282(32):23525-31.
71. Kwon HJ, Abi-Mosleh L, Wang ML, Deisenhofer J, Goldstein JL, Brown MS, et al. Structure of N-terminal domain of NPC1 reveals distinct subdomains for binding and transfer of cholesterol. Cell. 2009;137(7):1213-24.
72. Pfeffer SR. Clues to NPC1-mediated cholesterol export from lysosomes. Proceedings of the National Academy of Sciences of the United States of America. 2016;113(29):7941-3.
73. Wang ML, Motamed M, Infante RE, Abi-Mosleh L, Kwon HJ, Brown MS, et al. Identification of Surface Residues on Niemann-Pick C2 Essential for Hydrophobic Handoff of Cholesterol to NPC1 in Lysosomes. Cell Metabolism. 2010;12(2):166-73.
74. Li X, Lu F, Trinh MN, Schmiege P, Seemann J, Wang J, et al. 3.3 Å structure of Niemann-Pick C1 protein reveals insights into the function of the C-terminal luminal domain in cholesterol transport. Proceedings of the National Academy of Sciences of the United States of America. 2017;114(34):9116-21.
75. Trinh MN, Brown MS, Seemann J, Goldstein JL, Lu F. Lysosomal cholesterol export reconstituted from fragments of Niemann-Pick C1. eLife. 2018;7:e38564.
76. Long T, Qi X, Hassan A, Liang Q, De Brabander JK, Li X. Structural basis for itraconazole-mediated NPC1 inhibition. Nature communications. 2020;11(1):152.
77. Hoglinger D, Burgoyne T, Sanchez-Heras E, Hartwig P, Colaco A, Newton J, et al. NPC1 regulates ER contacts with endocytic organelles to mediate cholesterol egress. Nature communications. 2019;10(1):4276.
78. Luo J, Jiang L, Yang H, Song B-L. Routes and mechanisms of post-endosomal cholesterol trafficking: A story that never ends. Traffic (Copenhagen, Denmark). 2017;18(4):209-17.
79. Möbius W, van Donselaar E, Ohno-Iwashita Y, Shimada Y, Heijnen HF, Slot JW, et al. Recycling compartments and the internal vesicles of multivesicular bodies harbor most of the cholesterol found in the endocytic pathway. Traffic (Copenhagen, Denmark). 2003;4(4):222-31.
80. Ikonen E. Cellular cholesterol trafficking and compartmentalization. Nature Reviews Molecular Cell Biology. 2008;9(2):125-38.
81. Nieweg K, Schaller H, Pfrieger FW. Marked differences in cholesterol synthesis between neurons and glial cells from postnatal rats. Journal of neurochemistry. 2009;109(1):125-34.
82. Wang DQ. Regulation of intestinal cholesterol absorption. Annual review of physiology. 2007;69:221-48.
83. Altmann SW, Davis HR, Jr., Zhu LJ, Yao X, Hoos LM, Tetzloff G, et al. Niemann-Pick C1 Like 1 protein is critical for intestinal cholesterol absorption. Science (New York, NY). 2004;303(5661):1201-4.
84. Xiao C, Stahel P, Lewis GF. Regulation of Chylomicron Secretion: Focus on Post-Assembly Mechanisms. Cell Mol Gastroenterol Hepatol. 2019;7(3):487-501.

85. Duan Y, Gong K, Xu S, Zhang F, Meng X, Han J. Regulation of cholesterol homeostasis in health and diseases: from mechanisms to targeted therapeutics. Signal Transduct Target Ther. 2022;7(1):265.
86. Brown MS, Goldstein JL. A receptor-mediated pathway for cholesterol homeostasis. Science (New York, NY). 1986;232(4746):34-47.
87. Kanerva K, Uronen RL, Blom T, Li S, Bittman R, Lappalainen P, et al. LDL cholesterol recycles to the plasma membrane via a Rab8a-Myosin5b-actin-dependent membrane transport route. Developmental cell. 2013;27(3):249-62.
88. Lee SH, Lee J-H, Im S-S. The cellular function of SCAP in metabolic signaling. Experimental & Molecular Medicine. 2020;52(5):724-9.
89. Charman M, Kennedy BE, Osborne N, Karten B. MLN64 mediates egress of cholesterol from endosomes to mitochondria in the absence of functional Niemann-Pick Type C1 protein. Journal of lipid research. 2010;51(5):1023-34.
90. Kennedy BE, Charman M, Karten B. Niemann-Pick Type C2 protein contributes to the transport of endosomal cholesterol to mitochondria without interacting with NPC1. Journal of lipid research. 2012;53(12):2632-42.
91. Zhang J, Liu Q. Cholesterol metabolism and homeostasis in the brain. Protein Cell. 2015;6(4):254-64.
92. Zhou AL, Swaminathan SK, Curran GL, Poduslo JF, Lowe VJ, Li L, et al. Apolipoprotein A-I Crosses the Blood-Brain Barrier through Clathrin-Independent and Cholesterol-Mediated Endocytosis. The Journal of pharmacology and experimental therapeutics. 2019;369(3):481-8.
93. Arenas F, Garcia-Ruiz C, Fernandez-Checa JC. Intracellular Cholesterol Trafficking and Impact in Neurodegeneration. Front Mol Neurosci. 2017;10:382.
94. Lamri A, Pigeyre M, Garver WS, Meyre D. The Extending Spectrum of NPC1-Related Human Disorders: From Niemann-Pick C1 Disease to Obesity. Endocrine reviews. 2018;39(2):192-220.
95. Pentchev PG, Comly ME, Kruth HS, Patel S, Proestel M, Weintroub H. The cholesterol storage disorder of the mutant BALB/c mouse. A primary genetic lesion closely linked to defective esterification of exogenously derived cholesterol and its relationship to human type C Niemann-Pick disease. The Journal of biological chemistry. 1986;261(6):2772-7.
96. Tharkeshwar AK, Trekker J, Vermeire W, Pauwels J, Sannerud R, Priestman DA, et al. A novel approach to analyze lysosomal dysfunctions through subcellular proteomics and lipidomics: the case of NPC1 deficiency. Scientific reports. 2017;7:41408.
97. Lloyd-Evans E, Morgan AJ, He X, Smith DA, Elliot-Smith E, Sillence DJ, et al. Niemann-Pick disease type C1 is a sphingosine storage disease that causes deregulation of lysosomal calcium. Nature medicine. 2008;14(11):1247-55.
98. te Vruchte D, Lloyd-Evans E, Veldman RJ, Neville DC, Dwek RA, Platt FM, et al. Accumulation of glycosphingolipids in Niemann-Pick C disease disrupts endosomal transport. The Journal of biological chemistry. 2004;279(25):26167-75.
99. Lloyd-Evans E, Platt FM. Lipids on trial: the search for the offending metabolite in Niemann-Pick type C disease. Traffic (Copenhagen, Denmark). 2010;11(4):419-28.
100. Karten B, Vance DE, Campenot RB, Vance JE. Cholesterol accumulates in cell bodies, but is decreased in distal axons, of Niemann-Pick C1-deficient neurons. Journal of neurochemistry. 2002;83(5):1154-63.
101. Vanier MT. Lipid changes in Niemann-Pick disease type C brain: personal experience and review of the literature. Neurochemical research. 1999;24(4):481-9.
102. Vance JE, Karten B. Niemann-Pick C disease and mobilization of lysosomal cholesterol by cyclodextrin. Journal of lipid research. 2014;55(8):1609-21.
103. Kennedy BE, Madreiter CT, Vishnu N, Malli R, Graier WF, Karten B. Adaptations of energy metabolism associated with increased levels of mitochondrial cholesterol in Niemann-Pick type C1-deficient cells. The Journal of biological chemistry. 2014;289(23):16278-89.

104. Woś M, Szczepanowska J, Pikuła S, Tylki-Szymańska A, Zabłocki K, Bandorowicz-Pikuła J. Mitochondrial dysfunction in fibroblasts derived from patients with Niemann-Pick type C disease. Archives of Biochemistry and Biophysics. 2016;593:50-9.

105. Garver WS, Krishnan K, Gallagos JR, Michikawa M, Francis GA, Heidenreich RA. Niemann-Pick C1 protein regulates cholesterol transport to the trans-Golgi network and plasma membrane caveolae. Journal of lipid research. 2002;43(4):579-89.

106. Wheeler S, Sillence DJ. Niemann–Pick type C disease: cellular pathology and pharmacotherapy. Journal of neurochemistry. 2020;153(6):674-92.

107. Lebrand C, Corti M, Goodson H, Cosson P, Cavalli V, Mayran N, et al. Late endosome motility depends on lipids via the small GTPase Rab7. EMBO J. 2002;21(6):1289-300.

108. Ko DC, Gordon MD, Jin JY, Scott MP. Dynamic movements of organelles containing Niemann-Pick C1 protein: NPC1 involvement in late endocytic events. Molecular biology of the cell. 2001;12(3):601-14.

109. Salvioli R, Scarpa S, Ciaffoni F, Tatti M, Ramoni C, Vanier MT, et al. Glucosylceramidase mass and subcellular localization are modulated by cholesterol in Niemann-Pick disease type C. The Journal of biological chemistry. 2004;279(17):17674-80.

110. Reagan JW, Jr., Hubbert ML, Shelness GS. Posttranslational regulation of acid sphingomyelinase in niemann-pick type C1 fibroblasts and free cholesterol-enriched chinese hamster ovary cells. The Journal of biological chemistry. 2000;275(48):38104-10.

111. Kutchukian C, Vivas O, Casas M, Jones JG, Tiscione SA, Simó S, et al. NPC1 regulates the distribution of phosphatidylinositol 4-kinases at Golgi and lysosomal membranes. EMBO J. 2021;40(13):e105990.

112. Ko DC, Milenkovic L, Beier SM, Manuel H, Buchanan J, Scott MP. Cell-autonomous death of cerebellar purkinje neurons with autophagy in Niemann-Pick type C disease. PLoS genetics. 2005;1(1):81-95.

113. Pacheco CD, Kunkel R, Lieberman AP. Autophagy in Niemann-Pick C disease is dependent upon Beclin-1 and responsive to lipid trafficking defects. Human molecular genetics. 2007;16(12):1495-503.

114. Sarkar S, Carroll B, Buganim Y, Maetzel D, Ng AH, Cassady JP, et al. Impaired autophagy in the lipid-storage disorder Niemann-Pick type C1 disease. Cell reports. 2013;5(5):1302-15.

115. Ordonez MP, Roberts EA, Kidwell CU, Yuan SH, Plaisted WC, Goldstein LS. Disruption and therapeutic rescue of autophagy in a human neuronal model of Niemann Pick type C1. Human molecular genetics. 2012;21(12):2651-62.

116. Elrick MJ, Yu T, Chung C, Lieberman AP. Impaired proteolysis underlies autophagic dysfunction in Niemann-Pick type C disease. Human molecular genetics. 2012;21(22):4876-87.

117. Castellano BM, Thelen AM, Moldavski O, Feltes M, van der Welle RE, Mydock-McGrane L, et al. Lysosomal cholesterol activates mTORC1 via an SLC38A9-Niemann-Pick C1 signaling complex. Science (New York, NY). 2017;355(6331):1306-11.

118. Davis OB, Shin HR, Lim CY, Wu EY, Kukurugya M, Maher CF, et al. NPC1-mTORC1 Signaling Couples Cholesterol Sensing to Organelle Homeostasis and Is a Targetable Pathway in Niemann-Pick Type C. Developmental cell. 2021;56(3):260-76.e7.

119. Deleyto-Seldas N, Efeyan A. The mTOR-Autophagy Axis and the Control of Metabolism. Frontiers in cell and developmental biology. 2021;9:655731.

120. Koh CH, Whiteman M, Li QX, Halliwell B, Jenner AM, Wong BS, et al. Chronic exposure to U18666A is associated with oxidative stress in cultured murine cortical neurons. Journal of neurochemistry. 2006;98(4):1278-89.

121. Ribas GS, Pires R, Coelho JC, Rodrigues D, Mescka CP, Vanzin CS, et al. Oxidative stress in Niemann-Pick type C patients: a protective role of N-butyl-deoxynojirimycin therapy. International journal of developmental neuroscience : the official journal of the International Society for Developmental Neuroscience. 2012;30(6):439-44.

122. Klein A, Maldonado C, Vargas LM, Gonzalez M, Robledo F, Perez de Arce K, et al. Oxidative stress activates the c-Abl/p73 proapoptotic pathway in Niemann-Pick type C neurons. Neurobiology of disease. 2011;41(1):209-18.
123. Zampieri S, Mellon SH, Butters TD, Nevyjel M, Covey DF, Bembi B, et al. Oxidative stress in NPC1 deficient cells: protective effect of allopregnanolone. Journal of cellular and molecular medicine. 2009;13(9b):3786-96.
124. Hammerschmidt TG, Donida B, Raabe M, Faverzani JL, de Fátima Lopes F, Machado AZ, et al. Evidence of redox imbalance and mitochondrial dysfunction in Niemann-Pick type C 1 patients: the in vitro effect of combined therapy with antioxidants and β-cyclodextrin nanoparticles. Metabolic brain disease. 2023;38(2):507-18.
125. Yu W, Gong JS, Ko M, Garver WS, Yanagisawa K, Michikawa M. Altered cholesterol metabolism in Niemann-Pick type C1 mouse brains affects mitochondrial function. The Journal of biological chemistry. 2005;280(12):11731-9.
126. Loftus SK, Morris JA, Carstea ED, Gu JZ, Cummings C, Brown A, et al. Murine model of Niemann-Pick C disease: mutation in a cholesterol homeostasis gene. Science (New York, NY). 1997;277(5323):232-5.
127. Pentchev PG, Gal AE, Boothe AD, Fouks J, Omodeo-Sale F, Brady RO. A lysosomal storage disorder in mice characterized by the accumulation of several sphingolipids. Birth Defects Orig Artic Ser. 1980;16(1):225-30.
128. Smith D, Wallom KL, Williams IM, Jeyakumar M, Platt FM. Beneficial effects of anti-inflammatory therapy in a mouse model of Niemann-Pick disease type C1. Neurobiology of disease. 2009;36(2):242-51.
129. Platt N, Speak AO, Colaco A, Gray J, Smith DA, Williams IM, et al. Immune dysfunction in Niemann-Pick disease type C. Journal of neurochemistry. 2016;136 Suppl 1:74-80.
130. Love S, Bridges LR, Case CP. Neurofibrillary tangles in Niemann-Pick disease type C. Brain : a journal of neurology. 1995;118 (Pt 1):119-29.
131. Sawamura N, Gong JS, Garver WS, Heidenreich RA, Ninomiya H, Ohno K, et al. Site-specific phosphorylation of tau accompanied by activation of mitogen-activated protein kinase (MAPK) in brains of Niemann-Pick type C mice. J Biol Chem. 2001;276(13):10314-9.
132. Malnar M, Hecimovic S, Mattsson N, Zetterberg H. Bidirectional links between Alzheimer's disease and Niemann-Pick type C disease. Neurobiology of disease. 2014;72 Pt A:37-47.
133. Suzuki K, Parker CC, Pentchev PG, Katz D, Ghetti B, D'Agostino AN, et al. Neurofibrillary tangles in Niemann-Pick disease type C. Acta neuropathologica. 1995;89(3):227-38.
134. Bu B, Li J, Davies P, Vincent I. Deregulation of cdk5, hyperphosphorylation, and cytoskeletal pathology in the Niemann-Pick type C murine model. The Journal of neuroscience : the official journal of the Society for Neuroscience. 2002;22(15):6515-25.
135. Parra J, Klein AD, Castro J, Morales MG, Mosqueira M, Valencia I, et al. Npc1 deficiency in the C57BL/6J genetic background enhances Niemann-Pick disease type C spleen pathology. Biochem Biophys Res Commun. 2011;413(3):400-6.
136. Maue RA, Burgess RW, Wang B, Wooley CM, Seburn KL, Vanier MT, et al. A novel mouse model of Niemann–Pick type C disease carrying a D1005G-Npc1 mutation comparable to commonly observed human mutations. Human molecular genetics. 2011;21(4):730-50.
137. Praggastis M, Tortelli B, Zhang J, Fujiwara H, Sidhu R, Chacko A, et al. A murine Niemann-Pick C1 I1061T knock-in model recapitulates the pathological features of the most prevalent human disease allele. The Journal of neuroscience : the official journal of the Society for Neuroscience. 2015;35(21):8091-106.
138. Fiorenza MT, La Rosa P, Canterini S, Erickson RP. The Cerebellum in Niemann-Pick C1 Disease: Mouse Versus Man. The Cerebellum. 2023;22(1):102-19.
139. Yamada A, Saji M, Ukita Y, Shinoda Y, Taniguchi M, Higaki K, et al. Progressive neuronal loss in the ventral posterior lateral and medial nuclei of thalamus in Niemann-Pick disease type C mouse brain. Brain & development. 2001;23(5):288-97.

140. German DC, Quintero EM, Liang CL, Ng B, Punia S, Xie C, et al. Selective neurodegeneration, without neurofibrillary tangles, in a mouse model of Niemann-Pick C disease. The Journal of comparative neurology. 2001;433(3):415-25.

141. Luan Z, Saito Y, Miyata H, Ohama E, Ninomiya H, Ohno K. Brainstem neuropathology in a mouse model of Niemann-Pick disease type C. Journal of the neurological sciences. 2008;268(1-2):108-16.

142. Wu YP, Mizukami H, Matsuda J, Saito Y, Proia RL, Suzuki K. Apoptosis accompanied by up-regulation of TNF-alpha death pathway genes in the brain of Niemann-Pick type C disease. Molecular genetics and metabolism. 2005;84(1):9-17.

143. Li H, Repa JJ, Valasek MA, Beltroy EP, Turley SD, German DC, et al. Molecular, anatomical, and biochemical events associated with neurodegeneration in mice with Niemann-Pick type C disease. Journal of neuropathology and experimental neurology. 2005;64(4):323-33.

144. Sarna JR, Larouche M, Marzban H, Sillitoe RV, Rancourt DE, Hawkes R. Patterned Purkinje cell degeneration in mouse models of Niemann-Pick type C disease. The Journal of comparative neurology. 2003;456(3):279-91.

145. Martin KB, Williams IM, Cluzeau CV, Cougnoux A, Dale RK, Iben JR, et al. Identification of Novel Pathways Associated with Patterned Cerebellar Purkinje Neuron Degeneration in Niemann-Pick Disease, Type C1. International journal of molecular sciences. 2020;21(1):292.

146. Elrick MJ, Pacheco CD, Yu T, Dadgar N, Shakkottai VG, Ware C, et al. Conditional Niemann-Pick C mice demonstrate cell autonomous Purkinje cell neurodegeneration. Human molecular genetics. 2010;19(5):837-47.

147. Guix FX, Capitán AM, Casadomé-Perales Á, Palomares-Pérez I, Castillo ILd, Miguel V, et al. Increased exosome secretion in neurons aging in vitro by NPC1-mediated endosomal cholesterol buildup. Life Science Alliance. 2021;4(8):e202101055.

148. Demais V, Barthelemy A, Perraut M, Ungerer N, Keime C, Reibel S, et al. Reversal of Pathologic Lipid Accumulation in NPC1-Deficient Neurons by Drug-Promoted Release of LAMP1-Coated Lamellar Inclusions. The Journal of neuroscience : the official journal of the Society for Neuroscience. 2016;36(30):8012-25.

149. Roney JC, Li S, Farfel-Becker T, Huang N, Sun T, Xie Y, et al. Lipid-mediated motor-adaptor sequestration impairs axonal lysosome delivery leading to autophagic stress and dystrophy in Niemann-Pick type C. Developmental cell. 2021;56(10):1452-68.e8.

150. Yu T, Shakkottai VG, Chung C, Lieberman AP. Temporal and cell-specific deletion establishes that neuronal Npc1 deficiency is sufficient to mediate neurodegeneration. Human molecular genetics. 2011;20(22):4440-51.

151. Zervas M, Dobrenis K, Walkley SU. Neurons in Niemann-Pick disease type C accumulate gangliosides as well as unesterified cholesterol and undergo dendritic and axonal alterations. Journal of neuropathology and experimental neurology. 2001;60(1):49-64.

152. Karten B, Campenot RB, Vance DE, Vance JE. The Niemann-Pick C1 protein in recycling endosomes of presynaptic nerve terminals. J Lipid Res. 2006;47(3):504-14.

153. Mitroi DN, Pereyra-Gómez G, Soto-Huelin B, Senovilla F, Kobayashi T, Esteban JA, et al. NPC1 enables cholesterol mobilization during long-term potentiation that can be restored in Niemann–Pick disease type C by CYP46A1 activation. EMBO reports. 2019;20(11):e48143.

154. Xu S, Zhou S, Xia D, Xia J, Chen G, Duan S, et al. Defects of synaptic vesicle turnover at excitatory and inhibitory synapses in Niemann-Pick C1-deficient neurons. Neuroscience. 2010;167(3):608-20.

155. Burbulla LF, Mc Donald JM, Valdez C, Gao F, Bigio EH, Krainc D. Modeling Brain Pathology of Niemann-Pick Disease Type C Using Patient-Derived Neurons. Movement disorders : official journal of the Movement Disorder Society. 2021;36(4):1022-7.

156. Nave KA, Werner HB. Myelination of the nervous system: mechanisms and functions. Annu Rev Cell Dev Biol. 2014;30:503-33.

157. Zhang J, Liu Q. Cholesterol metabolism and homeostasis in the brain. Protein Cell. 2015;6(4):254-64.

158. Saher G, Brügger B, Lappe-Siefke C, Möbius W, Tozawa R, Wehr MC, et al. High cholesterol level is essential for myelin membrane growth. Nature neuroscience. 2005;8(4):468-75.
159. Weintraub H, Abramovici A, Sandbank U, Booth AD, Pentchev PG, Sela B. Dysmyelination in NCTR-Balb/C mouse mutant with a lysosomal storage disorder. Morphological survey. Acta Neuropathol. 1987;74(4):374-81.
160. German DC, Liang CL, Song T, Yazdani U, Xie C, Dietschy JM. Neurodegeneration in the Niemann–Pick C mouse: glial involvement. Neuroscience. 2002;109(3):437-50.
161. Takikita S, Fukuda T, Mohri I, Yagi T, Suzuki K. Perturbed myelination process of premyelinating oligodendrocyte in Niemann-Pick type C mouse. Journal of neuropathology and experimental neurology. 2004;63(6):660-73.
162. Yan X, Lukas J, Witt M, Wree A, Hubner R, Frech M, et al. Decreased expression of myelin gene regulatory factor in Niemann-Pick type C 1 mouse. Metabolic brain disease. 2011;26(4):299-306.
163. Yu T, Lieberman AP. Npc1 acting in neurons and glia is essential for the formation and maintenance of CNS myelin. PLoS genetics. 2013;9(4):e1003462.
164. Berghoff SA, Spieth L, Sun T, Hosang L, Depp C, Sasmita AO, et al. Neuronal cholesterol synthesis is essential for repair of chronically demyelinated lesions in mice. Cell reports. 2021;37(4):109889.
165. Sofroniew MV. Astrocyte Reactivity: Subtypes, States, and Functions in CNS Innate Immunity. Trends in immunology. 2020;41(9):758-70.
166. Pekny M, Pekna M. Astrocyte reactivity and reactive astrogliosis: costs and benefits. Physiological reviews. 2014;94(4):1077-98.
167. Baudry M, Yao Y, Simmons D, Liu J, Bi X. Postnatal development of inflammation in a murine model of Niemann-Pick type C disease: immunohistochemical observations of microglia and astroglia. Experimental neurology. 2003;184(2):887-903.
168. Karten B, Hayashi H, Francis GA, Campenot RB, Vance DE, Vance JE. Generation and function of astroglial lipoproteins from Niemann-Pick type C1-deficient mice. Biochem J. 2005;387(Pt 3):779-88.
169. Chen G, Li HM, Chen YR, Gu XS, Duan S. Decreased estradiol release from astrocytes contributes to the neurodegeneration in a mouse model of Niemann-Pick disease type C. Glia. 2007;55(15):1509-18.
170. Zhang M, Strnatka D, Donohue C, Hallows JL, Vincent I, Erickson RP. Astrocyte-only Npc1 reduces neuronal cholesterol and triples life span of Npc1-/- mice. Journal of neuroscience research. 2008;86(13):2848-56.
171. Butovsky O, Weiner HL. Microglial signatures and their role in health and disease. Nature Reviews Neuroscience. 2018;19(10):622-35.
172. Ransohoff RM, Cardona AE. The myeloid cells of the central nervous system parenchyma. Nature. 2010;468(7321):253-62.
173. Réu P, Khosravi A, Bernard S, Mold JE, Salehpour M, Alkass K, et al. The Lifespan and Turnover of Microglia in the Human Brain. Cell reports. 2017;20(4):779-84.
174. Huang Y, Xu Z, Xiong S, Sun F, Qin G, Hu G, et al. Repopulated microglia are solely derived from the proliferation of residual microglia after acute depletion. Nature neuroscience. 2018;21(4):530-40.
175. De Schepper S, Crowley G, Hong S. Understanding microglial diversity and implications for neuronal function in health and disease. Developmental Neurobiology. 2021;81(5):507-23.
176. Cronk JC, Filiano AJ, Louveau A, Marin I, Marsh R, Ji E, et al. Peripherally derived macrophages can engraft the brain independent of irradiation and maintain an identity distinct from microglia. The Journal of experimental medicine. 2018;215(6):1627-47.
177. Butovsky O, Jedrychowski MP, Moore CS, Cialic R, Lanser AJ, Gabriely G, et al. Identification of a unique TGF-β-dependent molecular and functional signature in microglia. Nature neuroscience. 2014;17(1):131-43.
178. Krasemann S, Madore C, Cialic R, Baufeld C, Calcagno N, El Fatimy R, et al. The TREM2-APOE Pathway Drives the Transcriptional Phenotype of Dysfunctional Microglia in Neurodegenerative Diseases. Immunity. 2017;47(3):566-81.e9.

179. Keren-Shaul H, Spinrad A, Weiner A, Matcovitch-Natan O, Dvir-Szternfeld R, Ulland TK, et al. A Unique Microglia Type Associated with Restricting Development of Alzheimer's Disease. Cell. 2017;169(7):1276-90.e17.
180. Hammond TR, Dufort C, Dissing-Olesen L, Giera S, Young A, Wysoker A, et al. Single-Cell RNA Sequencing of Microglia throughout the Mouse Lifespan and in the Injured Brain Reveals Complex Cell-State Changes. Immunity. 2019;50(1):253-71.e6.
181. Tan Y-L, Yuan Y, Tian L. Microglial regional heterogeneity and its role in the brain. Molecular psychiatry. 2020;25(2):351-67.
182. Colonna M, Butovsky O. Microglia Function in the Central Nervous System During Health and Neurodegeneration. Annual review of immunology. 2017;35:441-68.
183. Schafer DP, Lehrman EK, Kautzman AG, Koyama R, Mardinly AR, Yamasaki R, et al. Microglia sculpt postnatal neural circuits in an activity and complement-dependent manner. Neuron. 2012;74(4):691-705.
184. Schafer DP, Stevens B. Microglia Function in Central Nervous System Development and Plasticity. Cold Spring Harbor perspectives in biology. 2015;7(10):a020545.
185. Stevens B, Allen NJ, Vazquez LE, Howell GR, Christopherson KS, Nouri N, et al. The classical complement cascade mediates CNS synapse elimination. Cell. 2007;131(6):1164-78.
186. Badimon A, Strasburger HJ, Ayata P, Chen X, Nair A, Ikegami A, et al. Negative feedback control of neuronal activity by microglia. Nature. 2020;586(7829):417-23.
187. Shigemoto-Mogami Y, Hoshikawa K, Goldman JE, Sekino Y, Sato K. Microglia enhance neurogenesis and oligodendrogenesis in the early postnatal subventricular zone. The Journal of neuroscience : the official journal of the Society for Neuroscience. 2014;34(6):2231-43.
188. Hagemeyer N, Hanft K-M, Akriditou M-A, Unger N, Park ES, Stanley ER, et al. Microglia contribute to normal myelinogenesis and to oligodendrocyte progenitor maintenance during adulthood. Acta neuropathologica. 2017;134(3):441-58.
189. Lloyd AF, Davies CL, Miron VE. Microglia: origins, homeostasis, and roles in myelin repair. Curr Opin Neurobiol. 2017;47:113-20.
190. Rodríguez AM, Rodríguez J, Giambartolomei GH. Microglia at the Crossroads of Pathogen-Induced Neuroinflammation. ASN neuro. 2022;14:17590914221104566.
191. Woodburn SC, Bollinger JL, Wohleb ES. The semantics of microglia activation: neuroinflammation, homeostasis, and stress. Journal of neuroinflammation. 2021;18(1):258.
192. Kwon HS, Koh S-H. Neuroinflammation in neurodegenerative disorders: the roles of microglia and astrocytes. Translational neurodegeneration. 2020;9(1):42.
193. Guzman-Martinez L, Maccioni RB, Andrade V, Navarrete LP, Pastor MG, Ramos-Escobar N. Neuroinflammation as a Common Feature of Neurodegenerative Disorders. Front Pharmacol. 2019;10:1008.
194. Sala Frigerio C, Wolfs L, Fattorelli N, Thrupp N, Voytyuk I, Schmidt I, et al. The Major Risk Factors for Alzheimer's Disease: Age, Sex, and Genes Modulate the Microglia Response to Aβ Plaques. Cell reports. 2019;27(4):1293-306.e6.
195. Sebastian Monasor L, Müller SA, Colombo AV, Tanrioever G, König J, Roth S, et al. Fibrillar Aβ triggers microglial proteome alterations and dysfunction in Alzheimer mouse models. eLife. 2020;9.
196. Muzio L, Viotti A, Martino G. Microglia in Neuroinflammation and Neurodegeneration: From Understanding to Therapy. Frontiers in neuroscience. 2021;15:742065.
197. Boche D, Gordon MN. Diversity of transcriptomic microglial phenotypes in aging and Alzheimer's disease. Alzheimer's & Dementia. 2022;18(2):360-76.
198. Kavetsky L, Green KK, Boyle BR, Yousufzai FAK, Padron ZM, Melli SE, et al. Increased interactions and engulfment of dendrites by microglia precede Purkinje cell degeneration in a mouse model of Niemann Pick Type-C. Scientific reports. 2019;9(1):14722.
199. Boyle BR, Melli SE, Altreche RS, Padron ZM, Yousufzai FAK, Kim S, et al. NPC1 deficiency impairs cerebellar postnatal development of microglia and climbing fiber

refinement in a mouse model of Niemann-Pick Type C disease. Development (Cambridge, England). 2020.

200. Cougnoux A, Drummond RA, Collar AL, Iben JR, Salman A, Westgarth H, et al. Microglia activation in Niemann-Pick disease, type C1 is amendable to therapeutic intervention. Human molecular genetics. 2018;27(12):2076-89.

201. Gabandé-Rodríguez E, Pérez-Cañamás A, Soto-Huelin B, Mitroi DN, Sánchez-Redondo S, Martínez-Sáez E, et al. Lipid-induced lysosomal damage after demyelination corrupts microglia protective function in lysosomal storage disorders. EMBO J. 2019;38(2):e99553.

202. Williams IM, Wallom KL, Smith DA, Al Eisa N, Smith C, Platt FM. Improved neuroprotection using miglustat, curcumin and ibuprofen as a triple combination therapy in Niemann-Pick disease type C1 mice. Neurobiology of disease. 2014;67:9-17.

203. Peake KB, Campenot RB, Vance DE, Vance JE. Niemann-Pick Type C1 deficiency in microglia does not cause neuron death in vitro. Biochimica et biophysica acta. 2011;1812(9):1121-9.

204. Sitarska D, Tylki-Szymańska A, Ługowska A. Treatment trials in Niemann-Pick type C disease. Metabolic brain disease. 2021;36(8):2215-21.

205. Patterson MC, Di Bisceglie AM, Higgins JJ, Abel RB, Schiffmann R, Parker CC, et al. The effect of cholesterol-lowering agents on hepatic and plasma cholesterol in Niemann-Pick disease type C. Neurology. 1993;43(1):61-4.

206. Erickson RP, Garver WS, Camargo F, Hossain GS, Heidenreich RA. Pharmacological and genetic modifications of somatic cholesterol do not substantially alter the course of CNS disease in Niemann-Pick C mice. Journal of inherited metabolic disease. 2000;23(1):54-62.

207. Loftsson T, Jarho P, Másson M, Järvinen T. Cyclodextrins in drug delivery. Expert opinion on drug delivery. 2005;2(2):335-51.

208. Griffin LD, Gong W, Verot L, Mellon SH. Niemann-Pick type C disease involves disrupted neurosteroidogenesis and responds to allopregnanolone. Nature medicine. 2004;10(7):704-11.

209. Rosenbaum AI, Zhang G, Warren JD, Maxfield FR. Endocytosis of beta-cyclodextrins is responsible for cholesterol reduction in Niemann-Pick type C mutant cells. Proceedings of the National Academy of Sciences of the United States of America. 2010;107(12):5477-82.

210. Abi-Mosleh L, Infante RE, Radhakrishnan A, Goldstein JL, Brown MS. Cyclodextrin overcomes deficient lysosome-to-endoplasmic reticulum transport of cholesterol in Niemann-Pick type C cells. Proceedings of the National Academy of Sciences of the United States of America. 2009;106(46):19316-21.

211. Liu B, Turley SD, Burns DK, Miller AM, Repa JJ, Dietschy JM. Reversal of defective lysosomal transport in NPC disease ameliorates liver dysfunction and neurodegeneration in the npc1-/- mouse. Proceedings of the National Academy of Sciences of the United States of America. 2009;106(7):2377-82.

212. Calias P. 2-Hydroxypropyl-beta-cyclodextrins and the Blood-Brain Barrier: Considerations for Niemann-Pick Disease Type C1. Current pharmaceutical design. 2017;23(40):6231-8.

213. Ory DS, Ottinger EA, Farhat NY, King KA, Jiang X, Weissfeld L, et al. Intrathecal 2-hydroxypropyl-β-cyclodextrin decreases neurological disease progression in Niemann-Pick disease, type C1: a non-randomised, open-label, phase 1-2 trial. Lancet (London, England). 2017;390(10104):1758-68.

214. Berry-Kravis E, Chin J, Hoffmann A, Winston A, Stoner R, LaGorio L, et al. Long-Term Treatment of Niemann-Pick Type C1 Disease With Intrathecal 2-Hydroxypropyl-β-Cyclodextrin. Pediatric neurology. 2018;80:24-34.

215. Peake KB, Vance JE. Defective cholesterol trafficking in Niemann-Pick C-deficient cells. FEBS letters. 2010;584(13):2731-9.

216. Platt FM, Neises GR, Dwek RA, Butters TD. N-butyldeoxynojirimycin is a novel inhibitor of glycolipid biosynthesis. The Journal of biological chemistry. 1994;269(11):8362-5.

217. Stirnemann J, Belmatoug N, Camou F, Serratrice C, Froissart R, Caillaud C, et al. A Review of Gaucher Disease Pathophysiology, Clinical Presentation and Treatments. International journal of molecular sciences. 2017;18(2):441.
218. Cox T, Lachmann R, Hollak C, Aerts J, van Weely S, Hrebícek M, et al. Novel oral treatment of Gaucher's disease with N-butyldeoxynojirimycin (OGT 918) to decrease substrate biosynthesis. Lancet (London, England). 2000;355(9214):1481-5.
219. Zervas M, Somers KL, Thrall MA, Walkley SU. Critical role for glycosphingolipids in Niemann-Pick disease type C. Current biology : CB. 2001;11(16):1283-7.
220. Patterson MC, Vecchio D, Prady H, Abel L, Wraith JE. Miglustat for treatment of Niemann-Pick C disease: a randomised controlled study. The Lancet Neurology. 2007;6(9):765-72.
221. Pineda M, Juríčková K, Karimzadeh P, Kolnikova M, Malinova V, Insua JL, et al. Disease characteristics, prognosis and miglustat treatment effects on disease progression in patients with Niemann-Pick disease Type C: an international, multicenter, retrospective chart review. Orphanet journal of rare diseases. 2019;14(1):32.
222. Curelaru S, Zehavi Y, Almagor T, Spiegel R. Favorable outcomes following early onset oral miglustat in early infantile Niemann Pick Type C. Molecular Genetics and Metabolism Reports. 2021;27:100739.
223. Fecarotta S, Romano A, Della Casa R, Del Giudice E, Bruschini D, Mansi G, et al. Long term follow-up to evaluate the efficacy of miglustat treatment in Italian patients with Niemann-Pick disease type C. Orphanet journal of rare diseases. 2015;10(1):22.
224. Pipalia NH, Cosner CC, Huang A, Chatterjee A, Bourbon P, Farley N, et al. Histone deacetylase inhibitor treatment dramatically reduces cholesterol accumulation in Niemann-Pick type C1 mutant human fibroblasts. Proceedings of the National Academy of Sciences of the United States of America. 2011;108(14):5620-5.
225. Helquist P, Maxfield FR, Wiech NL, Wiest O. Treatment of Niemann–Pick Type C Disease by Histone Deacetylase Inhibitors. Neurotherapeutics. 2013;10(4):688-97.
226. Munkacsi AB, Hammond N, Schneider RT, Senanayake DS, Higaki K, Lagutin K, et al. Normalization of Hepatic Homeostasis in the Npc1(nmf164) Mouse Model of Niemann-Pick Type C Disease Treated with the Histone Deacetylase Inhibitor Vorinostat. The Journal of biological chemistry. 2017;292(11):4395-410.
227. Alam MS, Getz M, Haldar K. Chronic administration of an HDAC inhibitor treats both neurological and systemic Niemann-Pick type C disease in a mouse model. Science translational medicine. 2016;8(326):326ra23.
228. Brown A, Patel S, Ward C, Lorenz A, Ortiz M, DuRoss A, et al. PEG-lipid micelles enable cholesterol efflux in Niemann-Pick Type C1 disease-based lysosomal storage disorder. Scientific reports. 2016;6:31750.
229. Davidson J, Molitor E, Moores S, Gale SE, Subramanian K, Jiang X, et al. 2-Hydroxypropyl-β-cyclodextrin is the active component in a triple combination formulation for treatment of Niemann-Pick C1 disease. Biochimica et Biophysica Acta (BBA) - Molecular and Cell Biology of Lipids. 2019;1864(10):1545-61.
230. Kirkegaard T, Gray J, Priestman DA, Wallom KL, Atkins J, Olsen OD, et al. Heat shock protein-based therapy as a potential candidate for treating the sphingolipidoses. Science translational medicine. 2016;8(355):355ra118.
231. Mengel E, Patterson MC, Da Riol RM, Del Toro M, Deodato F, Gautschi M, et al. Efficacy and safety of arimoclomol in Niemann-Pick disease type C: Results from a double-blind, randomised, placebo-controlled, multinational phase 2/3 trial of a novel treatment. Journal of inherited metabolic disease. 2021;44(6):1463-80.
232. Kaya E, Smith DA, Smith C, Morris L, Bremova-Ertl T, Cortina-Borja M, et al. Acetyl-leucine slows disease progression in lysosomal storage disorders. Brain communications. 2021;3(1):fcaa148.
233. Fields T, Patterson M, Bremova-Ertl T, Belcher G, Billington I, Churchill GC, et al. A master protocol to investigate a novel therapy acetyl-L-leucine for three ultra-rare neurodegenerative diseases: Niemann-Pick type C, the GM2 gangliosidoses, and ataxia telangiectasia. Trials. 2021;22(1):84.

234. Vibert N, Vidal PP. In vitro effects of acetyl-DL-leucine (tanganil) on central vestibular neurons and vestibulo-ocular networks of the guinea-pig. The European journal of neuroscience. 2001;13(4):735-48.

235. Bremova-Ertl T, Claassen J, Foltan T, Gascon-Bayarri J, Gissen P, Hahn A, et al. Efficacy and safety of N-acetyl-L-leucine in Niemann-Pick disease type C. Journal of neurology. 2022;269(3):1651-62.

236. Patterson MC, Clayton P, Gissen P, Anheim M, Bauer P, Bonnot O, et al. Recommendations for the detection and diagnosis of Niemann-Pick disease type C: An update. Neurology Clinical practice. 2017;7(6):499-511.

237. Willem M, Tahirovic S, Busche MA, Ovsepian SV, Chafai M, Kootar S, et al. η-Secretase processing of APP inhibits neuronal activity in the hippocampus. Nature. 2015;526(7573):443-7.

238. Yamasaki A, Eimer S, Okochi M, Smialowska A, Kaether C, Baumeister R, et al. The GxGD motif of presenilin contributes to catalytic function and substrate identification of gamma-secretase. The Journal of neuroscience : the official journal of the Society for Neuroscience. 2006;26(14):3821-8.

239. Götzl JK, Mori K, Damme M, Fellerer K, Tahirovic S, Kleinberger G, et al. Common pathobiochemical hallmarks of progranulin-associated frontotemporal lobar degeneration and neuronal ceroid lipofuscinosis. Acta neuropathologica. 2014;127(6):845-60.

240. Xiang X, Werner G, Bohrmann B, Liesz A, Mazaheri F, Capell A, et al. TREM2 deficiency reduces the efficacy of immunotherapeutic amyloid clearance. EMBO molecular medicine. 2016;8(9):992-1004.

241. Radde R, Bolmont T, Kaeser SA, Coomaraswamy J, Lindau D, Stoltze L, et al. Abeta42-driven cerebral amyloidosis in transgenic mice reveals early and robust pathology. EMBO reports. 2006;7(9):940-6.

242. Yona S, Kim KW, Wolf Y, Mildner A, Varol D, Breker M, et al. Fate mapping reveals origins and dynamics of monocytes and tissue macrophages under homeostasis. Immunity. 2013;38(1):79-91.

243. Colombo A, Dinkel L, Müller SA, Sebastian Monasor L, Schifferer M, Cantuti-Castelvetri L, et al. Loss of NPC1 enhances phagocytic uptake and impairs lipid trafficking in microglia. Nature communications. 2021;12(1):1158.

244. Didusch S, Madern M, Hartl M, Baccarini M. amica: an interactive and user-friendly web-platform for the analysis of proteomics data. BMC genomics. 2022;23(1):817.

245. Demichev V, Messner CB, Vernardis SI, Lilley KS, Ralser M. DIA-NN: neural networks and interference correction enable deep proteome coverage in high throughput. Nature methods. 2020;17(1):41-4.

246. Cox J, Hein MY, Luber CA, Paron I, Nagaraj N, Mann M. Accurate proteome-wide label-free quantification by delayed normalization and maximal peptide ratio extraction, termed MaxLFQ. Molecular & cellular proteomics : MCP. 2014;13(9):2513-26.

247. Tyanova S, Temu T, Sinitcyn P, Carlson A, Hein MY, Geiger T, et al. The Perseus computational platform for comprehensive analysis of (prote)omics data. Nature methods. 2016;13(9):731-40.

248. Luo L, Ambrozkiewicz MC, Benseler F, Chen C, Dumontier E, Falkner S, et al. Optimizing Nervous System-Specific Gene Targeting with Cre Driver Lines: Prevalence of Germline Recombination and Influencing Factors. Neuron. 2020;106(1):37-65.e5.

249. Wiśniewski JR, Zougman A, Mann M. Combination of FASP and StageTip-based fractionation allows in-depth analysis of the hippocampal membrane proteome. Journal of proteome research. 2009;8(12):5674-8.

250. Rappsilber J, Ishihama Y, Mann M. Stop and go extraction tips for matrix-assisted laser desorption/ionization, nanoelectrospray, and LC/MS sample pretreatment in proteomics. Analytical chemistry. 2003;75(3):663-70.

251. Tusher VG, Tibshirani R, Chu G. Significance analysis of microarrays applied to the ionizing radiation response. Proceedings of the National Academy of Sciences of the United States of America. 2001;98(9):5116-21.

252. Hughes CS, Moggridge S, Müller T, Sorensen PH, Morin GB, Krijgsveld J. Single-pot, solid-phase-enhanced sample preparation for proteomics experiments. Nature protocols. 2019;14(1):68-85.
253. Rudan Njavro J, Vukicevic M, Fiorini E, Dinkel L, Müller SA, Berghofer A, et al. Beneficial Effect of ACI-24 Vaccination on Aβ Plaque Pathology and Microglial Phenotypes in an Amyloidosis Mouse Model. Cells. 2023;12(1):79.
254. Maloney MT, Wang X, Ghosh R, Andrews SV, Maciuca R, Masoud ST, et al. LRRK2 Kinase Activity Regulates Parkinson’s Disease-Relevant Lipids at the Lysosome. bioRxiv. 2022:2022.12.19.521070.
255. Logan T, Simon MJ, Rana A, Cherf GM, Srivastava A, Davis SS, et al. Rescue of a lysosomal storage disorder caused by Grn loss of function with a brain penetrant progranulin biologic. Cell. 2021;184(18):4651-68.e25.
256. Reifschneider A, Robinson S, van Lengerich B, Gnorich J, Logan T, Heindl S, et al. Loss of TREM2 rescues hyperactivation of microglia, but not lysosomal deficits and neurotoxicity in models of progranulin deficiency. EMBO J. 2022:e109108.
257. Ma Y, Hof PR, Grant SC, Blackband SJ, Bennett R, Slatest L, et al. A three-dimensional digital atlas database of the adult C57BL/6J mouse brain by magnetic resonance microscopy. Neuroscience. 2005;135(4):1203-15.
258. Bartos LM, Kunte ST, Beumers P, Xiang X, Wind K, Ziegler S, et al. Single-Cell Radiotracer Allocation via Immunomagnetic Sorting to Disentangle PET Signals at Cellular Resolution. Journal of nuclear medicine : official publication, Society of Nuclear Medicine. 2022;63(10):1459-62.
259. Gnörich J, Reifschneider A, Wind K, Zatcepin A, Kunte ST, Beumers P, et al. Depletion and activation of microglia impact metabolic connectivity of the mouse brain. Journal of neuroinflammation. 2023;20(1):47.
260. Xiang X, Wind K, Wiedemann T, Blume T, Shi Y, Briel N, et al. Microglial activation states drive glucose uptake and FDG-PET alterations in neurodegenerative diseases. Science translational medicine. 2021;13(615):eabe5640.
261. Roth S, Yang J, Cramer JV, Malik R, Liesz A. Detection of cytokine-induced sickness behavior after ischemic stroke by an optimized behavioral assessment battery. Brain Behav Immun. 2021;91:668-72.
262. Higashi Y, Murayama S, Pentchev PG, Suzuki K. Cerebellar degeneration in the Niemann-Pick type C mouse. Acta neuropathologica. 1993;85(2):175-84.
263. Ayata P, Badimon A, Strasburger HJ, Duff MK, Montgomery SE, Loh YE, et al. Epigenetic regulation of brain region-specific microglia clearance activity. Nature neuroscience. 2018;21(8):1049-60.
264. Ong WY, Kumar U, Switzer RC, Sidhu A, Suresh G, Hu CY, et al. Neurodegeneration in Niemann-Pick type C disease mice. Experimental brain research. 2001;141(2):218-31.
265. Pols MS, Klumperman J. Trafficking and function of the tetraspanin CD63. Experimental cell research. 2009;315(9):1584-92.
266. Domingues HS, Portugal CC, Socodato R, Relvas JB. Oligodendrocyte, Astrocyte, and Microglia Crosstalk in Myelin Development, Damage, and Repair. Frontiers in cell and developmental biology. 2016;4:71.
267. Stadelmann C, Timmler S, Barrantes-Freer A, Simons M. Myelin in the Central Nervous System: Structure, Function, and Pathology. Physiological reviews. 2019;99(3):1381-431.
268. Geltinger F, Schartel L, Wiederstein M, Tevini J, Aigner E, Felder TK, et al. Friend or Foe: Lipid Droplets as Organelles for Protein and Lipid Storage in Cellular Stress Response, Aging and Disease. Molecules (Basel, Switzerland). 2020;25(21).
269. Uribe-Querol E, Rosales C. Phagocytosis: Our Current Understanding of a Universal Biological Process. Frontiers in immunology. 2020;11:1066.
270. Bohlen CJ, Bennett FC, Tucker AF, Collins HY, Mulinyawe SB, Barres BA. Diverse Requirements for Microglial Survival, Specification, and Function Revealed by Defined-Medium Cultures. Neuron. 2017;94(4):759-73.e8.
271. Hammond N, Munkacsi AB, Sturley SL. The complexity of a monogenic neurodegenerative disease: More than two decades of therapeutic driven research into

Niemann-Pick type C disease. Biochimica et biophysica acta Molecular and cell biology of lipids. 2019;1864(8):1109-23.

272. Gouna G, Klose C, Bosch-Queralt M, Liu L, Gokce O, Schifferer M, et al. TREM2-dependent lipid droplet biogenesis in phagocytes is required for remyelination. The Journal of experimental medicine. 2021;218(10).

273. Guyton JR, Klemp KF. Early extracellular and cellular lipid deposits in aorta of cholesterol-fed rabbits. The American journal of pathology. 1992;141(4):925-36.

274. Pugach EK, Feltes M, Kaufman RJ, Ory DS, Bang AG. High-content screen for modifiers of Niemann-Pick type C disease in patient cells. Human molecular genetics. 2018;27(12):2101-12.

275. Fan M, Sidhu R, Fujiwara H, Tortelli B, Zhang J, Davidson C, et al. Identification of Niemann-Pick C1 disease biomarkers through sphingolipid profiling. Journal of lipid research. 2013;54(10):2800-14.

276. Weintraub H, Abramovici A, Sandbank U, Pentchev PG, Brady RO, Sekine M, et al. Neurological mutation characterized by dysmyelination in NCTR-Balb/C mouse with lysosomal lipid storage disease. Journal of neurochemistry. 1985;45(3):665-72.

277. Gallala HD, Sandhoff K. Biological function of the cellular lipid BMP-BMP as a key activator for cholesterol sorting and membrane digestion. Neurochemical research. 2011;36(9):1594-600.

278. Hidalgo-Gutiérrez A, González-García P, Díaz-Casado ME, Barriocanal-Casado E, López-Herrador S, Quinzii CM, et al. Metabolic Targets of Coenzyme Q10 in Mitochondria. Antioxidants (Basel, Switzerland). 2021;10(4).

279. Zhang L, Hu K, Shao T, Hou L, Zhang S, Ye W, et al. Recent developments on PET radiotracers for TSPO and their applications in neuroimaging. Acta pharmaceutica Sinica B. 2021;11(2):373-93.

280. Liddelow SA, Guttenplan KA, Clarke LE, Bennett FC, Bohlen CJ, Schirmer L, et al. Neurotoxic reactive astrocytes are induced by activated microglia. Nature. 2017;541(7638):481-7.

281. Meyer JH, Braga J. Development and Clinical Application of Positron Emission Tomography Imaging Agents for Monoamine Oxidase B. Frontiers in neuroscience. 2021;15:773404.

282. Qiao L, Yang E, Luo J, Lin J, Yan X. Altered myelination in the Niemann-Pick type C1 mutant mouse. Histology and histopathology. 2018;33(12):1311-21.

283. Yan X, Yang F, Lukas J, Witt M, Wree A, Rolfs A, et al. Hyperactive glial cells contribute to axonal pathologies in the spinal cord of Npc1 mutant mice. Glia. 2014;62(7):1024-40.

284. Pressey SN, Smith DA, Wong AM, Platt FM, Cooper JD. Early glial activation, synaptic changes and axonal pathology in the thalamocortical system of Niemann-Pick type C1 mice. Neurobiology of disease. 2012;45(3):1086-100.

285. Ohgami T, Kitamoto T, Tateishi J. Alzheimer's amyloid precursor protein accumulates within axonal swellings in human brain lesions. Neuroscience letters. 1992;136(1):75-8.

286. Mendonça DM, Chimelli L, Martinez AM. Quantitative evidence for neurofilament heavy subunit aggregation in motor neurons of spinal cords of patients with amyotrophic lateral sclerosis. Brazilian journal of medical and biological research = Revista brasileira de pesquisas medicas e biologicas. 2005;38(6):925-33.

287. Bäckström D, Linder J, Mo SJ, Riklund K, Zetterberg H, Blennow K, et al. NfL as a biomarker for neurodegeneration and survival in Parkinson disease. Neurology. 2020;95(7):e827-e38.

288. Minoshima S, Cross D, Thientunyakit T, Foster NL, Drzezga A. (18)F-FDG PET Imaging in Neurodegenerative Dementing Disorders: Insights into Subtype Classification, Emerging Disease Categories, and Mixed Dementia with Copathologies. Journal of nuclear medicine : official publication, Society of Nuclear Medicine. 2022;63(Suppl 1):2s-12s.

289. Cheng X-T, Xie Y-X, Zhou B, Huang N, Farfel-Becker T, Sheng Z-H. Characterization of LAMP1-labeled nondegradative lysosomal and endocytic compartments in neurons. Journal of Cell Biology. 2018;217(9):3127-39.

290. Cheng XT, Xie YX, Zhou B, Huang N, Farfel-Becker T, Sheng ZH. Revisiting LAMP1 as a marker for degradative autophagy-lysosomal organelles in the nervous system. Autophagy. 2018;14(8):1472-4.
291. Sobo K, Le Blanc I, Luyet PP, Fivaz M, Ferguson C, Parton RG, et al. Late endosomal cholesterol accumulation leads to impaired intra-endosomal trafficking. PloS one. 2007;2(9):e851.
292. Meneses-Salas E, García-Melero A, Kanerva K, Blanco-Muñoz P, Morales-Paytuvi F, Bonjoch J, et al. Annexin A6 modulates TBC1D15/Rab7/StARD3 axis to control endosomal cholesterol export in NPC1 cells. Cellular and Molecular Life Sciences. 2020;77(14):2839-57.
293. Ganley IG, Pfeffer SR. Cholesterol accumulation sequesters Rab9 and disrupts late endosome function in NPC1-deficient cells. The Journal of biological chemistry. 2006;281(26):17890-9.
294. Kobayashi T, Beuchat M-H, Lindsay M, Frias S, Palmiter RD, Sakuraba H, et al. Late endosomal membranes rich in lysobisphosphatidic acid regulate cholesterol transport. Nature cell biology. 1999;1(2):113-8.
295. Blanchette-Mackie EJ, Dwyer NK, Amende LM, Kruth HS, Butler JD, Sokol J, et al. Type-C Niemann-Pick disease: low density lipoprotein uptake is associated with premature cholesterol accumulation in the Golgi complex and excessive cholesterol storage in lysosomes. Proceedings of the National Academy of Sciences of the United States of America. 1988;85(21):8022-6.
296. Guix FX, Capitán AM, Casadomé-Perales Á, Palomares-Pérez I, López del Castillo I, Miguel V, et al. Increased exosome secretion in neurons aging in vitro by NPC1-mediated endosomal cholesterol buildup. Life Science Alliance. 2021;4(8):e202101055.
297. Marchetti A, Mercanti V, Cornillon S, Alibaud L, Charette SJ, Cosson P. Formation of multivesicular endosomes in Dictyostelium. Journal of cell science. 2004;117(Pt 25):6053-9.
298. Scott C, Higgins ME, Davies JP, Ioannou YA. Targeting of NPC1 to Late Endosomes Involves Multiple Signals, Including One Residing within the Putative Sterol-sensing Domain*. Journal of Biological Chemistry. 2004;279(46):48214-23.
299. Higgins ME, Davies JP, Chen FW, Ioannou YA. Niemann-Pick C1 is a late endosome-resident protein that transiently associates with lysosomes and the trans-Golgi network. Molecular genetics and metabolism. 1999;68(1):1-13.
300. Neufeld EB, Wastney M, Patel S, Suresh S, Cooney AM, Dwyer NK, et al. The Niemann-Pick C1 protein resides in a vesicular compartment linked to retrograde transport of multiple lysosomal cargo. The Journal of biological chemistry. 1999;274(14):9627-35.
301. Möbius W, Ohno-Iwashita Y, Donselaar EGv, Oorschot VMJ, Shimada Y, Fujimoto T, et al. Immunoelectron Microscopic Localization of Cholesterol Using Biotinylated and Non-cytolytic Perfringolysin O. Journal of Histochemistry & Cytochemistry. 2002;50(1):43-55.
302. Lusa S, Blom TS, Eskelinen EL, Kuismanen E, Månsson JE, Simons K, et al. Depletion of rafts in late endocytic membranes is controlled by NPC1-dependent recycling of cholesterol to the plasma membrane. Journal of cell science. 2001;114(Pt 10):1893-900.
303. Ilnytska O, Lai K, Gorshkov K, Schultz ML, Tran BN, Jeziorek M, et al. Enrichment of NPC1-deficient cells with the lipid LBPA stimulates autophagy, improves lysosomal function, and reduces cholesterol storage. The Journal of biological chemistry. 2021;297(1):100813.
304. Moreau D, Vacca F, Vossio S, Scott C, Colaco A, Paz Montoya J, et al. Drug-induced increase in lysobisphosphatidic acid reduces the cholesterol overload in Niemann-Pick type C cells and mice. EMBO reports. 2019;20(7):e47055.
305. Chen J, Cazenave-Gassiot A, Xu Y, Piroli P, Hwang R, DeFreitas L, et al. Lysosomal phospholipase A2 contributes to the biosynthesis of the atypical late endosome lipid bis(monoacylglycero)phosphate. Communications Biology. 2023;6(1):210.
306. Liu N, Tengstrand EA, Chourb L, Hsieh FY. Di-22:6-bis(monoacylglycerol)phosphate: A clinical biomarker of drug-induced phospholipidosis for drug development and safety assessment. Toxicology and applied pharmacology. 2014;279(3):467-76.

307. Hullin-Matsuda F, Kawasaki K, Delton-Vandenbroucke I, Xu Y, Nishijima M, Lagarde M, et al. De novo biosynthesis of the late endosome lipid, bis(monoacylglycero)phosphates. Journal of lipid research. 2007;48(9):1997-2008.
308. Raiborg C, Wenzel EM, Stenmark H. ER–endosome contact sites: molecular compositions and functions. EMBO J. 2015;34(14):1848-58.
309. Mengel E, Bembi B, Del Toro M, Deodato F, Gautschi M, Grunewald S, et al. Clinical disease progression and biomarkers in Niemann-Pick disease type C: a prospective cohort study. Orphanet journal of rare diseases. 2020;15(1):328.
310. Musalkova D, Majer F, Kuchar L, Luksan O, Asfaw B, Vlaskova H, et al. Transcript, protein, metabolite and cellular studies in skin fibroblasts demonstrate variable pathogenic impacts of NPC1 mutations. Orphanet journal of rare diseases. 2020;15(1):85.
311. Vanier MT, Wenger DA, Comly ME, Rousson R, Brady RO, Pentchev PG. Niemann-Pick disease group C: clinical variability and diagnosis based on defective cholesterol esterification. A collaborative study on 70 patients. Clinical genetics. 1988;33(5):331-48.
312. Kulinski A, Vance JE. Lipid homeostasis and lipoprotein secretion in Niemann-Pick C1-deficient hepatocytes. The Journal of biological chemistry. 2007;282(3):1627-37.
313. Gruenbacher G, Thurnher M. Mevalonate metabolism governs cancer immune surveillance. Oncoimmunology. 2017;6(10):e1342917.
314. Moebius FF, Fitzky BU, Lee JN, Paik Y-K, Glossmann H. Molecular cloning and expression of the human Δ7-sterol reductase. Proceedings of the National Academy of Sciences. 1998;95(4):1899-902.
315. Mollet J, Giurgea I, Schlemmer D, Dallner G, Chretien D, Delahodde A, et al. Prenyldiphosphate synthase, subunit 1 (PDSS1) and OH-benzoate polyprenyltransferase (COQ2) mutations in ubiquinone deficiency and oxidative phosphorylation disorders. The Journal of clinical investigation. 2007;117(3):765-72.
316. Schedin S, Pentchev PG, Brunk U, Dallner G. Changes in the levels of dolichol and dolichyl phosphate in a murine model of Niemann-Pick's type C disease. Journal of neurochemistry. 1995;65(2):670-6.
317. Cantagrel V, Lefeber DJ. From glycosylation disorders to dolichol biosynthesis defects: a new class of metabolic diseases. Journal of inherited metabolic disease. 2011;34(4):859-67.
318. Buczkowska A, Swiezewska E, Lefeber DJ. Genetic defects in dolichol metabolism. Journal of inherited metabolic disease. 2015;38(1):157-69.
319. Kosicek M, Gudelj I, Horvatic A, Jovic T, Vuckovic F, Lauc G, et al. N-glycome of the Lysosomal Glycocalyx is Altered in Niemann-Pick Type C Disease (NPC) Model Cells. Molecular & Cellular Proteomics. 2018;17(4):631-42.
320. Cawley NX, Sojka C, Cougnoux A, Lyons AT, Nicoli ER, Wassif CA, et al. Abnormal LAMP1 glycosylation may play a role in Niemann-Pick disease, type C pathology. PloS one. 2020;15(1):e0227829.
321. Uronen RL, Lundmark P, Orho-Melander M, Jauhiainen M, Larsson K, Siegbahn A, et al. Niemann-Pick C1 modulates hepatic triglyceride metabolism and its genetic variation contributes to serum triglyceride levels. Arterioscler Thromb Vasc Biol. 2010;30(8):1614-20.
322. Kennedy BE, LeBlanc VG, Mailman TM, Fice D, Burton I, Karakach TK, et al. Pre-symptomatic activation of antioxidant responses and alterations in glucose and pyruvate metabolism in Niemann-Pick Type C1-deficient murine brain. PloS one. 2013;8(12):e82685.
323. Olzmann JA, Carvalho P. Dynamics and functions of lipid droplets. Nature reviews Molecular cell biology. 2019;20(3):137-55.
324. Marschallinger J, Iram T, Zardeneta M, Lee SE, Lehallier B, Haney MS, et al. Lipid-droplet-accumulating microglia represent a dysfunctional and proinflammatory state in the aging brain. Nature neuroscience. 2020;23(2):194-208.
325. Smolič T, Tavčar P, Horvat A, Černe U, Halužan Vasle A, Tratnjek L, et al. Astrocytes in stress accumulate lipid droplets. Glia. 2021;69(6):1540-62.

326. Belazi D, Solé-Domènech S, Johansson B, Schalling M, Sjövall P. Chemical analysis of osmium tetroxide staining in adipose tissue using imaging ToF-SIMS. Histochemistry and Cell Biology. 2009;132(1):105-15.

327. Roca-Agujetas V, Barbero-Camps E, de Dios C, Podlesniy P, Abadin X, Morales A, et al. Cholesterol alters mitophagy by impairing optineurin recruitment and lysosomal clearance in Alzheimer’s disease. Molecular neurodegeneration. 2021;16(1):15.

328. Bailey AP, Koster G, Guillermier C, Hirst EM, MacRae JI, Lechene CP, et al. Antioxidant Role for Lipid Droplets in a Stem Cell Niche of Drosophila. Cell. 2015;163(2):340-53.

329. Li N, Sancak Y, Frasor J, Atilla-Gokcumen GE. A Protective Role for Triacylglycerols during Apoptosis. Biochemistry. 2018;57(1):72-80.

330. Liu L, Zhang K, Sandoval H, Yamamoto S, Jaiswal M, Sanz E, et al. Glial lipid droplets and ROS induced by mitochondrial defects promote neurodegeneration. Cell. 2015;160(1-2):177-90.

331. Ioannou MS, Jackson J, Sheu SH, Chang CL, Weigel AV, Liu H, et al. Neuron-Astrocyte Metabolic Coupling Protects against Activity-Induced Fatty Acid Toxicity. Cell. 2019;177(6):1522-35.e14.

332. Jürs AV, Völkner C, Liedtke M, Huth K, Lukas J, Hermann A, et al. Oxidative Stress and Alterations in the Antioxidative Defense System in Neuronal Cells Derived from NPC1 Patient-Specific Induced Pluripotent Stem Cells. International journal of molecular sciences. 2020;21(20):7667.

333. Raj Rai S, Bhattacharyya C, Sarkar A, Chakraborty S, Sircar E, Dutta S, et al. Glutathione: Role in Oxidative/Nitrosative Stress, Antioxidant Defense, and Treatments. ChemistrySelect. 2021;6(18):4566-90.

334. Fu R, Yanjanin NM, Bianconi S, Pavan WJ, Porter FD. Oxidative stress in Niemann-Pick disease, type C. Molecular genetics and metabolism. 2010;101(2-3):214-8.

335. Stepien KM, Roncaroli F, Turton N, Hendriksz CJ, Roberts M, Heaton RA, et al. Mechanisms of Mitochondrial Dysfunction in Lysosomal Storage Disorders: A Review. Journal of clinical medicine. 2020;9(8).

336. Zaidi N, Maurer A, Nieke S, Kalbacher H. Cathepsin D: A cellular roadmap. Biochemical and biophysical research communications. 2008;376(1):5-9.

337. Maharjan Y, Dutta RK, Son J, Wei X, Park C, Kwon HM, et al. Intracellular cholesterol transport inhibition Impairs autophagy flux by decreasing autophagosome–lysosome fusion. Cell Communication and Signaling. 2022;20(1):189.

338. Götzl JK, Brendel M, Werner G, Parhizkar S, Sebastian Monasor L, Kleinberger G, et al. Opposite microglial activation stages upon loss of PGRN or TREM2 result in reduced cerebral glucose metabolism. EMBO molecular medicine. 2019;11(6):e9711.

339. Cougnoux A, Drummond RA, Fellmeth M, Navid F, Collar AL, Iben J, et al. Unique molecular signature in mucolipidosis type IV microglia. Journal of neuroinflammation. 2019;16(1):276.

340. Nugent AA, Lin K, van Lengerich B, Lianoglou S, Przybyla L, Davis SS, et al. TREM2 Regulates Microglial Cholesterol Metabolism upon Chronic Phagocytic Challenge. Neuron. 2020;105(5):837-54.e9.

341. Monsorno K, Buckinx A, Paolicelli RC. Microglial metabolic flexibility: emerging roles for lactate. Trends in endocrinology and metabolism: TEM. 2022;33(3):186-95.

342. Lauro C, Limatola C. Metabolic Reprograming of Microglia in the Regulation of the Innate Inflammatory Response. Frontiers in immunology. 2020;11.

343. Zhao Y, Xu H. Microglial lactate metabolism as a potential therapeutic target for Alzheimer’s disease. Molecular neurodegeneration. 2022;17(1):36.

344. Rava A, La Rosa P, Palladino G, Dragotto J, Totaro A, Tiberi J, et al. The appearance of phagocytic microglia in the postnatal brain of Niemann Pick type C mice is developmentally regulated and underscores shortfalls in fine odor discrimination. Journal of cellular physiology. 2022;237(12):4563-79.

345. Floden AM, Combs CK. Microglia demonstrate age-dependent interaction with amyloid-β fibrils. Journal of Alzheimer's disease : JAD. 2011;25(2):279-93.

346. Daria A, Colombo A, Llovera G, Hampel H, Willem M, Liesz A, et al. Young microglia restore amyloid plaque clearance of aged microglia. EMBO J. 2017;36(5):583-603.

347. Anderson SR, Zhang J, Steele MR, Romero CO, Kautzman AG, Schafer DP, et al. Complement Targets Newborn Retinal Ganglion Cells for Phagocytic Elimination by Microglia. The Journal of neuroscience : the official journal of the Society for Neuroscience. 2019;39(11):2025-40.
348. VanRyzin JW, Marquardt AE, Argue KJ, Vecchiarelli HA, Ashton SE, Arambula SE, et al. Microglial Phagocytosis of Newborn Cells Is Induced by Endocannabinoids and Sculpts Sex Differences in Juvenile Rat Social Play. Neuron. 2019;102(2):435-49.e6.
349. DeBose-Boyd RA, Ye J. SREBPs in Lipid Metabolism, Insulin Signaling, and Beyond. Trends Biochem Sci. 2018;43(5):358-68.
350. Lee JH, Phelan P, Shin M, Oh BC, Han X, Im SS, et al. SREBP-1a-stimulated lipid synthesis is required for macrophage phagocytosis downstream of TLR4-directed mTORC1. Proceedings of the National Academy of Sciences of the United States of America. 2018;115(52):E12228-e34.
351. Ecker J, Liebisch G, Englmaier M, Grandl M, Robenek H, Schmitz G. Induction of fatty acid synthesis is a key requirement for phagocytic differentiation of human monocytes. Proceedings of the National Academy of Sciences. 2010;107(17):7817-22.
352. Mizutani M, Pino PA, Saederup N, Charo IF, Ransohoff RM, Cardona AE. The fractalkine receptor but not CCR2 is present on microglia from embryonic development throughout adulthood. Journal of immunology (Baltimore, Md : 1950). 2012;188(1):29-36.
353. Sahasrabuddhe V, Ghosh HS. Cx3Cr1-Cre induction leads to microglial activation and IFN-1 signaling caused by DNA damage in early postnatal brain. Cell reports. 2022;38(3):110252.
354. Kim C, Ho DH, Suk JE, You S, Michael S, Kang J, et al. Neuron-released oligomeric α-synuclein is an endogenous agonist of TLR2 for paracrine activation of microglia. Nature communications. 2013;4:1562.
355. Taylor RA, Sansing LH. Microglial responses after ischemic stroke and intracerebral hemorrhage. Clinical & developmental immunology. 2013;2013:746068.
356. Santos EN, Fields RD. Regulation of myelination by microglia. Science advances. 2021;7(50):eabk1131.
357. Hughes AN, Appel B. Microglia phagocytose myelin sheaths to modify developmental myelination. Nature neuroscience. 2020;23(9):1055-66.
358. Djannatian M, Radha S, Weikert U, Safaiyan S, Wrede C, Deichsel C, et al. Myelination generates aberrant ultrastructure that is resolved by microglia. The Journal of cell biology. 2023;222(3).
359. Cunha MI, Su M, Cantuti-Castelvetri L, Müller SA, Schifferer M, Djannatian M, et al. Pro-inflammatory activation following demyelination is required for myelin clearance and oligodendrogenesis. Journal of Experimental Medicine. 2020;217(5).
360. Foran DR, Peterson AC. Myelin acquisition in the central nervous system of the mouse revealed by an MBP-Lac Z transgene. The Journal of neuroscience : the official journal of the Society for Neuroscience. 1992;12(12):4890-7.
361. Cantuti-Castelvetri L, Fitzner D, Bosch-Queralt M, Weil MT, Su M, Sen P, et al. Defective cholesterol clearance limits remyelination in the aged central nervous system. Science (New York, NY). 2018;359(6376):684-8.
362. Boza-Serrano A, Ruiz R, Sanchez-Varo R, García-Revilla J, Yang Y, Jimenez-Ferrer I, et al. Galectin-3, a novel endogenous TREM2 ligand, detrimentally regulates inflammatory response in Alzheimer's disease. Acta neuropathologica. 2019;138(2):251-73.
363. Thomas L, Pasquini LA. Galectin-3-Mediated Glial Crosstalk Drives Oligodendrocyte Differentiation and (Re)myelination. Frontiers in cellular neuroscience. 2018;12:297.
364. Hoyos HC, Marder M, Ulrich R, Gudi V, Stangel M, Rabinovich GA, et al. The Role of Galectin-3: From Oligodendroglial Differentiation and Myelination to Demyelination and Remyelination Processes in a Cuprizone-Induced Demyelination Model. Advances in experimental medicine and biology. 2016;949:311-32.

365. Hoyos HC, Rinaldi M, Mendez-Huergo SP, Marder M, Rabinovich GA, Pasquini JM, et al. Galectin-3 controls the response of microglial cells to limit cuprizone-induced demyelination. Neurobiology of disease. 2014;62:441-55.
366. McNamara NB, Munro DAD, Bestard-Cuche N, Uyeda A, Bogie JFJ, Hoffmann A, et al. Microglia regulate central nervous system myelin growth and integrity. Nature. 2023;613(7942):120-9.
367. Park MH, Choi BJ, Jeong MS, Lee JY, Jung IK, Park KH, et al. Characterization of the Subventricular-Thalamo-Cortical Circuit in the NP-C Mouse Brain, and New Insights Regarding Treatment. Molecular therapy : the journal of the American Society of Gene Therapy. 2019;27(8):1507-26.
368. Marshall CA, Watkins-Chow DE, Palladino G, Deutsch G, Chandran K, Pavan WJ, et al. In Niemann-Pick C1 mouse models, glial-only expression of the normal gene extends survival much further than do changes in genetic background or treatment with hydroxypropyl-beta-cyclodextrin. Gene. 2018;643:117-23.
369. Liao F, Yoon H, Kim J. Apolipoprotein E metabolism and functions in brain and its role in Alzheimer's disease. Current opinion in lipidology. 2017;28(1):60-7.
370. Wang H, Eckel RH. What are lipoproteins doing in the brain? Trends in endocrinology and metabolism: TEM. 2014;25(1):8-14.
371. Mutka AL, Lusa S, Linder MD, Jokitalo E, Kopra O, Jauhiainen M, et al. Secretion of sterols and the NPC2 protein from primary astrocytes. The Journal of biological chemistry. 2004;279(47):48654-62.
372. Czernecki C, Dixit S, Riezman I, Innocenti S, Bornmann C, Pfrieger FW, et al. Cell type-specific assessment of cholesterol distribution in models of neurodevelopmental disorders. bioRxiv. 2022.
373. Patel SC, Suresh S, Kumar U, Hu CY, Cooney A, Blanchette-Mackie EJ, et al. Localization of Niemann-Pick C1 protein in astrocytes: implications for neuronal degeneration in Niemann- Pick type C disease. Proceedings of the National Academy of Sciences of the United States of America. 1999;96(4):1657-62.
374. Batiuk MY, Martirosyan A, Wahis J, de Vin F, Marneffe C, Kusserow C, et al. Identification of region-specific astrocyte subtypes at single cell resolution. Nature communications. 2020;11(1):1220.
375. Hasel P, Rose IVL, Sadick JS, Kim RD, Liddelow SA. Neuroinflammatory astrocyte subtypes in the mouse brain. Nature neuroscience. 2021;24(10):1475-87.
376. Xie C, Gong XM, Luo J, Li BL, Song BL. AAV9-NPC1 significantly ameliorates Purkinje cell death and behavioral abnormalities in mouse NPC disease. Journal of lipid research. 2017;58(3):512-8.
377. Lopez ME, Klein AD, Dimbil UJ, Scott MP. Anatomically defined neuron-based rescue of neurodegenerative Niemann-Pick type C disorder. The Journal of neuroscience : the official journal of the Society for Neuroscience. 2011;31(12):4367-78.
378. Oyanagi K, Kinoshita M, Suzuki-Kouyama E, Inoue T, Nakahara A, Tokiwai M, et al. Adult onset leukoencephalopathy with axonal spheroids and pigmented glia (ALSP) and Nasu-Hakola disease: lesion staging and dynamic changes of axons and microglial subsets. Brain pathology (Zurich, Switzerland). 2017;27(6):748-69.
379. Alturkustani M, Zhang Q, AlYamany B, Ang L-C. Loss of Ramified Microglia Precedes Axonal Spheroid Formation in Adult-Onset Leukoencephalopathy with Axonal Spheroids. Free Neuropathology. 2020;1:27.
380. Abellanas MA, Zamarbide M, Basurco L, Luquin E, Garcia-Granero M, Clavero P, et al. Midbrain microglia mediate a specific immunosuppressive response under inflammatory conditions. Journal of neuroinflammation. 2019;16(1):233.
381. Craner MJ, Fugger L. Axonal injury in reverse. Nature medicine. 2011;17(4):423-5.
382. Barsukova AG, Forte M, Bourdette D. Focal increases of axoplasmic Ca2+, aggregation of sodium-calcium exchanger, N-type Ca2+ channel, and actin define the sites of spheroids in axons undergoing oxidative stress. The Journal of neuroscience : the official journal of the Society for Neuroscience. 2012;32(35):12028-37.
383. Hernández-Camacho JD, Bernier M, López-Lluch G, Navas P. Coenzyme Q(10) Supplementation in Aging and Disease. Frontiers in physiology. 2018;9:44.

384. Hou L, Zhou X, Zhang C, Wang K, Liu X, Che Y, et al. NADPH oxidase-derived H(2)O(2) mediates the regulatory effects of microglia on astrogliosis in experimental models of Parkinson's disease. Redox biology. 2017;12:162-70.
385. Pizzinat N, Copin N, Vindis C, Parini A, Cambon C. Reactive oxygen species production by monoamine oxidases in intact cells. Naunyn-Schmiedeberg's archives of pharmacology. 1999;359(5):428-31.
386. Borroni E, Bohrmann B, Grueninger F, Prinssen E, Nave S, Loetscher H, et al. Sembragiline: A Novel, Selective Monoamine Oxidase Type B Inhibitor for the Treatment of Alzheimer's Disease. The Journal of pharmacology and experimental therapeutics. 2017;362(3):413-23.
387. Mallajosyula JK, Kaur D, Chinta SJ, Rajagopalan S, Rane A, Nicholls DG, et al. MAO-B elevation in mouse brain astrocytes results in Parkinson's pathology. PloS one. 2008;3(2):e1616.
388. Van Hoecke L, Van Cauwenberghe C, Dominko K, Van Imschoot G, Van Wonterghem E, Castelein J, et al. Involvement of the Choroid Plexus in the Pathogenesis of Niemann-Pick Disease Type C. Frontiers in cellular neuroscience. 2021;15:757482.
389. Strauss K, Goebel C, Runz H, Möbius W, Weiss S, Feussner I, et al. Exosome secretion ameliorates lysosomal storage of cholesterol in Niemann-Pick type C disease. The Journal of biological chemistry. 2010;285(34):26279-88.
390. Asai H, Ikezu S, Tsunoda S, Medalla M, Luebke J, Haydar T, et al. Depletion of microglia and inhibition of exosome synthesis halt tau propagation. Nature neuroscience. 2015;18(11):1584-93.
391. Hsieh K, Lee YK, Londos C, Raaka BM, Dalen KT, Kimmel AR. Perilipin family members preferentially sequester to either triacylglycerol-specific or cholesteryl-ester-specific intracellular lipid storage droplets. Journal of cell science. 2012;125(Pt 17):4067-76.
392. Timmers ER, Klamer MR, Marapin RS, Lammertsma AA, de Jong BM, Dierckx RAJO, et al. [18F]FDG PET in conditions associated with hyperkinetic movement disorders and ataxia: a systematic review. European Journal of Nuclear Medicine and Molecular Imaging. 2023.
393. Reifschneider A, Robinson S, van Lengerich B, Gnörich J, Logan T, Heindl S, et al. Loss of TREM2 rescues hyperactivation of microglia, but not lysosomal deficits and neurotoxicity in models of progranulin deficiency. EMBO J. 2022;41(4):e109108.
394. Dave A, Hansen N, Downey R, Johnson C. FDG-PET Imaging of Dementia and Neurodegenerative Disease. Seminars in Ultrasound, CT and MRI. 2020;41(6):562-71.
395. Stampanoni Bassi M, Iezzi E, Gilio L, Centonze D, Buttari F. Synaptic Plasticity Shapes Brain Connectivity: Implications for Network Topology. International journal of molecular sciences. 2019;20(24).
396. Lui H, Zhang J, Makinson SR, Cahill MK, Kelley KW, Huang HY, et al. Progranulin Deficiency Promotes Circuit-Specific Synaptic Pruning by Microglia via Complement Activation. Cell. 2016;165(4):921-35.
397. Lopez ME, Klein AD, Scott MP. Complement is dispensable for neurodegeneration in Niemann-Pick disease type C. Journal of neuroinflammation. 2012;9:216.
398. Zhan Y, Paolicelli RC, Sforazzini F, Weinhard L, Bolasco G, Pagani F, et al. Deficient neuron-microglia signaling results in impaired functional brain connectivity and social behavior. Nature neuroscience. 2014;17(3):400-6.
399. Sellgren CM, Gracias J, Watmuff B, Biag JD, Thanos JM, Whittredge PB, et al. Increased synapse elimination by microglia in schizophrenia patient-derived models of synaptic pruning. Nature neuroscience. 2019;22(3):374-85.
400. Evans WR, Hendriksz CJ. Niemann-Pick type C disease - the tip of the iceberg? A review of neuropsychiatric presentation, diagnosis and treatment. BJPsych bulletin. 2017;41(2):109-14.
401. Knox EG, Aburto MR, Clarke G, Cryan JF, O'Driscoll CM. The blood-brain barrier in aging and neurodegeneration. Molecular psychiatry. 2022;27(6):2659-73.

402. Ogawa Y, Sano T, Irisa M, Kodama T, Saito T, Furusawa E, et al. FcRγ-dependent immune activation initiates astrogliosis during the asymptomatic phase of Sandhoff disease model mice. Scientific reports. 2017;7:40518.

403. Yamaguchi A, Katsuyama K, Nagahama K, Takai T, Aoki I, Yamanaka S. Possible role of autoantibodies in the pathophysiology of GM2 gangliosidoses. The Journal of clinical investigation. 2004;113(2):200-8.

404. Politis M, Piccini P. Positron emission tomography imaging in neurological disorders. Journal of neurology. 2012;259(9):1769-80.

405. Werry EL, Bright FM, Piguet O, Ittner LM, Halliday GM, Hodges JR, et al. Recent Developments in TSPO PET Imaging as A Biomarker of Neuroinflammation in Neurodegenerative Disorders. International journal of molecular sciences. 2019;20(13).

406. Liu Y, Jiang H, Qin X, Tian M, Zhang H. PET imaging of reactive astrocytes in neurological disorders. European Journal of Nuclear Medicine and Molecular Imaging. 2022;49(4):1275-87.

407. Fukuda M. Rab27 Effectors, Pleiotropic Regulators in Secretory Pathways. Traffic (Copenhagen, Denmark). 2013;14(9):949-63.

408. Li C, Wei Z, Fan Y, Huang W, Su Y, Li H, et al. The GTPase Rab43 Controls the Anterograde ER-Golgi Trafficking and Sorting of GPCRs. Cell reports. 2017;21(4):1089-101.

409. Jongsma ML, Bakker J, Cabukusta B, Liv N, van Elsland D, Fermie J, et al. SKIP-HOPS recruits TBC1D15 for a Rab7-to-Arl8b identity switch to control late endosome transport. EMBO J. 2020;39(6):e102301.

410. Italiani P, Boraschi D. New Insights Into Tissue Macrophages: From Their Origin to the Development of Memory. Immune Netw. 2015;15(4):167-76.

Acknowledgments

First of all, I would like to thank my supervisor Prof. Dr. Harald Steiner, who supported my whole PhD and was always open for fruitful discussion. You encouraged me to try to understand also the biochemistry behind my results, which one sometimes tend to forget. Another big thank goes to my second supervisor Dr. Sabina Tahirovic. I acknowledge your supervision and your open doors for any question one could have. I appreciate all the time you took for our endless discussions and your support, especially in phases when experiments did not work out and my motivation was at the limit. I am very happy that I carried out my master's and PhD thesis in your laboratory. I could learn and grow a lot under your supervision. Thanks also for all collaborations which you established, by which, I could be part of further publications.

Next, I have to thank Dr. Alessio Colombo. From the first day on, you were teaching me all the techniques I needed for my PhD thesis. I could learn from you how to work efficiently that one always manages to have a coffee break at 3.30 pm. You always brought some fun into my daily life with your remarkable humour and were trying to teach me some proper Italian. I could and still can count on you, which is not self-evident. It was a pleasure to work with you on NPC and I am honoured to share with you the first author of our paper. Furthermore, I would like to thank Dr. Laura Sebastian and Dr. Jasenka Rudan-Njavro. I am so happy that I had you as my colleagues. You were supporting me in any kind of regards, cheering me up, giving me valuable advises and bringing positive energy into the lab. Each day with you was a fun day, regardless how stressful it was. Even the preparation of buffers or PFA was becoming entertaining. Every time we wanted to say goodbye, it ended up in hours of discussions about everything and anything. You are both just awesome! During the last period of this PhD thesis my colleague, Valerio Zenatti, was assisting me in the lab, which I appreciate a lot (and also to make the best coffee in the world). Thank you, Valerio.

I also want to acknowledge Dr. Stephan Müller. I appreciate all your time of explaining me how mass spectrometry works and also how to interpret and analyse the data. You were always answering my random questions about mathematics, statistics or pathway analysis.

A big thank goes to all my other collaborators, who gave valuable input for this thesis and made it possible to publish my first publication and hopefully now also the second one:

Prof. Dr. Matthias Brendel, Selina Hummel, Dr. Martina Fetting, Dr. Ludovico Cantuti-Castelvetri, Dr. Susanne Schneider, Dr. Todd Logan, Dr. Jung Suh, Dr. Gilbert di Paolo, Dr. Andree Schmidt, Dr. Stefan Roth and Brigitte Nuscher,

A major part of science is to discuss your results with other scientists in order interpret the data from different angles. Therefore, I would like to thank my TAC members Prof. Dr. Harald Steiner, Prof. Dr. Stefan Lichtenthaler and Prof. Dr. Michael Strupp, with whom I could discuss critically my data and who gave always valuable feedback. Furthermore, I would like to thank all the people in the Wednesday seminar and Dr. Lars Paeger, who all gave useful ideas for this thesis.

Furthermore, I want to thank all my colleagues from my laboratory and of the laboratory of Prof. Dr. Stefan Lichtenthaler, who emerged a nice working atmosphere with a lot of laughs, pranks and love. Especially during the times of lockdowns, I appreciated to have you as my colleagues. Thank you, Göki, Gözde, Georg, Laura, Marlene, Anna, Andree, Katrin, Stephan B., Stephan M., Anke, Marcel, Ben, Xiao, Iva, Mariagiovanna, Danilo and Sonja. It was of significance to have all of you as my colleague to carry out my PhD successfully. I also would like to thank Sabine Odoy, who was immediately helping us when machines were broken and also taking care of their maintenance. Furthermore, I want to acknowledge all the people working in the animal facility for their support regarding the animals. Especially, I would like to thank Krystyna, who was helping me a lot with my mouse lines.

There are many people who supported me outside of the laboratory. Zuallererst möchte ich meinen Eltern danken. Danke, dass ihr meinen gesamten akademischen Weg unterstützt habt und ihr euch immer um mich gekümmert habt, obwohl ich 250 km weit weg bin. Ich bin sehr dankbar dafür euch als meine Eltern zu haben. Danke für alles! I also want to thank my brother, who is also the most supportive brother one could wish for. Thank you for helping me with any question or problem I had regarding programming obstacles.

Next, I'd like to acknowledge my friends “die Habsburger”, who were by my side throughout my whole academic career. Every time I met you was relieving my stress and showed me what is really important in life. I am more than happy to had you and to have you in my life. Thank you for being you and for all your mental support!

A special thank goes to Julia and Laila, who were always helping me out when I was in difficult situations and were often preparing the most delicious dinner for me. Thanks for all your help!

Lastly, I want to thank Laura del Vecchio, the best dancing teacher in the world. Going to your dancing classes nearly every day after work and during the weekends was of importance for my mental health and cognitive performance at work. Your positive energy and thinking of life were contagious, and helped me a lot for my daily PhD work. If you would not be there, I would not have managed to carry out my PhD without any losses. Thank you!

Author Contributions

I hereby declare that the following authors contributed to the data presented in my thesis as following:

Dr. Alessio Colombo, co-first in Colombo and Dinkel *et al*. [243], performed the EGFR degradation assay, the DQ-BSA trafficking assay, the *ex vivo* myelin phagocytic assay, the validation of the MS analysis via western bot analysis, the PLP1 western blot analysis and the Fluoromyelin staining.

Selina Hummel performed the PET analysis and scRadiotracing.

Dr. Stephan Müller and Dr. Andree Schmidt performed the MS and IPA analysis.

Dr. Martina Fetting performed the EM analysis.

Dr. Stefan Roth performed the rotarod test.

Denali Therapeutics performed the lipidomic analysis.

Affidavit

LMU

LUDWIG-
MAXIMILIANS-
UNIVERSITÄT
MÜNCHEN

Promotionsbüro
Medizinische Fakultät

MMRS

Eidesstattliche Versicherung

Dinkel, Lina

Name, Vorname

Ich erkläre hiermit an Eides statt, dass ich die vorliegende Dissertation mit dem Titel:

Pathological Consequences of NPC1 Loss in Microglia on Brain Function

selbständig verfasst, mich außer der angegebenen keiner weiteren Hilfsmittel bedient und alle Erkenntnisse, die aus dem Schrifttum ganz oder annähernd übernommen sind, als solche kenntlich gemacht und nach ihrer Herkunft unter Bezeichnung der Fundstelle einzeln nachgewiesen habe.

Ich erkläre des Weiteren, dass die hier vorgelegte Dissertation nicht in gleicher oder in ähnlicher Form bei einer anderen Stelle zur Erlangung eines akademischen Grades eingereicht wurde.

München, 22.06.2023

Ort, Datum

Lina Dinkel

Unterschrift Doktorandin bzw. Doktorand

Publications

Research Articles

Colombo A*, **Dinkel L***, Müller SA, Sebastian Monasor L, Schifferer M, Cantuti-Castelvetri L, Koenig J, Vidatic L, Bremova-Ertl T, Lieberman AP, Hecimovic S, Simons M, Lichtenthaler SF, Strupp M, Schneider SA and Tahirovic S. Loss of NPC1 enhances phagocytic uptake and impairs lipid trafficking in microglia. Nature Communications (2021) ;12(1):1158. doi: 10.1038/s41467-021-21428-5. *contributed equally

Rudan Njavro J, Vukicevic M, Fiorini E, **Dinkel L**, Müller SA, Berghofer A, Bordier C, Kozlov S, Halle A, Buschmann K, Capell A, Giudici C, Willem M, Feederle R, Lichtenthaler SF, Babolin C, Montanari P, Pfeifer A, Kosco-Vilbois M and Tahirovic S. Beneficial Effect of ACI-24 Vaccination on Aβ Plaque Pathology and Microglial Phenotypes in an Amyloidosis Mouse Model. Cells (2023) ;12(1):79. doi: 10.3390/cells12010079.

Kunze LH, Ruch F, Biechele G, Eckenweber F, Wind-Mark K, **Dinkel L**, Feyen P, Bartenstein P, Ziegler S, Paeger L, Tahirovic S, Herms J and Brendel M. Long-Term Pioglitazone Treatment Has No Significant Impact on Microglial Activation and Tau Pathology in P301S Mice. International Journal of Molecular Sciences (2023);24(12):10106. doi: 10.3390/ijms241210106.

Dinkel L*, Hummel S*, Zenatti V, Colombo A, Sebastian Monasor L, Paeger L, Roth S, Hoffelner P, Bludau O, Suh J, Logan T, Schmidt A, Fetting M, Nuscher B, Rudan Njavro J, Prestel M, Bartos L, Wind K, Kunte S, Lindner S, Simons M, Lichtenthaler SF, Strupp M, Schneider SA, Di Paolo G, Liesz A, Bartenstein P, Herms J, Grosche A, Matthias Brendel M# and Tahirovic S#. Loss of NPC1 in myeloid cells drives neuroinflammation and leads to neuronal pathology. In preparation. *contributed equally, #shared correspondence.

Poster

Poster at AD/PD 2022 in Barcelona. Abstract title: Loss of NPC1 enhances phagocytic uptake and impairs lipid trafficking in microglia. Authors: **Dinkel L**, Colombo A, Müller SA, Sebastian Monasor L, Schifferer M, Cantuti-Castelvetri L, König J, Vidatic L, Bremova-Ertl T, Lieberman A.P, Hecimovic S, Simons M, Lichtenthaler S, Strupp M, Schneider S and Tahirovic S.

Oral Talks

Talk at AD/PD 2023 in Gothenburg. Abstract title: Loss of NPC1 in myeloid cells drives astrogliosis and neuronal pathology. Authors: **Dinkel L**, Hummel S, Sebastian Monasor L, Paeger L, Schmidt A, Roth S, Bartos L, Wind K, Colombo A, Lichtenthaler S, Liesz A, Herms J, Brendel M and Tahirovic S.